

PHASE STABILITY CONDITIONS OF CARBON DIOXIDE CLATHRATE HYDRATE IN THE PRESENCE OF ETHANOL AND ETHANOL + SALT AQUEOUS SOLUTIONS

Amir H. Mohammadi*

Institut de Recherche en Génie Chimique et Pétrolier (IRGCP), Paris Cedex, France

Received January 6, 2018; Accepted April 23, 2018

Abstract

This work reports the hydrate dissociation conditions of carbon dioxide in the presence of ethanol and ethanol + NaCl, KCl, CaCl₂, MgCl₂ aqueous solutions in the temperature and pressure ranges of (268.0 - 281.9)K and (1.39 - 4.10) MPa, respectively. The concentration of ethanol in aqueous solution was 0.1 mass fraction and the concentration of salt was 0.1 mass fraction. The equilibrium data were generated using an isochoric pressure-search method. These data are compared with the experimental data on hydrate dissociation conditions of carbon dioxide in the presence of pure water to prove the inhibition effects of the aforementioned aqueous solutions. It is shown that the studied aqueous solutions have thermodynamic inhibition effects on carbon dioxide clathrate hydrate.

Keywords: Gas hydrate; Ethanol; NaCl; KCl; CaCl₂; MgCl₂.

1. Introduction

Gas hydrates, or clathrate hydrates, are icelike crystalline compounds in which a small molecule(s), like carbon dioxide, methane, etc. is trapped in special cages of hydrogen-bonded water molecules under low-temperature and high pressure conditions. Pipeline blockages and other operational problems in petroleum industry can be blocked by formation of gas hydrates. Aqueous solutions of glycols and alcohols are typically used to inhibit formation of gas hydrates. The presence of salt in produced brine can also inhibit formation of gas hydrate. Knowledge of gas hydrate phase equilibria in the presence of aqueous solutions of glycol, alcohol and/or salt is important to estimate gas hydrate formation conditions. A study indicates that most of the latter data have been reported for methane hydrate dissociation conditions in the presence of salt and/or organic inhibitor aqueous solutions [1]. To the best of our knowledge, limited information is available in literature on carbon dioxide hydrate dissociation conditions in the presence of ethanol aqueous solutions [2] and there is no information on carbon dioxide hydrates dissociation conditions in the presence of ethanol + salt aqueous solutions. The latter experimental data could be important in developing predicting tools with the aim of studying the hydrate stability zones of sour reservoir fluids [1].

In this communication, we report carbon dioxide hydrate dissociation conditions in the presence of ethanol and ethanol + salt (NaCl, KCl, CaCl₂, MgCl₂) aqueous solutions at 0.1 mass fractions of ethanol and ethanol in the temperature and pressure ranges of (268.0 - 281.9) K and (1.39 - 4.10) MPa, respectively. The equilibrium data were generated using an isochoric pressure-search method [1-11]. The data reported in this study are compared with the experimental data on carbon dioxide hydrate dissociation conditions in the presence of pure water to study the inhibition effects of the aforementioned aqueous solutions.

2. Experimental section

2.1. Chemicals

The purities and suppliers of the chemicals used in this work are reported in Table 1. Aqueous solutions were prepared following the gravimetric method, using an accurate analytical balance (mass uncertainty ± 0.0001 g).

Table 1. Purities and suppliers of the chemicals*

Chemical	Supplier	Purity (%)
Carbon dioxide	Air Products	99.9
NaCl	Sigma Aldrich	99.5
KCl	Sigma Aldrich	99.5
CaCl ₂	Merck	98
MgCl ₂	Merck	98

* Deionized water was used in all experiments

2.2. Experimental apparatus

Briefly, the main part of the apparatus is a cylindrical vessel made of stainless steel, which can withstand pressures up to 10 MPa. The vessel has a volume of 57.5 cm³. A stirrer ensures sufficient agitation to facilitate reaching equilibrium. One platinum resistance thermometer (Pt100) inserted into the vessel is used to measure temperature within temperature measurement uncertainty, which is estimated to be less than 0.1 K. The pressure in the vessel is measured with a pressure transducer. Its accuracy is estimated to be better than 5 kPa.

2.3. Experimental method

Using an isochoric pressure-search procedure, the hydrate dissociation points were measured [1-11]. The vessel containing the aqueous solution (approximately 20 % by volume of the vessel was filled with the aqueous solution) was immersed into the temperature controlled bath, and the gas was supplied from a cylinder through a pressure regulating valve into the vessel. The vessel was evacuated before introducing any aqueous solution and gas. After getting temperature and pressure stability (far enough from the hydrate formation region), the valve between the vessel and the cylinder was closed. Subsequently, the temperature was slowly decreased to form the hydrate. Hydrate formation in the vessel was observed when a pressure drop at constant temperature was detected in a computer connected to a data acquisition unit. The temperature was then increased with steps of 0.1 K. At every temperature step, the temperature was kept constant with enough time to obtain an equilibrium state in the equilibrium cell [2-9]. Therefore, a pressure-temperature diagram was sketched for each experimental run, from which we determined the hydrate dissociation point [2-9]. During the dissociation of the hydrate crystals inside hydrate formation region, the pressure is gradually increased by increasing the temperature. However, outside this region, slighter pressure increase is observed during increase of temperature. Consequently, the hydrate dissociation point can be determined when the slope of the pressure-temperature diagram changes suddenly [2-9]. The maximum uncertainties for the hydrate dissociation temperatures and pressures are expected to be ± 0.1 K and ± 0.05 MPa based on our previous studies [2-9].

3. Results and discussion

Table 2 and Figure 1 report the experimental data. A semi-logarithmic scale has been used in this figure to show the data consistency, as the logarithm of hydrate dissociation pressure versus temperature has approximately linear behaviour [1].

In this figure, some selected experimental data from the literature on carbon dioxide hydrate dissociation conditions in the presence of pure water [10] have also been reported to prove thermodynamic inhibition effects of the studied aqueous solutions. The inhibition effect results in shifting hydrate dissociation conditions to high pressures/low temperatures due to

the presence of inhibitor in aqueous solution. On the other hand, satisfactory agreement between our data and the data reported in reference [10] for the carbon dioxide + water system proves the reliability of the experimental method employed in this work.

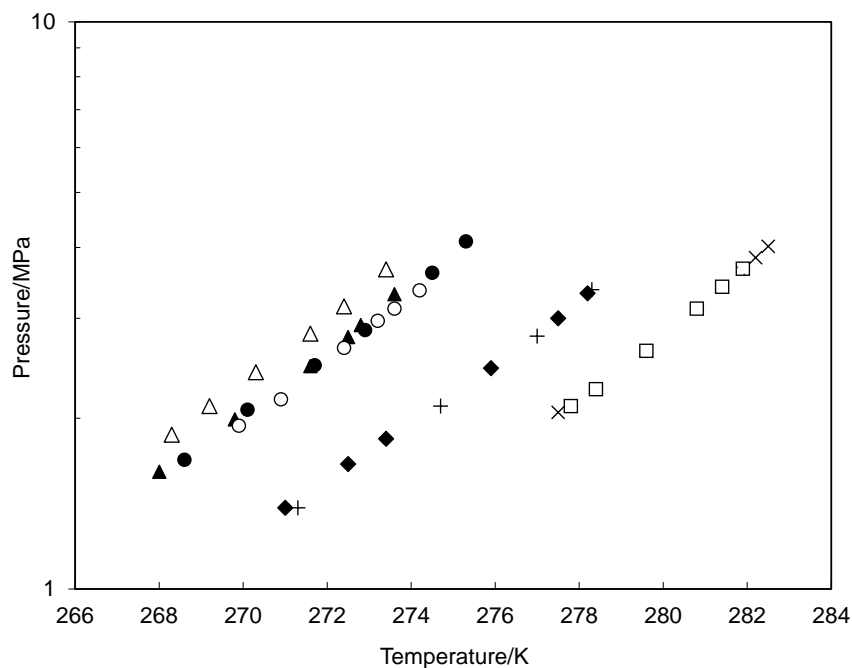


Figure 1. Carbon dioxide hydrate dissociation conditions in the presence of pure water, ethanol and ethanol + NaCl/ KCl/CaCl₂/MgCl₂ aqueous solutions. Symbols represent hydrate dissociation conditions. Carbon dioxide + water system: □, this work, ×, [10]. Carbon dioxide + 0.10 mass fraction ethanol + water system: ♦, this work, +, [2]. Carbon dioxide + 0.10 mass fraction ethanol + 0.10 mass fraction NaCl + water system: ●, this work. Carbon dioxide + 0.10 mass fraction ethanol + 0.10 mass fraction KCl + water system: ▲, this work. Carbon dioxide + 0.10 mass fraction ethanol + 0.10 mass fraction CaCl₂ + water system: ○, this work. Carbon dioxide + 0.10 mass fraction ethanol + 0.10 mass fraction MgCl₂ + water system: Δ, this work

Table 2. Carbon dioxide hydrate dissociation conditions in the presence of pure water, ethanol and ethanol + NaCl/ KCl/CaCl₂/MgCl₂ aqueous solutions.*

Temperature/K	Pressure/MPa	Temperature/K	Pressure/MPa	Temperature/K	Pressure/MPa
Pure water		0.10 Mass Fraction Ethanol + 0.10 Mass Fraction NaCl		0.10 Mass Fraction Ethanol + 0.10 Mass Fraction CaCl ₂	
277.8	2.10	268.6	1.69	269.9	1.94
278.4	2.25	270.1	2.07	270.9	2.16
279.6	2.63	271.7	2.48	272.4	2.66
280.8	3.12	272.9	2.86	273.2	2.97
281.4	3.41	274.5	3.61	273.6	3.12
281.9	3.67	275.3	4.10	274.2	3.36
0.10 Mass Fraction Ethanol		0.10 Mass Fraction Ethanol + 0.10 Mass Fraction KCl		0.10 Mass Fraction Ethanol + 0.10 Mass Fraction MgCl ₂	
271.0	1.39	268.0	1.61	268.3	1.87
272.5	1.66	269.8	1.99	269.2	2.10
273.4	1.84	271.6	2.47	270.3	2.41
275.9	2.45	272.5	2.78	271.6	2.82
277.5	3.00	272.8	2.92	272.4	3.15
278.2	3.32	273.6	3.31	273.4	3.66

Figure 1 indicates that data on carbon dioxide hydrate dissociation conditions in the presence of ethanol aqueous solution (0.10 mass fraction) are limited. The latter experimental

data is found in acceptable agreement with the previously reported data [2]. It should be mentioned that it has been previously reported that ethanol behaves as thermodynamic promoter rather than thermodynamic inhibitor at its high concentrations in aqueous solution (typically higher than 0.15 mass fraction) [11]. Therefore no attempt was done in the present work to study high concentrations of ethanol in aqueous solutions.

As can be observed in Figure 1. the presence of the studied salts (0.10 mass fraction) in ethanol aqueous solution (0.10 mass fraction) leads to more thermodynamic inhibition effects on carbon dioxide hydrate. In particular. MgCl₂ leads to more thermodynamic inhibition effect in comparison with other salts. NaCl. KCl and CaCl₂ have similar thermodynamic inhibition effects on hydrate formation in the carbon dioxide + 10 mass fraction ethanol + water system.

4. Conclusion

Carbon dioxide hydrate dissociation conditions in the presence of ethanol and ethanol + NaCl. KCl. CaCl₂. MgCl₂ aqueous solutions are reported in the temperature and pressure ranges of (268.0 - 281.9) K and (1.39 - 4.10) MPa. respectively. The aqueous solutions studied in this work show thermodynamic inhibition effects on carbon dioxide hydrate formation. Presence of the studied salts in ethanol aqueous solution increases thermodynamic inhibition effect and MgCl₂ leads to more inhibition effect. Similar thermodynamic inhibition effects on hydrate formation in the carbon dioxide + 10 mass fraction ethanol + water system are observed when using NaCl. KCl and CaCl₂ in ethanol aqueous solution.

References

- [1] Sloan ED. Koh CA. *Clathrate Hydrates of Natural Gases*. Third Edition. CRC Press. Taylor & Francis Group. Boca Raton. 2008.
- [2] Mohammadi AH. Richon D. *J. Chem. Eng. Data*. 2008; 53(2): 73 - 76.
- [3] Mohammadi AH. Richon D. *Ind. Eng. Chem. Res.*, 2009; 48: 7847-7851.
- [4] Mohammadi AH. Richon D. *J. Chem. Thermodynamics*. 2012; 44: 26-30.
- [5] Mohammadi AH. Richon D. *J. Chem. Eng. Data*. 2009; 54: 2338-2340.
- [6] Ohmura R. Takeya S. Uchida T. Ebinuma T. *Ind. Eng. Chem. Res.*, 2004; 43: 4964-4966.
- [7] B Tohidi. RW. Burgass. A Danesh. KK Østergaard. AC. Todd. *Ann. N.Y. Acad. Sci.*, 2000; 912: 924-931.
- [8] Mohammadi AH. Richon D. *J. Chem. Eng. Data*. 2011; 56: 5094-5097.
- [9] Mohammadi AH. Richon D. *Ind. Eng. Chem. Res.*, 2010; 49: 8865-8869.
- [10] Mohammadi AH. Andersen R., Tohidi B. *AIChE J.*, 2005; 51(10): 2825-2833.
- [11] Anderson R. Chapoy A. Haghghi H. Tohidi B. *J. Phys. Chem. C*. 2009; 113(28): 12602-12607.

To whom correspondence should be addressed: Amir H. Mohammadi. Institut de Recherche en Génie Chimique et Pétrolier (IRGCP). Paris Cedex. France.

OIL SLUDGE AS SOURCE OF A VALUABLE CARBON RAW MATERIAL

*Aleksey Mardupenko, Andrey Grigorov, Irina Sinkevich, Alena Tulskaya**

National Technical University "Kharkiv Polytechnic Institute", Kharkiv, Ukraine

Received January 17, 2018; Accepted April 23, 2018

Abstract

General trends of recovery of oil sludge into the commodity products are presented below. The technology of concentrating of the carbon part of oil waste was justified. The sequence of processes for refining of sludge into the road and construction bitumen, antiseptic and waterproof materials and lubes was presented as a structural scheme.

Keywords: *oil sludge; waste; refining; ecology; bitumen.*

1. Introduction

Oil sludge is the type of the common industrial waste, which considerably pollutes the environment. It appears during the exploitation of oil comprehensive treatment units and directly at the oil processing units. The general direction of the oil refineries development strategy is both decreasing of the harmful influence of the oil waste and increasing of the oil refining level. Therefore, oil sludge can be involved into the technological refining of carbon materials, which aims to the production of the different commodity components and goods.

Oil sludge is very hazardous due to its high toxicity (it pollutes rivers and ground water, soil and plants, atmosphere). It appears as a result of technological equipment exploitation (in vessels, pump stations, pipes etc.) and it is a water-oil emulsion mixed with the various mechanical admixtures (organic and inorganic). The stability of this system depends on its storage duration. During the storage light hydrocarbon fractions may be evaporated from the sludge and the amount of mechanical admixtures, which enter into sludge from the atmospheric dust may be decreased. It should be mentioned that the origin and composition of sludge will define the way of its utilization.

The simplest way of sludge utilization is the burning in the incinerators, which have special construction. A significant amount of ash, carbon dioxide and other dangerous gases appear during the burning. A valuable hydrocarbon raw material is used for production of electrical energy and another technological issues.

Considering the long world experience in the sludge processing, we can present the following perspective directions, which allow to obtain valuable commodity products as a structural scheme (fig. 1).

Shperber [5] describe the fuel composition for boiler, it has low viscosity, high stability, low corrosion activity and includes mazut, oil sludge and the waste of coal refining – pyrogenetic water. The components percentage in this composition is: oil sludge – 30-70 % (mass), pyrogenetic water – 0.5 – 5 % (mass), mazut is all the rest. The oil sludge is taken from the oil tank and contains 10-20 % of water. Vapour at a temperature about 363 – 368 K passes through the fuel composition, which should be emulsified for up to 20 – 30 minutes. The proposed composition can also be applied as a technological fuel, including at the heating supply companies. The composition includes oil sludge (60 % mass), heating oil (30 % mass), and kerosene or diesel fuel (10 % mass) [6]. There is also well-known a fuel composition, that contains fuel trap product (10 – 70%), heavy gas oil (30 – 90 %) as a product of catalytic

cracking or slow coking and heavy pyrolysis tar or fuel additives and home heating oil. The composition is obtained by mixing of fuel trap product with heavy gas oil and heating oil at a temperature about 300 – 325 K.

There is a high-stable fuel for heating room that contains oil sludge and sodium carboxylate in 1: (1-3) ratio in a general part of coal dust (40 – 60 %). Oil sludge can also be applied in the production of fuel briquettes for the communal-general needs, when the peat and the coal dust are mixed up to the homogeneous mass with the following adding of plasticizers in the amount of about 4 % (mass.). After that the mixture is soaked until it gets tight-plastic consistency, then it goes to the press where the fuel briquettes are formed under pressure up to 2.5 MPa. [\[9\]](#)

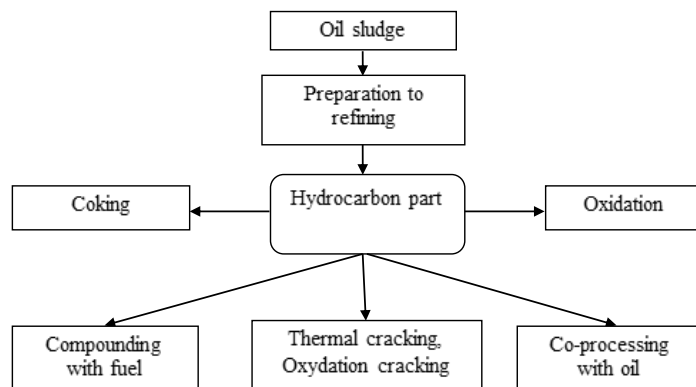


Fig. 1. Perspective directions of sludge processing

Hence, the hydrocarbon part of the oil sludge can be used as a valuable source for thermo-destructive processes of refinery that aim production of high-quality motor and boiler fuels components. Thereby we should consider the thermal cracking of oil sludge [\[10\]](#) which implies feeding of the sludge with an active hydrogen-donor additives as a raw material and its heat treatment in the cracking zone. Water may be applied as a hydrogen-donor additive, the raw material goes to the cracking zone as an oil-water emulsion under the supercritical pressure (about 22.5 – 35 kPa) and temperature about 600 – 750 K. The final products of cracking are gas C1 – C4 (1 % mass); low-boiling component (8 % mass, boiling point – about 430 K): fraction 430 -630 K (64 % mass); fraction 630-770 K (12 % mass); fraction above 770 K (15 % mass). The production of light distillate fraction can be possible through the thermal cracking and consecutive decreasing of the raw material temperature [\[11\]](#)

Then sludge is treated by the gas burner to get heated through the whole volume. Gas burner has a temperature about 780 K and the power density about 20 kW/m². The process also implies tanks for sludge and residue, tube furnace for sludge, pumps, reactors and furnace for inert gases. The emanating screen is placed inside the reactor and its surface is parallel to the oil sludge surface, the screen is heated up by the gas burner and the distance between screen and liquid surface is 30 – 300 mm. The sludge can be pretreated by waves through formation of wide frequency spectrum (from acoustic to light range in the treated area).

This process is followed by thermal cracking at 633 K and atmospheric pressure which leads to production of gaseous final products [\[12\]](#). There is also a way of oil sludge refining through the atmospheric thermal cracking at about 623 – 673 K in the cavitation zone in the electrical field with the strength about 0.5 – 2.0 kV/sm. Then gaseous and liquid products are mixed in the buffer vessel for transportation through the main pipeline.

There is also the technology of oxidation cracking of heavy oil sludge that includes pretreatment of sludge with removing of admixtures and heating up to 723 K. Then sludge is treated by the heated air (T = 800 K) and thermal cracking in the remote reactor (pressure in the reactor is about 0.12 MPa). The further stage is separation of the light oil fractions. Heavy residual product of the thermal cracking goes to the hardening machine or evaporation column [\[14\]](#).

Application of oil sludge as a binding component in the preparation of blend for half-coking of solid fuels [3] of at the slow-coking equipment where sludge is heated up and mixed with a recirculated material (heavy coking gasoil), the obtained secondary product is also heated up to 650 – 660 K and goes to the coking chamber. The coke and distillate are products of coking. Distillate goes to the rectification column for extracting of the light fractions and distillation residues.

Technical literature contains an information about methods of refining through oxidation and compounding which aim the production of components for road, construction and waterproof materials.

There is a technology of bitumen production by pretreatment of oil sludge (water content is less than 5 % mass, mechanical admixtures – less than 16.4 % mass), then raw material is separated into 2 flows, one of those flows is consistently heated up to 470 – 500 K with simultaneous light fractions stripping, then it is oxidized by the air at about 500 K throughout 6 – 20 hours for obtaining the oxidized tar. The second flow is heated to 480 – 650 K in the inert gas atmosphere.

The other part of the prepared raw material is heated up in the inert gases (nitrogen, argon etc.) to 500 – 660 K. That leads to the obtaining of vacuum tar with the simultaneous stripping of light and heavy petroleum products. Light and heavy petroleum fractions may be applied as a thinner or heating oil and as a raw material for cracking or hydrotreatment at the refineries. Then we calculate numerous indicators of oxidized and vacuum tar for their applying as the raw bitumen according to the RB 20/40. Analyzing these results according to the required properties of the commodity bitumen we can define the proportion of the oxidized and vacuum tar. After that tar will be compounded at 430 – 500 K [16]. Syroezhko [17] propose the composition for production of the cold asphalt concrete. The composition contains binding agent that includes sand (crushed granite), oil sludge (dehydrated, organic part is 60 – 80 % mass, mineral part – 2-4 % mass, sulphur – 3-5 % mass, water – the other) and bitumen. Also the binding agent may contain limestone mineral powder (5-6 % mass). There is also a composition of a cold asphalt concrete that includes bitumen, sulphur-containing fractions and oil sludge in the following ratio: bitumen МГ 70/130 – 6-6.5 %, sulphur-containing fractions 0-5 mm – 98-99 % mass, oil sludge – 1-2% mass [18]. The authors of [19] describe the material, which can be applied for waterproofing of underground structures, foundations and roofs. It contains of oil sludge (50-65 %), and filler (20 – 40 % mass) – clay or grinded expanded clay.

2. Further development of sludge refining processes

Analyzing the foregoing information it should be mentioned that processing of the oil sludge into the road and construction (e.g. waterproof elements) materials is the most reasonable from technical and economical point of view. This kind of processing implies simple equipment and operation practices. The presence of mechanical admixtures and water doesn't make negative effect. Thereby we propose the structural scheme of complex sludge processing (fig. 2) that stipulates particular separation of water and mechanical admixtures.

Water may be either applied as a technical circulating agent in the water cooling devices or in the oxidation column for temperature decrease and admixtures may be added to the commodity products as the filler or may be utilized on the landfills. The hydrocarbon agent which is released after preparation, contains paraffin-naphthenic hydrocarbons (30 – 50 % mass), cyclic aromatic hydrocarbons (25 – 29 % mass), tar (17 – 27 %), asphaltenes (4 – 14 % mass) [20]. The tar, asphaltenes, aromatic and paraffin hydrocarbons may be oxidized by air and solidified and that obstacle encourage the production of the high-quality bitumen. Thereby hydrocarbon component may be either oxidized in the column for production of commodity bitumen or be concentrated. During the concentration of the hydrocarbon component we can obtain atmospheric or vacuum concentrate (depending of the pressure) with the boiling point about 630-700 K and fuel fractions which can be applied as the components for motor and

boiler fuel. During the further processing bitumen enriched by adding the polymer components, fillers and fuel additives to increase its frost and wear resistance.

Then we add polymer component, fillers and fuel additives to the bitumen base, obtained by concentration ($T = 420 - 600$ K, constant mixing). After the 30 min heat treatment bitumen base turns into bitumen which can be qualified as classical oxidized bitumen.

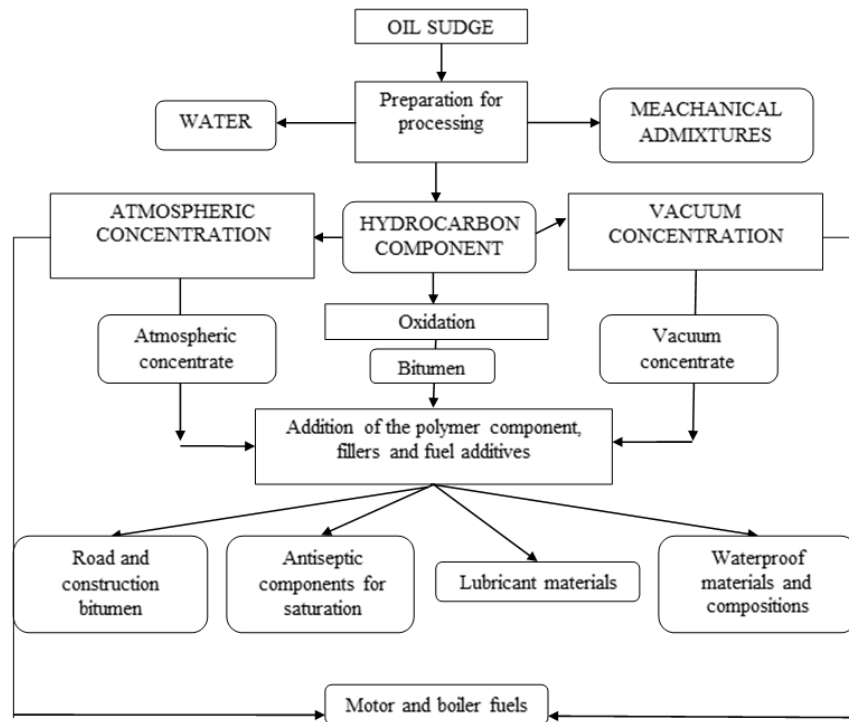


Fig 2. The structural scheme of complex sludge processing

The proposed scheme allows to obtain lubricants, antiseptic and waterproof materials by changing the concentration and chemical formula of the polymer component. It may be also applied for the processing of used motor oil, acid tar, oil fraction waste. The sequence of technological processes should be varied depending of the final products quality.

3. Conclusion

Using the long experience in the processing of oil sludge we have developed the principal scheme for production the antiseptic, waterproof materials and stable construction bitumen with a high adhesive and thermal strength. One of the most important point of the scheme is applying of the non-expensive and simple equipment, soft technological mode which allows to decrease the energy costs and, as a result – the cost price of the commodity product.

References

- [1] Official website of West Dala, LLP: <http://www.westdala.kz>.
- [2] Mazlova YeA. Problemy utilizatsii neftshlamov i sposoby ih pererabotki. Noosfera, 2001:p.52.
- [3] Gromov SN. Perspektivy sovmestnoy termicheskoy pererabotki neftshlamov (kislykh gudronov) i tverdykh goryuchikh iskopaemykh. Vestnik Sankt-Peterburgskogo gosudarstvennogo tekhnologicheskogo instituta (tekhnicheskiy universitet). 2014; 23: 69-71.
- [4] Shrubok AO. Perspektivy ispolzovaniya neftshlama v sostave toplivnoy kompozitsii. Trudy BGTU. Khimiya, tekhnologiya organiceskikh veshchestv i biotekhnologiya. 2010; 18: 57-60.
- [5] Shperber EA, RF Patent 2461606, 2012.
- [6] Kovalev SP, RF Patent 2411287, 2011.
- [7] Kuzora IE, RF Patent 2252244, 2005.
- [8] Shperber BE, RF Patent 2553998, 2016.

- [9] Agafonov RK, RF Patent 2174535, 2007.
- [10] Shukin VA. Sposob termicheskogo krekinga tyazhelykh nefteproduktov "ITER" [METHOD OF THERMAL CRAKING OF HEAVY OIL PRODUCTS "ITER"]. Patent RF, 2354681, 2009.
- [11] Chindyskin VA., RF Patent 2204583, 2003.
- [12] Nekipelov VM., RF Patent 2010117292, 2010
- [13] Nekipelov VM. RF Patent WO2010117292 A1, 2010
- [14] Galiev RG. RF Patent 2335525, C10G9/00, 2008.
- [15] Tausheva EV. RF Patent 2495088, C10B55/00, 2011.
- [16] Sukhonosova AN. Osnovnye napravleniya kvalifitsirovannogo ispolzovaniya kubovykh ostatkov vydeleniya dizelnykh fraktsiy iz neftesoderzhashchikh otkhodov. Ekologiya i promyshlennost Rossii. 2011; 12: 10-14.
- [17] Syroezhko AM. RF Patent 2535325, C08L95/00, 12.10.2014.
- [18] Sheina TV. RF Patent 2174498, C04B26/26, C08L95/00, 2001.
- [19] Shperber RE. RF Patent 2174498, C04B26/26, C08L95/00, 2001.
- [20] Desyatkin AA. Razrabotka tekhnologii utilizatsii neftyanykh shlamov [Development of the oil sludge disposal technology] (PhD Thesis), Ufa 2004.

To whom correspondence should be addressed: Dr. Alena Tulskaya, National Technical University "Kharkiv Polytechnic Institute", Kharkiv, Ukraine, fuel.khpi@gmail.com

EVALUATING THE ABILITY OF R FOR MODELING A COMMERCIAL SCALE VGO HYDROCRACKING PLANT USING ARTIFICIAL NEURAL NETWORK (ANN)

Sepehr Sadighi*, Seyed Reza Seif Mohaddecy

Research Institute of Petroleum Industry (RIPI), Catalysis Technologies Development Division, P.O. Box 14665137, Tehran, Iran

Received January 21, 2018; Accepted April 23, 2018

Abstract

This research is devoted to evaluating the ability of R software to model an industrial scale vacuum gas oil (VGO) hydrocracking plant using ANN (artificial neural network) modeling approach. R is an open source program for statistical computation and graphics that consists a language plus a run-time environment, and access to certain system functions. The input layer of ANN model developed for VGO hydrocracking plant consists age of catalyst, flow rates of fresh VGO and recycle streams and inlet temperatures of catalytic beds. Moreover, neurons in the output layer of ANN are yield of products including light gases (Gas), liquefied petroleum gas (LPG), light naphtha (LN), heavy naphtha (HN), kerosene (Ker) and diesel (Dis). Networks are trained and tested based on 68 data points gathered from the target commercial scale plant using 'neuralnet' package obtained from the CRAN repository. From results, it is concluded that R can predict product yields of all unseen data with high accuracy; therefore, it is an alternative for modeling chemical engineering processes without requiring any license or charges for an activation code.

Keywords: Modeling; Artificial Neural Network; Vacuum gas oil; Hydrocracking; R software.

1. Introduction

Process modeling is a computed based procedure that generally comprises using software to determine a system of interconnected elements which should be solved simultaneously so that the steady-state or dynamic nature of the system can be explained. These models are strictly demanded in favor of effective design, perfect control and predict product yields and qualities versus variables such as space velocity and temperature [1].

Within the field of chemical process modeling and simulation, the use of artificial neural networks (ANN) has evolved for a diverse range of engineering applications such as fitting experimental data, machine diagnostics, pattern recognition, quality control, signal processing, and process control, all topics of interest to chemists and chemical engineers [2]. ANNs represent the massive parallel interconnections of a simple neuron that functions as a collection system, and they are designed in an attempt to mimic the human brain in order to emulate human performance, i.e., to function intelligently [3]. ANNs have the advantage that they employ non-linear basis functions, and therefore are able to approximate far more complex non-linear behavior. Furthermore, they are fast and have very small requirements in terms of storage space and retrieval time, as all that needs to be stored is the coefficients of the approximation model [4]. In this technique, based on information compiled from the process and without any needs for identifying the physical and chemical characteristics of feed and products, desired outputs such as yield or conversion can be simulated [5].

ANNs have been extensively applied for modeling various chemical engineering processes [6-19]. In most of these studies, Neural Network (NN) Toolbox of Matlab software (Mathworks, Inc.) has been used to create, train, test, validate and visualize neural networks. The validity, reliability, robustness, and resiliency of NN Toolbox have been reported previously in many

studies, and there is no doubt about it. However, MathWorks products are regulated to use in support of academic and instructive activities, and the right to utilize these products for commercial purposes is absolutely prohibited. Hence, having a substitution for this powerful software, especially when acquiring the license for Matlab (international sanctions or financial problem for purchasing the license), is so beneficial, encouraging and promising.

As an option, R is free and open source software, authorizing anyone to apply and modify it. R can be seen as a dialect of S language (developed at AT&T) for which John Chambers was awarded the 1998 Association for Computing Machinery (ACM) software [20]. This software is licensed under the GNU General Public License, with copyright held by The R Foundation for Statistical Computing. It has about 5000 packages accessible from assorted repositories that study intensively in topics such as an artificial neural network (ANN), the adaptive neuro-fuzzy system (ANFIS), stochastic boosting, data mining, nonlinear optimization, and bio-informatics.

To evaluate and examine the validity and reliability of ANN models implemented in R, the present study uses ANN modeling techniques to predict the yield of products in an industrial scale VGO hydrocracking plant. Based on the actual data obtained from the target plant, feed-forward structures are composed of 7, 3 and 1 neurons in the input, hidden and output layers, respectively. After training the constructed ANN model by accessible R packages, the capability of the developed network to predict yields of hydrocracking products is tested.

2. Process description

Table 1. Specifications of the fresh VGO in the target process [19]

Variable	Unit	Value
Fresh feed flow rate	m ³ /h	163.7
Density	kg/m ³	911
Total sulfur	wt%	1.4
ASTM Distillation, D1160		
IBP	°C	333
10%	°C	389
30%	°C	414
50%	°C	434
70%	°C	453
90%	°C	481
FBP	°C	500

In the target hydrocracking process, the VGO feed (see Table 1) obtained from the vacuum distillation tower is mixed with unconverted oil (offtest), and then is mixed with hydrogen. This flow is passed through heat exchangers and heaters (Figure 1), and it is introduced to three parallel reactors which each of them have four catalytic fixed beds. They contain 15%, 25%, 30% and 30% of the total catalyst weight percentage, respectively. In the first bed, hydrotreating reactions are carried out to remove sulfur, nitrogen and metal compounds. The second, third and fourth catalytic beds often perform the hydrocracking reactions.

Along the hydrocracking reactor, quenching systems are provided for the purpose of controlling exothermic reactions (hydrotreating and hydrogenation). This facility injects hydrogen into the output stream leaving 1st, 2nd and 3rd beds to reduce its temperature, and therefore preserve the catalyst from excessive coke formation.

Furthermore, at the top of the reactor, ceramic balls are used to distribute the feed, and also prevent from the entrance of physical impurities into the reactor. The product, after passing through heat exchangers and air coolers, enters the high pressure separator (HPS). The hydrogen gas leaving HPS with the purity of 86.3 mol% is mixed with the make-up hydrogen (purity of 96.5 mol%), and then its major part is added to the feed of the reactor. The other fraction of this stream is injected between the catalytic beds to control the reaction temperature.

The effluent of HPS enters the low pressure separator (LPS) and is separated into two streams, i.e., sour gas and liquid product. The former enters the desulfurization unit, and the latter is introduced to the debutanizer tower. The liquid product leaving this tower enters the main fractionation column to obtain the hydrocracking products, i.e., light gas, LPG, light and heavy naphtha, kerosene, and diesel.

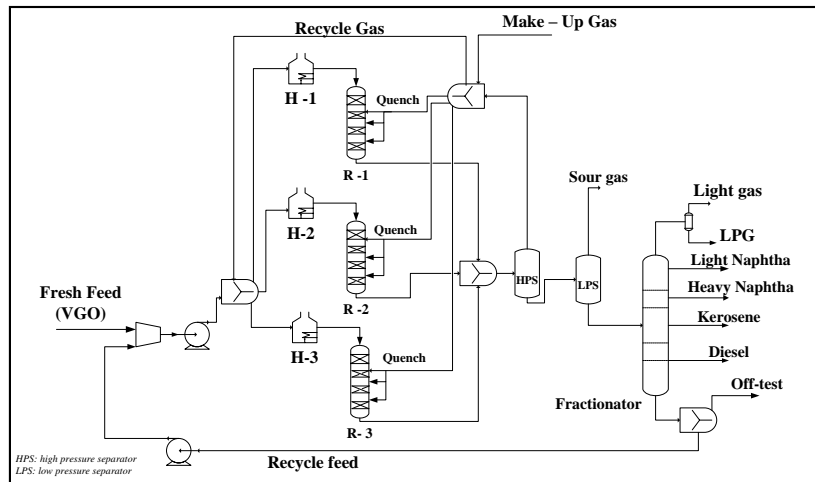


Figure 1. Block flow diagram (BFD) of the target VGO hydrocracking plant [19]

3. Developing the artificial neural network model in the R environment

R is a language and environment for statistical computing and graphics which was developed at Bell Laboratories (formerly AT&T, now Lucent Technologies) by John Chambers and colleagues. R provides a wide variety of statistical (linear and nonlinear modelling, classical statistical tests, time-series analysis, classification, and clustering) and graphical techniques, and is highly extensible. The advantage of using this software is its availability as free software under the terms of the Free Software Foundation's GNU General Public License in source code form.

In this research, neural networks for predicting yields of VGO hydrocracking products including light gases (Gas), liquefied petroleum gases (LPG), light naphtha (LN), heavy naphtha (HN), kerosene (Ker) and diesel (Dis) are implemented in R software (Version 3.4.1, Copyright 2017). The package 'neuralnet' (Version 1.33) obtained from the CRAN repository is applied to develop and construct the corresponding ANN models. This package permits resilient settings through custom-choice of error and activation function, and also the calculation of generalized weights [21] is implemented. The globally convergent algorithm of 'neuralnet' is based on the resilient back-propagation without weight back-tracking and additionally modifies one learning rate, either the learning rate associated with the smallest absolute gradient [22].

The most widely employed networks have one hidden layer only. Each node within a given layer is connected to all of the nodes of the previous layer. The node sums up the weighted inputs and bias, and it passes the result through a linear function as follows [23]:

$$a_j = \sum_{i=0}^m w_{ji} y_i + b_j \quad (1)$$

where w_{ji} is the weight that goes from the input (i) to the hidden neuron (j); b is the bias to the node, and y_i is the input unit of the neuron. By utilizing an activation function (f), the output of the neuron can be written as follows:

$$Z_j = f(a_j) \quad (2)$$

By using 'neuralnet' package, a feed-forward ANN with one hidden layer is developed to simulate the target industrial scale VGO hydrocracking plant. The input layer of the ANN model consists of catalyst (Age), volume flow rates of fresh VGO (Vflow) and recycle stream (Rflow) and temperature of the catalytic beds (i.e., Tb1, Tb2, Tb3, and Tb4). The output layer has one node which is the yield of the intended hydrocracking products. For each of them, an individual neural network is constructed. It should be mentioned that to prevent from memorizing instead of learning, only 3 neurons are selected for the hidden layer such that the number of coefficients is less than the number of actual data. To evaluate the accuracy

of the model, the absolute average deviation (AAD%) between the actual and predicted data is calculated as follows:

$$AAD\% = \frac{\sum_{n=1}^{N_t} \sqrt{\frac{(y_n^{actual} - y_n^{model})^2}{y_n^{actual}^2}}}{N_t} \times 100 \quad (3)$$

where y and N_t are output variables (i.e. yield of hydrocracking products) and number of data points, resp.; superscripts actual and model show the actual (or real) and the predicted values, resp.

4. Results and discussions

During the period of data collection (about 557 days), 69 valid points are obtained which is randomly divided into two categories including training and testing datasets by using the 'sample' command of the R software. These groups consist 41 and 28 data points (60% and 40% of total data), respectively. All data points are scaled based on the maximum and minimum values of the actual data. In the next step, up to reaching the minimum relative mean squared error (RMSE), networks are trained by using 'neuralnet' package installed in the R environment. The number of iterations, AAD% of training and testing datasets for a yield of hydrocracking products, i.e. Gas, LPG, LN, HN, Ker, and Dis are presented in Table 2, respectively. From this table, it can be concluded that R can learn the pattern of hydrocracking yields satisfactory with an acceptable number of iterations (less than 200). The total CPU time for training each network is less than 1 sec which can be an advantage for developing ANNs using R software.

Table 2. Number of iterations and AAD% of training and testing data for VGO hydrocracking neural networks

Product	AAD%_train	Steps	AAD%_test
Gas	0.0672	192	0.0923
LPG	0.172	174	0.302
LN	0.175	183	0.366
HN	0.183	134	0.295
Ker	0.114	82	0.164
Dis	0.184	189	0.315

of training data, and resiliency of the ANN model.

Structures (topology) of ANNs which are constructed by R for Gas, LPG, LN, HN, Ker, and Dis are illustrated in Figures 2 to 7, respectively. As seen, each network has 24 weights and 4 biases, totally 28 coefficients. As mentioned before, for training a network, there are 41 data points for the yield of each hydrocracking product. Hence, the degree of freedom (DOF) for each ANN is equal to 17. This positive DOF fairly prevents from memorizing (over learning) instead of training. However, increasing the number of data points enhances the reliability

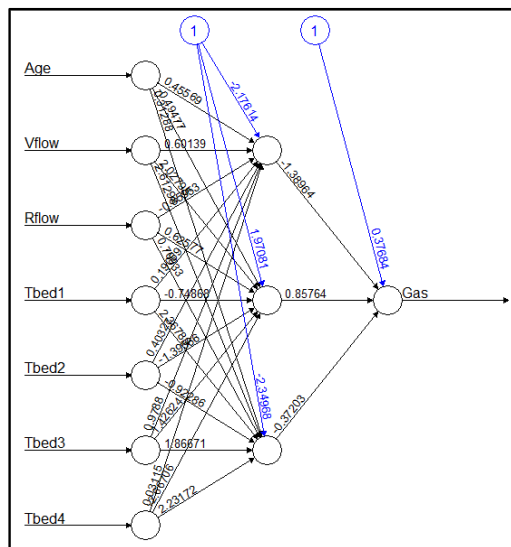


Figure 2. Structure of ANN constructed by R for predicting the yield of gas

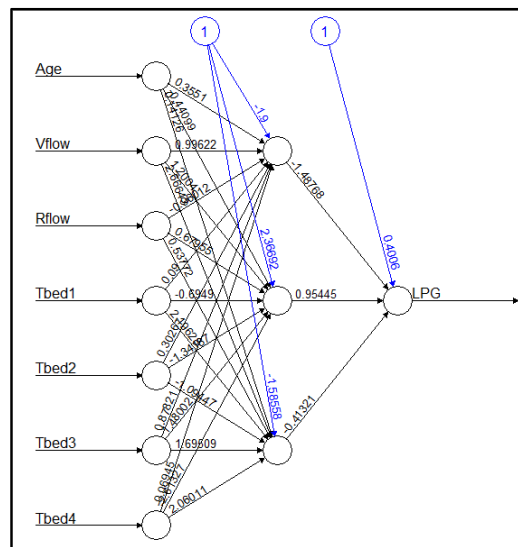


Figure 3. Structure of ANN constructed by R for predicting the yield of LPG

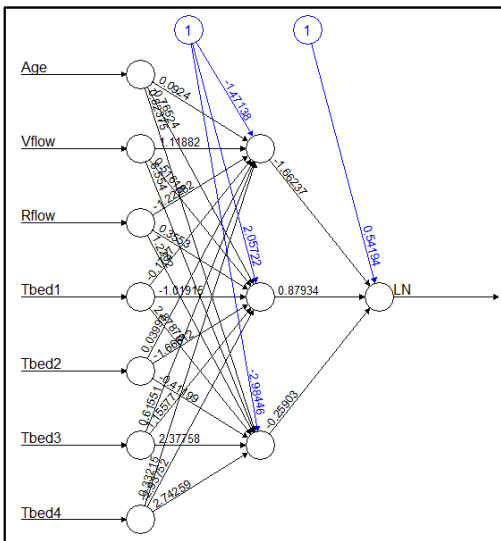


Figure 4. Structure of ANN constructed by R for predicting the yield of LN

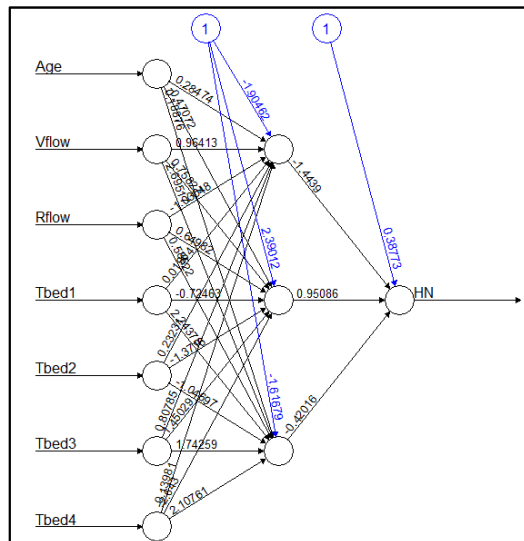


Figure 5. Structure of ANN constructed by R for predicting the yield of HN

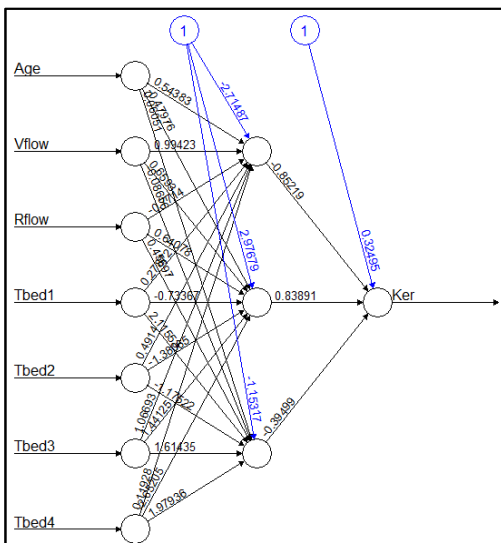


Figure 6. Structure of ANN constructed by R for predicting the yield of kerosene

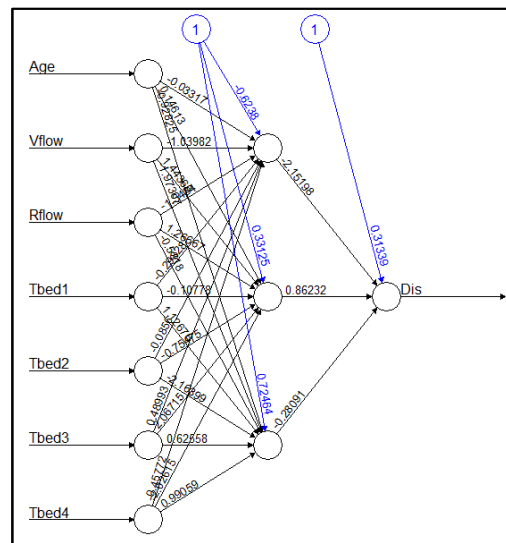


Figure 7. Structure of ANN constructed by R for predicting the yield of diesel

After training the ANNs, the unforeseen (predicting) data set is entered into the model, and the corresponding yield for each product is estimated and de-scaled using the 'compute' command in the R. As seen from Table 2, the AAD% of predicting data for all products are higher than the AAD% of testing data points, and also it is close to the AAD% of trained data. In order to further examine the reliability of the model, actual yields of Gas, LPG, LN, HN, Ker, and Dis are sketched versus the predicted values as parity plots in Figures 8 to 12, respectively. All these figures are generated by graphical tools provided in the R software. As seen, ANNs implemented in the R environment has high accuracy, and therefore they can be utilized for the purpose of sensitivity analysis and optimizing the target commercial scale VGO hydrocracking process or monitoring the activity of the catalyst. We suppose that the observed deviations can be due to random errors of measurement, and some abnormal conditions in the process, such as decreasing pressure of pumps and compressors, swinging in the quench flow rate or reaching the flood condition in the separation towers.

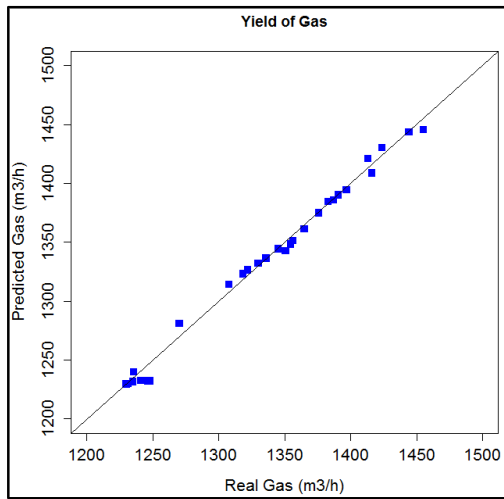


Figure 8. Comparison between actual and predicted values of gas yield predicted by R

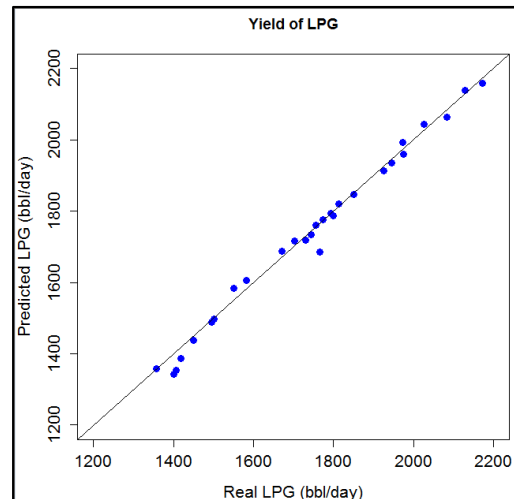


Figure 9. Comparison between actual and predicted values of LPG yield predicted by R

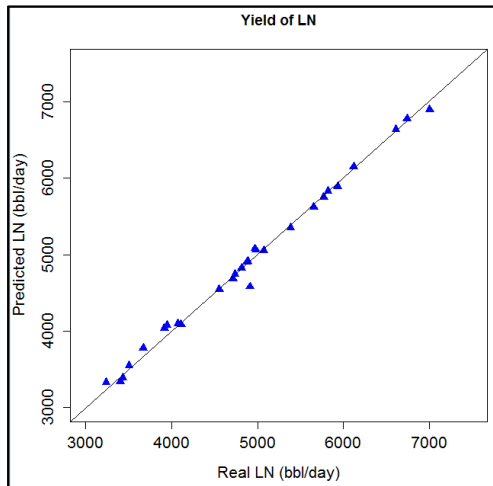


Figure 10. Comparison between actual and predicted values of LN yield predicted by R

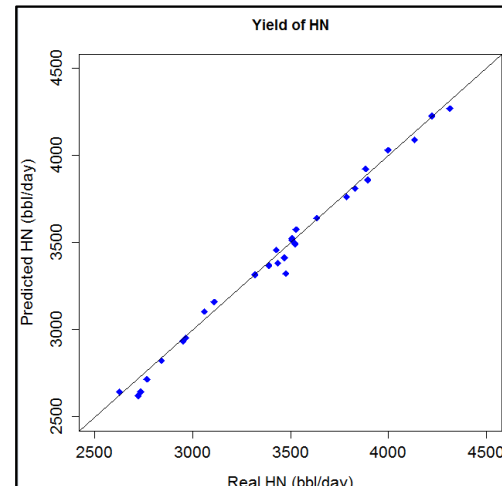


Figure 11. Comparison between actual and predicted values of HN yield predicted by R

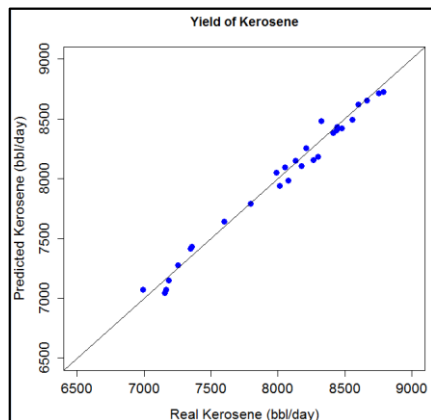


Figure 12. Comparison between actual and predicted values of kerosene yield predicted by R

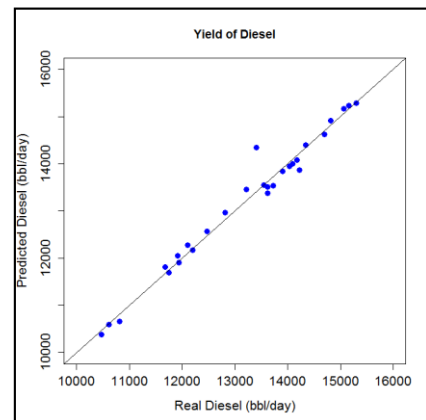


Figure 13. Comparison between actual and predicted values of diesel yield predicted by R

5. Conclusions

This research discussed the accuracy and reliability of R software and 'neuralnet' package for modeling yield of products in a commercial scale VGO hydrocracking plant using ANN technique. ANN models were trained and tested on the basis of 69 actual data points gathered from the target plant. For training, 60% of data points were randomly selected, and training procedure was carried out applying the back-propagation method. Other points were utilized to investigate predicting ability of ANN models constructed in R environment. These models were designed based on a feed-forward neural network with 7 neurons in the input layer and 3 neurons in the hidden layer. Input neurons were the age of catalyst, fresh and recycle feed flow rates and bed temperatures. The output neurons were yields of VGO hydrocracking products including light gases, LPG, light and heavy naphtha, kerosene and diesel. For each product, an individual network was implemented in the R. Results showed that R could predict the yield of products for testing points with the AAD% of 0.092%, 0.302%, 0.366%, 0.294%, 0.164% and 0.315%, respectively. The high accuracy of observed predictions can confirm the reliability of R to be used as free software with no license restrictions in modeling chemical engineering processes when ANN methodology can be executed as a modeling strategy.

References

- [1] Sadighi S. J. Chem. Eng. Jap., 2016; 49(12): 979.
- [2] Himmelblau DM. Ind. Eng. Chem. Res., 2008; 47: 5782.
- [3] Kusumoputro B, Sutarya D, Faqih A. Int. J. Technol., 2016; 4: 709.
- [4] Franke LLC, Chatzopoulos K, Rigopoulos S. Combust. Flame, 2017; 185: 245.
- [5] Sadighi, S, Zahedi S, Hayati R, Bayat M. Ener. Technol., 2013; 1: 743.
- [6] Taskin H, Kubat C, Uygun O, Arslankaya S. Comput. Chem. Eng., 2006; 30: 850.
- [7] Bas D, Dudak FC, Boyaci IH. J. Food Eng., 2007; 79: 622.
- [8] Riverol, C.: Pilipovik, M. V., Chem. Eng. J., 2007;133: 133.
- [9] Bhutani N, Rangaiah GP, Ray AK. Ind. Eng. Chem. Res., 2006; 45: 7807.
- [10] Niaezi A, Towfighi J, Khataee AR. Rostamizadeh, Petrol. Sci. Technol, 2007; 25: 967.
- [11] Istadi I, Amin NAS. Ind. Eng. Chem. Res. Catal., 2006; 45:6655.
- [12] Istadi I, Amin NAS. Bull. Chem. React. Eng. Catal., 2007; 2: 37.
- [13] Zahedi G, Mohammadzadeh S, Moradi M. Energy&Fuels, 2008; 22: 2671.
- [14] Alhajree I, Zahedi GR, Manan ZA, Mohammad Zadeh S. J. Pet. Sci. Eng., 2011; 78: 627.
- [15] Vasseghian Y, Ahmadi M. J. Chem. Pet. Eng., 2014; 48(2): 125.
- [16] Sadighi S, Mohaddecy RS. Int. J. Technol., 2013; 2: 102-111.
- [17] Sadighi S, Mohaddecy R, Norouzian A. Bull. Chem. React. Eng. Catal., 2015; 10: 210.
- [18] Sadighi S, Ghorbani Y. Petrol. Coal, 2017; 59(6): 777.
- [19] Sadighi S, Mohaddecy SR, Abbasi A. Int. J. Technol., 2018, under publishing.
- [20] Torgo L. Data Mining with R, 1st ed.; CRC Press, Taylor & Francis Group; London/New York, 2011.
- [21] Intrator O. Intrator, N.: Using Neural Nets for Interpretation of Nonlinear Models. Proceedings of the Statistical Computing Section, 1993, 244-249, San Francisco: American Statistical Society.
- [22] Fritsch S, Guenther F, Suling M, Mueller SM. Package 'neuralnet': Training of Neural Networks, 2016, <https://cran.r-project.org/web/packages/neuralnet/neuralnet.pdf>.
- [23] Haykin S, Hamilton O. Neural Networks. 2nd ed., Prentice Hall International, Upper Saddle River, NJ, 1998.

To whom correspondence should be addressed: Dr. Sepehr Sadighi, Research Institute of Petroleum Industry (RIPI), Catalysis Technologies Development Division, P.O. Box 14665137, Tehran, Iran

GEOCHEMICAL ANALYSIS OF SHALE SAMPLES FROM EWEKORO FORMATION, BENIN BASIN (NIGERIA)

Uzochukwu Kingsley Benjamin, Olumuyiwa Temitope Akinsanpe and Chibuike Lawrence Chidolue

Department of Geology, Obafemi Awolowo University, Ile-Ife. Nigeria

Received January 17, 2018; Accepted April 23, 2018

Abstract

Utilizing four shale samples from a mine at Ibese, Southwest, Nigeria, this study evaluated the source rock potential of the shales of the Ewekoro Formation, Benin Basin. The four shale samples, Sample-1, Sample-2, Sample-3 and Sample-4, were analysed for their total organic carbon (TOC) content, elemental concentration of major, trace and transition elements as well as the type of organic matter they contain. Using the $\log(\text{Fe}_2\text{O}_3/\text{K}_2\text{O})$ versus $\log(\text{SiO}_2/\text{Al}_2\text{O}_3)$ classification technique for terrigenous sediments, the samples were classified as iron-rich shales. The paleo-redox condition of deposition for the sediments was determined using the Vanadium-Chromium ratio (V/Cr). V/Cr ratios of 0.9, 1.3, 0.7 and 1.0 were estimated for Sample-1, Sample-2, Sample-3 and Sample-4 respectively. V/Cr ratio below 2.0 is indicative of sediment deposition in an oxic environment. The weight percentage of the total organic carbon of the samples ranged from 0.076 - 0.585 wt. %; this low values are indicative of poor to fair source rock potential. The kerogen extracts from Samples 1 through to 3 were interpreted as Type IV kerogen, while the extracts from Sample-4 were classified as Type III kerogen. The results of this study show that the shales of the Ewekoro Formation of the Benin Basin have poor to fair source rock potential. The constituent Type IV kerogen of Samples 1 - 3 are incapable of generating oil or gas, while the Type III kerogen of Sample-4 can generate gas and little oil.

Keywords: Ewekoro Formation, Benin Basin, Source rock potential, Elemental analysis.

1. Introduction

Benin Basin is an extensive coastal sedimentary basin at the margin of Gulf of Guinea. It is part of a system of West African Atlantic margin basins developed during the period of the rifting associated with the separation of South American and African plates and subsequent opening of Gulf of Guinea in the Late Jurassic to Early Cretaceous [2-3]. The basin stretches along the coast of Nigeria, Benin Republic, Togo and Ghana.

An Upper Cretaceous petroleum system, characterized by Type II-III kerogens with an average total organic carbon (TOC) content of 2.9 wt. %, has been established in the Basin Basin (e.g., Kaki *et al.* [45]). Oil is currently being produced in the Aje Field from Upper Cretaceous sandstone facies of the Abeokuta Group. With recent exploration data and geochemical evaluations of bituminous sand outcrops from onshore areas of the basin in southwest Nigeria suggesting the existence of a Lower Cretaceous petroleum system (e.g. Kaki *et al.* [45]), the Benin Basin is proofing to be a basin with significant hydrocarbon potential. This study is aimed at evaluating the source rock potential of shales of the post-Cretaceous Ewekoro Formation.

2. Geological setting

The study area is located within BENIN Basin, which is an extensive coastal sedimentary basin on the margin of Gulf of Guinea. It is part of a system of West African Atlantic margin basins developed during the period of the rifting associated with the separation of South Amer-

rican and African plates and subsequent opening of Gulf of Guinea in the late Jurassic to early Cretaceous [2-3].

The basin stretches along the coast of Nigeria, Benin Republic, Togo and Ghana in the margin of the Gulf of Guinea. Figure 1 shows the Nigerian section of the BENIN basin. It is separated from Niger Delta in the Eastern section by Benin Hinge Line and Okitipupa Ridge and marks the continental extension of the chain fracture zone [4-6]. It is bounded on the west by Ghana Ridge, and has been interpreted as the Romanche fracture zone [3,7]. The basin fill covers a broad arc-shaped profile, attaining about 13 km maximum width in the onshore at the basin axis along Nigerian and Republic of Benin boundary. This narrows westwards and eastwards to about 5 km [8-9].

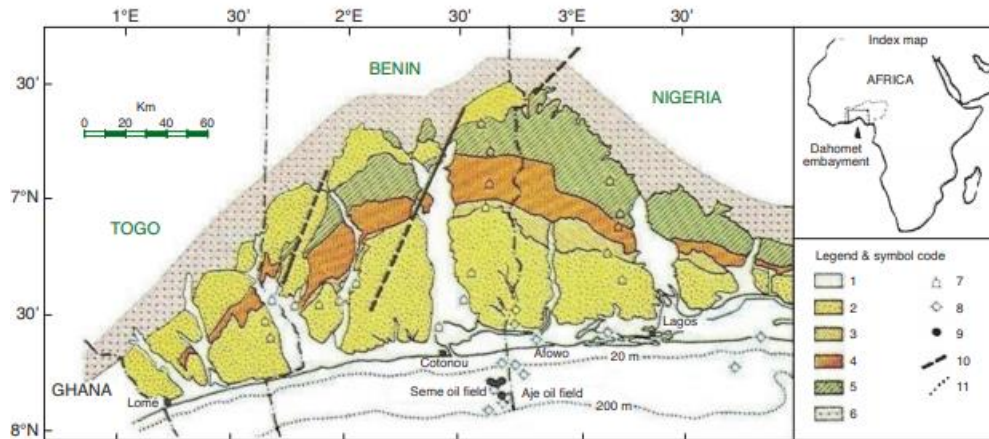


Figure 1. The Benin Basin within the "Dahomey Embayment"; 1-6 represent Formations; 1- Alluvium (Recent); 2- Benin-Ijebu (Pleistocene/Upper Miocene); 3- Oshoshun (Middle Eocene); 4- Imo shale (Lower Eocene/Paleocene); 5- Araromi shale and Turonian sandstone (Upper Cretaceous); 6- Pre-Cambrian crystalline basement; 7- Core hole or water well; 8- Dry well; 9- Oil well; 10- Faults; 11- Water depth contour (after Kaki *et al.* [45])

The tectonic framework along the continental margin of the BENIN basin is controlled by Cretaceous fracture zones expressed as trenches and ridges in the deep Atlantic, the basin is characterized by both block and transform faulting [10].

Adediran and Adegoke [11] proposed a four stage evolutionary model for the Gulf of Guinea Basin (BENIN Basin inclusive) as follows:

Stage 1 – The deposition of thick clastic sediments mostly immature sandstones and fresh water shales in the intracratonic basin.

Stage 2 – Reworked sands and silt intercalated with shales of fluviatile-lacustrine origin deposited within the grabens during a period of tectonic activity, erosion and sedimentation

Stage 3 – Paralic sequence (in the northern basins) and evaporitic deposits (in the southern basins) marking the beginning of marine incursion into the basin after the separation of South America from Africa.

Stage 4 –Marine sediments rich in fauna and flora marking the final stage of the development of the Gulf of Guinea Basins.

3. Lithostratigraphy of BENIN BASIN

The stratigraphic setting of the BENIN Basin has been described in detail in the works of Adegoke [12], Ogbe [13], Kogbe [14], Billman [15], Omatsola and Adegoke [16], Ako *et al.* [17], Okosun [41], Adekeye [19] and Adekeye *et al.* [20]. The recognized formations from the oldest to the youngest include: Abeokuta Group which comprises of Ise, Afowo and Araromi Formations (Cretaceous), Ewekoro Formation (Paleocene), Akinbo Formation (Late Paleocene – Early Eocene), Oshosun Formation (Eocene), Ameki Formation, Ogwashi-Asaba Formation and Benin Formation.

3.1. ISE FORMATION

This is the oldest formation in the BENIN Basin. It unconformably overlies the basement complex of southwestern Nigeria. It consists of conglomerates and grits at the base, and in turn overlain by coarse to medium grained sands with interbedded kaolinite. The Conglomerates are unimbricated and at some locations, ironstones occur [\[21\]](#). The age is Neocomian to Albian based on the recovered Sporomorohs.

3.2. AFOWO FORMATION

This formation overlies the Ise Formation. It is composed of sandstones with interbeds of shales, siltstones and clay. The sandy facies are tar bearing while the shales are organic rich [\[22\]](#). The lower part of this formation is transitional with mixed brackish to marginal horizons that alternate with well sorted, subrounded sands indicating a littoral or estuarine near shore environment of deposition [\[23\]](#). Turonian to Maastrichtian age has been assigned to this formation on the basis of palynological assemblage.

3.3. ARAROMI FORMATION

This formation overlies the Afowo Formation and has been described as the youngest Cretaceous sediment in the eastern BENIN Basin [\[16\]](#). It consists essentially of sand, overlain by dark-grey shales and interbedded limestone, marl and occasionally lignite bands. The formation is very similar in composition to the upper part of the Awgu Formation and the Nkporo Shale of the Anambra Basin [\[15\]](#), but their occurrence in separate basins with different geologic histories and lack of adequate outcrop sections necessitate a separate nomenclature. Observations made by Okosun [\[41\]](#) support the inclusion of thin interbeds of sandstone, shelly limestone and shale in the formation. A Maastrichtian to Paleocene age has been assigned to this formation [\[16\]](#).

3.4. EWEKORO FORMATION

This formation overlies the Araromi Formation in the eastern BENIN Basin. It is one of the lithostratigraphic units under Imo Group. Elueze and Nton [\[24\]](#) has reported that the limestone is of shallow marine origin owing to abundance of coralline algae, gastropods, pelecypods, echinoids fragments and other skeletal debris.

3.5. AKINBO FORMATION

Overlying the Ewekoro Formation is the Akinbo Formation which is made up of shale and clayey sequence [\[13\]](#). The claystone are concretionary and are predominantly kaolinite. Lenses of limestone from Ewekoro Formation grades into the Akinbo shale very close to the base. The base of the formation is defined by the presence of glauconitic band with lenses of limestone [\[13,21\]](#). The formation is Paleocene to Eocene in age on the basis of the recovered microfossil assemblages.

3.6. OSHOSUN FORMATION

This formation overlies the Akinbo Formation. It consists of greenish-grey clay and shale with interbeds of sandstones. The shale is thickly laminated and glauconitic. The basal beds are thinly laminated, occasionally mottled with pockets of grits. According to Okosun [\[18\]](#), the basal beds consist of any of the following facies; Sandstones, Mudstones, Claystones, Clayey shale. The shales of the Oshosun Formation have highly variable colours, ranging from light grey, brownish grey, purple through green, bluish grey to dark grey and black. These dark coloured highly fossiliferous shales pass upwards into a yellowish grey, faintly laminated, unfossiliferous, slightly calcareous and glauconitic shales with thin phosphatic beds. The shales get sandier and show alternation of grey to green shales with brownish soft clayey sandstones towards the top of the formation. This formation is phosphate bearing [\[25\]](#). The formation is dated Eocene based on the recovered fauna and microfossil assemblages.

3.7. AMEKI FORMATION

The Ilaro Formation of some workers [14,26] is assigned to this formation wholly or in part by Reyment [27], Antolini [28] and Adegoke [12]. This formation overlies conformably the Oshosun Formation and consists of massive, yellowish, poorly consolidated, cross-bedded sandstone. The formation is dated Middle Eocene based on the molluscs recovered from it.

3.8. OGWASHI-ASABA FORMATION

This formation consists of a sequence of coarse-grained sandstone, light coloured clays and carbonaceous shale within which are intercalations of lignite seams of Continental origin [29,40]. Reyment [27] suggested an Oligocene to Miocene age for the Ogwashi-Asaba Formation, but palynological study by Jan du Chene *et al.* [29] yielded a Middle Eocene age for the basal part. The lignite seams found within the Ogwashi-Asaba Formation are commonly brownish to black in colour and vary in thickness from few millimeters to a maximum of 6 m. They are thinly laminated and fissile with leaf and woody framents.

3.9. BENIN FORMATION

This is the youngest stratigraphic sequence in the eastern BENIN Basin. It is also known as the Coastal Plain Sands [25]. It overlays the Ilaro Formation unconformably. It consists of poorly sorted sands with lenses of clays. The sands are in parts cross-bedded and show transitional to continental characteristics. The age is from Oligocene to Recent. The stratigraphy of BENIN Basin is shown in Table 1.

Table 1. Stratigraphy of BENIN Basin

Period	Jones and Hockey [25]		Omatsola and Adegoke [16]		Agagu [46]	
	Age	Formation	Age	Formation	Age	Formation
Quaternary	Recent	Alluvium			Recent	Alluvium
Tertiary	Pleistocene	Coastal Plain Sand	Pleistocene	Coastal Plain Sand	Pleistocene	Coastal Plain Sand
	Oligocene-Eocene	Ilaro	Oligocene-Eocene	Ilaro	Oligocene-Eocene	Ilaro
	Paleocene	Ewekoro	Paleocene	Oshosun, Akinbo	Paleocene	Oshosun, Akinbo, Ewekoro
Cretaceous	Late Senonian	Abeokuta	Maastrichtian	Araromi, Afowo	Maastrichtian	Araromi, Afowo
			Neocomian	Ise	Neocomian	Ise
Precambrian Crystalline Basement Rocks						

4. Methodology

4.1. Samples

Four (4) samples were analysed in this study. The samples were sourced from Dangote Cement Mines at Ibese, Ogun State, sampling was done at vertical spacing interval of 1m. The samples are shales and are described in Table 2. The samples range in elevation of about 39m to 42m.

Table 2. Sample description

Sample number	Sampling elevation(m)	Rock Type	Colour	Grain Size	Structure	Minerals Observable In Hand Specimen
1	39	Shale	Dark Coloured	Fine	Fissility	Clay Minerals
2	40	Shale	Dark Coloured	Fine	Fissility	Clay Minerals
3	41	Shale	Dark Coloured	Fine	Fissility	Clay Minerals
4	42	Shale	Dark Coloured	Fine	Fissility	Clay Minerals

4.2. Elemental analysis

Major, minor and trace elements of the sample were determined by Proton-induced X-ray emission (PIXE) technique at the centre for Energy Research and Development (CERD) O.A.U, Ile-Ife. The samples were first oven dried at 45-50 degree Celsius. The dried samples were ground with a grinding machine at the workshop in the Department of Geology O.A.U and prepared into pellets of 11mm diameter without binder.

The PIXE experiments were performed using a 3.0 MeV proton beam obtained from the CERD ion beam analysis (IBA) facility. The facility is centered on a NEC 5SDH 1.7MV Pelletron Accelerator, equipped with a radiofrequency charge exchange ion source. The ion source is equipped to provide proton and helium ions. The end-station consists of an Aluminium chamber of about 150 cm diameter and 180 cm height. It has four ports and window. Port 1 at 165° is for the RBS detector, port 2 at 135° is for PIXE detector, port 3 at 30° is for the ERDA detector; the window at 0° is for observing the beam position and the size, while port 4 at 225° is for PIGME. The chamber has a sample ladder that can carry 11 (eleven) 13 mm diameter samples. The end-station has a turbo pump and a variable beam collimator to regulate beam size, and isolation value.

Shale standard (NIST) GRS5 was used for the determination of the element values which was subsequently used for analysing the shale samples and to assure the accuracy of the experimental procedure. The measurements were carried out with a beam spot of 4mm in diameter and a low beam current of 3-6 nA. The irradiation was for about 10-20 minutes. A Canberra Si(Li) detector Model ESLX 30-150, beryllium thickness of 25 μm , with full width half maximum (FWHM) of 150 eV at 5.9 KeV, with the associated pulse processing electronics, and a Canberra Genie 2000 (3.1) MCA card interfaced to a PC were used for the X-rays data acquisition. With respect to the beam director, the sample's normal was located at 0° and the Si (Li) detector at 45°. The PIXE set-up was calibrated using some pure element standards and NIST geological standard, NBS278.

4.3. Organic carbon determination

The organic carbon was determined in the Department of Soil science, Faculty of Agriculture, O.A.U, Ile-Ife. 0.5 g of the powdered samples was weighed on the balance and poured into a conical flask. 10ml of potassium dichromate ($\text{K}_2\text{Cr}_2\text{O}_7$) and 20 ml of concentrated H_2SO_4 was added and it was left for 30 minutes, after 200 ml of distilled water was added to the sample, then 10mL of H_2PO_4 was added to the sample and 0.2 g of Sodium Fluoride was equally added to the sample. It was then back titrated with ammonium ferrous sulphate to reach a greenish end point.

4.4. Kerogen isolation

The kerogen isolation was carried out in the Geochemistry laboratory of the Department of Geology, Obafemi Awolowo University, Ile-Ife.

Kerogen was isolated, using the standard technique of acid digestion with HCl/HF. The acid digestion procedures were carried out in the fume cupboard. About 5g of the powdered sample (dry) was placed in beaker, and distilled water added to wet the sample. It was then treated with conc. HCl (40%) to remove carbonates, washed three times with distilled water in order to remove all traces of acid.

The sample was then treated with con. HF (52%) to digest silica. This step was carried out in two stages. Conc. HF was slowly poured on the sample, until the beaker was 2/3 full. It was left for three hours, after which the HF was carefully poured off into a waste reagent bottle. HF was added a second time and the sample left to stand for two hours. The HF was also poured off and the sample left to stand in distilled water, overnight before washing. The samples were then centrifuged at 2000 rpm for two minutes each, three times in distilled water, then once in acetone and lastly, twice with distilled water. The kerogen concentrate was then placed in a dish and oven dried at 146°F (58°C) and stored in glass vials. No attempt was made to further demineralise the kerogen by a float-sink technique, using ZnBr_2 or other heavy liquid.

A small portion of kerogen was disaggregated and mounted on microscope glass slides. These slides were then examined under a petrographic microscope.

5. Results and discussions

The result of the elemental analysis is shown in tables 3 - 6. The elemental analysis is interpreted based on the major, trace and transition elements contents of the studied samples.

Table 3. Elements and their concentration in Sample 1

Z	Element	Concentration (ppm)	Concentration Error	Z	Element	Concentration (ppm)	Concentration Error
11	Na	322.0	±63.92	11	Na	270.9	±65.75
12	Mg	35723.5	±146.47	12	Mg	32628.1	±143.56
13	Al	96030.3	±172.85	13	Al	101183.5	±182.13
14	Si	297292.0	±267.56	14	Si	294344.6	±264.91
15	P	717.7	±65.74	15	P	622.8	±66.76
16	S	13866.7	±84.59	16	S	13047.9	±83.51
19	K	9875.9	±59.26	17	Cl	606.0	±48.18
20	Ca	6544.6	±51.05	19	K	11073.7	±62.01
22	Ti	6652.7	±46.57	20	Ca	7022.4	±53.37
23	V	203.4	±35.41	22	Ti	6670.6	±48.03
24	Cr	214.7	±15.54	23	V	283.5	±35.58
25	Mn	189.3	±15.83	24	Cr	217.6	±16.30
26	Fe	40436.6	±133.44	25	Mn	193.8	±15.95
29	Cu	328.7	±107.32	26	Fe	40404.0	±133.33
30	Zn	875.8	±187.77	30	Zn	1570.3	±194.25

Table 5. Elements and their concentration in Sample 3

Z	Element	Concentration (ppm)	Concentration Error	Z	Element	Concentration (ppm)	Concentration Error
11	Na	221.1	±64.83	11	Na	317.1	±66.40
12	Mg	34139.6	±146.80	12	Mg	39986.7	±151.95
13	Al	97959.0	±176.33	13	Al	92485.3	±175.72
14	Si	293816.2	±264.43	14	Si	298332.2	±268.50
15	P	786.2	±62.90	15	P	1203.8	±63.80
16	S	12002.3	±79.22	16	S	11635.0	±77.95
17	Cl	496.9	±44.22	17	Cl	1111.9	±45.25
19	K	11100.9	±59.94	19	K	8879.5	±55.05
20	Ca	11003.5	±62.72	20	Ca	9926.5	±57.57
22	Ti	6839.4	±48.56	22	Ti	5941.7	±44.56
23	V	180.7	±36.30	23	V	257.3	±33.35
24	Cr	265.0	±16.43	24	Cr	239.4	±15.70
25	Mn	184.9	±15.46	25	Mn	258.0	±15.33
26	Fe	41888.7	±138.23	26	Fe	38579.2	±131.17
29	Cu	203.7	±95.86	28	Ni	123.4	±51.03
30	Zn	1133.7	±183.21	30	Zn	1212.4	±170.34
40	Zr	345.6	±160.36				

5.1. Sample classification

The four samples were classified on the basis of their iron, potassium, silicon and aluminium concentrations using the Heron [30] classification scheme for terrigenous sedimentary rocks. In the Heron [30] classification, the $\log(\text{Fe}_2\text{O}_3/\text{K}_2\text{O})$ is plotted against $\log(\text{SiO}_2/\text{Al}_2\text{O}_3)$. The advantage of this classification is that it can be used to identify shales, sandstones, arkose and carbonate rocks in-situ from geochemical logs, using neutron activation and gamma-ray tools [31].

Table 4. Elements and their concentration in Sample 2

Z	Element	Concentration (ppm)	Concentration Error	Z	Element	Concentration (ppm)	Concentration Error
11	Na	270.9	±65.75	11	Na	270.9	±65.75
12	Mg	32628.1	±143.56	12	Mg	32628.1	±143.56
13	Al	101183.5	±182.13	13	Al	101183.5	±182.13
14	Si	294344.6	±264.91	14	Si	294344.6	±264.91
15	P	622.8	±66.76	15	P	622.8	±66.76
16	S	13047.9	±83.51	16	S	13047.9	±83.51
19	K	606.0	±48.18	19	K	606.0	±48.18
20	Ca	11073.7	±62.01	20	Ca	11073.7	±62.01
22	Ti	7022.4	±53.37	22	Ti	7022.4	±53.37
23	V	6670.6	±48.03	23	V	6670.6	±48.03
24	Cr	283.5	±35.58	24	Cr	283.5	±35.58
25	Mn	217.6	±16.30	25	Mn	217.6	±16.30
26	Fe	193.8	±15.95	26	Fe	193.8	±15.95
29	Cu	40404.0	±133.33	29	Cu	40404.0	±133.33
30	Zn	1570.3	±194.25	30	Zn	1570.3	±194.25

Table 6. Elements and their concentration in Sample 4

Z	Element	Concentration (ppm)	Concentration Error	Z	Element	Concentration (ppm)	Concentration Error
11	Na	317.1	±66.40	11	Na	317.1	±66.40
12	Mg	39986.7	±151.95	12	Mg	39986.7	±151.95
13	Al	92485.3	±175.72	13	Al	92485.3	±175.72
14	Si	298332.2	±268.50	14	Si	298332.2	±268.50
15	P	1203.8	±63.80	15	P	1203.8	±63.80
16	S	11635.0	±77.95	16	S	11635.0	±77.95
17	Cl	1111.9	±45.25	17	Cl	1111.9	±45.25
19	K	8879.5	±55.05	19	K	8879.5	±55.05
20	Ca	9926.5	±57.57	20	Ca	9926.5	±57.57
22	Ti	5941.7	±44.56	22	Ti	5941.7	±44.56
23	V	257.3	±33.35	23	V	257.3	±33.35
24	Cr	239.4	±15.70	24	Cr	239.4	±15.70
25	Mn	258.0	±15.33	25	Mn	258.0	±15.33
26	Fe	38579.2	±131.17	26	Fe	38579.2	±131.17
29	Cu	123.4	±51.03	29	Cu	123.4	±51.03
30	Zn	1212.4	±170.34	30	Zn	1212.4	±170.34
40	Zr	345.6	±160.36				

The classification of the samples is as follows;'

Sample 1 = Fe-Shale
 Sample 2 = Fe-Shale
 Sample 3 = Fe-Shale
 Sample 4 = Fe-Shale

5.2. Major elements

The variation of the concentration of major elements across various sampling elevation are shown Table 7. For most silicate rocks, oxygen, silicon, aluminium, sodium, magnesium, calcium and iron are major elements [32], major elements are those elements whose crustal abundances are greater than 1%. The concentration of potassium, sodium, iron, magnesium, aluminium, calcium and silicon were determined.

Table 7. Correlation matrix of trace and transition elements in the samples

	Titanium	Vanadium	Chromium	Manganese	Iron	Zinc
Titanium	1.0000					
Vanadium	-0.4771	1.0000				
Chromium	0.0625	-0.5265	1.0000			
Manganese	-0.9902	0.4581	0.0616	1.0000		
Iron	0.9475	-0.6408	0.3754	-0.9018	1.0000	
Zinc	-0.0454	0.7859	-0.0899	0.0991	-0.1134	1.0000

Potassium (K): The concentration of potassium varies from 8879.50 – 11100.90 ppm in Samples 1, 2, 3 and 4. Sample 4 from the sampling elevation of 42 m has the least concentration of 8879.50 ppm, while Sample 3 from the sampling elevation of 41 m has the highest concentration of 11100.90 ppm. The average concentration in the samples is 10232.50 ppm; this value is attributed to the high abundance of clay minerals formed from K-feldspar.

Sodium (Na): The values of its concentration in Samples 1, 2, 3 and 4 vary from 221.10 - 322.00 ppm. Sample 3 from the sampling elevation of 41m has the least concentration of 221.10 ppm and Sample 1 from sampling elevation of 39m has the highest concentration of 322.00 ppm. The average concentration is 282.77 ppm. The average concentration of sodium in the samples is low, which may be as a result of substitution of Na^+ for K^+ .

Iron (Fe): The values of its concentration in Samples 1, 2, 3 and 4 vary from 38579.20 - 41888.70 ppm. Sample 4 has the lowest concentration with a value of 38579.20 ppm while Sample 3 has the highest concentration with a value of 41888.70 ppm. The average concentration is of iron in the samples is 40327.13 ppm; this supports the classification of the studied samples as Iron rich shales using the Herron classification scheme.

Magnesium (Mg): The concentration of Mg in Samples 1, 2, 3 and 4 vary from 32628.10 – 39986.70 ppm. Sample 2 has the least concentration with a value of 32628.10 ppm, while Sample 4 has the highest concentration with a value of 39986.70 ppm. The average concentration of the element in the samples is 35619.48 ppm; this is probably due to the infiltration of Mg^{2+} into the shales from the surrounding carbonate rocks that are rich in Mg^{2+} .

Aluminium (Al): The concentration of Al in Samples 1, 2, 3 and 4 ranges from 101183.50 – 92485.30 ppm. Sample 4 has the least value of 101183.50 ppm, while Sample 2 has the highest value of 92485.30 ppm. The average concentration is of the element is 96914.53 ppm; this significantly low value is interpreted as indicating that some aluminium ions had been substituted for magnesium ions.

Silicon (Si): The concentration of Si in Samples 1, 2, 3 and 4 ranges from 293816.20 – 298332.20 ppm. Sample 3 has the least concentration with a value of 293816.20 ppm while Sample 4 has the highest concentration with a value of 298332.20 ppm. The average concentration of the element is 295946.30 ppm; this is expected because silicon is the second most abundant element in the Earth crust.

Calcium (Ca): The concentration of Ca in the Samples ranges from 6544.60 – 11003.50 ppm. Sample 1 from sampling elevation of 39m has the least concentration with a value of 6544.60 ppm while Sample 3 has the greatest concentration with a value of 11003.50 ppm. The average concentration of the element is 8624.25 ppm; this value is rather high for a terrigenous sedimentary rock. It is interpreted that the calcium ions must have been sourced from the surrounding limestone and gypsum.

Silicon has the highest average abundance of 295946.30 ppm followed by aluminium with a value of 96914.50 ppm, while calcium and sodium have the least abundances with values of 8624.25 ppm and 282.77 ppm respectively.

5.3. Trace and transition metals

An element that occurs in minute but detectable quantities in minerals and rocks, much less than 1% is a trace element, all elements except the most common rock forming elements (O, Si, Al, Fe, Ca, Na, K, Mg, and Ti) generally occur as trace elements, except where locally concentrated in their ores.

The International Union for Pure and Applied Chemistry (IUPAC) defines a transition element as an element that has an incomplete d-subshell in either the neutral atom or its ions. The trace and transition elements analysed in the samples are: titanium, vanadium, chromium, manganese, iron and zinc, their concentration (in ppm) at different sampling elevations are shown in Table 8.

Table 7 shows the correlation coefficients of the transition elements in samples. The following pairs have strong positive correlation; iron and titanium (0.9475), zinc and chromium (0.7859). While titanium and manganese (-0.9902), iron and manganese (-0.9018) have strong negative correlation.

Table 8. Some trace element ratios to evaluate paleoredox condition according to Jones and Manning [37]; Hatch and Levant [42]; Kimura and Watanabe [43]

Element ratios	Oxic	Dysoxic	Suboxic to Anoxic	Euxinic
Ni/Co	< 5	5 to 7	> 7	
V/Cr	< 2	2 to 4.25	> 4.25	
U/Th	< 0.75	0.75 - 1.25	> 1.25	
V/(Ni +V)	< 0.46	0.46 - 0.60	0.54 - 0.82	> 0.84
V/Sc	< 9.1			

5.4. Paleo-redox condition

A number of authors have used V/Cr ratio as an index of paleooxygenation [33-35]. Bjorlykke [35] reported the incorporation of Cr in the detrital fraction of sediments and its possible substitution for Al in the clay structure. Vanadium may be bound to organic matter by the incorporation of V^{4+} into porphyrins, and is generally found in sediments deposited in reducing environments [36]. According to Jones and Manning [37], the V/Cr ratios above 2 indicate anoxic conditions.

The V/Cr ratio was determined for the samples, Sample 1 has a ratio of 0.9, Sample 2 has 1.3, Sample 3 has a ratio of 0.7 and Sample 4 has a ratio of 1.0. All samples have ratios that are below 2 which indicate that they were deposited in oxic environments.

5.5. Total organic carbon (TOC)

The guidelines for assessing the source rock potential of shales [38], shown in Table 9 was used to characterize the source rock potential of the samples, Sample 1 has a percentage carbon of 0.076 which is less than 0.5 and it is indicative that the source rock potential is poor. Sample 2 has a percentage carbon of 0.232 which is less than 0.5; this is indicative of a poor source rock potential.

Table 9. Guidelines for assessing the source rock potential of shales [38]

Source rock potential	TOC (wt. %)
Poor	0.0 - 0.5
Fair	0.5 - 1.0
Good	1.0 - 2.0
Very Good	2.0 - 5.0
Excellent	>5.0

Sample 3 has a percentage carbon of 0.195 which is less than 0.5 this indicates that the source rock potential of the rock is poor. Sample 4 has a percentage carbon of 0.585 which is between 0.5 and 1.0 this value indicates that the source rock potential of the rock is fair.

Table 10 shows the total organic carbon of the studied sample while Fig. 3 shows the plot of the percentage carbon of the samples against their respective sampling elevation.

Table 10. The total organic carbon (TOC) of studied samples

Sample number	Sampling elevation (m)	(TOC) (wt. %)	Source rock potential
1	39	0.076	Poor
2	40	0.232	Poor
3	41	0.195	Poor
4	42	0.585	Fair

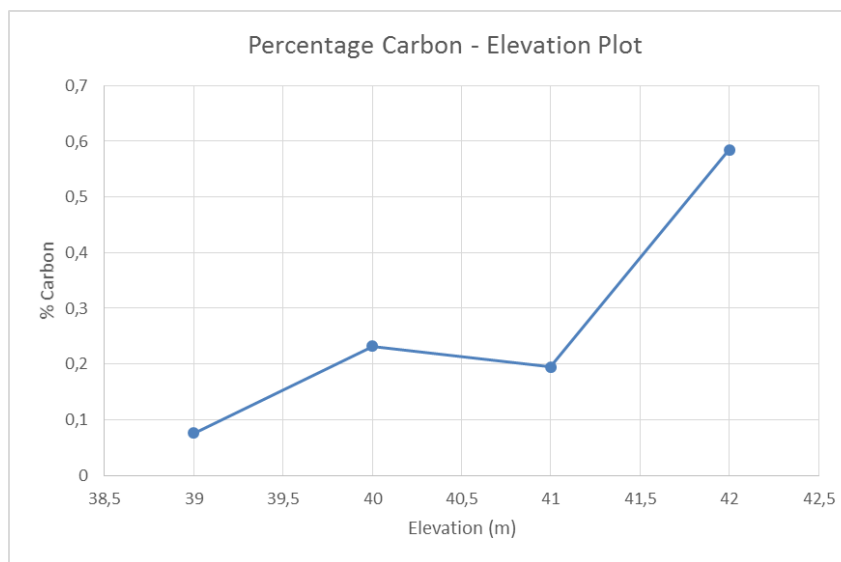


Figure 3. Plot of percentage Carbon of samples (1-4) versus elevation

5.6. Organic matter types

The accumulation of organic matter in sediments is controlled by a limited number of geological conditions [39]. The main factors that control the accumulation of organic matter include the production of the biomass and the degradation processes and transport of the organic matter.

The quantity and quality of the organic matter accumulated in sediment are basically the result of the combined influence of the biomass productivity, biochemical degradation and of the organic matter depositional processes. The accumulation is practically restricted to sediment deposited in aquatic environments, which must receive a certain minimum amount of organic matter.

In subaerial sediments, organic matter is easily destroyed by chemical or microbial oxidation. It is necessary balanced conditions between the energy level in a body of water and

rate sedimentation to preserve and concentrate organic matter in sediments. This organic matter can be supplied on the form of particulate organic matter (in particles) or as dissolved organic matter (dissolved organic components).

Organic matter in sedimentary rocks mainly exists as kerogen, kerogen are types of disseminated organic matter that exist in impermeable sediments, it is insoluble in normal petroleum solvents e.g. Carbon bisulphide, this characteristic distinguishes kerogen from bitumen. There are four types of kerogen; Type I, Type II, Type III and Type IV.

The kerogen isolated from Samples 1, 2, 3 and 4 were studied under a petrographic microscope, the kerogen extracts from samples 1, 2 and 3 are black in colour, composed of recycled organic matter and are therefore classified as type IV which is incapable of generating oil or gas. The kerogen extract in sample 4 is brown in colour and it is composed of recycled organic matter and amorphous matter, subsequently it is classified as kerogen type III which is gas prone and generates little oil. Figures 4-7 shows photomicrographs of the kerogen contained in the studied samples.

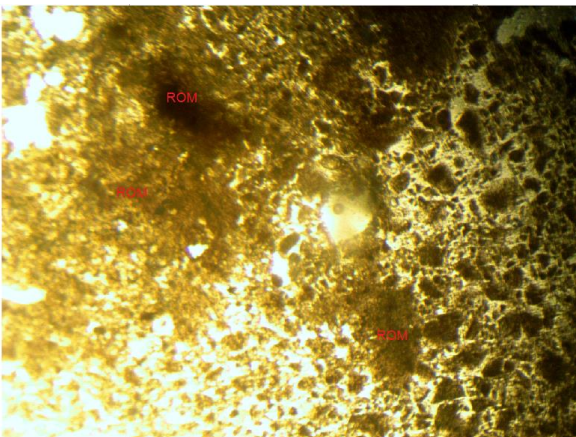


Figure 4 Photomicrograph of Sample 1 (39m) (magnification: x40) ROM –recycled organic matter

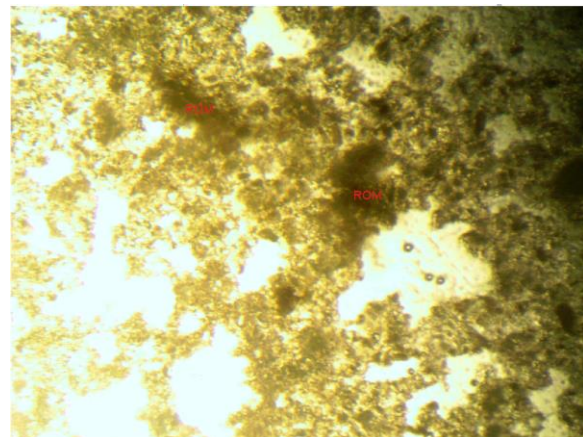


Figure 5. Photomicrograph of Sample 2 (40m) (magnification: x40)

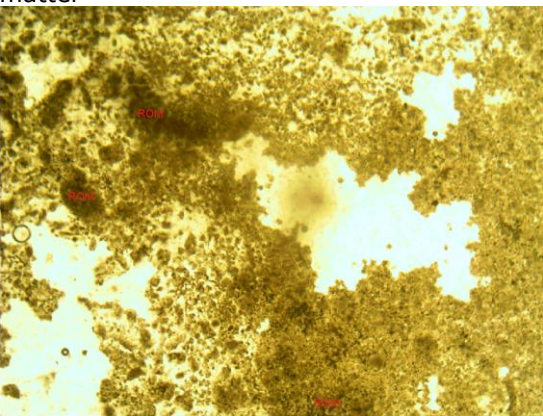


Figure 6. Photomicrograph of Sample 3 (41m) (magnification: x40), ROM –recycled organic matter

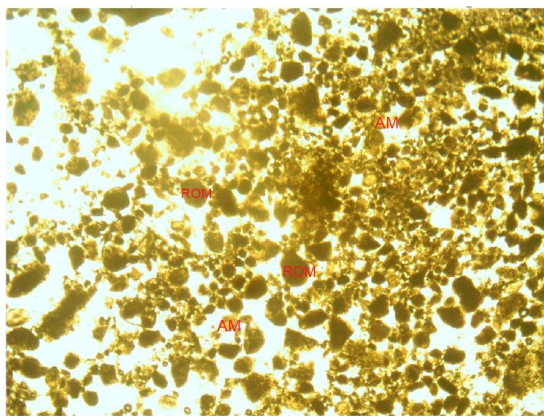


Figure 7. Photomicrograph of sample 4 (42m) (magnification: x40), ROM –recycled organic matter, AM-amorphous matter

6. Conclusion

This study used organic and inorganic geochemical techniques to evaluate the variations of major and trace elements, and organic matter type in the analysis of four samples from Dangote Cement Mines located at Ibese, Ogun State.

Using the Herron classification scheme, this study shows that the four studied samples are all iron-rich shales. The similarities in the distribution pattern of the element concentration in the samples indicated that the samples have the same provenance, which is a felsic plutonic rock.

The V/Cr ratio determined for the samples indicate that the paleo-redox condition in which the sediments were deposited was oxic; this is responsible for the low total organic carbon (TOC) of the samples which ranges from 0.076 – 0.585, indicating that the source rock potential of the rocks range from poor to fair.

The organic matter contained in samples 1 – 3 is Type IV kerogen which is incapable of yielding hydrocarbon, while sample 4 contains Type III kerogen which yields gas and little oil.

References

- [1] Lewis (JR) RW and Bandeira CS. The use of petroleum well samples and Data for Geochemical Prospecting of metals in Sedimentary Basins. *Jour. Geochem. Expl.*, 1981 15(1): 251-260.
- [2] Burke KC, Dessaуважи TFJ and Whiteman AJ. Opening of the Gulf of Guinea and geological history of the Benue depression and Niger Delta. *Nature Physical Science Series*, 1971; 233: 51 – 55.
- [3] Whiteman AJ. Nigeria- Its Petroleum Geology, Resources and Potential: London, Graham and Trotman, 1 and 2, 1982:394 pp.
- [5] Onuoha KO. Structural features of Nigeria's coastal margin: an assessment based on age data from wells. *Journal of African Earth Sciences*, 1999; 29(03): 485-499.
- [6] Wilson RCC and Willians CA. (1979): Oceanic transform structures and the developments of Atlantic continental margin sedimentary basin a review. *Journal of Geological Society of London*, 1979; 136: 311– 320.
- [7] Burke K, McGregor DS and Cameron NR. In Arthur, T.J., McGregor DS and Cameron NR. (Edited), *Petroleum Geology of Africa: New Themes and Developing Technologies*. Geological Society, London, Special Publications, 2003; 207: 21-60.
- [8] Coker SJL and Ejedawe JE. Petroleum prospect of the Benin basin Nigeria. *Journal of Mining and Geology*, 1987; 23(01): 7 – 43.
- [9] Coker SJL. Field excursion guide to tar sand outcrops in Benin Basin. Nigerian Association of Petroleum Explorationists, 2002; Mini-Conference, 32 pp.
- [10] Almeida FFM and Black R. Comparaison structurale entre le Nord-Est du Brésil et l'Ouest Africain, *Symposium on Continental Drift*, Montevideo, Uruguay, 16-19 Oct. 1967
- [11] Adediran SA and Adegoke OS. Evolution of the sedimentary basins of the Gulf of Guinea. In: *Current Research in Africa Earth Sciences*, Matheis and Schandeimeier (eds).Balkema, Rotterdam, 1987; pp. 283 - 286.
- [12] Adegoke OS. Eocene stratigraphy of Southern Nigeria. *Mem. Bur. Rech. Geol. Mins.*, 1969; 23 - 46.
- [13] Ogbe FGA. Stratigraphy of strata exposed in the Ewekoro quarry, Western Nigeria. *Cont. on African Geology* Ibadan (1970).
- [14] Kogbe CA. Paleogeographic history of Nigeria from Albian times. In: Kogbe C. A (ed), *Geology of Nigeria*. Elizabethan Publishers, Lagos, 1974; 237 – 252.
- [15] Billman HG. Offshore Stratigraphy and palaeontology of the BENIN Embayment. *Proc. Of 7th African Micropaleontology Colloquium*, Ile-Ife, Nigeria. 1976; 2-42.
- [16] Omatsola ME and Adegoke OS. (1981): Tectonic Evolution and Cretaceous Stratigraphy of BENIN Basin, *Journal of Min. Geol.*, 1981; 18(1): 130-137.
- [17] Ako BD, Adegoke OS and Petters SW. (1980): Stratigraphy of the Oshosun Formation in South - Western Nigeria. *Jour. Min. Geol.*, 1980; 17: 97 - 106.
- [18] Okosun EA. Review of the Early Tertiary Stratigraphy of Southwestern Nigeria. *Jour. Min. And Geol.*, 1998; 34(1): 27 - 35.
- [19] Adekeye OA. Aspects of the sedimentology, geochemistry and hydrocarbonpotentials of Cretaceous - Tertiary sediments in BENIN Basin of Southwestern Nigeria. 207 p., Unpublished Ph.D Thesis,1998, University of Ilorin, Ilorin.
- [20] Adekeye OA, Akande SO, Erdtman BD, Samuel O J and Hetenyi M. (2006): Hydrocarbon Potential Assessment of the Upper Cretaceous – Lower Tertiary Sequence in the BENIN Basin Southwestern Nigeria. *NAPE Bulletin.*, 2006; 19(1): 50 - 60

- [21] Nton ME. Sedimentology and Geochemical Studies of rock units in the Eastern BENIN Basin, Southwestern Nigeria. Ph.D Thesis, 2001; University of Ibadan, Ibadan, unpublished, 315p.
- [22] Enu EI. Nature and occurrence of tarsands in Nigeria. In: Ako, B.D and Enu, E.I., (Eds) occurrence, utilization and economics of tarsands. Nigeria Mining and Geosciences Society publication on tar sands workshop. Olabisi Onabanjo University, Ago - Iwoye.,1990: 11 - 16.
- [23] Nton ME, Ikahane PR and Tijani MN. Aspect of Rock - Eval studies of the Maastrichtian - Eocene sediments from subsurface, in the Eastern BENIN Basin Southwestern Nigeria. Eur. J. Scientific Res., 2009; 25(3): 417 - 427.
- [24] Elueze AA and Nton ME. Organic geochemical appraisal of limestones and shales in part of eastern BENIN Basin, South - western Nigeria. Journal of Mining and Geology, 2004; 40(1): 29 - 40.
- [25] Jones HA and Hockey RD. Geology of Parts of Southwestern Nigeria. Geological Survey Bulletin, 1964; 31: 87.
- [26] Slanksy M. Contribution a letude geologique du basin sedimentaire cotier du BENIN et du Togo. Bureau du Recherches geologiques et minieres, Mem. 1962; 11. 270pp.
- [27] Reyment RA. Aspects of the Geology of Nigeria. University of Ibadan Press, Nigeria. 1965; 145
- [28] Antolini P. Eocene phosphate in the BENIN Basin. Journal of Mining Geology, 1968; 3(1-2): 17 - 23.
- [29] du Chêne J, Onyike MS and Sowunmi MA. Some New Eocene Pollen of the Ogwashi - Asaba Formation, Southeastern Nigeria. Revista De Espanol Micro Paleontologie, 1978; 10: 285 - 322.
- [30] Herron MM. Geochemical classification of terrigenous sands and shales from core or log data. J. Sed. Petrol., 1988; 58: 820-829.
- [31] Herron MM and Herron SL. Geological application of geochemical well logging. In: Hurst A., Lovell M.A and Morton A.C (eds), Geological application of wireline logs, Spec. Publ. Geol. Soc., 1990; 48: 165-175.
- [32] White WM. Geochemistry. John Wiley and Sons Ltd., Hoboken, 2013; 668 pp.
- [33] Dill H. Metallogenesis of early Paleozoic graptolite shales from the Graefenthal Horst (northern Bavaria Federal Republic of Germany). Economic Geology, 1986; 81: 889- 903.
- [34] Dill H, Teshner M and Wehner H. Petrography, inorganic and organic geochemistry of Lower Permian Carboniferous fan sequences (Brandschiefer Series) FRG: constraints to their palaeogeography and assessment of their source rock potential. Chemical Geology, 1988; 67(3-4): 307-325.
- [35] Bjørlykke K. Geochemical and mineralogical influence of Ordovician island arcs on epicontinental clastic sedimentation: A study of Lower Palaeozoic sedimentation in the Oslo region, Norway. Sedimentology, 1974; 21(2): 251 -272.
- [35] Nagarajan R, Madhavaraju J, Nagendra R, Armstrongaltrin JS and Moutte J. Geochemistry of Neoproterozoic shales of the Rabanpalli Formation, Bhima Basin, Northern Karnataka, southern India: implications for provenance and paleoredox conditions. Revista Mexicana de Ciencias Geológicas, 2007; 24(2):150-160.
- [36] Shaw TJ, Geiskes JM and Jahnke RA. Early diagénésis in differing depositional environments: the response of transition metals in pore water: Geochimica et Cosmochimica Acta, 1990; 54(5): 1233-1246.
- [37] Jones B and Manning DAC. Comparison of geological indices used for the interpretation of paleo-redox conditions in ancient mudstones. Chemical Geology, 1994; 111: 111 -129.
- [38] American Association of Petroleum Geologist (AAPG): [http://wiki.aapg.org/Total_organic_carbon \(TOC\)](http://wiki.aapg.org/Total_organic_carbon_(TOC)).
- [39] Tissot BP and Welte DH. Petroleum Formation and Occurrence. Springer-Verlag, Berlin. 1984; 699 pp.
- [40] Kogbe CA. Paleogeographic history of Nigeria from Albian times. In: Kogbe C.A (ed), Geology of Nigeria, Elizabethan publishers, Lagos, 1976; 15 - 35.
- [41] Okosun EA. (1990): A review of the Cretaceous stratigraphy of the BENIN Embayment, West Africa. Cretaceous Research, 1990; 11: 17-27.
- [42] Hatch JR and Leventhal JS. Relationship between inferred redox potential of the depositional environment and geochemistry of the Upper Pennsylvanian (Missourian) Stark Shale Member of the Dennis Limestone, Wabaunsee County, Kansas, U.S.A. Chemical Geology, 1992; 99: 65-82.

- [43] Kimura H and Watanabe Y. Oceanic anoxia at the Precambrian-Cambrian boundary. *Geology*, 2001; 21: 995-998.
- [44] Billman HG. Offshore Stratigraphy and Palaeontology of the BENIN Embayment, West Africa: Nigerian Association of Petroleum Explorationists Bulletin, 1992; 72, 121-130.
- [45] Kaki C, d'Almeida GAF, Yalo N and Amelina S. Geology and petroleum systems of the offshore Benin Basin (Benin). *Oil & Gas Science and Technology-Rev. IFP Energies nouvelles*, 2013; 68(2) 363-381
- [46] Agagu OK. A Geology Guide to Bituminous Sediment in Southwestern Nigeria. Unpubl. Report, Department of Geology, University of Ibadan.1985, 25p

To whom correspondence should be addressed: Dr. Uzochukwu Kingsley Benjamin, Department of Geology, Obafemi Awolowo University, Ile-Ife. Nigeria

STRATEGIC PATENT ANALYSIS OF REAL TIME OPTIMIZATION APPLICATIONS IN UPSTREAM SECTION OF OIL AND GAS INDUSTRY

Behnam Baloochy, Mahdi Ahmadi Marvast, Saeid Shokri, Majid Kakavand*

Process Development Division, Research Institute of Petroleum Industry, Tehran 14665-137, IRAN

Received January 23, 2018; Accepted April 23, 2018

Abstract

The patents were classified in terms of date, zone, country and owner(s) in time period of 1985 to 2010. The analysis showed that USA was the largest country for technology patent registration; Schlumberger was the pioneer company and in 2008, the most number of patents granted. Patent analysis of this study helped to determine the current technology trend and addressed the roadmap for developing the next generation of RTPO and associated technologies.

Keywords: *Real time optimization; Patent analysis; Oil and Gas Upstream Industry; Technology trend; Real time production optimization.*

1. Introduction

In the field of technology management, use of information or documents, patent applications and data analysis is an important asset. In general, patent analysis, can provide useful information that through analysis and evaluation of the information, a technology can be fully understood [1].

The sequence of decisions made during patent analysis clearly has legal consequences. Based on Skinner's definition of a good decision maker, a number of key decision points were identified [2]:

- Decide what is searchable- frame the search problem as distinct from the original request.
- Decide what can be expected from the search, given the available sources of information and their limitations, budgetary constraints, legal deadlines and company timeframe. Communicate it to others.
- Decide on the timing and sequence of decisions to be made during the search. Plan a strategy for searching (use of online databases, Internet sources, print publications or expert contacts), document the search pathway and reasons for following it.
- Decide where uncertainty will arise and manage it effectively- use methods of retrieval that will reduce uncertainty (e.g. citation searching to identify relevant coding), question and respond to results as they come up, revise the strategy accordingly, aim for comprehensiveness.
- Decide how best to work with risks, and understand their consequences. Keep up to date with search tools, their strengths and weaknesses, be informed about legal processes, and maintain confidentiality.
- Decide how to identify opportunities and create alternatives. Be a detective, challenge assumptions, question the results (what exactly does it mean if you have zero hits?).
- Decide how to deal with complexity and ambiguity. Decide when you have finished a search, organize electronic files and papers, document the search strategies and choices made, and annotate the results.
- Legal decisions are made by attorneys as a consequence.

One of the main challenges in the chemical processes is how to best operate the plant under different conditions such as feed compositions, production rates, energy availability and feed/

product prices. One of the techniques that have received considerable attention in the process industry is Real-Time Optimization (RTO). RTO attempts to optimize plants profit as operating conditions change continuously [3-10].

Nowadays, promoting RTO is a competition for capital within producing corporations. The project teams that are aware of this fact and then clearly outline the purpose, benefits, costs and strategic business alignment of their proposals will be in a beneficial position to secure funding. Because RTO is still an emerging discipline, classifying projects of this character is still dependent on an individual's viewpoint.

In oil and gas upstream industry, the RTO technology has several applications [11-20]. These applications can be divided into two main areas: Real Time Production Optimization (RTPO) and Real Time Drilling Optimization (RTDO).

This paper intended to enable classification of RTPO in an objective manner and to determine the current technology trend and the next generation of RTPO and associated technologies.

2. Patent search policy

Recently some novel tools have become available for patent research, and some old ones have been enhanced. For now, discussions still continue about the best techniques of patent search. The reality is that in order to accomplish a serious search, all possible relevant policies should be applied. In many situations, smart use of keywords combined with classifications is the main way to go [21-22].

In various cases, the patent classification system is some years behind technology development. In such instances, the main approach is the "shotgun search", using one or more patent classifications to employ a wide range of keyword search strategies. Such search strategies must make smart use of proximity operators to recover documents that include search terms which meaningfully grouped together. Often such searches still produce hundreds of potentially relevant patents. Reviewing several hundred documents an hour is best done with a good computer connection to a "text only" version of a service, which allows rapid display of keywords in context of full text. It is normally appreciated that patent abstracts are superficial and poorly done, and the real nuggets of truth may be buried under the boilerplate somewhere in the summary, claims or description of embodiments of a patent document. Often the description of the prior art highlights some old patent beyond the reach of electronic indexing [21-22].

2.1. Keyword searching

The main drawback of keyword searching is the English language as it is used and abused. However, here in detail are the specific problems:

- ✓ Poor translations: Probably 40% of US patents are filed from abroad, by people who may not use your favorite set of buzzwords for describing their technology. A great many Japanese translations are terrible, on the level of blind Martians describing an elephant. Machine translations are not always the worst source of garbage.
- ✓ Too many synonyms: In the area of chemistry, a compound may have twenty names, depending on the country or field of use. Use Chemical Abstracts to search with the CA registry number.
- ✓ Generic vs specific: There is always a chance that a patent out there dominates because it claims whole genera of applications or substances. Search for general terms as well as specific details.
- ✓ No spelling standards: Some people assume all databases are cast in American English. The World Patent Index, one of the best international databases, is created in the UK and full of British terms.
- ✓ Really bad titles and abstracts: No regulation decrees that these fields should aid in retrieval, and not all databases are created equal – some vendors provide titles and abstracts

enhanced by skilled indexers, whereas most others simply dump raw data from patent office files into their databases.

- ✓ Innovative lexicography: Everyone drafting patents is allowed to create novel terminology to describe inventions and ascribe new meanings to words. The system encourages bizarre descriptions.
- ✓ Errors and omissions: There are thousands of examples of obvious mistakes in titles and names of inventors and assignees as well as other important data such as cited patents. Very few of the errors in issued patents are ever corrected by the database suppliers, who often add their own.
- ✓ Date limitations: Most databases only go back about 30 years or so for searchable abstracts or text. Before that, there is only patent classification, unless you use such sources as Chemical Abstracts that have lately provided back-file coverage.

Systematic keyword searching involves drafting a grid of narrow, broad, and related terms, grouped together in proximity and related to other groups of terms expressing functionality or application. The terms must then be searched in rotation including every conceivable permutation and combination.

2.2. General and technical keyword specification

Keyword selection is one of the most important steps in patent search. It is directly related to the aim of the project. These keywords can be extracted from technical documents or discussion with researchers and expert persons. For the topic of "real time optimization in upstream oil and gas industry", following keywords was selected:

Dynamic real time optimization; Model Predictive Control; Non-linear Model Predictive Control; Gas Lift systems; Real time optimization of drilling parameters; weight on bit, bit rotation speed for obtaining maximum drilling rate as well as minimizing the drilling cost; Real time monitoring; Well regime analysis; Reducing time to decision; Data-integration; Real-time reservoir characterization, real-time formation pressure; Real time data acquisition; High frequency data; Real time Production Data Management System; real-time monitoring and surveillance of the field; Real time field modeling; Dynamic Reservoir Monitoring; dynamic behavior of the reservoir; digital oilfield technology; Logging While Drilling; Intelligent Well Completion; SMART completion; SMART Well; SMART artificial lift; SMART field

2.3. Patent classification

Patent classification is based on professionals in patent office who make judgment calls to classify patent documents according to the subject matter claimed. Therefore, classified patent files should be a perfect search tool. Unfortunately, the decisions of classifiers are often subjective, incomplete and random. There are several patent classifications such as European CLAssification (ECLA) and International Patent Classification (IPC).

3. Strategic analysis

Research activities in all over the world are high-priced. On the other hand, research projects are performed on the knowledge boundaries. This fact increases the risk and uncertainty of the research projects. In this situation, patents are one of the largest sources of strategic information in the world. Three types of strategic information can be extracted by patent analysis:

- 1) Technology trajectory: In a world that is changing ever more quickly, being able to look ahead and understand which aspects of that world will be changing, and to what extent, is a valuable tool for any innovator. Technology trajectory refers to a single branch in the evolution of a technological design of a product/service, with nodes representing separate designs.
- 2) Technological orientation of major companies: Patent analysis can help to find research concentration of main companies in several fields of technology and anticipate their future movement trend.

3) Appropriate joint ventures for strategic research projects: Patent analysis can introduce authentic joint ventures for the long time planning of research projects.

After patent search, classification and screening for "real time optimization in upstream section of oil and gas industry", the strategic analysis was performed. The analysis includes time trend of patent registration, geographical distribution of patents and policy specification of related companies in the field of the technology.

3.1. Time trend of patent registration

The number of registered patents per year in a specific field of technology can represent the history of activity in the technology. Figure 1 shows the number of patents per year for RTPO technology.

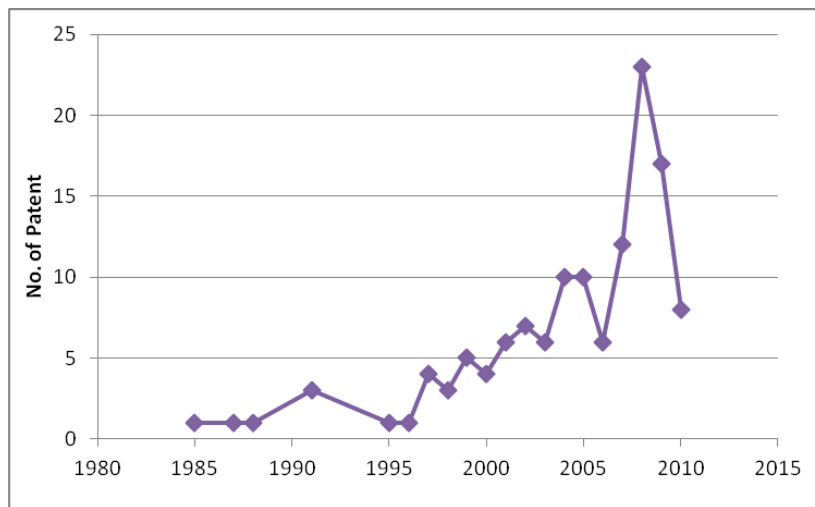


Figure 1. Number of patents per year for "real time optimization in oil and gas upstream"

This figure represents the increasing of investment in the research of the technology. However, in 2009 there is a reduction which extends to 2010.

3.2. Geographical distribution of patents

Totally, 129 patents are identified in this research that registered in different countries. According to geographical classification, 89 out of 129 cases are registered in the USA. Table 1 compares the number of registered patents in different region of the world for the field of the technology.

Table 1. Number of registered patents in different countries for RTPO technology (US: United States of America, WO: World Intellectual Property Organization (WIPO), EP: European Patent Office, EA: Eurasian Patent Organization, OA: African Intellectual Property Organization)

Region	No. of Patents	Region	No. of Patents
Total	129	EA	2
US	89	OA	3
WO	51	US,EP,WO	19
EP	24		

Figure 2 incorporates time trend of figure 1 and geographical distribution of table 1 to show an interesting statistics of the technology growth. The 19 patents which registered in all three well known regions (US, EP and WO) are those with most economic potential and should be technically focused in more details.

While US patent registration rate is the highest, WO patent rate is higher than EP ones. It reveals more inventor interests to grant patents in WO than EP.

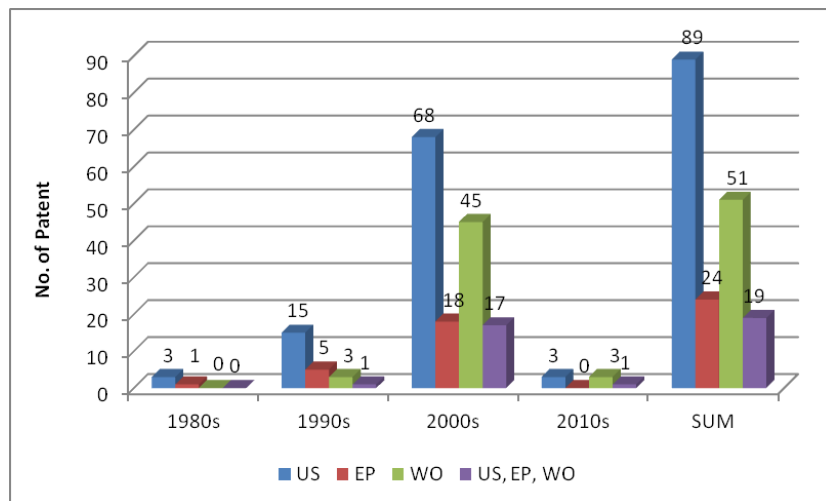


Figure 2. Time trend of patent registration in world regions

Table 2 shows the number of registered patents in different countries. The top 10 countries is shown in Figure 3. This shows that the USA, Canada and China anticipated being the most interesting markets for the technology.

Table 2. Country distribution of the technology's patent registration.

No.	Country	Number of patents	No.	Country	Number of patents
1	United States	89	13	Austria	2
2	Canada	41	14	India	2
3	China	35	15	Denmark	2
4	Norway	27	16	Egypt	2
5	Australia	23	17	Netherlands	1
6	United Kingdom	22	18	Korea	1
7	Mexico	11	19	Italy	1
8	Brazil	12	20	Arkansas	1
9	Germany	12	21	Czechoslovakia	1
10	Russia	10	22	Indonesia	1
11	France	5	23	Colombia	1
12	Japan	4	24	Hong Kong	1

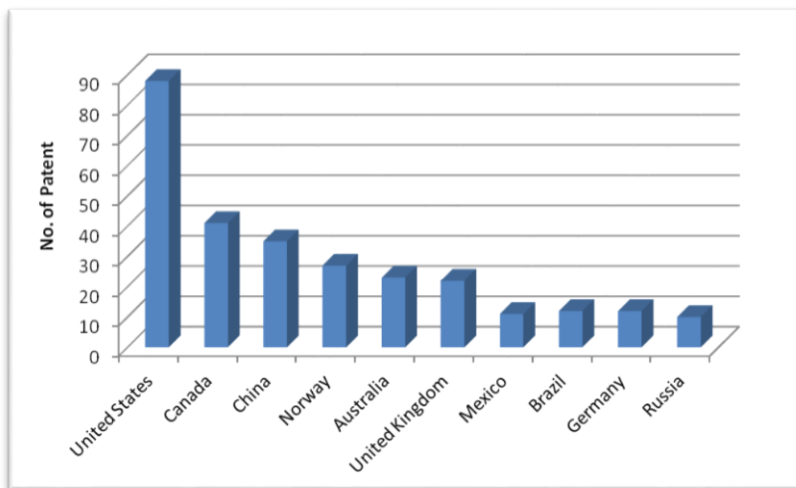


Figure 3. Number of patent for top 10 countries

3.3. Policy specification of related companies

A study of collected documents in this research can be a powerful tool for identifying and classifying of the most active organizations and companies in the field of the technology. The most active companies are shown in figure 4. It is seen that "Schlumberger" has registered two times patents than Halliburton which is on the 2nd place.

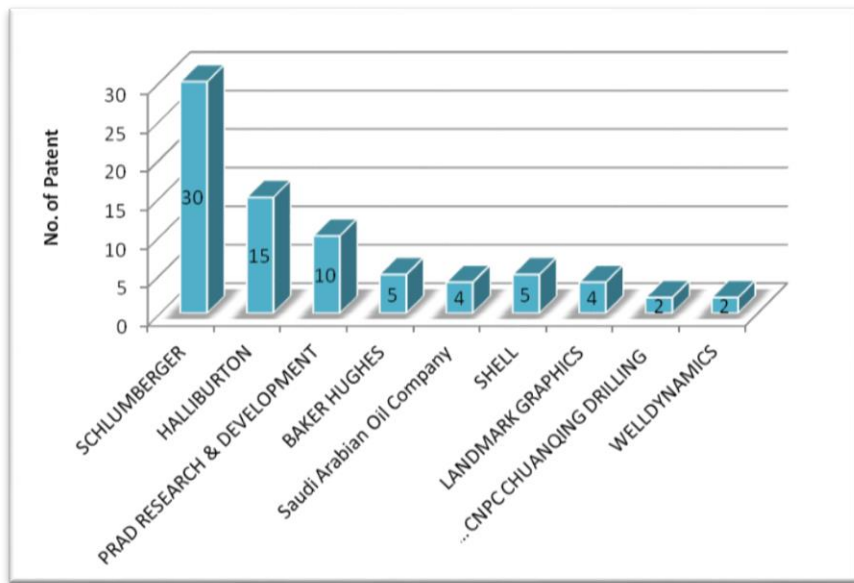


Figure 4. The most owner of patent in the field RTPO

Even though "Halliburton" ranks the second largest patent registration, the time trend for patent registration reveals that "Prad Research & Development" which is on rank three, is more active in the last years of study (Figure 5). This is the same for "Baker Hughes" and "Saudi Arabian Oil Company" which rank four and five in the number of patents. "Schlumberger" has both the most number of patents and most active company in the studied years.

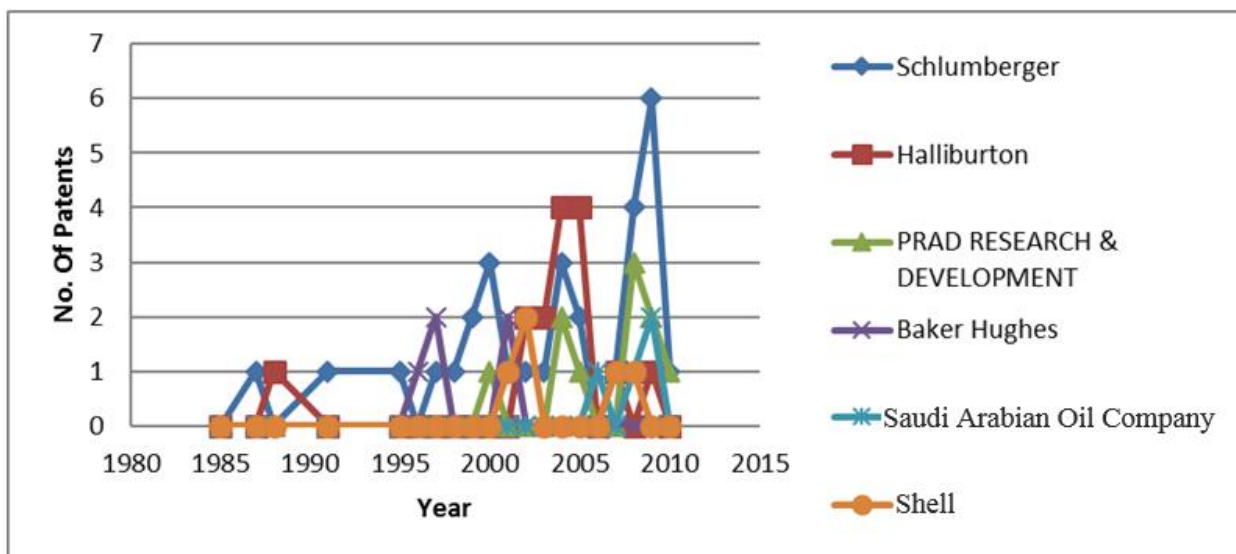


Figure 5. Companies patent registration over time

4. Conclusions

Being innovative is inevitable action for companies in the promptly changing economic environment and tough competition of second decade of 21st century. A successful product must balance three components: marketing, technology, and user experience. Technology plays a key role among these three. Developing a technology development strategy provides competitive materials and processes, resulting in a superior product. The first step for devising a technology development strategy is to decide if the technology is worth an investment and how the technology would develop in the future. Patent analysis is one of the best tools to draw a technology development strategy for companies. In this research, a patent analysis of real time production optimization (RTPO) technology was accomplished in terms of strategic considerations. The analysis includes time trend of patent registration, geographical distribution of patents and policy specification of related companies. In accordance with time trend of patent registration, it is seen a rapid increasing of patent registration. This fact shows the growing importance of this technology in the studied years. Also, the study of geographical and companies policy demonstrates that the investment on the "real time optimization in upstream section of oil and gas industry" increased in the past years in developed regions. These facts illustrate the promising perspective of the technology.

References

- [1] Bagheri SK. Patent Analysis in Research Institutes of Developing Countries. 14th International Conference for Management of Technology, IAMOT, Vienna, Austria, 2005, May 22-26.
- [2] Deboys J. Decision pathways in patent searching and analysis. *World Patent Information*, 2004; 26: 83-90.
- [3] Basak K, Abhilash KS, Ganguly S, Saraf DN. Online optimization of a crude distillation unit with constraints on product properties. *Industrial Engineering Chemistry Research*, 2002; 41: 1557-1568.
- [4] Forbes JF, Marlin TE. Design cost: a systematic approach to technology selection for model-based real-time optimization. *Computers and Chemical Engineering*, 1996; 20: 717-734.
- [5] Lauks UE, Vassbinder RJ, Valkenburg PJ, van Leeuwen C. On-line optimization of an ethylene plant. *Computers & Chemical Engineering*, 1992; 16: S213-S220.
- [6] Ouyang F, Zhang J, Fang W. Optimizing product distribution in the heavy oil catalytic cracking (MIP) process. *Petroleum Science and Technology*, 2017; 35(13): 1315-1320
- [7] Riyahin M, Atashi H and Mohebbi-Kalhor D. Optimization of reaction condition on the product selectivity of Fischer-Tropsch synthesis over a Co-SiO₂/SiC catalyst using a fixed bed reactor. *Petroleum Science and Technology*, 2017; 35(11): 1078-1084
- [8] Shokri S, Sadeghi MT, Ahmadi Marvast M. Soft Sensor Design for Hydrodesulfurization Process using Support Vector Regression based on WT and PCA; *J. Cent. South Univ.*, 2015; 22: 511.
- [9] Fan Q, Lü Z, Yan X, Guo M. Chemical process dynamic optimization based on hybrid differential evolution algorithm integrated with Alopex; *J. Cent. South Univ.* 2013; 20: 950.
- [10] Kakae AH, Rahnama P, Paykani A, Mashadi B. Combining artificial neural network and multi-objective optimization to reduce a heavy-duty diesel engine emissions and fuel consumption; *J. Cent. South Univ.*, 2015, 22: 4235.
- [11] Bieker HP, Slupphaug O, Johansen TA. Real-Time Production Optimization of Offshore Oil and Gas Production Systems: A Technology Survey. SPE 99446-MS, prepared for presentation in Intelligent Energy Conference and Exhibition, 2006, 11-13 April, Amsterdam, The Netherlands.
- [12] Mochizuki S, Saputelli LA, Kabir CS, Cramer R, Lochmann MJ, Reese RD, Harms LK, Sisk CD, Hite JR, Escoria A. Real Time Optimization: Classification and Assessment. SPE Annual Technical Conference and Exhibition, 2004 Houston, Texas, USA.
- [13] Loo E, Arango F, Millan A. Real-Time Drilling Optimization in Sihil Field with Remote Operation Center. SPE Latin American & Caribbean Petroleum Engineering Conference, 2010, Lima, Peru.
- [14] Kashkooli SHB, Masihi M. Pishvaei MR. Dynamic Optimization of Water Flood Reservoirs with the Variational Approach. *Petroleum Science and Technology*, 2014; 32(3): 289-296
- [15] Darabi H, Masihi M. Well Placement Optimization Using Hybrid Optimization Technique Combined with Fuzzy Inference System; *Petroleum Science and Technology*, 2013; 31(5): 481-491

- [16] Zhu X, Li J, Tong H. Mechanism analysis and process optimization of sand and plug removal with rotating jet in horizontal well; *J. Cent. South Univ.*, 2013, 20: 1631.
- [17] Kulkarni RN, Belsvik YH and Reme AB. Smart-Well Monitoring and Control: Snorre B Experience", *SPE 109629-MS*, *SPE Annual Technical Conference and Exhibition*, 2007; 11-14 November, Anaheim, California, U.S.A.
- [18] Cai M, Yin H, Zhong H, Fu Ch. Productivity prediction model and optimal configuration of herringbone multilateral well; *J. Cent. South Univ.*, 2013, 20: 770.
- [19] Sinha SP, Al-Kandar I and Al-Anezi Kh. Using an Integrated Approach to Production Optimization in A Mature Field: Burgan Field, *Search and Discovery Article 40182*, 2006.
- [20] Eldersen MS. Production experience from smart wells in Oseberg field, *Paper SPE 62953*, Presented at the *SPE Annual Technical Conference and Exhibition* held in Dallas, Texas, 2000, 1-4 October.
- [21] Schwander P. An evaluation of patent searching resources: comparing the professional and free on-line databases. *World Patent Information*, 2000; 22(3): 147-165.
- [22] Godoe H. System failure, innovation policy and patents: Fuel cells and related hydrogen technology in Norway 1990-2002. *Energy Policy*, 2006; 34: 1697-1708.

To whom correspondence should be addressed: Dr. Mahdi Ahmadi Marvast, Process Development Division, Research Institute of Petroleum Industry, Tehran 14665-137, IRAN, e-mail: ahmadim@ripi.ir

ENHANCED DELINEATION OF GLACIAL CLASTIC RESERVOIRS BY THE APPLICATION OF PETRO-ELASTIC WELL CORRELATION AND SEISMIC INVERSION: CASE STUDY

Abubaker Alansari¹, Ahmed Mohamed Ahmed Salim¹, Hammad Tariq Janjuhah¹, Nuri Mohamed Fello²*

¹ Department of Geosciences, University Technology PETRONAS, 32610, Perak, Malaysia

² National Oil Corporation (NOC), Tripoli, Libya

Received January 23, 2018; Accepted April 23, 2018

Abstract

The Murzuq Basin is an intracratonic basin located in the South and Southwest (SW) Libya. Glacial Ordovician sandstones are the primary reservoir. However, identifying the top of the upper Ordovician reservoir and the interpretation of intra-Ordovician sequence directly from seismic using conventional methods are well-known challenges in the exploration and production of Murzuq basin. Even with the advent of 3D seismic and dense well database. Therefore, a detailed seismic and well data analysis of the study area was carried out. Sand-shale elastic baseline cut-offs and Vp and Vs cross-over were incorporated into the petro-elastic wireline interpretation. Also, post-stack seismic inversion was applied to generate elastic attributes (acoustic impedance and modelled VpVs). Vp and Vs cross-over successfully outlined the sand cycles when the Vp is located on the right side of the track, whereas the appearance of Vp on the left side indicates the presence of shale units. Seismic inversion provided a better lateral continuity and vertical top and inter reservoir events separation, which has improved their traceability. The VpVs attribute illuminated the reservoir area by the low percentage ratios of 1.6 and 1.8, which is the expected range for sand bodies with emphasis to their upper, mid and lower contacts. Hence, elastic properties derived from both wells and seismic enhanced the delineation of the top of the Upper Ordovician unconformity unit of Mamuniyat Formation (top reservoir) and enabled clear distinction between a non-reservoir unit of upper Ordovician formation (Bir-Tlaksin) and the primary reservoir.

Keywords: Upper Ordovician reservoir; Petroleum system; Post stack seismic inversion; Petro-elastic; Murzuq basin.

1. Introduction

The Murzuq Basin is one of a range of North African intracratonic basins. It is located in south-west Libya, covering some 35,000 km², which is filled with sediments that range in age from the Precambrian to Quaternary. The Gergaf Arch borders the basin to the north, the Thimboka Arch to the west and the Tibisti Arch to the east (Figure 1). Former studies have demonstrated that the structural evolution of the basin was a result of several distinct major tectonic phases that affected the whole North Africa [1]. These phases include the Pan-African orogeny in the Precambrian; Cambrian extension; Cambrian to Carboniferous alternating extension and compression; late Carboniferous (Hercynian) uplift; late Triassic-Early Jurassic and early Cretaceous rifting, mid-Cretaceous (Austrian); late Cretaceous-Tertiary (Alpine) compression; Neogene-Recent uplift, and volcanic activity (Figure. 2) [1-4].

The Murzuq Basin is considered to be one of the producing areas in Libya with recoverable oil volume of 2300 MMbI [4-6]. As a result, the basin has been prioritised for extensive exploration activities, especially after the discovery of the giant Elephant oil field by British Operator Lasmo in 1998 [7]. The increase in oil prices in the mid-1990s to early 2000s (albeit with fluctuations) allowed oil companies to invest in exploration, even in isolated areas with costly exploration fees. Accordingly, some multi-international oil companies increased their explora-

tory operation within the basin and succeeded in adding several oil discoveries to the near oil field exploration campaigns in North-West Murzuq basin. However, all exploration efforts made in the South- SW part of the basin has been suspended without announcing any economic findings.

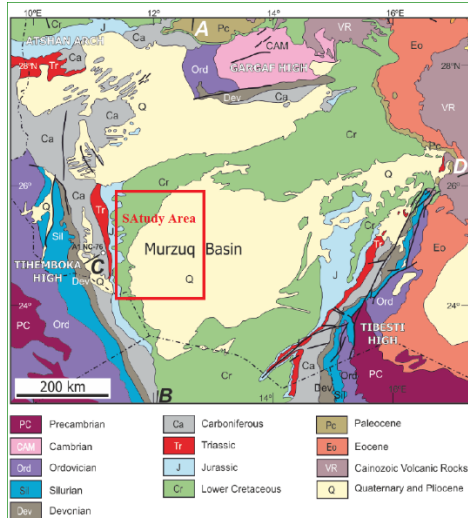


Fig. 1. The boundary of Murzuq Basin and study area location edited from (Shalbak [\[19\]](#))

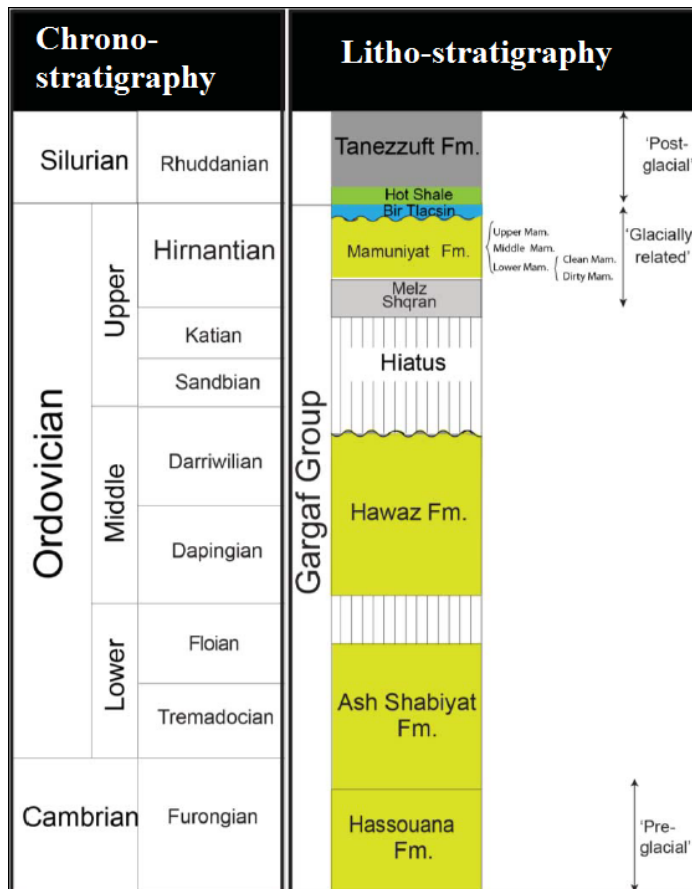


Fig. 2. Stratigraphic column of Murzuq basin (McDougall [\[24\]](#))

The absence of any high-quality dataset and the interpretation of existent ones in the south-SW Murzuq basin has severely affected the outcome of the exploration activities on this side of the basin. Meanwhile, only 2D seismic data were acquired in the latest exploration activities. Furthermore, identifying the tops and bottom of upper Ordovician reservoir unit as well as the interpretation of intra-Ordovician sequence are well-known pitfalls in the exploration and production of Murzuq basin, even with the advent of 3D seismic and dense well database [\[8\]](#). It has been a frequent practice to use the lower contact of Silurian hot-shale as a top reservoir in all Murzuq basin. Due to it is strong continues reflection resulted from strong impedance contrast between the Silurian shale and underlying Ordo-vician sand. Therefore, attention has been drawn in the latest years to the incorporation of pre and post-stack seismic inversions into latest studies. Especially in the Northern part of the basin, such as the con temporary study by [\[9\]](#),

which used coloured inversion to improve the detection of this reservoir. However, to the best of our knowledge, pre and post-stack seismic inversions are yet to be applied to the South-SW part of the basin.

Therefore, this paper is an attempt to enhance the delineation of the upper Ordovician reservoir by integration of petro-elastic interpretation methods to the available database at South-SW part of the Murzuq basin.

The results will provide the basis to identify reservoir characteristics from seismic and wells. Also, overcoming the traditional practice of picking the bottom of lower Silurian (strong negative impedance) source rock as the top reservoir contact. Achieving the objectives will ensure that the factors controlling the delineation of the upper Ordovician reservoir in the Southwestern part of the Murzuq Basin are rationally examined through the interpretation of inverted well calibrated post-stack seismic data.

2. Petroleum system elements

There are three proven oil reservoirs in the Murzuq Basin (SW Murzuq), namely: Ordovician sandstones of Hawaz; Ordovician sandstones of Mamuniyat, and Devonian sandstones of the Awaynat Wanin Formation [\[10\]](#). The Silurian Tanezzuft Formation is the primary source rock for the Basin and also provides the regional seal for the Ordovician reservoirs (Figure. 2). For this paper, the only upper Ordovician reservoir (Mamuniyat Fm.) of Lower Palaeozoic plays (Ordovician sandstones of Hawaz and Mamuniyat) will be covered.

2.1. Reservoirs

The reservoir varies across the Murzuq Basin between Mamuniyat and Hawaz, while a combination of both characterises some areas. The Mamuniyat Formation consists of sandstones that are medium to coarse-grained, and moderately to poorly sorted. The sandstones are clean, with porosity varying from 7% up to 20% with an average of 11%, while their permeability can reach 1600 mD with an average of 300 mD. The reservoir properties of the Hawaz formation are moderated by the amount of fluvio-tidal channels present in the primary reservoir zones. The average porosity of the Hawaz reservoir is approximately 13% with permeability values ranging between 1-20 mD in the Lower Shoreface facies and up to 50-700 mD in the channel facies [\[11\]](#).

2.1.1. Hawaz Formation

Some studies have characterised the depositional environment of Hawaz Formation as a gently dipping shelf covered by epicontinental seas with a broad coastal plain area that is fragmented by channels [\[12-13\]](#). The models of the Hawaz Formation consist of a sequence of stacked sedimentary packages. That belongs to the shelf (burrowed) and lower shoreface facies association in the bottom part, followed by fining upwards fluvio-tidal channel sandstones in the middle part, which are overlain by burrowed shelf and lower shoreface sediments in the uppermost part. These sedimentary rocks were intensely eroded and carved by ice streams afterwards (late Ordovician glaciation) to form a unique terrain of cliffs and incised valleys [\[14\]](#).

2.1.2. Mamuniyat Formation

The Mamuniyat Formation depositional environment is interpreted as a relatively deep marine, to fluvial sedimentary sequence [\[15-16\]](#). Massive volumes of outwash sands and gravel were deposited over a glacial-fluvial outwash plain due to the melting of glacial overburden. Braided deltas were subsequently developed where the outwash streams come in contact with the coastline [\[17\]](#). In some areas, these deltas prograded across a thin shelf until their transported sediment was redeposited in the edges and borders of turbiditic fans. The coarse glacial-fluvial sands were then reworked in a shallow marine environment to generate near-shore bar features away, in sheltered areas between the braided deltas [\[17\]](#). The Top Mamuniyat Formation consists of a lower unit of coarse-grained braided channel sandstones

and deposits covered by the very coarse-grained unit. While the Middle Mamuniyat is a heterogeneous mix of fine-grained delta front to delta plain sediments in the lower part, which are abruptly covered by coarser grained delta plain/distributary channel sediments [18]. The Lower Mamuniyat is also variable and comprises primarily fluvial distributary channel and shallow marine sandstones [10,12,19].

3. Dataset and methodology

The study area is covered by a dense 2D seismic grid that was acquired in different stages. Moreover, some exploration and water wells are drilled. However, only three wells (Brine Sands) will be used for this study.

3.1. Well data

The wells drilled in the area were correlated to obtain them. All the wells have relevant wireline logs that include Gamma-ray (GR), Resistivity, Sonic, Neutron and Density logs from which the vertical distribution of the petroleum system members within this region and accurate synthetic seismograms were derived (Figure 3).

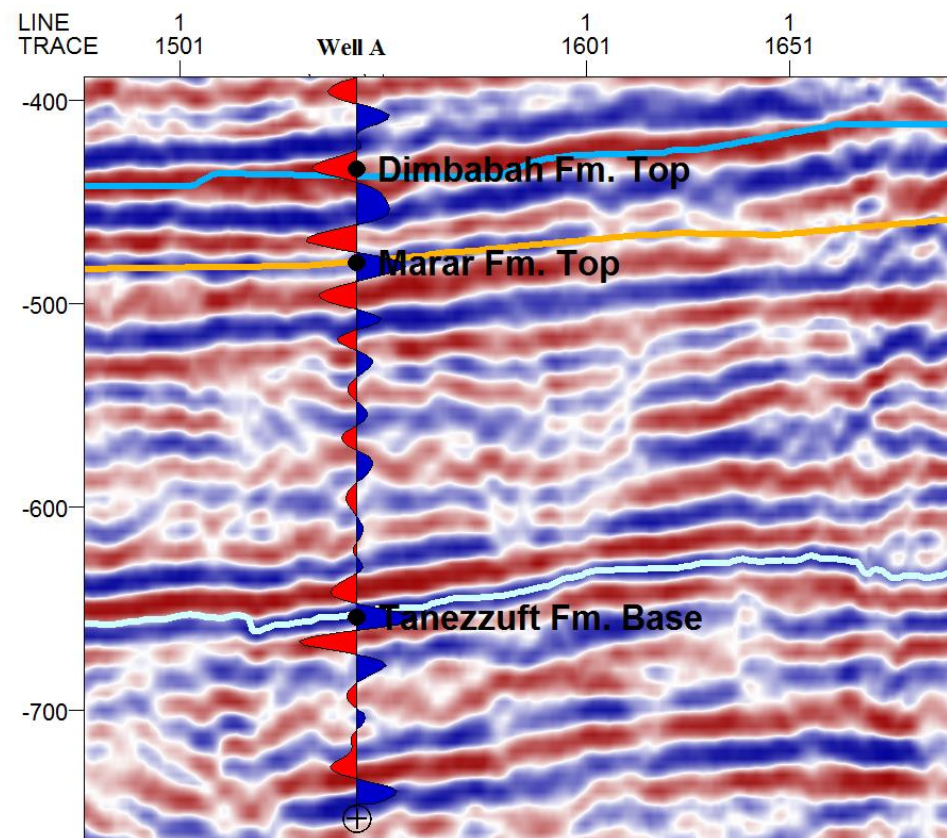


Fig. 3. Seismic well tie used for conventional seismic interpretation

3.1.1. Petrophysical interpretation of wireline logs

$$V_{sh} = \frac{GR_{log} - GR_{min}}{GR_{max} - GR_{min}} \quad (1)$$

For porosity determination, a combination method of neutron porosity, density and sonic logs will be applied to obtain more favourable total porosity (ϕ_{total}) (Asquith and Gibson 1982).

$$\phi_N = \text{Neutron Porosity from the logs} \quad (2)$$

$$\phi_D = \frac{\rho_{ma} - \rho_{log}}{\rho_{ma} - \rho_{fl}} \quad (3)$$

where: ϕ_D = density porosity; ρ_{ma} = matrix density; ρ_{log} = bulk density from log and ρ_{fl} = Fluid density.

$$\phi_S = \frac{\Delta t_{log} - \Delta t_{ma}}{\Delta t_{fl} - \Delta t_{ma}} \quad (4)$$

where: ϕ_S = sonic derived porosity; Δt_{ma} = matrix transit time; Δt_{log} = sonic transit time from log and Δt_{fl} = fluid transit time.

After that total porosity will be obtained by averaging three determined porosity types above (density, neutron and sonic)

$$\phi_{total} = \frac{\phi_S + \phi_D + \phi_N}{3} \quad (5)$$

3.1.2. Estimation of elastic properties of reservoir rocks

For the three wells available for this study, compressional sonic log is available, but the shear wave sonic exist in only one well

3.2.1. Share wave estimation (Vp) and Vp/Vs ratio

Several methods will be used for Vs estimation; these methods included Castagna "mudrock line", Greenberg-Castagna, and correlation regressions. After that, the above methods will be compared, and one of them will be selected based on its accuracy when compared to the measured Vs from well A.

3.2.2. Gassman fluid substitution

The wells used here represents brine sands which caused a lower impedance contrast between shale and sand unit. Therefore, Gassmann fluid substitution is applied (100% brine and 70 % oil & gas) to improve the P-impedance contrast if gas case logs used as input for post-stack seismic inversion. Below here is workflow of the substitution

$$K_{sat} = K_{dry} + \frac{\left(1 - \frac{K_{dry}}{K_{sat}}\right)^2}{\frac{\phi}{K_f} + \frac{1-\phi}{K_{ma}} - \frac{K_{dry}}{K_{ma}^2}} \quad (6)$$

$$\mu_{sat} = \mu_{dry} \quad (7)$$

where K_{dry} , K_f And K_{ma} are the bulk moduli of the dry rock, trapped fluids and rock matrix (GPa) respectively; and ϕ is the fractional porosity of the rock .Shear moduli of the dry and saturated rock (GPa) are denoted by μ_{dry} and μ_{sat} , respectively. It is worth stating that corrected log derived density values were used as an input for ρ_{sat} and ρ_{ma} (density of saturated and matrix rock). These density values were derived from the equation below.

$$\rho_{fl} = S_w \rho_w + (1 - S_w) \rho_{hc} \quad (8)$$

where, S_w is water saturation, ρ_w = density of formation water and ρ_{hc} = density of hydrocarbon. The mass balance equation will be used for calculating the bulk density of the mixed fluid rock;

$$\rho_b = \rho_g + (1 - \phi) + \rho_{fl} \phi \quad (9)$$

ρ_b = bulk density; ρ_g = formation's grain density; ϕ = total porosity and ρ_{fl} is density of the fluid occupying the pores.

Then, fluid modulus will be estimated by using Wood's equation;

$$K_{fl} = \left(\frac{S_w}{K_w} + \frac{(1-S_w)}{K_{hc}} \right)^{-1} \quad (10)$$

where, K_{fl} is Fluid modulus, K_w represents bulk modulus of brine and K_{hc} denotes hydrocarbon bulk modulus.

Elastic properties of a medium (the compressional and shear wave velocity of a rock), Vp and Vs , can be estimated for any saturation by using the equations below;

$$Vp = \sqrt{\frac{K_{sat} + 4\mu_{sat}/3}{\rho_{sat}}} \quad (11)$$

$$Vs = \sqrt{\frac{\mu_{sat}}{\rho_{sat}}} \quad (12)$$

where K_{sat} and μ_{sat} are the bulk and shear moduli of saturated rock (GPa), respectively, while the ρ_{sat} is the bulk density of saturated rock (g/cm³). The bulk and shear moduli of saturated

3.2. Seismic data

The conventional seismic data interpretation was constrained to three wells (A, B and C). Five Horizons were identified (Top Zarzartine, Top Tigouentourine, Base Tanezzuft, Top Mamuniyat and Basement) and tied to the wells. However, for this study, three horizons (Basement, Ordovician Base Tanezzuft and Permian Top Tigouentourin) were prioritised and wholly interpreted. Ordovician Base Tanezzuft shale is the critical horizon that can be traced easily within the area since it directly overlies the critical Ordovician sandstone reservoirs, hence it has frequently been used for the mapping. Synthetic Seismogram was generated using check-shots data, corrected sonic and density, which were then tied to the seismic for calibration and referenced to interpreted 2D seismic lines. After that, the study area was mapped based on the seismic interpretation. Finally, two seismic lines that cross through well A&C were selected as a candidate for post-stack seismic inversion analysis

3.3. Post Stack Seismic Inversion

In this paper, two post-stack 2D seismic lines (X&Y) (Figures 4. 5), which cross through two wells (C and A), were inverted using model-based inversion where the acoustic impedance was calculated at each well location before wavelet estimation and seismic well tie (Figure. 6). A reasonable match between seismic and synthetic data was achieved with only 3 ms shift was applied (Figure. 6).

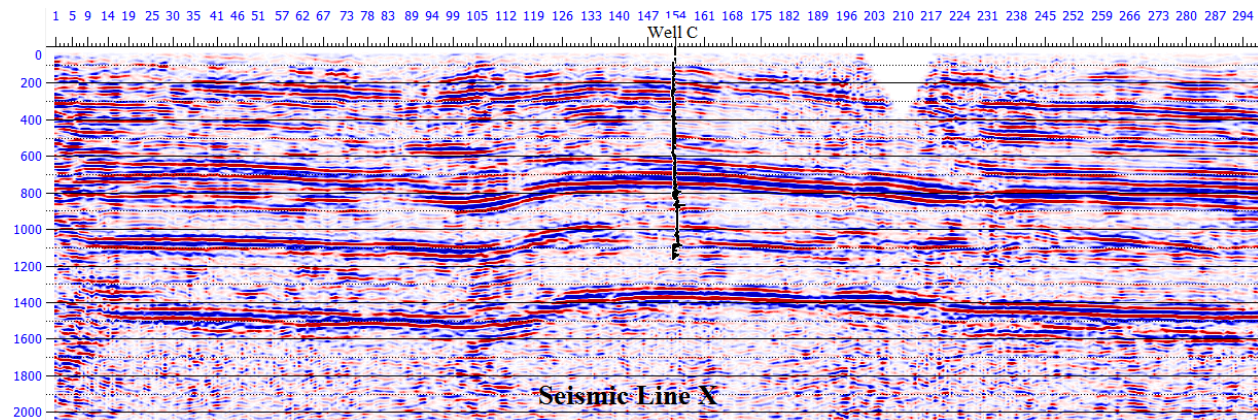


Fig. 4. 2D seismic section X

3.3.1. Vp/Vs Computation

For Vp/Vs modelling inverted acoustic impedance and original seismic lines will be used as an input for multi-attribute analysis and neural network training for both seismic lines. Then the multi-seismic attributes and neural network will be used to generate the relationship which then calibrated with the estimated Vp/Vs from the wells before applying it to the seismic lines.

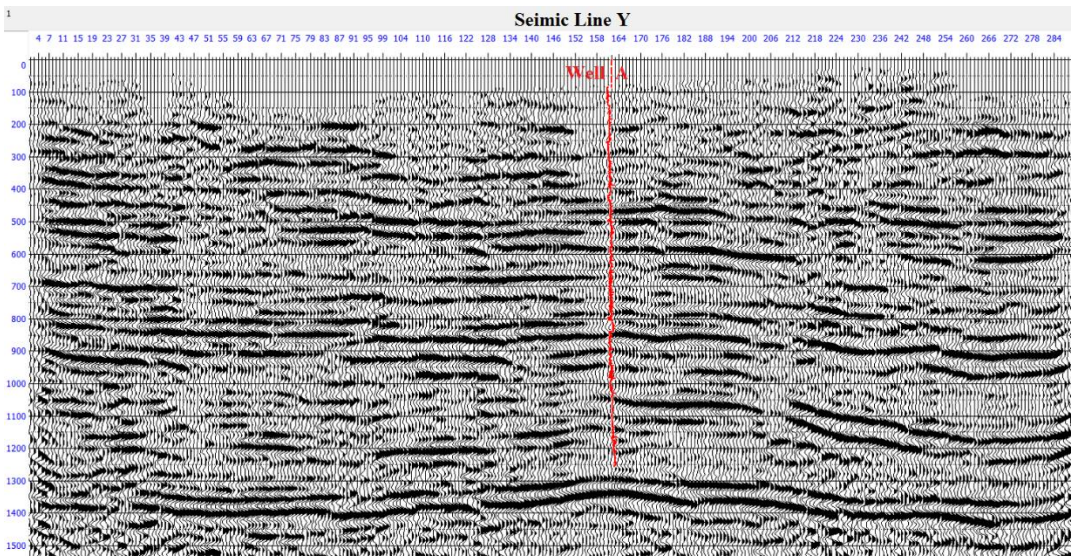


Fig. 5. 2D seismic section Y

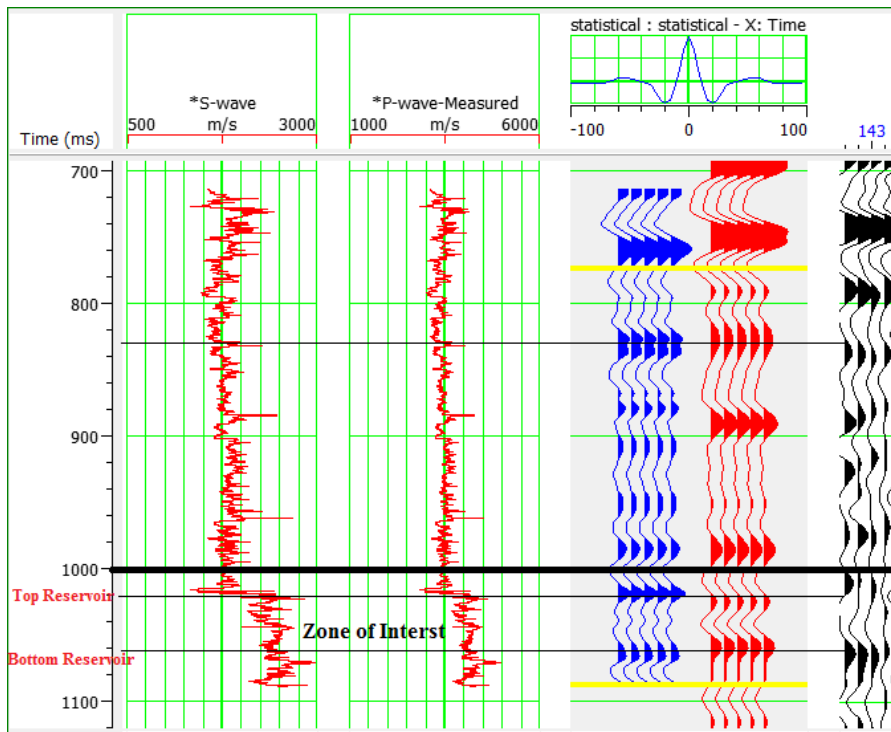


Fig. 6. Seismic well tie analysis for inversion process

4. Results and discussion

4.1. Wireline interpretation

Petrophysical properties (Vsh, SW and Porosity) were derived from the available wireline logs using conventional log analysis. However, this analysis was inadequate to achieve optimum separation of the upper and intra-Ordovician reservoir units and their unconformities. Especially the lower contact between Mamuniyat and Hawaz Formations, illustrated by red circle (Figure 7), even though a combination of porosity, gamma ray, sonic, neutron porosity and density was used with a particular colour template that reflects the cut-off values of shale and sand unit observed from all the wells. Furthermore, the gradual facies

change from the sandy-shale of Bir Tlaksin Formation to shaly-sand of the Upper Mamuniyat is not detected in the areas were the Bir Tlaksin Formation is thinner (Figure 7). The fluid substituted P-impedance shows a fit of the brine case (blue Curve) with original case (black Curve) confirming the fact of being a dry reservoir (Figure 8). Whereas the oil and gas cases showed lower PI values in sand zone and superimposed with the initial case at shale zones as expected (Figure 9).

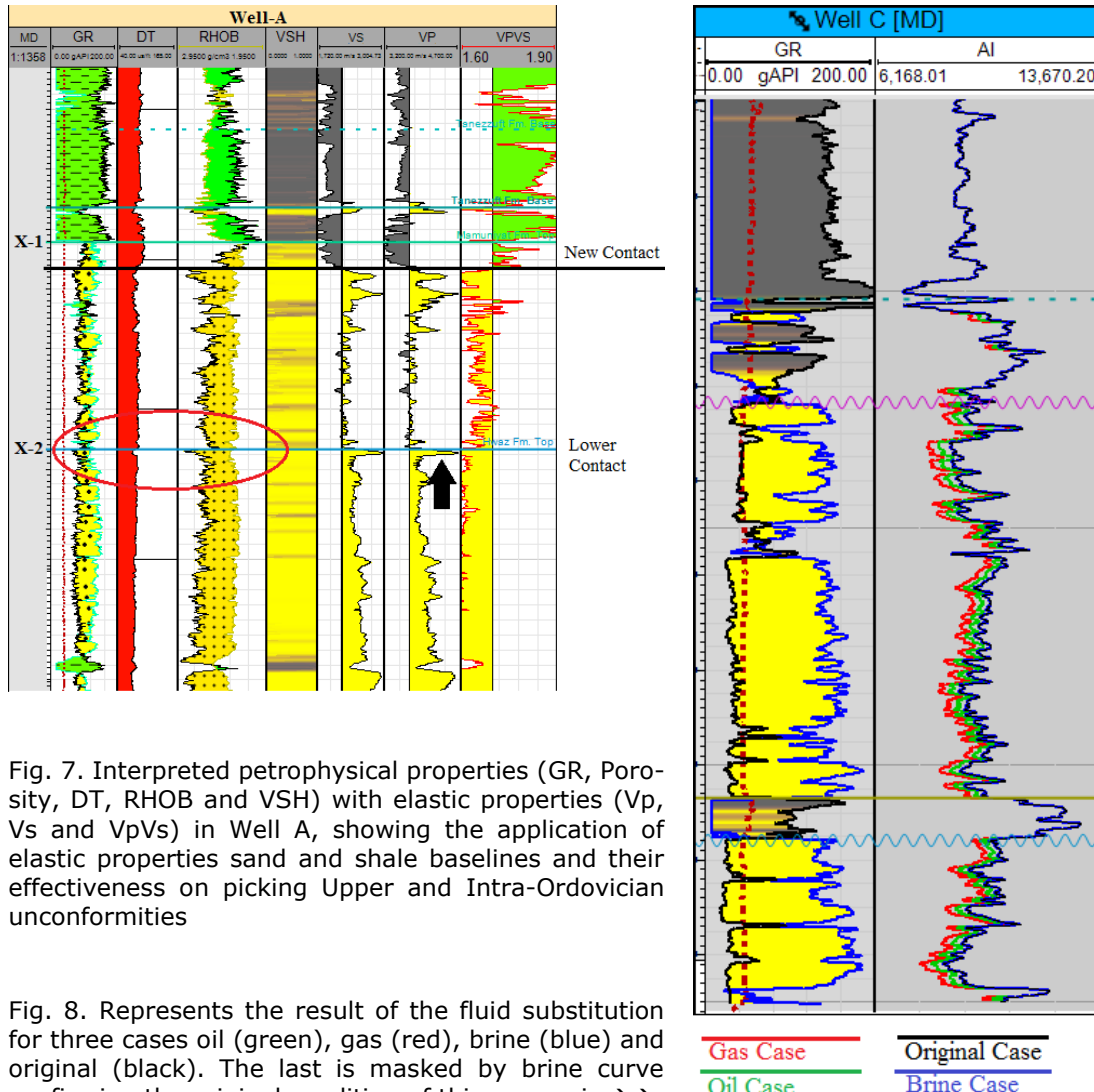


Fig. 7. Interpreted petrophysical properties (GR, Porosity, DT, RHOB and VSH) with elastic properties (Vp, Vs and Vp/Vs) in Well A, showing the application of elastic properties sand and shale baselines and their effectiveness on picking Upper and Intra-Ordovician unconformities

Fig. 8. Represents the result of the fluid substitution for three cases oil (green), gas (red), and brine (blue) and original (black). The last is masked by brine curve confirming the original condition of this reservoir →

4.1.1. Sand-shale elastic properties baseline cut-offs

Vs estimated using Greenberg-Castagna showed a closer fit to the measured shear wave in well A. Therefore, it was selected and used for velocity ratio calculation and input for petro-elastic correlations. Vp, Vs and Vp/Vs ratio values for sand and shale units were identified by running several petro-elastic cross plots such as GR in the x-axis against GR/Vs (y-axis) (Figure. 10). The average values representing the lithology end members were then selected. Moreover, used as a baseline and colour the template on the correlation panel (Figure. 7). The elastic properties identified the top of the Upper Ordovician unconformity unit of Mamuniyat Formation and allowed shifting it a couple of meters down. Also, the intra-Ordovician unconformity on the top of Hawaz formation is delineated with an increase of both S and P waves

leading to a decrease of their ratio, which was due to abrupt change from the eroded lower dirty upper Ordovician reservoir to the top of the paleo-high Hawaz formation (Figure. 7).

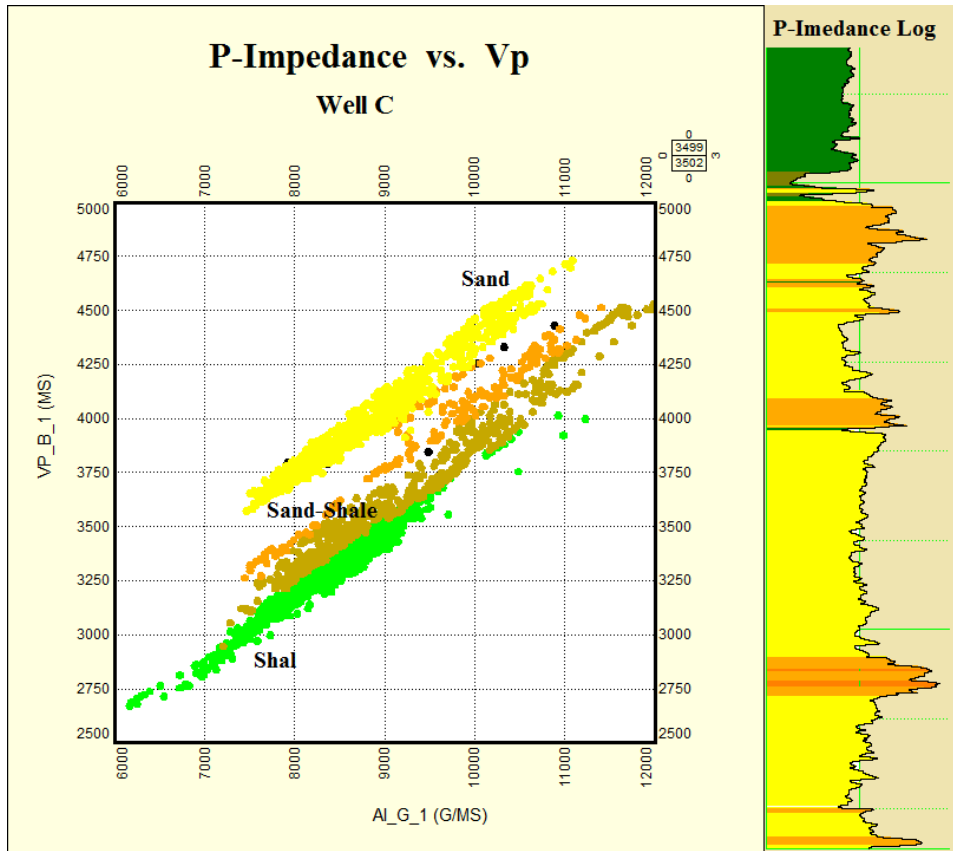


Fig. 9. The cross plot of P-Impedance gas case vs. Vp initial case showing the enhanced separation between sand shale facies after the fluid substitution application

4.1.2. *Vp and Vs cross-over*

The technique of 'log Cross-over' is widely used in wireline interpretation, especially neutron density logs, but it has not been implemented with elastic properties. This technique was adapted here using standard Vp scale and reverse Vs scale curves (Figure. 11). Sand cycles appear when the Vp (shown in red) is located on the right side of the track, whereas the appearance of Vp on the left side indicates the presence of shale units (Figure 11). The larger the separation between both curves (Vp and Vs), the cleaner the identified lithology. Conversely, the tighter the cross-over, the higher the mixture of sand and shale units. By applying this method, we were able to quickly identify the two main Ordovician unconformities and their internal zones. the upper Ordovician unconformity illuminated by sizeable thin separation followed by series of tight and larger separations with Vp curve to the right (Figure 12). While the second dirty zone of the upper Ordovician reservoir named M1 (Figure. 11), is characterised by a combination of tight and medium separations with Vp curve. The location of the Vp curve (right to the left) reflects the percentage of shale and sand for each layer. The lower zone top (M2) of the reservoir can be openly discriminated by a more consistent medium to small separation without an overlay of both curves and with a remarkable location of Vp to the left and Vs to the right within the whole zone. Finally, the lower contact of the reservoir can be identified either by; if the lower shaly member of Melaz Shuqrani formation exists the contact delineated small separation with Vp curve to the left and Vs to the right such as in well C (figure. 11). However, if the above-stated formation is eroded the contact will be reflected by a significant funnel to bell separation with Vp curve to the right. The

distance of the crossover is controlled by the percentage and thickness of clean coarse sandstones of the top Hawaz unconformity (well B and A figure. 11).

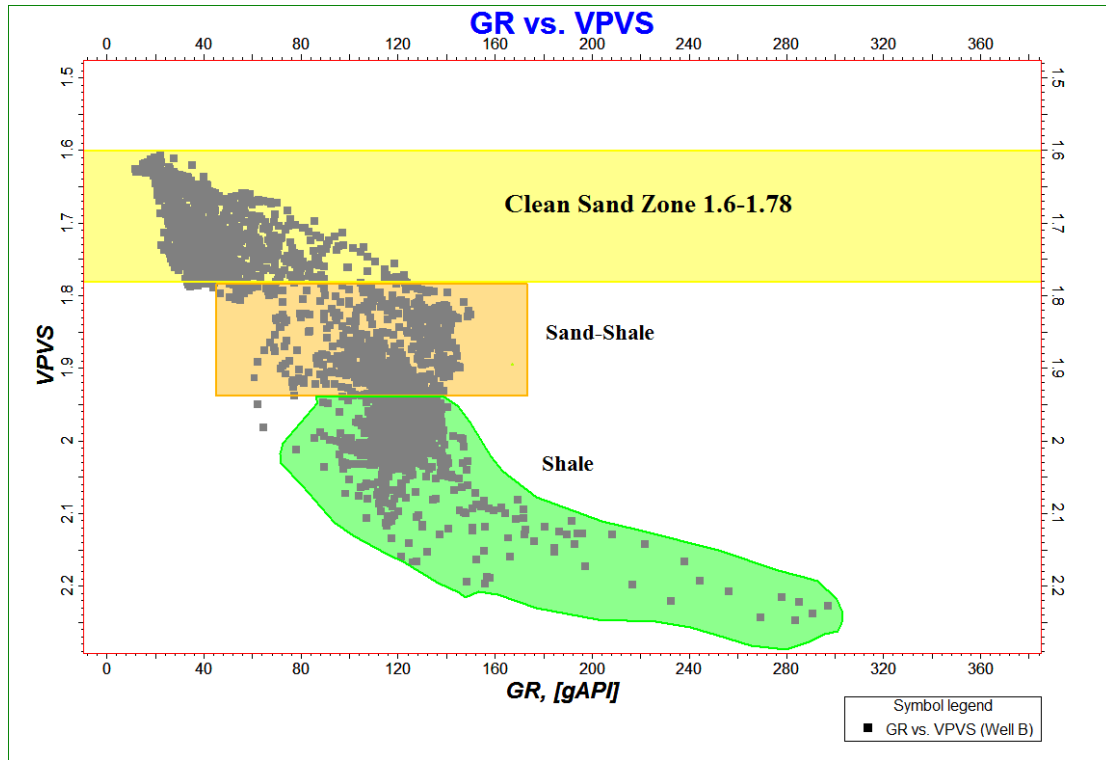


Fig. 10. The cross plot of Gamma ray log vs VpVs log, showing how the shale and sand cut-offs values were selected to be used for elastic properties estimation

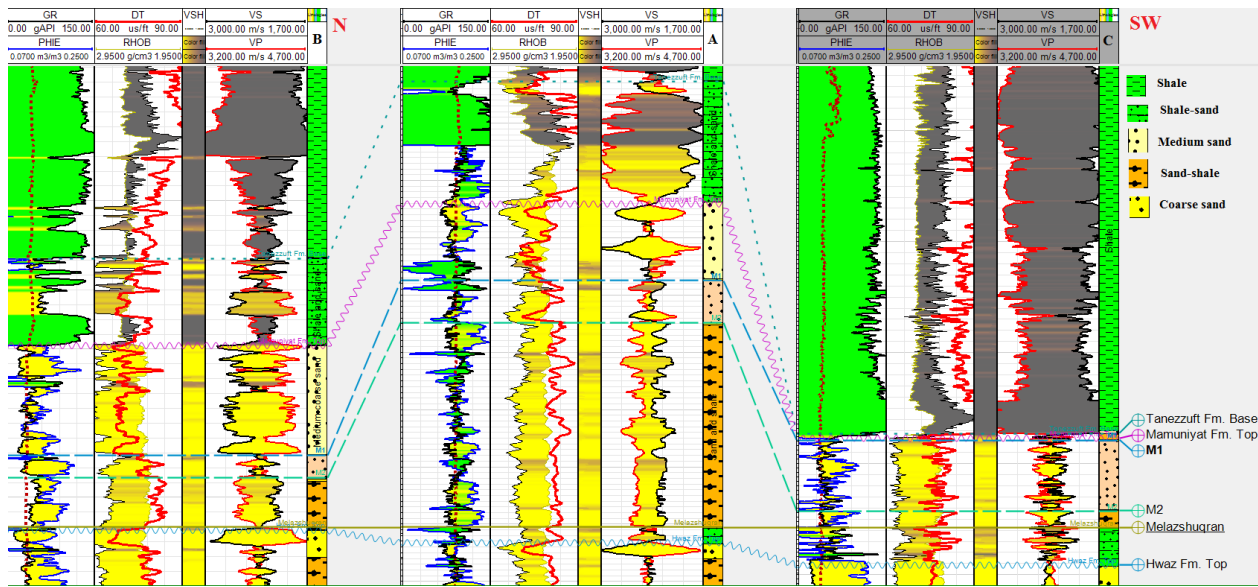


Fig. 11. N-SW Petro-elastic correlation panel for the tree wells representing the new suggested contacts of upper and Intra-Ordovician unconformities by the VP and Vs cross over nature

4.2. Conventional seismic interpretation

Structure maps of the Basement, Base Tanezzuft and Top Tiguentourine were generated from the interpreted 2D seismic lines. The Base Tanezzuft structure map showed the highest

relief in North, West and the central part of the study area, and the lowest relief in the south and south-east parts (Figure. 12). The identified structures may fall into two main trap types: Paleogeomorphologic traps that were generated as a result of glacial erosion during the Ordovician time when the melting glaciers cut through the Hawaz formation producing the erosion of its upper part. The Hawaz Formation then overlain by either the younger Silurian Tanezuft formation or in some areas of older Upper Ordovician Mamuniyat Formation. This trap type forms the most crucial plays in the Murzuq Basin, where the vast amounts of hydrocarbon were trapped within this basin. Inverted anticline Traps or Fault Blocks Traps which have been formed as a result of Cenozoic inversion: is mainly a structural three-way dip closures with an assumed sealed fault closing the fourth side in the Mamuniyat Formation and shares the same Hot Shale as the source rock with Tanezuft shales as the seal. Thickness maps were generated to infer formation thicknesses covering between Base Tanezuft and Basement shows that areas below the paleo-geomorphologic and inverted anticlines are thicker than the surrounding areas (Figure. 13).

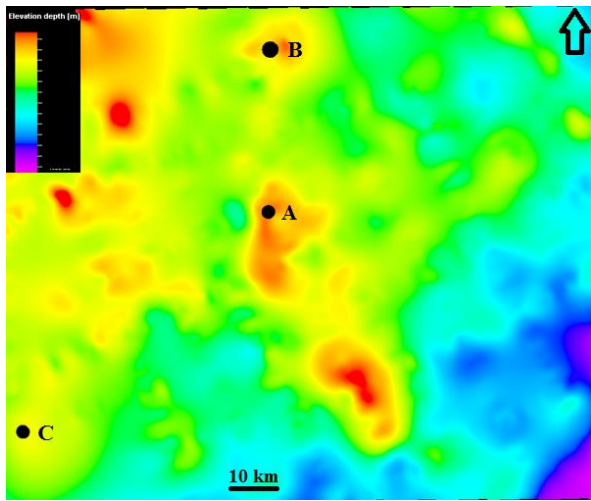


Fig. 12. Depth structure map of base Silurian 'Hot shale' interpreted used conventional 2D seismic data

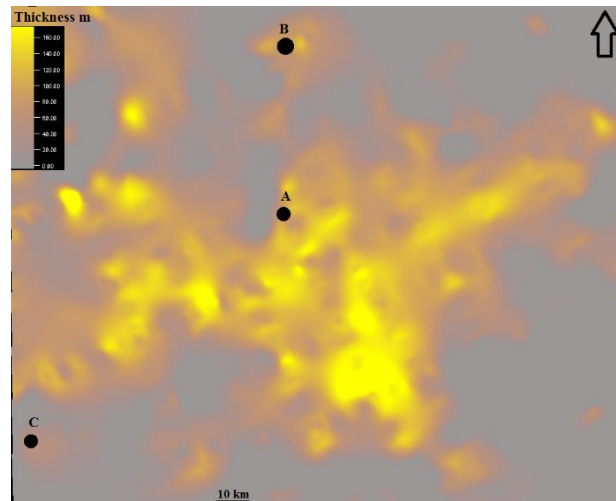


Fig. 13. Thickness map between Base Hot shale and basement. Representing the distribution of sand bodies in (yellow) and thinner in (dark grey)

4.3. Post Stack Seismic Inversion

A post-stack seismic inversion is a tool for inverting seismic trace into acoustic impedance to achieve practical geological results [21]. Post-stack inversion is a proper natural step to improve the stratigraphic interpretation units captured by post-stack seismic data. This type of seismic inversion has been universally used as an effective method for oil and gas exploration and production in several sedimentary basins. Usually, the primary focus of seismic inversion is to overcome the main challenges that might be encountered during the conventional seismic interpretation such as play system accurate delineation in the exploration level and estimation of petrophysical properties at the reservoir scale. Das *et al.* and Kumar *et al.* [22-23] stated the subsurface geology could be represented by stacked planes with parallel layers in all seismic inversion methods

The considered window for elastic properties estimation covers between 800-1175 ms. all values above or below this range might be erroneous.

In seismic Line X, the inverted impedance increases downward, except some upper and lower seismic sections that are not within the available well data. The significant change in acoustic impedance around 1025ms to 1075 ms of Well C indicates the top of Upper Ordovician reservoir, which overlies the short low impedance zone at 1100-1150ms indicating the Intra-Ordovician reservoir unit (Figure 14). In comparison to the original seismic line (Figure. 4), this inversion provided a better lateral and vertical events separation, which has improved the

traceability of the top reservoir event when compared to the original seismic data. The lower impedances are encountered at more shaly successions, while the medium impedances represent the sandy layers (Figure, 14). The section also represents a possibility of defining intra-Ordovician unconformity between the upper Ordovician Mamuniyat reservoir and Hawaz formation (Figures. 14).

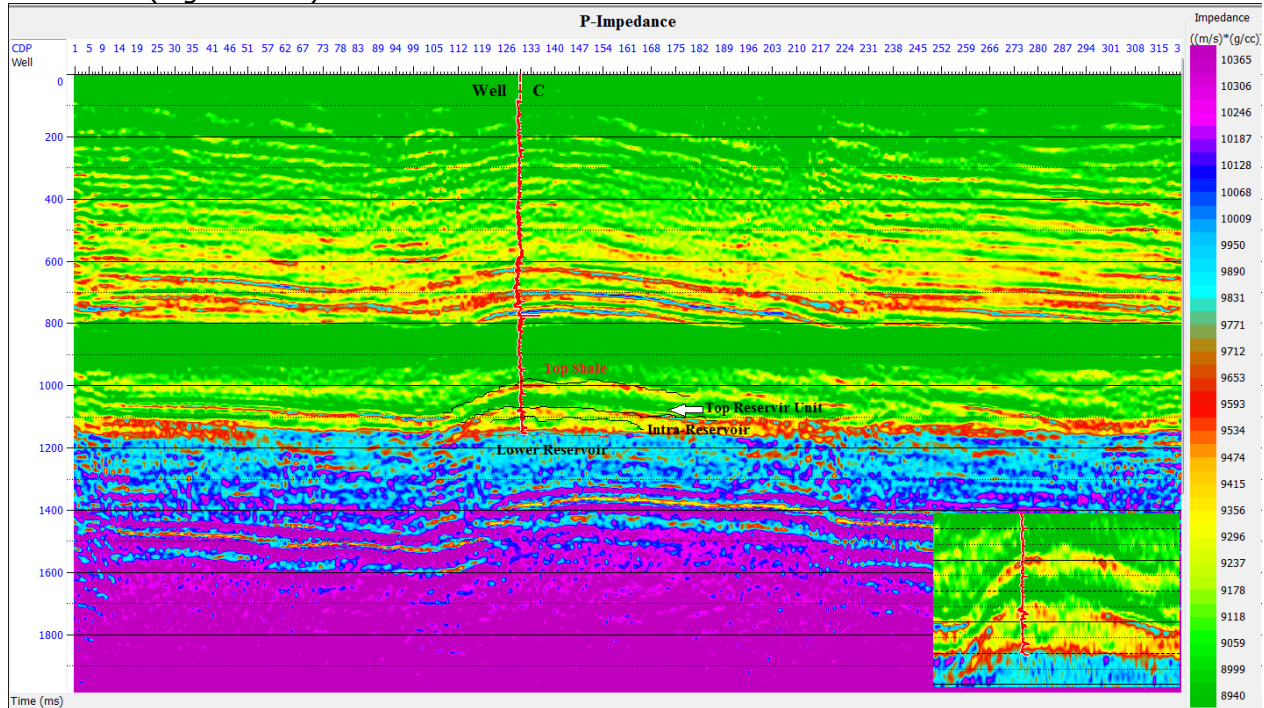


Fig. 14. Representing inverted acoustic impedance from seismic line X, with enhanced delineation of the upper Ordovician reservoir components

Using the above AI attributes, the primary structure has been delineated with a possibility of identifying the reservoir contacts and generate more accurate structure maps for the zones of interest (Figure. 14). The first top contact represents the shale zones and the second denotes the primary zone of interest (Top upper Ordovician reservoir) shown in Figure 14. The last two lines within the same figure suggest the intra-Ordovician reservoir unit and top Hawaz formation respectively.

Before modelling V_p/V_s from seismic, we cross-plotted Acoustic Impedance from seismic with V_p/V_s estimated from wells (Figure. 15) which has helped on classifying the lithological contents based on their elastic responses. The cross plot has enabled identification of four main lithological classes; 1) hot shale, with V_p/V_s of around 2.18 and PI of 5500-7700 $(m/s)*(g/cc)$. 2) Shale contents with broader ranges of V_p/V_s (1.8-2) and PI (7700-9200 $(m/s)*(g/cc)$). 3) The sand zone which characterised by the range of 1.65-1.78 velocity ratio and 8700-10500 $(m/s)*(g/cc)$ P-impedance. Finally, the mixed zone of shale-sand covers some parts of shale and sand zones (Figure. 15).

The predicted V_p/V_s from the seismic data (figure. 16) using neural network showed a better match to the one estimated from wells comparing to the curve generated using multi-attribute one (Figure. 16). Therefore, the former was used for generating V_p/V_s attribute from both 2D seismic lines.

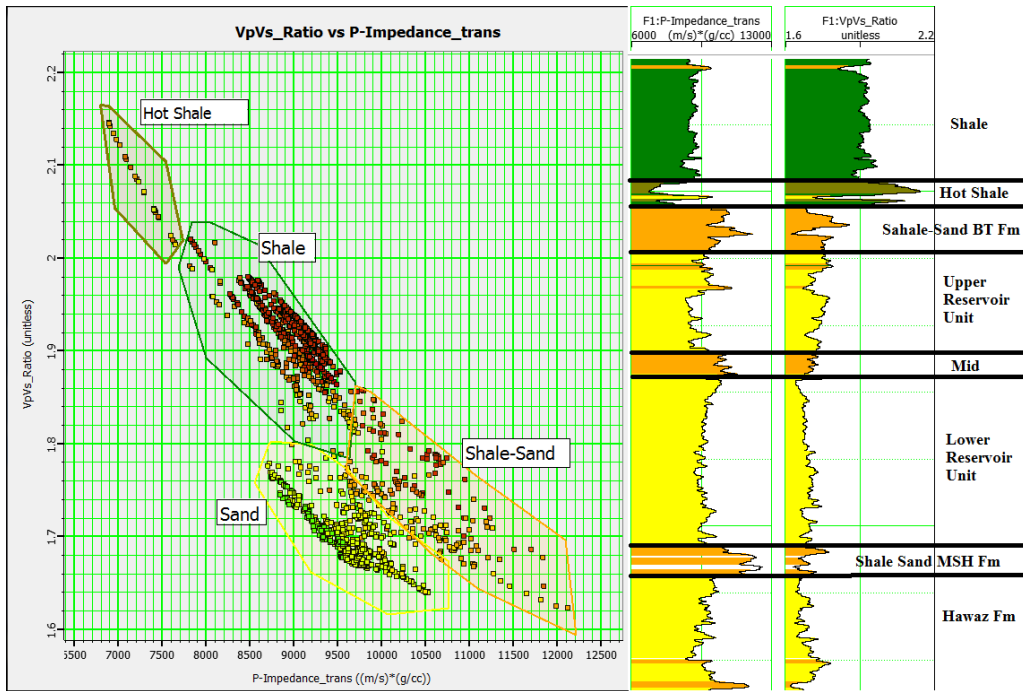


Fig. 15. The cross plot of P-Impedance vs. VpVs estimated from wells, which has helped on classifying the lithological contents based on their elastic responses. Namely, Hot shale (olive green), sand (yellow), Shale (Green) and shale Sand (orange)

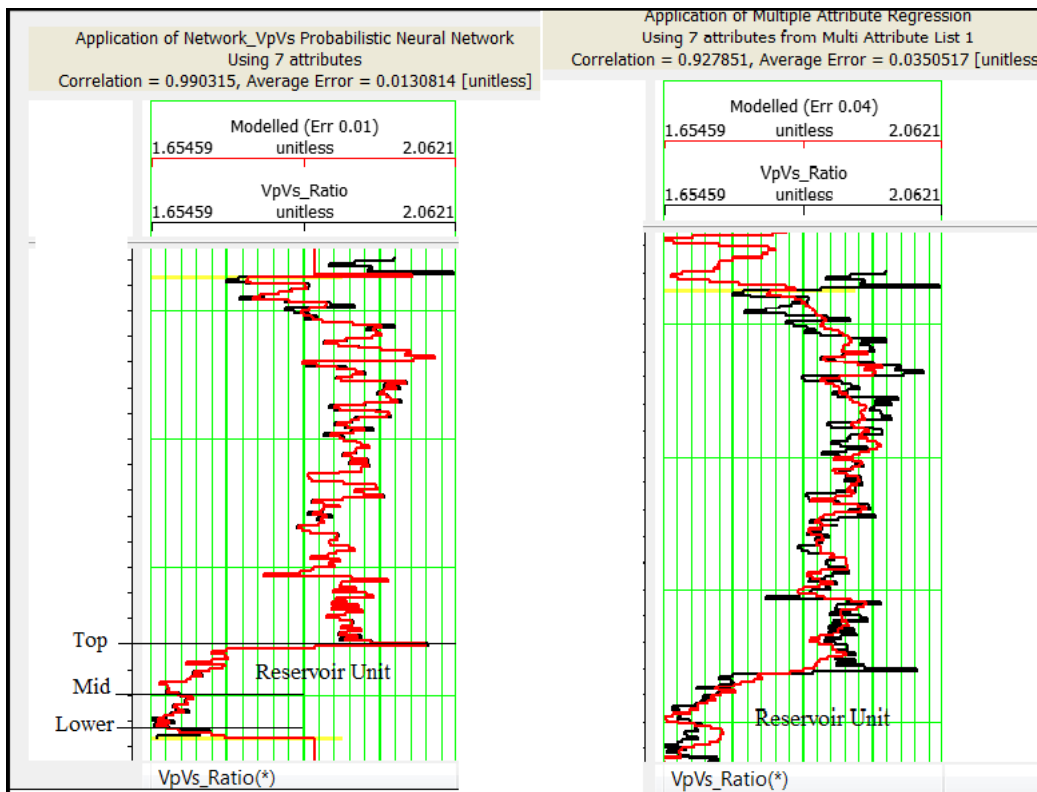


Fig. 16. Representing the comparison of predicted VpVs using probabilistic neural network (left) and multiple attribute regression using 7 attributes (right)

In the seismic section X, VpVs (Figure. 17) accurately predicted the top source rock formation at 1000ms near the well location, which continues in the opposite direction. Furthermore, the contact between Silurian Source rock and upper Ordovician reservoirs was precisely picked at 1100 ms near the well location. Unlike Acoustic impedance attributes, VpVs ratio picked the sand body as one set for this seismic section (Figure.17).

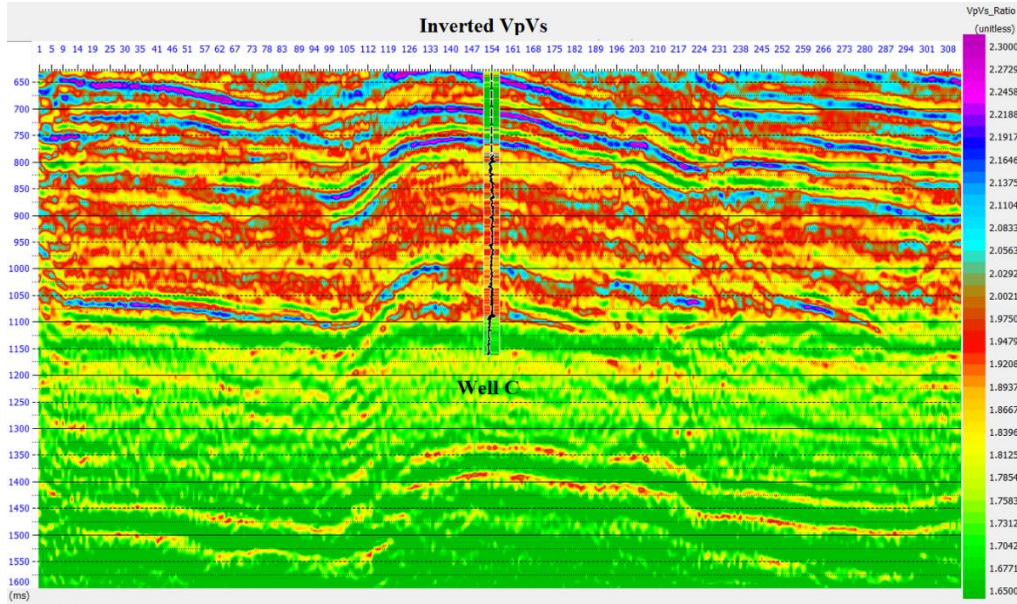


Fig. 17. Representing inverted Vp and Vs ratio at seismic line X, with precise delineation of the top reservoir at 1100 ms

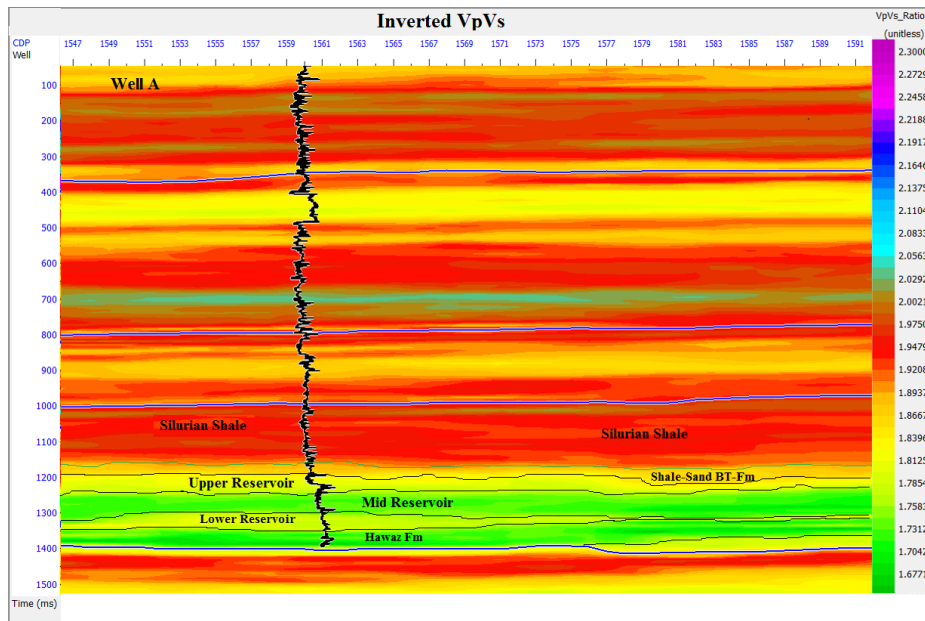


Fig. 18. Representing inverted Vp and Vs ratio from seismic line Y, showing the three main reservoir zones vertical and lateral distribution

For the seismic Line Y (Figure. 5), VpVs was generated using a workflow explained in the section 3.3.1. The VpVs attribute showed the reservoir area falls within the low percentage ratios between 1.6 and 1.8, which is the expected range for sand bodies with emphasis to their upper, mid and lower contacts (Figure. 18). Also showed how the interpreted horizons

using conventional seismic data did not manage to pick even some of the 'marker events' such as Horizons in Figure 18. Therefore, reinterpretation results can be reproduced by using the above-illustrated workflow, which indeed uncovers more facts on the lateral and vertical distribution of the primary producing reservoir by only utilising the existent database for this region.

5. Conclusion

This paper showed the effectiveness of combining petro-elastic correlation on enhancing the delineation of the upper Ordovician reservoir. The combination allowed the allocation of contacts between gradually interbedded clastic sediments. Also, the incorporation of simple elastic seismic attributes into prospect evaluation yielded a better delineation of the upper Ordovician main reservoir. By separating the sandy-shale of Bir Tlacsin formation from the upper reservoir unit in both seismic and wells, will undoubtedly improve the structural mapping of reservoir units by avoiding the assumption of using lower hot-shale contact as a top reservoir. It also provided vital details regarding the lithological variations and quality of the play fairways system in the South-South/West Murzuq Basin. Therefore, applying this simple, fast approach will help unearth specific features of petroleum systems by only reinterpreting the existing data set, which will hopefully trigger the exploration spotlight to this area again.

Acknowledgments

We would like to send our special gratitude to NOC for their cooperation and giving the permission to publish this paper. Our thanks also goes to Dr Adnan Aqrawi for his constructive comments and advice.

References

- [1] Craig J, Rizzi C, Said F, Thusu B, Luning S, Asbali A, Keeley M, Bell J, Durham M, Eales M. Structural styles and prospectivity in the Precambrian and Palaeozoic hydrocarbon systems of North Africa. *The Geology of East Libya*, 2008; 4: 51-122.
- [2] Craig J, Grigo D, Rebora A, Serafini G, Tebaldi E. From Neoproterozoic to Early Cenozoic: exploring the potential of older and deeper hydrocarbon plays across North Africa and the Middle East. *Geological Society, London, Petroleum Geology Conference series 2010*. Geological Society of London, pp. 673-705.
- [3] Davidson L, Beswetherick S, Craig J, Eales M, Fisher A, Himmali A, Jho J, Mejrab B, Smart J. The structure, stratigraphy and petroleum geology of the Murzuq Basin. *Southwest Libya-Chapter 2009:14*.
- [4] Davidson L, Beswetherick S, Craig J, Eales M, Fisher A, Himmali A, Jho J, Mejrab B, Smart J. The structure, stratigraphy and petroleum geology of the Murzuq Basin, Southwest Libya. *Geological Exploration of the Murzuq Basin*. Elsevier, Amsterdam 2000: 295-320.
- [5] El Diasty WS, El Beialy S, Anwari T, Batten D, 2017. Hydrocarbon source potential of the Tanezzuft Formation, Murzuq Basin, south-west Libya: An organic geochemical approach. *Journal of African Earth Sciences*, 2017; 130: 102-109.
- [6] Galushkin Y, Eloghi S, Sak M. 2014. Burial and thermal history modelling of the Murzuq and Ghadames Basins (Libya) using the GALO computer programme. *Journal of Petroleum Geology*, 2014; 37: 71-93.
- [7] Hallett D, Clark-Lowes D. *Petroleum geology of Libya*. Elsevier 2017.
- [8] Ron Martin MR, Erquiaga M, Blake B, Buitrago J, Reveron J, Obregon F, Cobos C, González Muñoz JM. Seismic Expression of Intra-Ordovician Unconformities in Murzuq Basin (Libya) through Pre-stack Inversion & Modelling, 2016.
- [9] Abushalah Y, Serpa L. Using instantaneous frequency and coloured inversion attributes to distinguish and determine the sandstones facies of the Late Ordovician Mamuniyat reservoir, R-field in Murzuq Basin. *Libya. Interpretation* 4, T507-T519, 2016.
- [10] El-Ghali MAK. Depositional environments and sequence stratigraphy of paralic glacial, paraglacial and postglacial Upper Ordovician siliciclastic deposits in the Murzuq Basin, SW Libya. *Sedimentary Geology*, 2005; 177: 145-173.

- [11] Abouessa A., Diagenetic properties of the Hawaz Formation, Murzuq Basin, Libya, Fourth Symposium on the Sedimentary Basins of Libya. The Geology of Southern Libya, 2012: 47-82.
- [12] Aziz A. 2000. Stratigraphy and hydrocarbon potential of the Lower Palaeozoic succession of License NC-115, Murzuq Basin, SW Libya-Chapter 16.
- [13] Le Heron D, Meinholt G, Elgadry M, Abutarruma Y, Boote D. Early Palaeozoic evolution of Libya: perspectives from Jabal Eghei with implications for hydrocarbon exploration in Al Kufrah Basin. *Basin Research*, 2015; 27: 60-83.
- [14] Denis M, Guiraud M, Konaté M, Buoncristiani J-F. Subglacial deformation and water-pressure cycles as a key for understanding ice stream dynamics: evidence from the Late Ordovician succession of the Djado Basin (Niger). *International Journal of Earth Sciences*, 2010; 99: 1399-1425.
- [15] Dupouy M, Desaubliaux G, Nosjean N, Lloyd A, Cherif R. Integrated sedimentological case study of glacial Ordovician reservoirs in the Illizi Basin, Algeria, 79th EAGE Conference and Exhibition 2017-Workshops.
- [16] Girard F, Ghienne J.-F, Rubino J-L, Channelized sandstone bodies ('cordons') in the Tassili N'Ajjer (Algeria & Libya): snapshots of a Late Ordovician proglacial outwash plain. *Geological Society, London, Special Publications*, 2012; 368: 355-379.
- [17] Moreau J, Joubert J-B. Glacial sedimentology interpretation from borehole image log: Example from the Late Ordovician deposits, Murzuq Basin (Libya). *Interpretation*, 2016; 4: B1-B16.
- [18] Le Heron D, Armstrong H, Wilson C, Howard J, Gindre L. Glaciation and deglaciation of the Libyan Desert: the Late Ordovician record. *Sedimentary Geology*, 2010; 223: 100-125.
- [19] Shalbak FA. Palaeozoic petroleum systems of the Murzuq Basin. Libya 2015.
- [21] Das B, Chatterjee R, Singha DK, Kumar R. 2017. Post-stack seismic inversion and attribute analysis in shallow offshore of Krishna-Godavari basin, India. *Journal of the Geological Society of India*, 2017; 90: 32-40.
- [22] Kumar R, Das B, Chatterjee R, Sain K. 2016. A methodology of porosity estimation from inversion of post-stack seismic data. *Journal of natural Gas science and engineering*, 2016; 28: 356-364.
- [23] Lee K, Yoo D, McMechan GA, Hwang N, and Lee GH. A Two-Dimensional Post-Stack Seismic Inversion for Acoustic Impedance of Gas and Hydrate Bearing Deep-Water Sediments Within the Continental Slope of the Ulleung Basin, East Sea, Korea. *Terrestrial, Atmospheric & Oceanic Sciences*, 2013; 24(3): 295-310.
- [24] McDougall ND, Tawengi K, JG Quin, and Vila Pont J. Depositional environments and largescale sediment architecture in the Upper Ordovician of the Murzuq Basin, SW Libya (Melaz Shuqrani and Mamuniyat Formations, EAGE, 2nd North African/Mediterranean Petroleum and Geoscience Conference 2005, Abstract volume, 8.

To whom correspondence should be addressed: Abubaker Alansari, Department of Geosciences, University Technology PETRONAS, 32610, Perak, Malaysia

PREDICTING THE YIELD OF COKE AND ITS BYPRODUCTS ON THE BASIS OF ULTIMATE AND PETROGRAPHIC ANALYSIS

D. V. Miroshnichenko^{1*}, L. Saienko², D. Demidov³, S. V. Pyshyev

¹ National Technical University «Kharkiv Polytechnic Institute», 61002, Kharkiv, 2 Kirpichova Str., Ukraine

² Kharkiv National University of Civil Engineering and Architecture, 61002, Kharkiv, 40 Sumska Str., Ukraine

³ Kharkiv State auto-transport College, 61003, Kharkiv, 28 Constitution Square, Ukraine

⁴ Department of Chemical Technology of oil and Gas Processing, Institute of Chemistry and Chemical Technology, Lviv Polytechnic National University, St. Bandery 12, Lviv, Ukraine

Received January 24, 2018; Accepted April 23, 2018

Abstract

It is established that the yield of coke and its primary byproducts may be predicted on the basis of ultimate and petrographic analysis of the coal (blend) employed. The contribution of individual groups of petrographic components in the coal to the yield of coke and its primary byproducts is determined; coal from the Ukraine, Russia, and the United States is considered. The method developed for predicting the yield of coke and its primary byproducts on the basis of petrographic data is tested at Alchevskoks and Makeevkoks.

Keywords: coal; ultimate analysis; petrographic analysis; coke yield; byproduct yield.

1. Introduction

Analysis of the literature on predicting the yield of coke and its primary byproducts permits the following conclusions [1].

- 1) Due to the increased content of petrographically inhomogeneous coal in current coking blend, predicting the yield of coke and its primary byproducts solely on the basis of the volatile matter is no longer satisfactory.
- 2) The yield of coke and its primary byproducts may most expediently be predicted on the basis of ultimate and petrographic analysis of the coal (blend) employed.

2. Experimental

In the present work, we consider three samples including coal from Ukraine, Russia, and the United States, which constitutes the bulk of the blend at Ukrainian coke plants [2]. Note that un-oxidized coal is considered, so as to eliminate the influence of oxidation on the yield of coke and its primary byproducts [3-9].

Table 1 presents the maximum, minimum, and mean values of the characteristics for the chosen coal. The mean ash content is greatest for Russian coal ($A^d_{me} = 8.9\%$) and least for Ukrainian coal ($A^d_{me} = 7.4\%$), with a value of 8.5% for coal from the United States. Note that the maximum (41.6-42.7%), minimum (16.8-19.3%), and mean (29.8-32.0%) volatile matter is similar for all coals. That indicates similar ranges of this yield in all three groups of coal.

The plastic-layer thickness y fluctuates broadly for the coal from each country. Table 2 presents the maximum, minimum, and mean values for the content of individual elements and the corresponding structural characteristics [10-18]. We see that the mean content of carbon, hydrogen, and oxygen is similar for the coal samples from Ukraine, Russia, and the United States.

As expected, the maximum total sulfur content ($S^{d,t,me} = 1.5\%$) and minimum nitrogen content ($N^{daf,me} = 1.6\%$) are found for coal from Ukraine, and the minimum total sulfur content ($S^{d,t,me} = 0.6\%$) and maximum nitrogen content ($N^{daf,me} = 2.2\%$) for coal from Russia, while the values for coal from the United States are intermediate ($S^{d,t,me} = 1.0\%$; $N^{daf,me} = 1.7\%$).

Table 1. Properties of coal samples from Ukraine, Russia, and the United States

Coal source (number of samples)	Value	Proximate analysis, %			Thickness of the plastic lager, mm
		A ^d	S ^{d,t}	V ^{daf}	y
Ukraine (40)	Max	13.0	2.99	42.7	29
	Min	2.1	0.48	16.8	6
	Mean	7.4	1.49	32.0	15
Russia (23)	Max	13.3	1.93	41.6	25
	Min	3.9	0.27	19.3	0
	Mean	8.9	0.61	29.8	12
United States (18)	Max	10.0	3.23	42.4	31
	Min	6.8	0.43	17.7	10
	Mean	8.5	0.99	31.6	18
All the coal (81)	Max	13.3	3.23	42.7	31
	Min	2.1	0.27	16.8	0
	Mean	8.1	1.10	31.3	15

Table 2. Ultimate composition and structural parameters of coal samples from Ukraine, Russia, and the United States

Coal source (number of samples)	Value	Ultimate composition, %					Structural parameters	
		C ^{daf}	H ^{daf}	N ^{daf}	S ^{d,t}	O ^{daf,d}	f _a	cA
Ukraine (40)	Max	90.3	6.3	2.2	3.0	9.3	0.75	0.81
	Min	81.9	4.1	0.2	0.5	1.3	0.63	0.72
	Mean	86.1	5.6	1.6	1.5	5.2	0.69	0.77
Russia (23)	Max	91,0	6,2	2,8	1,9	9,3	0,75	0,82
	Min	81,7	4,8	1,0	0,3	1,3	0,63	0,72
	Mean	87,3	5,6	2,2	0,6	4,3	0,69	0,78
United States (18)	Max	89,5	6,3	2,3	3,2	5,9	0,74	0,81
	Min	84,2	4,9	1,4	0,4	2,8	0,65	0,74
	Mean	87,0	5,8	1,7	1,0	4,5	0,68	0,77
All the coal (81)	Max	91,0	6,3	2,8	3,2	9,3	0,75	0,81
	Min	81,7	4,1	0,2	0,3	1,3	0,63	0,72
	Mean	86,6	5,7	1,8	1,1	4,8	0,69	0,77

Table 3 presents the maximum, minimum, and mean values of the petrographic characteristics. The coal samples correspond to all metamorphic stages: from $R_o = 0.58\%$ to $R_o = 1.77\%$.

Coal from Ukraine (Table 3) is mainly petrographically uniform ($Vt_{me} = 84\%$), while coal from Russia and the United States is petrographically non-uniform ($Vt_{me} = 68-69\%$). The mean total content of fusinized components is 12%, 30%, and 27% for coal from Ukraine, Russia, and the United States, respectively. The mean liptinite content is low for all the groups ($L_{me} = 1-4\%$), with the exception of some samples from Ukraine ($L_{me} = 18\%$) and the United States ($L_{me} = 11\%$). These characteristics should be reflected in the yield of coke and its primary byproducts from the coal samples.

The yield of coke and its primary byproducts is determined by means of 20-g laboratory apparatus (designed in accordance with the relevant Ukrainian DSTU State Standard [6]). Table 4 presents the experimental values of the yield of coke and its primary byproducts in the dry ash-free state (*daf*). The coke yield in the dry ash-free state (%) is calculated from the formula

$$B_{co}^{daf} = \frac{B_{co}^d - A^d}{100 - A^d} * 100 \quad (1)$$

where B_{co}^{daf} is the byproduct yield in the dry state, %; A^d is the ash content of the coal (blend), %. The yield of the byproduct in the dry ash-free state (%) is calculated from the formula

$$B_{bp}^d = \frac{B_{bp}^d * 100}{100 - A^d} \quad (2)$$

where B_{bp}^d is the byproduct yield in the dry state, %; A^d is the ash content of the coal (blend), %.

3. Results and discussion

According to Table 4, the mean yield of the products is different for the different samples. Thus, for coal from Ukraine, the yield is greatest for hydrogen sulfide and pyrogenetic water; for coal from Russia, the yield is greatest for coke, ammonia, and carbon dioxide; and for coal from the United States, the yield is greatest for tar, raw benzene, nonsaturated hydrocarbons, and gas.

Table 5 shows the pair correlation coefficients for the product yields and the ultimate composition (and also the corresponding structural parameters). For coal from Ukraine, the yield of coke, tar, and raw benzene is determined, to a degree of 71.4–72.7%, by the carbon content (pair correlation coefficients 0.845–0.850); for pyrogenetic water, the correlation is only 65% ($r = 0.806$). The correlation between the product yields and the hydrogen content is weaker: 66.3–70.6%. The correlation of the product yields with the oxygen content is markedly less than for the carbon and hydrogen contents: 37.6–69.89%.

For coal from Russia and the United States, the pair correlation coefficients of the product yields the ultimate composition are higher than for Ukrainian coal; the with determination coefficient is as much as 87.0%.

Note that the structural parameters calculated from the ultimate composition are more closely correlated with the product yields than are the concentrations of individual elements. The yield of coke and its primary byproducts may be most precisely predicted on the basis of the degree cA of molecular association of the coal. For all the groups of coal, the pair correlation coefficients of cA are as follow: with the coke yield, 0.889–0.942; with the tar yield – (0.886–0.947); with the raw-benzene yield – (0.894–0.914); and with the yield of pyrogenetic water – (0.833–0.894).

The structural parameters here considered are relatively closely correlated with one another, according to [19]. Any of them may provide a quantitative estimate of the metamorphic stage, aromatic content, and molecular association of the organic mass for a particular coal sample. Hence, to predict the yield of coke and its primary byproducts, we may use a single structural parameter; we might select cA on account of its particularly close correlation with the yield of coke and its primary byproducts.

Table 6 presents formulas for predicting the yield of coke and its primary byproducts on the basis of cA , for the groups of coal from Ukraine, Russia, and the United States and for all the samples.

We see that the yield of coke and its primary byproducts may be predicted with sufficient accuracy on the basis of cA . The formulas for all the coal samples describe the yields as a function of cA with a multiple-correlation coefficient $r = 0.855–0.905$ and determination coefficient $D = 73.1–82.0\%$. The standard error SE of the yield calculations is consistent with the requirements of the relevant Ukrainian State Standard.

Table 3. Petrographic characteristics of coal samples from Ukraine, Russia, and the United States

Coal source (number of samples)	Value	Mean vitrinite reflectance R_{0v} , %	Petrographic composition (disregarding mineral impurities), %						Stages of vitrinite metamorphism, %				
			Vt	Sv	I	L	ΣFC	<0.50	0.50– 0.64	0.65– 0.89	0.90– 1.19	1.20– 1.39	1.40– 1.69
Ukraine (4)	Max	1.77	96	1	32	18	32	7	90	98	86	96	58
	Min	0.59	53	0	4	0	4	0	0	0	0	0	0
	Mean	1.03	84	0	12	4	12	1	12	31	29	14	2
Russia (23)	Max	1.60	99	4	83	7	83	11	81	94	91	94	18
	Min	0.58	16	0	0	0	0	0	0	0	0	0	0
	Mean	1.01	68	1	30	1	30	1	11	23	41	17	1
United States (18)	Max	1.56	82	3	40	11	40	1	17	92	95	71	4
	Min	0.74	54	0	13	0	0	0	0	0	0	0	0
	Mean	1.03	69	1	27	4	27	0	1	26	53	11	8
All the coal (81)	Max	1.77	99	4	83	18	83	11	90	98	99	94	58
	Min	0.58	16	0	0	0	0	0	0	0	0	0	0
	Mean	1.02	76	1	21	3	21	1	9	28	38	14	1

Table 4. Yield of coke and its primary byproducts from Ukraine, Russia, and the United States

Coal source (number of samples)	Value	Yield of coke and its primary byproducts (daf), %								
		coke	tar	raw benzene	C_mH_n	NH_3	H_2S	CO_2	H_2O_{pyr}	gas
Ukraine (40)	Max	84.78	7.81	1.83	0.95	0.39	0.92	2.27	5.90	18.09
	Min	63.79	1.62	0.47	0.33	0.20	0.10	0.19	2.82	8.91
	Mean	72.34	5.43	1.36	0.63	0.29	0.46	0.88	4.33	14.30
Russia (23)	Max	81.32	7.80	1.97	1.04	0.73	0.34	3.39	5.71	17.14
	Min	63.48	1.76	0.44	0.12	0.15	0.03	0.59	1.30	11.48
	Mean	73.92	4.48	1.17	0.68	0.51	0.13	1.53	3.83	13.76
United States (18)	Max	83.55	8.23	2.20	1.32	0.46	0.57	1.58	5.17	16.61
	Min	65.06	2.43	0.43	0.40	0.13	0.03	0.27	1.55	11.07
	Mean	72.38	5.63	1.43	0.77	0.32	0.25	0.95	3.97	14.31
All the coal (81)	Max	84.78	8.23	2.20	1.32	0.73	0.92	3.39	5.90	18.09
	Min	63.48	1.62	0.43	0.12	0.13	0.03	0.19	1.30	5.54
	Mean	72.80	5.14	1.31	0.70	0.37	0.28	1.12	4.04	14.1

Petroleum and Coal

Table 5. Pair correlation coefficients

Characteristic	B^{daf}_{co}	B^{daf}_{tar}	B^{daf}_b	B^{daf}_{pyr}
Ukraine				
C^{daf}	0.848	-0.850	-0.845	-0.806
H^{daf}	-0.824	0.814	0.840	0.753
O^{daf}	-0.726	0.728	0.720	0.679
f_a	0.878	-0.872	-0.885	-0.813
cA	0.889	-0.886	-0.894	-0.833
Russia				
C^{daf}	0.901	-0.876	-0.892	-0.885
H^{daf}	-0.843	0.903	0.790	0.808
O^{daf}	-0.836	0.804	0.832	0.811
f_a	0.909	-0.930	-0.874	-0.877
cA	0.922	-0.929	-0.894	-0.894
United States				
C^{daf}	0.935	-0.940	-0.908	-0.811
H^{daf}	-0.883	0.889	0.860	0.823
O^{daf}	-0.910	0.902	0.893	0.793
f_a	0.928	-0.933	-0.905	-0.842
cA	0.942	-0.947	-0.914	-0.843
All the coal				
C^{daf}	0.861	-0.853	-0.833	-0.843
H^{daf}	-0.831	0.850	0.823	0.750
O^{daf}	-0.749	0.734	0.795	0.715
f_a	0.895	-0.899	-0.873	-0.830
cA	0.905	0.906	-0.882	-0.855

Table 6. Formulas for predicting the yield of coke and its primary byproducts on the basis of the structural parameter cA

Source of coal	Formula	Statistical estimates		
		r	$D, \%$	$SE, \%$
Ukraine	$B^{daf}_{co} = 216.83cA - 93.489$	0.889	79.1	0.472
	$B^{daf}_{tar} = -64.066cA + 54.427$	0.886	78.4	0.288
	$B^{daf}_b = -12.773cA + 11.124$	0.894	79.9	0.175
	$B^{daf}_{pyr} = -27.226cA + 25.155$	0.833	69.2	0.296
Russia	$B^{daf}_{co} = 192.39cA - 75.262$	0.922	85.0	0.499
	$B^{daf}_{tar} = -63.730cA + 53.903$	0.929	86.3	0.294
	$B^{daf}_b = -14.690cA + 12.559$	0.894	79.9	0.149
	$B^{daf}_{pyr} = -36.900cA + 32.442$	0.894	79.9	0.276
United States	$B^{daf}_{co} = 206.26cA - 86.072$	0.942	88.5	0.469
	$B^{daf}_{tar} = -65.460cA + 55.915$	0.947	89.7	0.274
	$B^{daf}_b = -20.167cA + 16.923$	0.914	83.6	0.134
	$B^{daf}_{pyr} = -31.326cA + 28.034$	0.843	71.0	0.289
All the coal	$B^{daf}_{co} = 204.67cA - 84.501$	0.904	81.8	0.483
	$B^{daf}_{tar} = -65.017cA + 55.176$	0.905	82.0	0.281
	$B^{daf}_b = -14.652cA + 12.581$	0.882	77.8	0.145
	$B^{daf}_{pyr} = -31.808cA + 28.556$	0.855	73.1	0.281

Since the prediction of the yield of coke and its primary byproducts is systematic, while the ultimate composition is not determined in plant laboratories, as a rule, it is expedient to predict the yield of coke and its primary byproducts on the basis of petrographic data, which are routinely gathered in quality control of the coal arriving at the plant [1, 20, 21].

On the basis of experience with petrographic analysis of coal and coking blend, we may establish limits on the vitrinite reflectance corresponding to the ranks of coal generally employed in coking, regardless of the source of the coal. In the analysis of reflectograms, we recommend the table of correspondences proposed in [22].

Note that the composition and structure of inertinite also change with metamorphism of the coal. However, in view of the insignificant changes in its properties on thermal destruction and the instrumental difficulties in determining the stage of development, we only consider the total inertinite content in the coal.

We divide the organic mass into eight groups when determining the contribution of the petrographic components to the yield of coke and its primary byproducts:

- six vitrinite components corresponding to the ranks $R_o \leq 0.64\%$, $R_o = 0.65-0.89\%$, $R_o = 0.90-1.19\%$, $R_o = 1.20-1.39\%$, $R_o = 1.40-1.69\%$, and $R_o = 1.70-2.20\%$;
- a fusinized component combining inertinite and semivitrinite;
- a liptinite component.

The liptinite corresponding to rank $R=1.20-1.39\%$ is combined with the vitrinite of the same rank, on account of its low content and similar properties [23].

Table 7 presents this division into groups, with the corresponding cA values, calculated by the solution of the following system of linear equations (m equations with n unknowns) on the basis of the Gauss method [24-26]

$$\left\{ \begin{array}{l} \mathbf{a}_{11}\mathbf{x}_1 + \mathbf{a}_{12}\mathbf{x}_2 + \dots + \mathbf{a}_{1n}\mathbf{x}_n = \mathbf{b}_1, \\ \mathbf{a}_{21}\mathbf{x}_1 + \mathbf{a}_{22}\mathbf{x}_2 + \dots + \mathbf{a}_{2n}\mathbf{x}_n = \mathbf{b}_2, \\ \dots \\ \mathbf{a}_{m1}\mathbf{x}_1 + \mathbf{a}_{m2}\mathbf{x}_2 + \dots + \mathbf{a}_{mn}\mathbf{x}_n = \mathbf{b}_m. \end{array} \right. \quad (3)$$

Here the coefficients a_{11} , ..., a_{nm} correspond to the content of the specific petrographic groups in the given coal sample, %; b_1 , ..., b_m are the values of the structural parameter cA or the yield of coke and its primary byproducts for the given sample; x_1 , ..., x_n are the values of the structural parameter cA or the yield of coke and its primary byproducts corresponding to the content of the specific petrographic group.

It appears from Table 7 that, as the vitrinite develops metamorphically, the degree of molecular association of the coal's organic mass increases; the value of cA is least for liptinite, which is the least structured maceral.

In Table 8 and in the figure 1, we present conversion coefficients from the organic mass of the petrographic components in coal from Ukraine, Russia, and the United States to the organic mass of coke and its primary byproducts; statistical estimates are also provided. Note that the conversion coefficients from the vitrinite component to coke increase from group I to group VI, while the conversion coefficients to tar, raw benzene, and pyrogenetic water decline.

Analysis of the conversion coefficients for groups VII and VIII confirms that the coke yield is lower from liptinite macerals than from inertinite macerals, while the yield of tar, raw benzene, and gas is higher.

On the basis of the combined data for coal from Ukraine, Russia, and the United States, Table 9 presents universal formulas for predicting the yield of coke and its primary byproducts for blend containing coal from different sources; statistical estimates are also provided.

Overall, conversion of the vitrinite component in coal's organic mass to coke, tar, raw benzene, and pyrogenetic water follows familiar patterns: as the coke's level of metamorphic development increases, the coke yield increases, while the yield of tar, raw benzene, and pyrogenetic water declines [27].

Table 7. Division of the coal's organic mass into groups and corresponding mean *cA* values

Group	Petrographic components in group	Notation and mathematical formula for group	Degree of molecular association <i>cA</i>
I	vitrinite $R_0 \leq 0.64\%$	$V_{tI} = (V_t < 0.64)V_t/100$	0.70
II	vitrinite $R_0 = 0.65-0.89\%$	$V_{tII} = (V_t^{0.65-0.89}V_t)/100$	0.75
III	vitrinite $R_0 = 0.90-1.19\%$	$V_{tIII} = (V_t^{0.90-1.19}V_t)/100$	0.77
IV	vitrinite and liptinite $R_0 = 1.20-1.39\%$	$V_{tIV} = (V_t^{1.20-1.39}V_t + L^{1.20-1.39}L)/100$	0.81
V	vitrinite $R_0 = 1.40-1.69\%$	$V_{tV} = (V_t^{1.40-1.69}V_t)/100$	0.84
VI	vitrinite $R_0 = 1.70-2.20\%$	$V_{tVI} = (V_t^{1.70-2.20}V_t)/100$	0.91
VII	liptinite	$L = (L^{<0.64} + L^{0.65-0.89} + L^{0.90-1.19})L/100$	0.67
VIII	Inertinite and semivitrinite	$I + S_v = I + S_v$	0.78

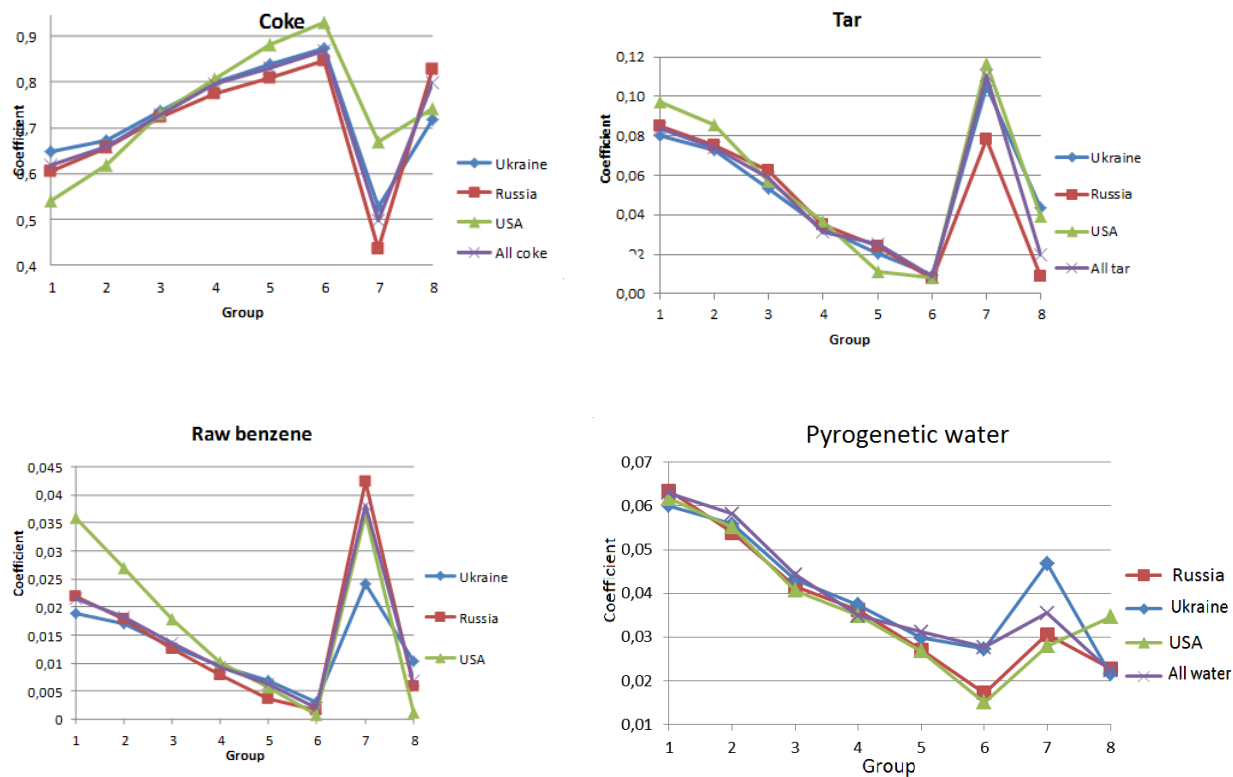


Fig.1. Conversion coefficients from the organic mass of the petrographic components (from Ukraine, Russia and the United States) to the organic mass of coke and its primary byproducts

For the proposed formulas, the correlation coefficients are high (0.970–0.997), as are the determination coefficients (94.0–99.5%). The standard error is 0.41%, 0.28%, 0.09%, and 0.19% in predicting the yield of coke, tar, raw benzene, and pyrogenetic water, respectively. That is within the permissible error according to the relevant Ukrainian State Standard. Hence, the formulas may be regarded as suitable for the prediction of the yield of coke and its primary byproducts on the basis of petrographic analysis.

The proposed prediction method is tested for data from Alchevsk and Makeevsk coke plants. Coke production at Alchevskkoks includes traditional coking of ordinary coal blend (batteries 5–8) with wet slaking of the coke and coking of rammed blend with wet slaking (battery 9) and dry slaking (battery 10) of the coke [28–30]. At Makeevkoks, coking of ordinary coal blend is employed (batteries 1–4), with wet slaking [28, 31–33].

Petroleum and Coal

Table 8. Conversion coefficients from the organic mass of the petrographic components in coals from Ukraine, Russia, and the United States to the organic mass of coke and its primary byproducts

Characteristic	Group								Statistical estimates		
	I	II	III	IV	V	VI	VII	VIII	r	D, %	SE, %
Coal from Ukraine											
B ^{daf} _{co}	0.647 9	0.672 2	0.735 3	0.79793	0.837 9	0.874 1	0.525 7	0.716 5	0.99 8	99. 5	0. 42 8
B ^{daf} _{tar}	0.079 8	0.072 9	0.053 5	0.0333	0.020 4	0.009 4	0.104 8	0.043 6	0.99 6	99. 1	0. 17 0
B ^{daf} _b	0.018 8	0.017 0	0.013 0	0.0095	0.006 8	0.003 0	0.024 2	0.010 3	0.97 6	95. 2	0. 08 0
B ^{daf} _{pyr}	0.060 0	0.055 8	0.432	0.0373	0.029 8	0.027 3	0.046 8	0.021 5	0.97 2	94. 5	0. 18 9
Coal from Russia											
B ^{daf} _{co}	0.605 5	0.655 1	0.724 0	0.7736	0.808 7	0.846 7	0.435 7	0.827 5	0.99 9	99. 8	0. 23 7
B ^{daf} _{tar}	0.085 1	0.075 0	0.062 6	0.0352	0.023 9	0.007 3	0.078 0	0.008 9	0.99 6	99. 2	0. 17 5
B ^{daf} _b	0.021 9	0.017 9	0.012 5	0.0079	0.003 7	0.001 6	0.042 4	0.005 9	0.98 4	96. 7	0. 08 7
B ^{daf} _{pyr}	0.063 4	0.053 9	0.041 5	0.0362	0.027 1	0.017 2	0.030 6	0.022 8	0.98 7	97. 2	0. 20 0
Coal from United States											
B ^{daf} _{co}	0.539 6	0.618 5	0.730 3	0.8073	0.881 5	0.929 0	0.669 0	0.741 5	0.99 8	99. 7	0. 25 3
B ^{daf} _{tar}	0.097 3	0.085 5	0.056 9	0.0369	0.011 4	0.008 1	0.116 4	0.039 1	0.98 9	97. 7	0. 21 4
B ^{daf} _b	0.035 9	0.027 0	0.017 9	0.0101	0.005 7	0.000 7	0.036 6	0.001 2	0.99 2	98. 4	0. 05 8
B ^{daf} _{pyr}	0.061 7	0.055 1	0.040 7	0.0349	0.026 8	0.015 1	0.028 0	0.034 6	0.96 5	93. 1	0. 19 6

Table 9. Formulas for predicting the yield of coke and its primary byproducts on the basis of the petrographic composition of the coals

Formula	Statistical estimates		
	r	D, %	SE, %
B ^{daf} _{co} = 0.6184 Vt _I + 0.658 Vt _{II} + 0.7286 Vt _{III} + 0.7954 Vt _{IV} + 0.8298 Vt _V + 0.8690 Vt _{VI} + 0.4978 L + 0.7984 (I + S _v)	0.997	99.5	0.41
B ^{daf} _{tar} = 0.0838 Vt _I + 0.0742 Vt _{II} + 0.0586 Vt _{III} + 0.0316 Vt _{IV} + 0.0254 Vt _V + 0.0085 Vt _{VI} + 0.1105 L + 0.0198 (I + S _v)	0.987	97.4	0.28
B ^{daf} _b = 0.0215 Vt _I + 0.0183 Vt _{II} + 0.0136 Vt _{III} + 0.0093 Vt _{IV} + 0.006 Vt _V + 0.0019 Vt _{VI} + 0.0382 L + 0.0068 (I + S _v)	0.970	94.0	0.09
B ^{daf} _{pyr} = 0.0630 Vt _I + 0.0582 Vt _{II} + 0.0443 Vt _{III} + 0.0349 Vt _{IV} + 0.0312 Vt _V + 0.0277 Vt _{VI} + 0.0355 L + 0.0223 (I + S _v)	0.973	94.7	0.19

Mean monthly data regarding the proximate analysis of production blend and the yield of coke and its primary byproducts are analyzed. The petrographic characteristics of the mean monthly blend are calculated from its ultimate composition and rank composition, with the utilization of data from coke plants on the petrographic characteristics of coal from individual suppliers employed by the plants.

Table 10 presents the maximum, minimum, and mean values for the technological characteristics of the coal blend supplied to the coke batteries during the test period. We see that, as a result of features of the ramming technology [34-35], the rammed blend sent to batteries 9 and 10 has higher mean working moisture content ($W_{t,me} = 11.3\text{--}11.5\%$) than the ordinary blend sent to batteries 5-8 at Alchevskoks (10.0%) and batteries 1-4 at Makeevkoks (8.7%).

Table 10. Proximate analysis of the coal blends

Battery	Value	Proximate analysis, %			
		$W_{t,t}$	A ^d	S ^{d,t}	V ^d
Alchevskoks					
5-8	Max	11.1	8.8	1.87	30.0
	Min	8.7	8.1	1.01	24.9
	Mean	10.0	8.6	1.49	27.4
9	Max	12.3	8.9	1.54	31.7
	Min	10.9	7.7	0.92	25.8
	Mean	11.5	8.4	1.30	28.8
10	Max	11.5	8.9	1.46	31.7
	Min	10.9	7.7	0.92	26.3
	Mean	11.3	8.4	1.27	28.3
Makeevskoks					
1-4	Max	10.6	8.5	0.91	27.4
	Min	7.4	7.8	0.70	24.7
	Mean	8.7	7.9	0.78	25.4

The ash content and total sulfur content are lower in the rammed blend at Alchevskoks: 8.4 and 1.27-1.30%, as against 8.6 and 1.49%, respectively, for the ordinary blend. On account of the elevated content of high volatile coal in the rammed blend, the volatile matter (in the dry ash-free state) is higher: 30.7-30.9%, on average, as against 29.6% and 27.6% for the ordinary blend (Table 10).

Table 11 presents the petrographic characteristics of the coal blend used in statistical analysis. The blend in batteries 5-8 is characterized by a mean vitrinite reflectance of 1.05%. The blend contains 79% vitrinite-group macerals and 19% fisinised components.

The coal blend at batteries 9 and 10 is characterized by low vitrinite reflectance (0.97%). Ramming permits the use of a high proportion of petrographically inhomogeneous coal in the blend, as is evident from the content of fisinised components ($\Sigma FC_{me} = 25\%$). The elevated content of vitrinite corresponding high volatile coals (51%) should lead to decrease in coke yield and increase in the yield of its primary byproducts in comparison with the blend at batteries 5-8.

The mean vitrinite reflectance of the blend at Makeevkoks is 1.11%. The blend contains 85% vitrinite-group macerals and 13% lean components.

Table 12 presents the production information regarding the yield of coke and its primary byproducts that is subjected to statistical analysis. The yield data are presented for the dry (*d*) and dry ash-free (*daf*) states.

Conversion of data from the dry state to the ash-free state eliminates the influence of the ash content in the blend on the yield of coke and its primary byproducts and hence the chemical potential of solely the coal's organic component may be assessed, as shown in [6].

Petroleum and Coal

Table 11. Petrographic characteristics of coal blends

Battery	Value	Mean vitrinite reflectance R_{0r} , %	Petrographic composition, %						Stages of vitrinite metamorphism, %					
			V_t	S_v	I	L	ΣFC	<0.50	0.50-0.64	0.65-0.89	0.90-0.89	1.20-1.19	1.40-1.39	1.70-2.59
<i>Alchevskkoks</i>														
5-8	Max	1.17	86	2	23	3	24	1	7	40	57	39	25	2
	Min	0.96	73	0	11	1	12	0	2	19	17	6	1	0
	Mean	1.05	79	1	18	2	19	0	4	28	41	17	9	1
9	Max	1.13	82	1	31	6	32	2	14	53	46	10	28	6
	Min	0.89	65	0	15	2	15	0	4	31	24	2	0	0
	Mean	0.97	71	1	25	3	25	1	9	41	35	7	6	2
10	Max	1.13	82	1	31	6	32	2	14	53	46	10	28	6
	Min	0.89	65	0	15	2	15	0	4	31	24	2	0	0
	Mean	0.97	71	1	25	3	25	1	9	41	35	7	6	2
<i>Makeevskkoks</i>														
1-4	Max	1.18	89	1	17	2	18	2	16	6	91	34	3	0
	Min	0.97	80	0	9	1	10	0	0	0	60	7	0	0
	Mean	1.11	85	0	13	2	13	0	3	3	75	19	0	0

Table 12. Yield of coke and its primary byproducts for coal samples

Battery	Value	B_{co}^d	Yield of coke and its primary byproducts, %			B_{tar}^d	B_{tar}^{daf}	B_b^d	B_b^{daf}
			B_{co}^{daf}	B_{tar}^{daf}	B_{tar}^d				
<i>Alchevskkoks</i>									
5-8	Max	78.49	76.59	4.48	4.89	4.89	1.30	1.42	
	Min	76.05	73.83	9.92	3.20	3.20	0.98	1.07	
	Mean	77.24	75.11	3.61	3.95	3.95	1.13	1.23	
9	Max	76.06	73.78	4.75	5.18	5.18	1.39	1.52	
	Min	72.71	70.21	3.09	3.39	3.39	1.04	1.13	
	Mean	74.22	71.87	3.82	4.17	4.17	1.19	1.30	
10	Max	74.66	72.25	4.75	5.18	5.18	1.39	1.52	
	Min	71.62	68.99	3.09	3.39	3.39	1.04	1.13	
	Mean	72.71	70.23	3.82	4.17	4.17	1.19	1.30	
<i>Makeevskkoks</i>									
1-4	Max	80.39	78.72	3.79	4.13	4.13	1.28	1.39	
	Min	75.98	73.83	3.11	3.38	3.38	1.04	1.13	
	Mean	77.68	75.75	3.41	3.70	3.70	1.15	1.25	

Petroleum and Coal

The mean coke yield, in both the dry state and the dry ash-free state, is higher for ordinary blend than for rammed blend. Dry slaking at coke battery 10 reduces the coke yield by 1.42% (in the dry state) and 1.64% (in the dry ash-free state) in comparison with battery 9. Note that, on account of the large volatile matter from the blend in batteries 9 and 10, the yield of tar and raw benzene is also higher than for batteries 5–8 at Alchevskoks and 1–4 at Makeevkoks.

To compare the laboratory and plant yields of coke and its primary byproducts, the petrographic characteristics calculated for the mean monthly production blend at Alchevskoks and Makeevkoks are substituted into the formulas in Table 9.

The calculation results are compared with plant data regarding the yields, and the mean conversion coefficients from laboratory values to production data are calculated. Thus, for conversion from the calculated yields of coke and its primary byproducts to production data, we use the coefficients

$$k_i = B^{pr_i}/B^{ca_i}, \quad (4)$$

where B^{pr_i} is the production value of the yield of coke and its primary byproducts, %; B^{ca_i} is the calculated value of the yield of coke and its primary byproducts, %.

The mean conversion coefficient from the calculated total yield of coke and its primary byproducts to the production value is

$$\bar{k} = \frac{k_1 + \dots + k_i}{i} \quad (5)$$

where i is the number of values used in the calculations.

Table 13 presents the mean error in calculating the yield of coke and its primary byproducts. We see in Table 13 that the yield of coke obtained in laboratory conditions is close to the production value ($k = 0.9763$ – 1.0200). The yield of tar and raw benzene in laboratory conditions is overestimated: $k = 0.7851$ – 0.7914 and 0.9423 – 0.9618 , respectively. That confirms the following opinion [36]: "The laboratory yields cannot agree precisely with the production values since loss of chemical products is inevitable in plant conditions but is minimized in laboratory conditions."

Table 13. Conversion coefficients from laboratory (calculated) values to plant values

Battery	Product	Conversion coefficient	Standard error SE, %
Alchevskoks			
5-8	B^{daf}_{co}	1.0227	0.384
	B^{daf}_{tar}	0.7914	0.134
	B^{daf}_b	0.9618	0.049
9	B^{daf}_{co}	0.9991	0.290
	B^{daf}_{tar}	0.7851	0.111
	B^{daf}_b	0.9423	0.036
10	B^{daf}_{co}	0.9763	0.290
	B^{daf}_{tar}	0.7851	0.111
	B^{daf}_b	0.9423	0.036
Makeevskoks			
1-4	B^{daf}_{co}	1.0230	0.408
	B^{daf}_{tar}	0.7326	0.168
	B^{daf}_b	0.9945	0.041

Analysis of the production yields of coke, tar, and raw benzene and laboratory yields (for a five-section furnace, in accordance with State Standard GOST 18635–73 [37]) from blend of the same quality indicates that the coke yield in laboratory conditions agrees with the production yields at a level of 99%, with figures of 89% and 96% for tar and raw benzene [36].

Thus, the relations between the laboratory and production values obtained in the present work and in [36] are very close [38].

On the basis of the research at Alchevskkoks and Makeevkoks, methods of calculating the yield of coke and its primary byproducts on the basis of petrographic analysis of the blend have been developed, with allowance for the conditions of blend preparation and coke slaking.

4. Conclusions

- (1) We have established theoretically and confirmed experimentally that the yield of coke and its primary byproducts may be predicted on the basis of ultimate and petrographic analysis of the coal (blend) employed.
- (2) We have determined the contribution of individual groups of petrographic components in coal from the Ukraine, Russia, and the United States to the yield of coke and its primary byproducts.
- (3) The method developed for predicting the yield of coke and its primary byproducts on the basis of petrographic data has been tested at Alchevskkoks and Makeevkoks.

Symbols

A^d	ash content of coal in the dry state, %;
V_{daf}	volatile matter in the dry ash-free state, %;
S_t^d	sulphur of coal in the dry state, %;
cA	the degree of molecular association;
f_a	the aromatic content of the structure;
R_0	mean vitrinite reflection coefficient, %;
Vt	vitrinite, %;
Sv	semivitrinite, %;
I	inertinite, %;
L	liptinite, %;
ΣFC	sum of fusinized components, %;
y	thickness of the plastic layer, mm;
r	multicorrelation coefficient;
D	determination coefficient, %;
SE	standard error, %.
$B_{co}^{daf}, B_{tar}^{daf}, B_b^{daf}, B_{pyr}^{daf}$	the yield of coke, tar, raw benzene and pyrogenetic water, %;
$C_{daf}^{daf}, H_{daf}^{daf}, N_{daf}^{daf}, O_{daf}^{daf}$	carbon, hydrogen, nitrogen and oxygen in the dry, ash-free state, %;

References

- [1] Golovko MB, Miroshnichenko DV and Kaftan YuS. Predicting the yield of coke and its primary byproducts. *Coke and Chemistry*, 2011; 54(9): 331–338.
- [2] Gusak VG and Drozdnik ID. Rank structure and technological properties of coal imported to Ukraine. *Uglekhim. Zh.*, 2011; 1-2: 3-11.
- [3] Mukina NV, Zhdan SP, Chernousova EP. Predicting the yield of coking products on the basis of elementary analysis of the initial coal. *Uglekhim. Zh.*, 2011; 3-4: 12–19.
- [4] Miroshnichenko DV. Crushing properties of coal. *Coke and Chemistry* 2013; 56(12): 449–455.
- [5] Miroshnichenko DV, Drozdnik ID, Kaftan YS, Bidolenko NB, Desna NA. Coking of coal batch with different content of oxidized coal. *Coke and Chemistry*. 2012; 55(5): 155–164.
- [6] Golovko MB, Drozdnik ID, Miroshnichenko DV, Kaftan YS. Predicting the yield of coking byproducts on the basis of elementary and petrographic analysis of the coal. *Coke and Chemistry*, 2012; 55(6): 204–214.
- [7] Miroshnichenko DV, Drozdnik ID, Kaftan YuS. Kinetic oxidation characteristics of coal. *Coke and Chemistry*, 2012; 55(3): 87–96.
- [8] Miroshnichenko DV, Drozdnik ID, Kaftan YuS. Laboratory and trial industrial coking of coal batch with different contents of oxidized coal. *Coke and Chemistry*, 2012; 55(5): 155–164.
- [9] Miroshnichenko DV. Influence of oxidation on the packing density of coal. *Coke and Chemistry*. 2014; 57(5): 183–191.
- [10] Gusak VG, Drozdnik ID, Kaftan YuS. Comparison of the composition, structure, and properties of metamorphically equivalent Donets Basin coal and US coal. *Coke and Chemistry*, 2012; 55(4): 119–126.
- [11] Davidzon OR and Drozdnik ID. Structural-chemical and technological characteristics of Donets Basin coal with different degrees of reduction. *Coke and Chemistry*, 2007; 50(3): 50–54.

[12] Davidzon DR, Shchendrik TG, Pashchenko LV, and Simonova VV. Structural features of coal from Krasnoarmeiskaya-Zapadnaya No. 1 mine (Donets Basin) for potential use in coking, *Sb. nauch. st. XI Mezhdunar. nauch.-tekhn. konf. Ekologiya i zdorov'e cheloveka (Proceedings of the Eleventh International Conference on Ecology and Human Health)*, Shchelkino, Crimea, 2003; 1: 104–110.

[13] Shchendrik TG, Simonova VV, Pashchenko LV and Davidzon DR. Structural features of coal samples from Krasnoarmeiskaya-Zapadnaya No. 1 mine with different plastometric characteristics. *Nauch.-tekhn. konf. Protsessy i tekhnologii ispol'zovaniya otkhodov khimicheskogo proizvodstva: tezisy dokl. (Abstracts of the Proceedings of a Conference of Processing Technology for Chemical Wastes)*, Donetsk, 2005.

[14] Gyul'maliev AM, Golovin GS and Gagarin SG. *Klassifikatsiya goryuchikh iskopaemykh po strukturno-khimicheskii pokazatelyam i osnovye puti ispol'zovaniya iskopaemykh uglei (Structural and Chemical Classification of Fossil Fuels and Their Basic Applications)*, Moscow: NTK Trek, 2007.

[15] van Krevelen DW and Shuyer J. *Coal Science*, Amsterdam: Elsevier, 1957.

[16] Gyul'maliev AM, Golovin GS and Gladun TG. *Teoreticheskie osnovy khimii uglya. (Theoretical Principles of Coal Chemistry)*, Moscow: Izd. MGTU, 2003.

[17] Gagarin SG, Lesnokova EB and Shulyakovskaya LV. Assessing the aromatic structure of lignites, *Khim. Tverd. Topl.*, 1993; 1: 3–11.

[18] Veselovskii VS, Khimicheskaya priroda goryuchikh iskopaemykh. (Chemical Nature of Fossil Fuels), Moscow: Izd. Akademii Nauk SSSR, 1955.

[19] Ulanovskii ML. Analysis of the structural parameters of Donets and Lvov-Volynsk coal. *Coke and Chemistry*, 2012; 55(2): 37–42.

[20] Gagarin SG. Regression analysis of the composition and properties of macerals in Kuznets Basin coal with different degrees of reduction. *Koks Khim.*, 1998; 2: 2–6.

[21] Gagarin SG and Ulanov NN. Composition and properties of coal macerals. *Koks Khim.*, 1997; 4: 7–13.

[22] Kaftan YuS, Drozdnik ID, Miroshnichenko DV. Basic principles for the formulation of batch containing coal from different basins. *Uglekhim. Zh.*, 2010; 3-4: 25–31.

[23] Eremin IV, Lebedev VV and Tsikarev DA. *Petrografiya i fizicheskie svoistva uglei. (Petrography and Physical Properties of Coal)*, Moscow: Nedra, 1980.

[24] Il'in VA and Poznyak EG. *Lineinaya algebra: uch. dlya vuzov. (Linear Algebra: A University Textbook)*, Moscow: Fizmatlit, 2004, 6th ed.

[25] Korn G and Korn T. *Mathematical Handbook for Scientists and Engineers*, New York: Dover, 1968.

[26] Kremer NSh, Putko BA, Trishin IM and Fridman MN. *Vysshaya matematika dlya ekonomistov. (Higher Mathematics for Economists)*, Moscow: YuNITI-DANA, 2007, 3rd ed.

[27] Glushchenko IM. *Petrograficheskaya kharakteristika i ee znachenie dlya otsenki svoistv uglei. (Petrographic Characteristics and the Assessment of Coal Properties)*, Moscow: Nedra, 1971.

[28] Analysis of the state of the furnaces and basic shops at Ukrainian coke plants (as of January 1, 2010), Scientific Report NIR-6277, Kharkov: Giprokokos, 2010.

[29] Kovalev ET, Vasil'ev YuS, Kuznichensko VM. Theory and practice of high-quality blast-furnace coke production from rammed batch with limited clinkering properties. *Uglekhim. Zh.*, 2009; 3-4: 24–30.

[30] Danilov AB, Kachtryan RA, Kovalev ET, and Bannikov LP. Reconstruction of the byproduct shop as a priority at OAO Alchevskkoks. *Uglekhim. Zh.*, 2009; 3-4: 64–68.

[31] Kolomiichenko AI. Priorities in the development of Ukrainian coke production: Commemorating the eighti- eth anniversary of Makeevsk coke plant. *Uglekhim. Zh.*, 2012; 5-6: 5–10.

[32] Kolomiichenko AI, Kovalev ET and Starovoit AG. Trends in the development of coke production at ChAO Makeevkoks. *Uglekhim. Zh.*, 2012; 5-6: 11–17.

[33] Goranskii PYu, Bulanyi SM, Cherkasov II. Batch preparation in the production of high-quality coke at ChAO Makeevkoks. *Uglekhim. Zh.*, 2012; 5-6: 20–26.

[34] Chub VE, Dzekunov SN, Mokritskikh AD. Influence of various factors on the loss of rammed coal on charging in the coke furnaces. *Uglekhim. Zh.*, 2002; 3-4: 15–18.

[35] Kuznichenko VM, Karpov AV, Lobov AA. Coke production with rammed coal batch. *Koks Khim.*, 1996; 8: 18–20.

[36] Komelenets MS, Novikov VN, Gorelov PN and Noskova LV. Standardization of the laboratory determination of coke-plant yields. *Koks Khim.*, 1977; 3: 32–34.

- [37] GOST (State Standard) 18635-73: Coal: Method of determining the yield of coking products, 1973.
- [38] Danilov AB, Verdibozhenko GS, Drozdnik ID. Practical use of petrographic data in predicting coke-plant yields. *Coke and Chemistry*, 2012; 55(11): 419-422.

To whom correspondence should be addressed: Dr. D. V. Miroshnichenko, National Technical University «Kharkiv Polytechnic Institute», 61002, Kharkiv, 2 Kirpichova Str., Ukraine, dvmir79@gmail.com

INDUSTRIAL OPERATION ANALYSIS OF Pt-Re REFORMING CATALYST AT THE INDUSTRIAL UNIT BY PREDICTIVE MODELLING METHOD

Emilia D. Ivanchina¹, Ekaterina S. Chernyakova¹, Inna V. Pchelintseva (Yakupova)¹, Gajni Zh. Sejtenova², Rizagul' M. Dyusova²*

¹ Tomsk Polytechnic University, Russia

² S. Toraighyrov Pavlodar State University, Kazakhstan

Received February 5, 2018; Accepted April 27, 2018

Abstract

Analysis of the PR-51 catalyst operation effectiveness of the reforming process was conducted with mathematical modelling method using. The main characteristics of PR-51 reforming catalyst were calculated. It was found that the catalyst has proven to be appropriate in operation and ensure high selectivity. It is shown that the product yield increases by 3-5%mass with octane number 96-97.

Keywords: catalytic reforming; Pt-Re catalyst; kinetic and instrumental methods; mathematical modelling method; product yield.

1. Introduction

The main characteristics of the yield of catalytic naphtha reforming process depend strongly on the catalyst properties. Catalytic reforming catalyst is quite expensive component, so the big practical importance has detailed study of all process with its participation [1-3].

The efficiency of petroleum products production is mostly determined by the level of the process technology, its technological and economic productivity. Increasing the level of reforming efficiency directly leads to the production costs reduction [4]. In the modern production, the solution of this kind of problem becomes possible due to a detailed study of the processes taking place in reactors on the catalyst, and without these the chemical process is not feasible. Investigation, development and introduction of new catalysts in the industry, improvement of production equipment (reactors, heat exchangers, etc.), technological schemes - all these aspects directly influence the resource efficiency of catalytic reforming [1].

Nowadays catalytic naphtha reforming process is one of the most important processes in oil-refining, and it requires in constant control and enhancement, which could be realized by carrying out of continuous monitoring and analysis of catalyst operation. Based on this kind of data it could be argued about resource efficiency of catalysts and oil raw materials on any oil-refinery [5].

Activity, stability and selectivity are the most important indicators of catalyst operation [6-7]. During operation, the catalyst undergoes physicochemical changes, which contribute to decrease in the initial activity [8-10].

Catalyst activity depends on its composition, preparation method, physical conditions of metal and acid function [11-14]. Polymetallic catalysts containing 3 and more metals are the most active ones [15-19].

Activity and selectivity decreasing could be caused by [20-21]:

- coke deposition;
- poisoning due to chemisorption of some impurity (such as heavy metals);
- loss of active substances (chlorine);
- erosion and breakage;

- hydrothermal aging, that is, loss of surface area (metallic area and support area). At industrial operation of catalysts it should carry out investigations, which allow determining its composition, structure, containing of impurities and develop methods of its activity regeneration.

The aim of this study is analysis of industrial reforming catalyst PR-51 by predictive modelling method. This catalyst has shown high performance during 17 years of its operation.

2. Object and method of research

Catalytic reforming unit LG-35-8/300B is an important object of Ltd «Kinef» in Russia and intended for obtaining of individual aromatic hydrocarbons of benzene and toluene. In contradistinction to other catalytic reforming units, working for the production of high-octane components, the reforming unit LG-35-8/300B the next technological blocks for [22]:

- selective hydrogenation of unsaturated hydrocarbons;
- extraction with solvent regeneration;
- rectification of the extract to individual aromatic hydrocarbons.

A distinctive feature of PR-51 catalyst is presence of active centers, containing pairs of Lewis acid sites of different strengths. These pairs are surface platinum complexes $\text{PtCl}_x\text{O}_y\text{L}_z$ ($\text{Pt}\text{o-L}_z$), where platinum ions (Pto) act as soft Lewis centers, L_z act as rigid Lewis centers and are cations Al^{3+} of crystal lattice Al_2O_3 [23]. The main physio-chemical characteristics are shown in Table 1.

Table 1. Main characteristics of catalysts PR-51 and AP-10 [21-23]

Indicator/Catalyst	Unit	PR-51	AP-10
Pt	%mass	0.25	0.10
Re	%mass	0.30	-
Cl(F)	%mass	1.0	-
Fe	%mass	0.02	0.017
Na_2O	%mass	0.02	0.02
Diameter	mm	2.8 (1.6)	2.6-3.0
Bulk density	kg/dm^3	0.67-0.68	0.6-0.8

Description and control of catalyst operation main criteria realize by measurement of elementary stages rates of catalytic process and reaction under different parameters changing, which have influence on the rate of reaction (concentration of reacting substances, temperature, etc.). This kind of catalyst properties research is called «kinetic» and explains formalized mechanism of reaction opens physio-chemical mechanism of concrete processes up and allows getting initial data for optimal management by the whole industrial process, determining kinetic parameters of reactions occurring.

However despite of all possibilities of kinetic method, it is not possible to realize its comprehensive application. First of all, relations of process rate and its separate stages from different technological parameters represent complicated dependencies of exponential functions, which could be solved with specialized computer program using only. And secondly, real processes are always accompanied by processes of mass and heat transfer, which could misrepresent information about catalytic process rate.

That's why for comprehensive analysis of catalyst operation beside kinetic methods of study instrumental ones have also been using. This group of methods allows determining the structure of catalyst surface (where chemical reaction occurs), activation form of reacting substances, and explaining the surface reaction mechanism on the concrete platinum contact.

Type of instrumental method is chosen depending on catalyst characteristic demanding. There is a variety of instrumental methods (Table 2).

Thus, the most complete representation about catalyst operation and processes on its surface could be obtained only at cooperative analysis with instrumental and kinetic methods. Of course, the results of these analyses represent a big array of integrated complementary data. That is why the solution of such problems becomes possible only with the development

of mathematical models, based on totality of data obtained by kinetic and instrumental methods.

Table 2. Instrumental methods of catalysts study and control [20]

Catalyst characteristic	Method of study	Catalyst characteristic	Method of study
Chemical composition	X-fluorescence	Structure of catalyst chemical compounds	Thermogravimetric analysis
	Neutron diffraction		Differential thermal analysis
	Atomic-emission spectroscopy		Mössbauer spectroscopy
Structure of catalyst chemical compounds	Atomic adsorption	The texture of catalysts and carriers (porosity, specific surface, etc.)	BET theory
	Nuclear magnetic resonance spectroscopy		Porosimetry
	X-ray crystallography		Chemisorption
	Infrared spectroscopy		X-ray crystallography

Mathematical model using allows avoiding of complicated and expensive experiences [24-27]. Results obtained with mathematical model can optimize catalyst composition for its characteristics improving: activity, selectivity and stability.

The conditions of catalyst operation are not constant: technological conditions at oil-refinery could be changed for a number of reasons [5]. Besides, the composition of raw material is not fixed and could be different depending on oil-field.

Mathematical modelling method allows carrying out a comprehensive analysis of the catalytic reforming unit operation, what helps to increase product yield and decrease production costs.

Improving the stability and selectivity of the catalyst as well as reducing catalyst deactivation is a vital issue for enhancing the efficiency and yield of the catalytic naphtha reforming process. Thus, mathematical modelling method based on physio-chemical regularities of the process is the most objective one for catalyst operation assessment. That is why this method was used for monitoring of industrial unit LG-35-8/300B Ltd «Kinef» and the comprehensive analysis of catalyst operation has been done.

3. Experimental

In June 1999 in three reactors P-2, P-3, P-4 of reforming block the fresh catalyst PR-51 was loaded in quantity of 24433 kg and in 2009 the amount of 873 kg was made in reactor P-2. The total amount of catalyst is 25306 kg. During the repair period in 2009 in reactor P-5 the catalyst AP-10 was loaded in quantity of 7000 kg (Table 3).

Table 3. AP-10 catalyst operation data

Nº	Regeneration data	The amount of recycled raw materials, t	Nº	Regeneration data	The amount of recycled raw materials, t
1	06.2000	296 435	8	07.2012	1 127 210
2	06.2001	300 000	9	11.2012	707 71
3	07.2002	294 028	10	02.2014	545 224
4	06.2003	270 028	11	04.2015	473 032
5	06.2004	294 826	12	07.2015	23 100
6	08.2006	727 208	13	till 13.04.2016	236 073
7	07.2009	1 234 061			

The total amount of recycled raw materials PR-51 catalyst (from load till 13.04.2016) using is 5 891 996 ton. Main indicators of reforming block operation are performed in Table 4.

Table 4. Main indicators of reforming block operation with PR-51 catalyst using conditions: Pressure – 1.35 MPa, hydrogen-rich gas circulation ratio- 1200-1300 Nm³/m³

Name/Number of cycle	I (1999-2000)	V (2003-2004)	VI (2004-2006)	VII (2006-2009)	VIII (2009-2012)	XIII (2015-2016)
Consumption of raw materials, m ³ /h	55	60	60	62	64	62
Fractional composition of raw material, IBP/50 %/EBP, °C	71/81/103	71/82/102	71/81/98	71/80/94	71/78/92	71/77/96
The average temperature at the reactor inlet	486	486	486	482	482	482
Hydrogen concentration in HRG, % vol.	81.6	83.9	86.5	86.5	86.5	79.9
Stable reformate yield, % mass.	82.6	84.8	87.2	87.0	88.0	87
Aromatic compounds output after extraction block, % mass., including	33.2	33.7	33.6	31.5	30.8	35.07
Benzene	13.8	14.0	16.7	17.0	17.1	19.4
Toluene	17.7	17.8	15.5	13.1	12.6	14.6
Aromatic compounds output after reforming block, % mass.	36.5	36.2	36.0	34.0	33.5	32.5
Cycle duration, months	12	12	24	34	36	24*

*Data of October 2016

According to the results of laboratory studies, the reforming catalyst PR-51 has proven to be appropriate in operation. The aromatic hydrocarbons concentration in a stable catalyst corresponds to 35.07 %mass., with the norm not less than 35 %mass. Hydrogen concentration in hydrogen-rich gas is at the level of 79.9 %vol. In general, the decrease in hydrogen concentration by 5 % is observed in comparison with the previous (84.9 % vol. at 22.07.15).

Based on industrial operation data and laboratory studies computer modelling system «Aktivnost» using the monitoring of PR-51 catalyst was done. The results are performed in Table 5.

Table 5. The monitoring of PR-51 catalyst

Date	13.04.16	17.05.16	25.05.16	07.06.16	29.06.16	27.07.16	23.08.16
Activity	1.02	1	0.99	0.87	0.88	0.94	0.75
Recycled raw material, t	236073	272387	280939	289762	305352	334725	349302
Reactors inlet temperature. °C	482	482	482	482	482	482	477
Consumption of raw materials. m ³ /h	62.5	63	63	40	42	62	32
Aromatics, %mass	34.53	33.12	32.58	33.87	32.34	29.74	27.98
Hydrogen output, %	1.57	1.43	1.41	1.34	1.35	1.26	1.06
Coke, %mass.	2.4	2.75	2.83	2.89	3	3.25	3.3
Hydrogen, %	79.9	79.1	79.1	83.6	78.8	79.4	79.6
Product yield	90.4	91.26	91.19	89.87	89.58	92.33	91.73
Par/(Naft+Arom) in feedstock	1.44	1.45	1.46	1.43	1.57	1.48	1.62
n-Par/i-Par in feedstock	0.9	0.92	1	0.93	0.97	1.02	1.01

Analyzing the results. it could be concluded that the catalyst has shown the effective operation.

4. Conclusions

More than 20 years of industrial operation experience of naphtha reforming catalysts PR-51. PR-71 and PR-81 has shown that catalysts of PR family ensure high activity and selectivity. It is shown in product yield increasing by 3-5%mass. with octane number 96-97. Hydrogen

concentration increasing by 3-5%vol. in circulating gas. benzene and toluene content decreasing in with a general increase in the aromatic hydrocarbons content.

Acknowledgements

The research is carried out at National Research Tomsk Polytechnic University and within the framework of National Research Tomsk Polytechnic University Competitiveness Enhancement Program grant.

References

- [1] Chernyakova ES. Ivanchina ED. Yakupova IV. Vinidiktova MV. Seytenova GZ. Coke formation reduction in the catalytic reforming reactors at the optimal catalyst activity. *Pet. Coal*, 2016; 58(2): 746-752.
- [2] Tregubenko VY. Udras IE. Zatolokina EV. Smolikov MD. Kir'yanov DI. Arbuzov AB. Gulyaeva TI. Belyi AS. The synthesis and investigation of the reforming catalysts for the reduced aromatics content gasoline obtaining. *Procedia Eng.*, 2015; 113: 144-151.
- [3] Elsayed HA. Menoufy MF. Shaban SA. Ahmed HS. Heakal BH. Optimization of the reaction parameters of heavy naphtha reforming process using Pt-Re/Al₂O₃ catalyst system. *Egypt. J. Pet.*, 2017; 26: 885-893.
- [4] Koksharov AG. Faleev SA. Chernyakova ES. Ivanchina ED. Yakupova IV. Chuzlov VA. Bifunctional pt-re reforming catalysts properties modelling. *Pet. Coal*, 2016; 58(7): 726-731.
- [5] Zbarsky VL. Gilin VF. Toluene and its nitroderivatives. Editorial URSS. Moscow. 2000: 272.
- [6] Barrientos J. Montes V. Boutonnet M. Jaras S. urther insights into the effect of sulfur on the activity and selectivity of cobalt-based Fischer-Tropsch catalysts. *Catal. Today*, 206; 275: 119-126.
- [7] Simson A. Farrauto R. Castaldi M. Steam reforming of ethanol/gasoline mixtures: Deactivation. regeneration and stable performance. *Appl. Catal., B*. 2011; 106: 295-303.
- [8] Barbarias I. Artetxe M. Lopez G. Arregi A. Bilbao J. Olazar M. Influence of the conditions for reforming HDPE pyrolysis volatiles on the catalyst deactivation by coke. *Fuel Process. Technol.*, 2018; 171: 100-109.
- [9] Dong XJ. He YJ. Shen JN. Ma ZF. Multi-zone parallel-series plug flow reactor model with catalyst deactivation effect for continuous catalytic reforming process. *Chem. Eng. Sci.*, 2018; 175: 306-319.
- [10] Sharma YC. Kumar A. Prasad R. Upadhyay SN. Ethanol steam reforming for hydrogen production: Latest and effective catalyst modification strategies to minimize carbonaceous deactivation. *Renewable Sustainable Energy Rev.*, 2017; 74: 89-103.
- [11] Mang T. Breitscheidel B. Polanek P. Knözinger H. Adsorption of platinum complex on silica and alumina: Preparation of non-uniform metal distributions within support pellets. *Appl. Catal. A: General*, 1993; 106: 239-258.
- [12] Shelimov B. Lambert JF. Che M. Didillon B. Initial Steps of the Alumina-Supported Platinum Catalyst Preparation: A Molecular Study by 195Pt NMR. UV-Visible. EXAFS. and Raman Spectroscopy. *J. Catal.*, 1999; 185: 462-478.
- [13] Shelimov BN. Lambert JF. Che M. Didillon B. Molecular-level studies of transition metal-support interactions during the first steps of catalysts preparation: platinum speciation in the hexachloroplatinate/alumina system. *J. Mol. Catal. A: Chem.*, 2000; 158: 91-99.
- [14] Marceau E. Carrier X. Che M. Impregnation and Drying. in: K.P. de Jong (Ed.). *Synthesis of Solid Catalysts*. Wiley-VCH. Weinheim. 2009; 59-82.
- [15] Kolesnikov IM. Catalysis and catalysts production. «Tehnika». TUMA GRUPP. Moscow. 2004; p.400.
- [16] Moroz EM. Zyuzin DA. Tregubenko VYu. Udras IE. Belyi AS. Likhobobov VA. Effect of structural defects in alumina support on the formation and catalytic properties of the active component of reforming catalysts. *Reac. Kinet. Mech. Cat.*, 2013; 110: 459-470.
- [17] Jiao WQ. Yue MB. Wang YM. He MY. Synthesis of morphology-controlled mesoporous transition aluminas derived from the decomposition of alumina hydrates. *Microporous Mesoporous Mater.*, 2012; 147: 167-177.
- [18] Kul'ko EV. Ivanova AS. Litvak GS. Kryukova GN. Tsybulya SV. Preparation and Microstructural and Textural Characterization of Single-Phase Aluminum Oxides. *Kinet. Catal.*, 2004; 45: 714-721.
- [19] Vicerich MA. Espezel C. Benitez VM. Influence of gallium on the properties of Pt-Re/Al₂O₃ naphtha reforming catalysts. *Appl. Catal. A: General*, 2011; 407: 49-55.

- [20] Rahimpour MR. Jafari M. Iranshahi D. Progress in catalytic naphtha reforming process: a review. *Appl. Energy*. 2013; 109C: p.83
- [21] Belyj AS. Pashkov VV. Kir'yanov DI. Smolikov MD. Golinsky DV. Udras IE. Experience of commercial production and operation of new reforming catalysts of PR family. *Russian Chemical Journal*. 2007; 51: 60-68
- [22] E-Him. Petrochemical technologies. <http://e-him.ru/>.
- [23] Smolikov MD. Kir'yanov DI. Kolmagorov KV. Udras IE. Zatolokina EV. Belyj AS. Experience of commercial production and operation of new reforming catalysts PR-81 and SHPR-81. *Catal. Ind.*, 2013; (6): 36-41.
- [24] Chsherbakova Y. Dolganova I. Belinskaya N. Benzene alkylation with ethylene process mathematical modeling. *Proceedings - 2012 7th International Forum on Strategic Technology. IFOST 2012*, 2012; Article Number 6357494.
- [25] Ivashkina E. Nazarova G. Ivanchina E. Belinskaya N. Ivanov S. The Increase in the Yield of Light Fractions During the Catalytic Cracking of C-13-C-40 Hydrocarbons. *Curr. Org. Synth.*, 2017; 14 (3): 353-364.
- [26] Novaes LR. Resende NS. Salim VM. Secchi AR. Modeling. simulation and kinetic parameter estimation for diesel hydrotreating. *Fuel*, 2017; 209: 184-193.
- [27] Ancheyta J. Mederos FS. Mathematical modeling and simulation of hydrotreating reactors: Cocurrent versus countercurrent operations. *Appl. Catal. A*, 2007; 332: 8-21.

To whom correspondence should be addressed: Dr. Emilia D. Ivanchina. Department of Fuel Engineering and Chemical Cybernetics. Tomsk Polytechnic University. 30. Lenin Avenue. Tomsk. 634050. Russia; tel.: (+7-3822) 60-63-33; fax: (+7-3822) 56-38-65; e-mail: ied@tpu.ru

REDUCTION OF THE QUALITY RESERVE WITH THE USE OF PREDICTIVE MODELS IN THE MOTOR FUEL PRODUCTION

*Vyacheslav A. Chuzlov^{*1}, Galina Y. Nazarova¹, Aleksandra A. Kislynskaya¹, Rizagul' M. Dyussova¹, Gajni Zh. Sejtenova², Madeniet A. Elubaj²*

¹ Tomsk Polytechnic University, 30, Lenin Avenue, Tomsk, 634050, Russia

² S. Toraighyrov PSU, 64, Lomov Str., Pavlodar, 140008, Kazakhstan

Received January 31, 2018; Accepted April 27, 2018

Abstract

The paper describes a method for reducing the margin for the quality of automotive gasoline based on the use of predictive models for the process of catalytic cracking and compounding of automotive gasolines sensitive to changes in hydrocarbon composition and physical and chemical properties of processed raw materials, as well as technological modes of operation of industrial apparatuses. Continuous calculation of the individual composition and properties of the mixing components, as well as the constant adjustment of commercial gasoline formulations in real time, allows to receive motor fuels fully complying with the modern ecological standards of EURO-5, as well as to reduce the cost of finished products by 10-12% due to a decrease in the share of high-value flows, as well as the quality margin for the octane number of commercial gasolines, the content of sulfur, aromatic hydrocarbons and benzene in their composition.

Keywords: catalytic cracking; blending; mathematical modelling; motor fuel production; computer system.

1. Introduction

The growing demand for motor fuels of a high class of environmental safety necessitates the development of optimal recipes [1]. Forecasting the composition of gasolines with specified properties is possible when using components for which characteristics are known: octane numbers, yield, content of aromatic hydrocarbons and olefins, etc. The efficiency of the fuel is determined by the release of energy during combustion and depends both on the properties of the individual components and on the properties of the fuel compositions, which are determined by the chemical interaction of hydrocarbons not only at the compounding stage, but also at each separate stage of gasoline components preparation (catalytic cracking, reforming, etc.).

The wide introduction of the processes of deep processing of petroleum feedstock [2], including catalytic cracking with the involvement of residues of secondary oil refining processes, provides a significant share of gasoline components in the commodity product (about 30-40%). The high content of unsaturated and aromatic hydrocarbons of cracked fuels causes limitations when they are involved in the compounding process. At the same time, the yield and quality of cracking gasoline is largely determined by the composition of the processed raw materials [3-6]. Thus, enhanced coke formation on the catalyst during the processing of highly aromatized raw materials with the involvement of secondary process residues leads to an unbalanced temperature regime, a loss of catalyst activity and a decrease in the yield of the target product-gasoline.

To optimize the process of gasoline preparation, it is necessary to take into account the influence of a large number of factors at each stage of the process for the production of gasoline components on the octane number of mixed gasoline, taking into account the hydro-

carbon composition of the processed raw materials, the activity of the catalysts and their operating modes.

With the use of mathematical models of the processes of processing hydrocarbon mixtures that are complex in composition, it is possible to take into account the hydrocarbon composition of the processed raw materials, the thermodynamic and kinetic regularities of the production of gasoline components, the deactivation of catalysts, the interactions between the hydrocarbons that make up the gasoline, which cause deviations of the octane numbers from additivity [7-11].

The use of the «Compounding» system [12] in the planning of commercial gasoline production allows to reduce the percentage of involvement of expensive components (MTBE, alkylates) by increasing the share of reformate and gasoline catalytic cracking in commodity gasoline, which allows to achieve economic efficiency of the compounding process.

Continuous calculation of commercial gasoline formulations in on-line mode, taking into account the change in the composition of processed raw materials in the process of production of components of commercial gasoline, allows to receive motor fuels fully complying with the modern ecological standards of EURO-5, as well as to reduce the cost of finished products by 10-12% the proportion of expensive flows, as well as the quality margin for the octane number of commercial gasolines, the content of sulfur, aromatic hydrocarbons and benzene in their composition.

The aim of the work is to increase the efficiency of the process of compounding of gasolines taking into account the composition of the processed raw materials in the process of catalytic cracking.

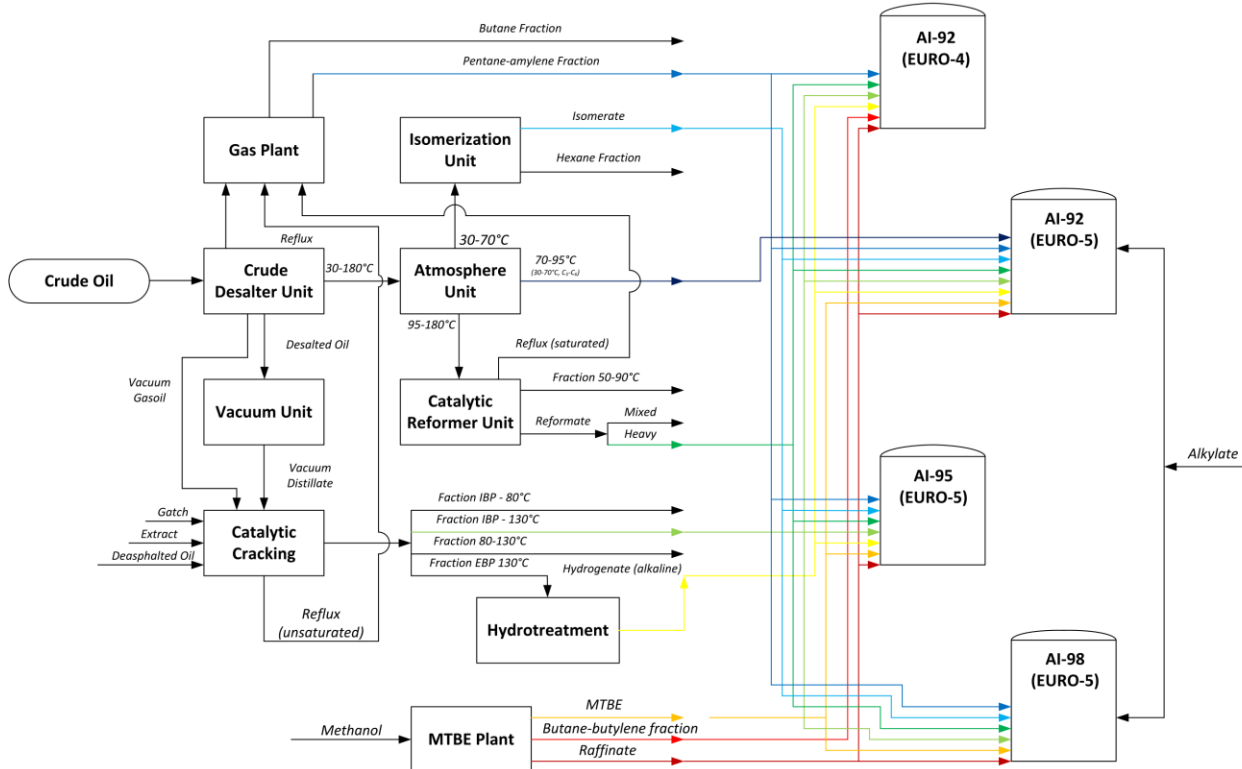


Figure 1. Block diagram of gasoline production process

2. Object of the research

The object of the current research is the flow chart of motor fuel production that consists of catalytic stage of motor fuel production and blending. The multi-stage processes of motor fuel production are performed according to the following scheme:

Catalytic cracking gasolines secondary often subjected to distillation for separation into narrower fractions to increase the octane fuel fund. Narrow fractions of gasoline (IBP -130°C, EBP-130°C can be used up to 100% by volume in the formulations of gasoline AI-80 and AI-92 and up to 20% in the formulations of gasoline AI-95 and AI-98.

3. Reduction of the reserve as quality with the use of prediction models in the manufacturing of motor fuels

In this work, a study was made of the effect of changing the composition of catalytic cracking gasoline on the formulation of commercial motor gasoline. To calculate the composition and properties of catalytic cracking gasolines, a computer modeling system is developed that is sensitive to changes in the composition of processed raw materials and technological modes of operation of industrial devices.

3.1 Development of the model of the catalytic cracking process for prediction the yield and composition of gasoline, taking into account the group composition of the processed raw materials

The mathematical model of the cracking process is written on the basis of the hydrocarbon transformation scheme and is represented by a system of ordinary differential equations of material and heat balance of reactants according to the contact time for an ideal displacement reactor with initial conditions $\tau=0$, $C_i=C_{i0}$. $T_0=T_{b.r.}$:

$$\begin{cases} \frac{dC_i}{d\tau} = W_j \\ \rho_m c_m \frac{dT}{d\tau} = \sum_{j=1}^n (\pm \Delta H_j) W_j \end{cases}$$

where dC_i – is the change in the concentration of the i -group of hydrocarbons, mol/l; τ – time of contact, s; W_j – is the rate of chemical reaction; dT – is the change in the flow temperature, K; ΔH_j – is the thermal effect of the chemical reaction at the thermal equilibrium temperature of the feedstock and catalyst, kJ/mol; ρ_m , c_m – density and heat capacity of the flow, kg/m³, kJ/kg · K; $T_{b.r.}$ – reaction initiation temperature, K.

The transformation scheme is formed by the results of a complex of laboratory studies to determine the composition and quality of raw materials and process products and the thermodynamic analysis of the reaction process at the cracking temperature and includes 12 pseudo-components (Table. 1).

Table 1. Characterization of hydrocarbon groups in the transformation scheme

Group in the scheme	Group in the scheme
GF Parafins	Paraffins $C_{13}-C_{40+}$
HMW Naphthenes	Mono and bicyclic naphthenes with long substituents C_1-C_{25} (average number of naphthenic rings - 2,1 ÷ 2,3 units)
HMW Aromatics	Mono and poly aromatic hydrocarbons with long substituents (average number of aromatic rings - 2,3 ÷ 2,8 units, average number of naphthenic rings 1,3 ÷ 1,4 units)
CAH	Condensed aromatic compounds
GF Parafins	Paraffins C_5-C_{11+}
GF Isoparafins	Isoparaffins C_5-C_{11+}
GF Olefins	Olefins C_5-C_{11+}
GF Naphthenes	Naphthenes C_5-C_{11+}
GF Aromatics	Aromatic hydrocarbons C_6-C_{12+}
PPF	Hydrocarbons $C_3H_6+ C_3H_8$
BBF	Hydrocarbons $C_4H_8+ C_4H_{10}$
Gases	Gases $C_1+C_2+C_5+C_6+$

Thus, the scheme of transformations (fig. 2) is oriented to predicting the group composition of the gasoline fraction, taking into account the reversibility of reactions in the chain of chemical transformations in accordance with [12].

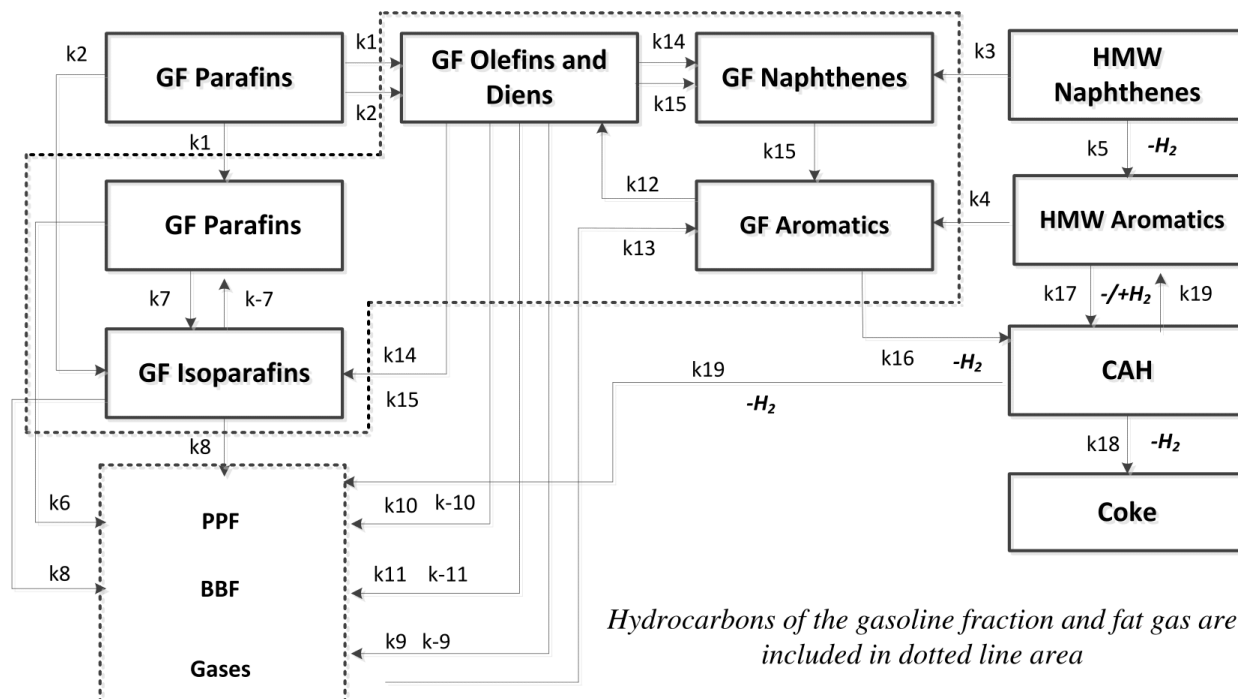


Figure 2. Scheme of hydrocarbon transformations for the catalytic cracking process and the rate constant of forward and reverse reactions at the cracking temperature 518°C

The mathematical model allows calculating the consumption and selection of products from the installation, including the output and content of coke on the catalyst, the content of PPF and BBF in the gas, the group and hydrocarbon composition of the gasoline fraction (Fig.3), depending on the composition of the feedstock and the technological mode of operation of the reactor.

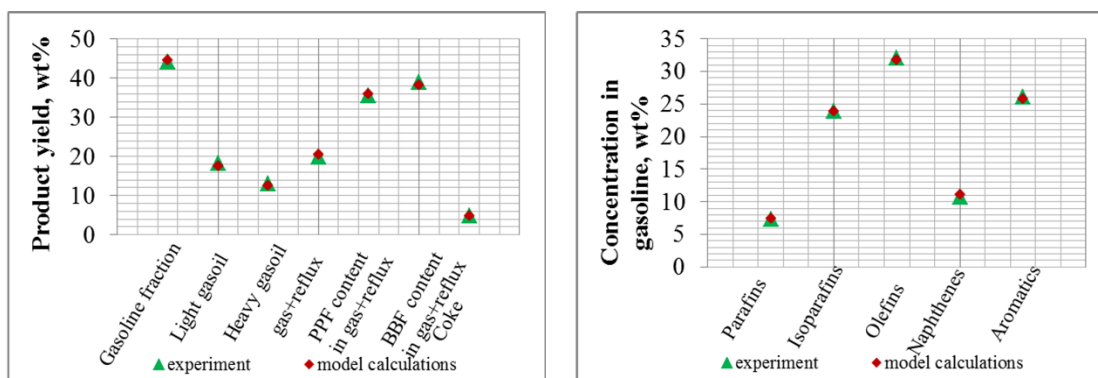


Figure 3. Verification of catalytic cracking mathematical model

The maximum relative error in the selection of products is not more than 5.0% of mass, in the group composition of gasoline cracking - no more than 4.0% of mass.

Figure 4 and Table 2 show that the composition of the feedstock has a significant effect on the yield and group composition of the target product - the gasoline fraction and coke.

When working on raw materials with a high content of saturated hydrocarbons (2.32 units), gasoline selection is higher (44.63%), gasoline, moreover, is characterized by a high content

of paraffinic hydrocarbons of normal and branched structure (7.45 and 23.84 % of mass, respectively). With a higher concentration of aromatic hydrocarbons and resins in the catalytic cracking feed, the yield of coke (5.17%) is higher than when processing a vacuum distillate with a high content of saturated hydrocarbons (4.76% of mass, respectively), which causes deactivation of the catalyst and a reduction in the yield of the target product (43.81%). Gasoline is characterized by a high content of aromatic hydrocarbons and olefins (27.4 and 32.61% of mass) during the course of reactions of dealkylation of aromatic hydrocarbons, cracking and dealkylation of naphthenic and naphthene-aromatic compounds.

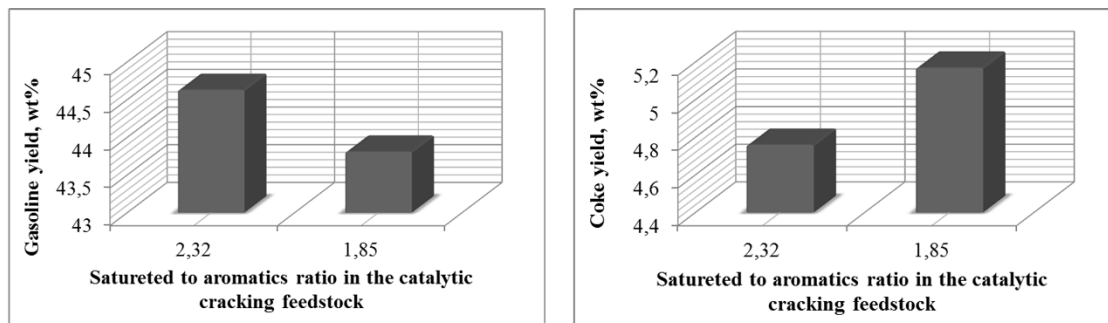


Figure 4. Selection by gasoline and coke of the catalytic process with a change in the composition of the processed raw materials

Table 2. The influence of the group composition of raw materials on the group composition of gasoline (calculation by model)

HC group	The ratio of saturated hydrocarbons to aromatic in the feedstock cracking	
	2.32	1.85
Paraffins, %mass.	7.45	7.06
Isoparaffins, %mass.	23.84	22.27
Olefins, %mass.	31.82	32.61
Naphthenes, %mass.	11.15	10.66
Aromatics, % mass.	25.74	27.40

When optimizing the process to increase the production of the gasoline fraction directed to the compounding step, it is important to take into account that the target product of the industrial plant – the gasoline fraction passes through a maximum in the range of 520 – 525°C (Fig. 5) with increasing process temperature, due to an increase in the reaction rate of hydrocarbon cracking gasoline fraction into fatty gas components.

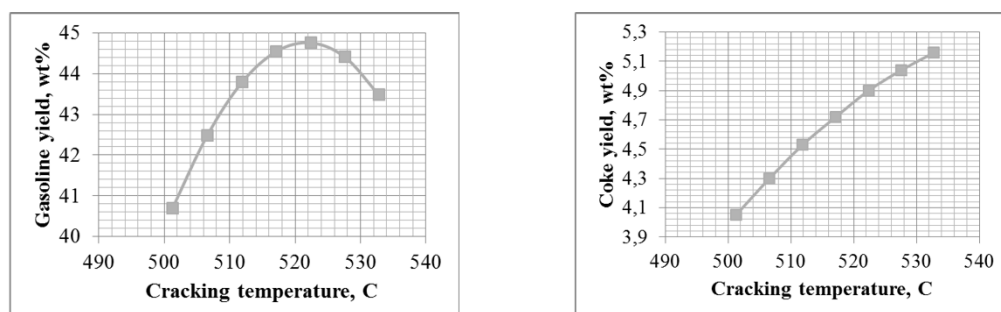


Figure 5. Gasoline and coke yield depending on the cracking temperature

Therefore, it is important to optimize the technological regime of the reactor operation depending on the composition of the processed feedstock and the temperature of the catalyst stream after regeneration in order to obtain the maximum yield of the gasoline fraction [13].

In this paper, a study was made of the effect of changing the composition of catalytic cracking fuels on the formulation of commercial motor gasoline. Calculation of the composition and properties of catalytic cracking gasoline was carried out using a developed computer modeling system that is sensitive to changes in the composition of processed raw materials and technological modes of operation of industrial devices. The calculated compositions and physico-chemical properties of catalytic cracking gasolines are presented in the Table 3.

Table 3. Estimated compositions and properties of catalytic cracking gasolines

Parameter	Gasoline fraction IBP -130°C		Gasoline fraction. IBP -130°C	
	26.04.2017	27.04.2017	26.04.2017	27.04.2017
RON	94.40	95.41	96.17	98.19
MON	87.16	88.11	87.55	89.25
Reid vapour pressure, kPa	13.11	13.40	67.73	68.20
Density of flow, kg/m ³	811.05	812.95	692.43	693.45
Flow viscosity, Pa.s	54.08	54.31	34.86	35.16
N-paraffins, %mass.	8.95	8.54	6.78	6.57
Iso-paraffins, %mass.	7.84	7.11	29.64	27.34
Naphthenes, %mass.	13.05	12.31	10.44	10.05
Olefins, %mass.	5.72	5.95	42.46	44.91
Benzene, %vol.	0.00	0.00	0.90	1.00
Aromatics, %vol.	64.44	66.09	10.61	11.07
Sulfur, %mass.	0.00	0.00	0.06	0.06

Based on the results of the calculations presented in Table 3, due to the change in the composition of the feedstock of the catalytic cracking process, the RON of gasoline of catalytic cracking oscillates in the interval of 1-2 points, the group composition changes. The influence of the composition and physicochemical properties of catalytic cracking gasoline on the formulation of commercial gasolines of various grades is shown in the Tables 4-5.

Table 4. The results of calculating the formula of gasoline AI-92-K-5

Component	26.04.2017	27.04.2017	Parameter	Value
MTBE from the installation	2.9	2.9	RON	92.09
Gasoline fraction 70-95°C	4.3	4.3	MON	85.28
Alkylate purchased	2.0	2.0	Reid vapour pressure, kPa	97.95
Pentane-ethylene fraction	5.0	5.5	Olefins, %	6.65
C4 fraction raffinate	7.5	7.5	Benzene, %	0.50
Heavy reformat	32.7	32.7	Aromatic hydrocarbons, %vol.	34.83
Reformat of light straight naphtha	28.2	28.2	Sulfur, %mass.	0.0009
Gasoline fraction EBP -130°C	15.8	15.0		
Gasoline fraction IBP -130°C	1.5	1.8		
TOTAL	100.0	100.0		

Thus, the change in the hydrocarbon composition of the processed feedstock in the catalytic cracking unit leads to the need to adjust the formulation of commercial motor gasoline, taking into account the change in the composition and properties of the catalytic cracking stream as one of the main components of mixing. As a result of the increase in the RON of the IBP - 130°C, it became possible to involve a more significant amount of the 70-95 ° C gasoline fraction in the process of producing AI-92-K-5 gasoline, the share of expensive MTBE and alkylate fluxes during the preparation of «Super 98» gasoline.

4. Conclusions

1. The mathematical model of the catalytic cracking process is suitable for predicting, depending on the composition of the feedstock and the technological mode of operation of the reactor:
 - consumption and selection of products from the plant (stable gasoline, total gas and reflux selection, light gas oil, heavy gas oil, coke)
 - BBF and PPF content and total flow in the catalytic cracking of gas (gas + Reflux);
 - group and hydrocarbon composition of the gasoline fraction
 - temperature of the cracking process taking into account the thermal effect of the chemical reactions of the process.
2. Using the model of the catalytic cracking process, it is possible to predict the yield of light fractions and coke, depending on the composition of the processed raw materials and the mode of operation of the apparatus. In the future, accounting for the activity of the catalyst will allow us to evaluate the effect of the raw material composition and the technological regime of the reactor operation on the degree of its deactivation, and the regeneration operation regimes for predicting the activity of the equilibrium catalyst and reducing the loading of the fresh catalyst.
3. Complex application of mathematical models of processes of catalytic cracking and compounding of commercial gasolines makes it possible to assess the effect of changing the composition of processed raw materials and technological conditions on the composition and properties of the components of mixing and, consequently, on the formulation of motor gasolines. Thus, as a result of an increase in the RON of the IBP -130°C, it became possible to involve a more significant amount of the 70-95°C gasoline fraction in the process of producing AI-92-K-5 gasoline, the share of expensive MTBE and alkylate fluxes during the preparation of «Super 98» gasoline.

References

- [1] Ivanchina ED, Kirgina MV, Chekantsev NV, Sakhnevich BV, Sviridova EV, Romanovskiy RV. Chem. Eng. J., 2015; 282: 194-205.
- [2] Khadzhiev SN, Gerzeliev IM, Kapustin VM, Kadiev KhM, Dement'Ev KI, Pakhmanova OA. Petroleum Chemistry, 2011; 51(1): 32.
- [3] Doronin VP, Lipin PV, Potapenko OV, Sorokina TP, Korotkova NV, Gordenko VI. Catalysis in Industry, 2014; 6(4): 307.
- [4] Gerzeliev IM, Dement'Ev KI, Khadzhiev SN. Petroleum Chemistry, 2015, 55(6): 481.
- [5] Doronin VP, Potapenko OV, Lipin PV, Sorokina TP. Fuel, 2013; 106: 757.
- [6] Lipin PV, Doronin VP, Gulyaeva TI. Petroleum Chemistry, 2010; 50(5): 362.
- [7] Dmitriev VM, Gandga TV, Dolganov IM, Pisarev MO, Dolganova IO, Sizova EN, Ivashkina EN. Pet Coal, 2015; 57(6): 691.
- [8] Chsherbakova Y, Dolganova I, Belinskaya N. 7th International Forum on Strategic Technology 2012; 1.
- [9] Dolganov IM, Pisarev MO, Ivashkina EN, Dolganova IO.:Pet Coal, 2015; 57(4): 328.
- [10] Dolganova I.O., Dolganov I.M., Ivashkina, E.N., Ivanchina, E.D. Pet Coal, 2012; 54(3), 213.
- [11] Kirgina MV, Ivanchina ED, Dolganov IM, Chekantsev NV, Kravtsov AV, Fu F. Chemistry and Technology of Fuels and Oils, 2014; 50(1): 17.
- [12] Parmon VN. Thermodynamics of non-equilibrium processes for chemists.-Dolgoprudnii: Intellekt, 2015: 472.
- [13] Ivashkina E., Nazarova G., Ivanchina E., Belinskaya N., Ivanov S. Current Organic Synthesis 2017; 14(3): 353-364

To whom correspondence should be addressed: Dr. Vyacheslav A. Chuzlov, Tomsk Polytechnic University, 30, Lenin Avenue, Tomsk, 634050, Russia, chuva@tpu.ru

COMPARATIVE APPROACH TO OPTIMUM SELECTION OF ARTIFICIAL LIFT SYSTEM

Kevin Chinwuba Igwilo¹, Emeka Emmanuel Okoro¹ and Samuel Ubanatu²

¹ Petroleum Engineering Department, Covenant University Ota, Nigeria

² Petroleum Engineering Department, Federal University of Technology Owerri, Nigeria

Received December 11, 2017; Accepted March 19, 2018

Abstract

Artificial lifts are used around the world in approximately 85% of the wells and its overall efficiency cannot be overestimated. The specific lift method for a particular application is largely accomplished by production engineers; they apply both field / operational experience, and modern knowledge. This quality has been recognized as a defect in most engineering disciplines and have led to sub-optimal design in projects. Improper selection of artificial lifts can lead to a reduction in production and a significant increase in operating costs. Once a decision is made about the type of lift that will be installed in a well, whether or not this method is chosen optimally for the existing conditions of the well; very little can be done after installation. This paper analyzed the selection criteria for various artificial lift techniques and illustrate why the selection made is the most suitable technique to be applied in that particular well condition. For optimum decision making, the study considered the characteristics of the reservoir, their operational and design characteristics, the location of the facility and the artificial lift system economic. The economic evaluation of each case was carried out taking into account the capital and operating cost for each option.

Keywords: Artificial Lift; Optimum Lift Selection; Decision Matrix.

1. Introduction

The in-situ fluids naturally flow from the reservoir to the surface when the well is completed if the fluid/pore pressure is sufficient to lift the fluid from the matrix and transfer it to the well and lift it to the surface. During the production of the reservoir, the pressure will decrease and this will probably lead to an increase in water cut and a gas fraction decrease. This will prevent the in-situ fluids in the formation not to flow out easily into the well or even stop the flow of liquid. To prevent production decline, it is necessary to use some techniques. Thus, to raise the fluids to the surface, additional energy must be added and applying artificial lift technology will add energy to the fluid. An artificial lift is a method used to lower the pressure at the bottom hole of a well in order to maintain production from the reservoir and accelerate well production. It adds energy to the well fluid, which when it enters the available energy, which is naturally provided in the reservoir itself; flows well at a very economical performance. Nevertheless, the artificial lift system is extensive and diverse, and the key to selection does not necessarily depend on the simplest method; but on the most suitable method. A common method that is often used to select an artificial lift system are based on feedback or acquaintance, rather than a strategic optimization plan. An additional component for proper planning of optimum selection of the artificial lift method must be initiated during design, drilling and completion. There are a number of well parameters needed to select the best wellbore system. These include downhole pressure, the type of liquid to be discharged, the amount of fluid to be produced, the geometry of the well, the location well (offshore or land) and the total depth of the well. Not having this parameters/information can make the selection more difficult.

The choice of the right method of artificial lift is crucial for the long-term profitability of most oil and gas wells. Poor choice can reduce production and significantly increase operating costs [1]. In addition, a change in the type of lift already installed in a well will cost money and it implies that an incorrect system was chosen initially. Though, production engineers must constantly check the efficiency of the lift method to change operating parameters or even to assess how to change it; but it usually remains unchanged after selection. Clegg *et al.* [1] compared the main characteristics of the selection of the eight main artificial lift methods and gave practical guidance on the effectiveness and operational capabilities of methods based on proven real technologies.

The optimization of production and the savings in the costs of the artificial lift system are interdependent and can be achieved by properly planning a strategic project that takes into account the individual characteristics of the well and the actual operational capabilities of the lifting system.

It is important to choose the lift system that best suits the well from the widespread range of artificial lifts; taking into account the location, depth, expected yield, storage characteristics and other factors available. This study was developed from the five (5) P's for artificial lift systems developed by the service companies from their practical experience. These P's are represented in the slogan, "Proper Planning Prevents Poor Performance". This study ensures that the most appropriate artificial lift systems are selected based on the conditions and limitations in the well reservoir and the surface [1].

2. Literature

Optimal decision-making is a constant problem in the technique for production. The dynamic nature of the wells, other formation conditions and the company's policy during the project can cause complications. Technological constraints, existing cost structures and reservoir characteristics affect the optimal production strategies. There are no single calculation or a simple solution to solving all production situations. Conversely, there are several strategies for artificial lift and possible combinations to achieve the desired results within acceptable limits. Sometimes technical envelopes and functions of the artificial lift system overlap. Depending on the situation, it is necessary to fill the lifting gap, but other scenarios depend on the most effective time to switch the artificial lift system. Combining systems and effectively switching the system in the production of the optimum amount of oil at a low cost per barrel is not an easy task for Production Engineer [2].

In 1994, more than 900,000 wells were discovered worldwide [2]. Only 7% of them proceeded naturally, and the remaining 93% required some form of artificial lift. The average yield per well was less than 70 bpd. An artificial lift is a method of reducing bottom hole pressure of the formation so as to increase the rate of well production. When producing from the well, the potential energy is converted into kinetic energy associated with fluid motion. This disperses the potential energy of the reservoir, reducing the flow and eventually make the flow to cease. In production stage of a well, it may be economical to maintain or even increase production rates using artificial lift to compensate for the dissipation of reservoir energy.

2.1. Natural flow of a well

The natural flow occurs when the pressure in the reservoir exceeds the pressure loss through the producing well from the subsurface to the surface (Fig. 1). This occurs under two conditions:

- 1) Normal or over-pressured reservoir. In this case, the pore and the in-situ fluid pressure with respect to their depth exerts a pressure below the reservoir pressure. Many unconventional deposits are over-pressured, so this usually leads to a natural flow for a short period of time in most cases.
- 2) The velocity of the fluid in the well gives sufficient gas production to carry the liquid obtained to the surface. It is usually called the "critical rate" for the liquid lifting.

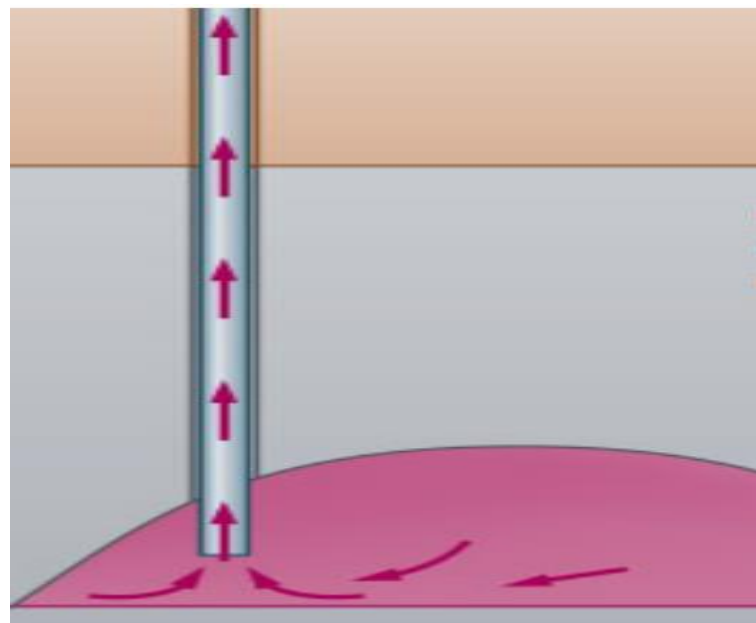


Figure 1. Primary production in a reservoir

The simplified technique to calculate where this condition exists is found in Turner *et al.* [3]. The correlation of Turner can correlate the critical velocity with the properties of the reservoir fluid, the surface pressure and the cross-sectional area of the fluid flow.

The natural decrease in accumulated reservoir pressure affects the flow of oil, gas or water, which causes instability and reduces production. The pressure and heat of the reservoir allows dissolved natural gas to always be present in the oil. When the oil is produced from the reservoir through the well, the pressure drops. At this stage, the gas will be out of the oil thereby expanding in volume. Expanding gas in the gas cap also helps maintain the pressure in the oil column high enough to allow oil to flow to the surface without artificial lift. The water of the aquifer can also maintain pressure in the oil column. This is called a natural flow, because the oil flowed to the surface without artificial help. The natural flow can be maintained by ensuring artificially high reservoir pressures (example, by pumping water or gas into non-production wells in the same field). Natural flow is the cheapest way of production; thus, we make every effort to keep it as long as possible.

2.2. Artificial lift

Neely *et al.* [4] defined some methods of artificial lift and studied the method of application, disadvantages, advantages and limitations of each method. Geographical and environmental conditions were considered as one of the main factors in the choice of selecting artificial lift and other sub-factors such as; reservoir fluid characteristics and pressure, the productivity index and inflow performance. Hwang and Yoon [5] used the concept of order of preference, based on a similarity to the ideal solution model (TOPSIS). The main idea of this program is that the most suitable method is the shortest distance from the ideal solution, and the worst method is the furthest from the ideal solution. Thus, the artificial lift methods should be evaluated in the range from 0 to 10.

According to the Schlumberger report, the value of 1 is evaluated perfectly, the 10-point conversion scale is 7. The value of 2 is considered fair, the 10-point scale is 7; and the value of 3 is considered unsatisfactory. Because the value is 3 on a 10-point scale. Each method of artificial lift has operational limitations.

Valentine *et al.* [6] used the "Optimal Pumping Unit Search" (OPUS) to select an artificial lift. OPUS was an intelligent integrated system with artificial lift method characteristics. It had the ability to monitor the technical and financial aspects of the artificial lift method. The

technical and financial evaluation of this procedure was carried out using specific computer algorithms. The final results of OPUS were obtained in three stages:

- 1) Introduction of well data into the program
- 2) Data analysis
- 3) Recommendations of experts with technical and economic considerations

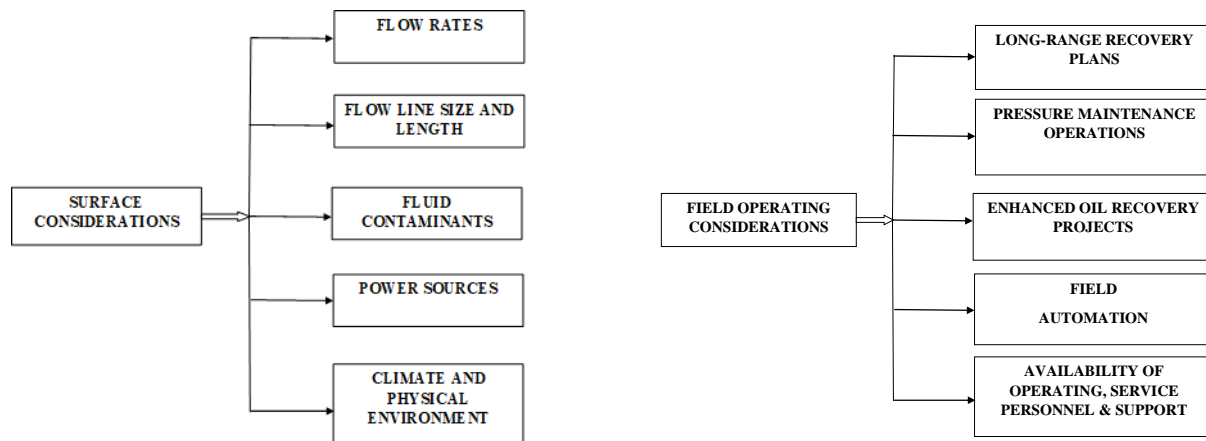
Clegg [7] cited economic factors such as income, maintenance costs and investment as the basis for choosing artificial lift. He believed that the chosen method of artificial lifting could provide the maximum production rate with minimum operating costs. Clegg *et al.* [4] studied the operational and structural characteristic of artificial lift method and classified them into three types based on comparison and development of global capability of artificial lift method.

Espin *et al.* [8] used SEDLA to select artificial lifts. SEDLA was a computer program with the characteristics of an artificial method of investigation. This program includes: Expert modules, design modules and economic modules. Module 1 is a specialized module that includes a knowledge base consisting of human knowledge, accessible theoretical knowledge and calculations of the "general rule" type. Module 2 includes a simulation program and component specifications for all the lifting methods considered. Module 3 is an economic evaluation module that includes a cost database and a cost analysis program that calculates the profitability of the lift.

3. Methodology

This paper adopts the study of some criteria presented in the form of input parameters in accessing and comparing the various types of artificial lift systems mentioned. These selection criteria are classified as follows:

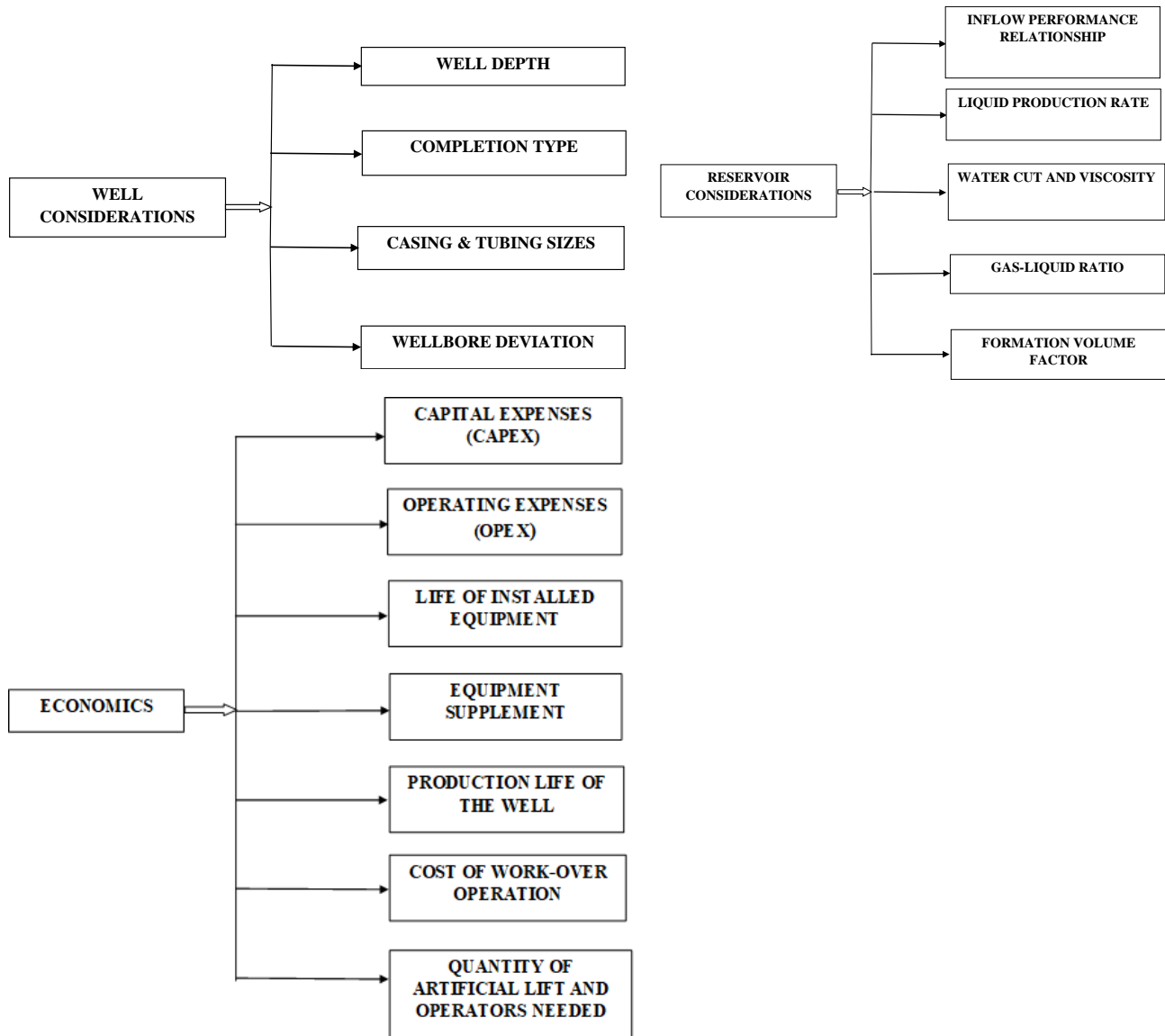
1. Surface conditions
2. Field operating conditions
3. Reservoir Characteristics
4. Well considerations
5. Field location
6. Economics



According to Clegg *et al.* [4], the initial capital costs play an important role in establishing the required artificial lift. However, operating costs are more important than the initial capital costs throughout the entire life cycle of the well. It is important to ensure the installation of reliable equipment, which will lead to a reduction in operating costs and a reduction in production costs. The key issues affecting operating costs are energy efficiency and reliability. Work-over cost depends on the location of the operating area, as well as on the terms of the contract service (which requires high costs for remote areas).

Another important factor affecting operating costs is the number of wells that require the installation of an artificial lift. The number of employers who will need to install and monitor equipment will affect operating costs.

For the purpose of this study, the data were mainly obtained from a review of related literature, all of which were published and unpublished and includes conference paper, journals, seminars and textbooks.



3.1. Method of selection

The study covers the well and reservoir formation characteristics, operating conditions of the well, the location of the deposit and small economic analysis; in achieving the research objective, the range of values was formed in accordance with each parameter to access the artificial lift system excluding the economic analysis.

In this study, about 100 variants of all input parameters for the artificial lift system were used, and it was found that the ratio of the simple probability matrix presented in the table 1 is the optimal artificial lift system.

Table 1. Decision Matrix for ArtLOp

Parameters	Artificial Lift Systems						Probability
	Gas Lift	ESP	SRP	PCP	HP	Total	
Production Rate							
0-1,000	•	•	•	•	•	5	100.00%
1,001-2,000	•	•	•	•	•	5	100.00%
2,001-3,000	•	•	•	•	•	5	100.00%
3,001-4,000	•	•	•	•	•	5	100.00%
4,001-5,000	•	•	•	•		4	80.00%
5,001-10,000	•	•	•			3	60.00%
10,001-15,000	•	•				2	40.00%
15,001-30,000	•	•				2	40.00%
30,001-45,000	•	•				2	40.00%
Above 45,000		•				1	20.00%
Well Depth							
0-2,500	•		•	•	•	4	80.00%
2,501-5,000	•		•	•	•	4	80.00%
5,001-7,500	•		•	•	•	4	80.00%
7,501-10,000	•	•	•		•	4	80.00%
10,001-12,500	•	•	•		•	4	80.00%
12,501-15,000	•	•	•		•	4	80.00%
15,001-17,500		•			•	2	40.00%
17,501-20,000		•				1	20.00%
Above 20,000		•				1	20.00%
Casing Size							
4.500		•			•	2	40.00%
5.000		•			•	2	40.00%
5.500	•	•	•	•	•	5	100.00%
6.625	•	•	•	•	•	5	100.00%
7.000	•	•	•	•	•	5	100.00%
7.625	•	•	•	•	•	5	100.00%
8.625	•	•	•	•	•	5	100.00%
9.625	•	•	•	•	•	5	100.00%
10.625	•	•	•	•	•	5	100.00%
Above 10.625	•	•	•	•	•	5	100.00%
Wellbore Deviation							
0-10	•	•	•	•	•	5	100.00%
11-20	•	•	•	•	•	5	100.00%
21-30	•	•	•	•	•	5	100.00%
31-40	•	•	•	•	•	5	100.00%
41-50	•	•	•	•	•	5	100.00%
51-60	•	•	•	•	•	5	100.00%
61-70	•	•	•	•	•	5	100.00%
71-80		•	•	•	•	4	80.00%
81-90	7.	•	•	•	•	3	60.00%
Temperature							
0-50		•	•	•	•	4	80.00%
51-100		•	•	•	•	4	80.00%
101-150	•	•	•	•	•	5	100.00%
151-200	•	•	•	•	•	5	100.00%
201-250	•				•	4	80.00%

Parameters	Artificial Lift Systems						Probability
	Gas Lift	ESP	SRP	PCP	HP	Total	
251-300	•		•		•	3	60.00%
301-350	•		•		•	3	60.00%
351-400	•		•		•	3	60.00%
401-450	•		•		•	3	60.00%
451-500	•		•		•	3	60.00%
Above 500	•		•			2	40.00%
Flowing Pressure							
Less than 1,000	•	•	•	•	•	5	100.00%
Greater than 1,000	•	•	•	•	•	5	100.00%
Water Cut							
0-10	•	•	•	•	•	5	100.00%
11-20	•	•	•	•	•	5	100.00%
21-30	•	•	•	•	•	5	100.00%
31-40	•	•	•	•	•	5	100.00%
41-50	•	•	•	•	•	5	100.00%
51-60		•	•	•	•	4	80.00%
61-70		•	•	•	•	4	80.00%
71-80		•	•	•	•	4	80.00%
81-90		•	•		•	3	60.00%
91-100		•	•		•	3	60.00%
Fluid Viscosity							
0-20	•	•	•	•	•	5	100.00%
21-40	•		•	•	•	4	80.00%
41-60	•		•	•	•	4	80.00%
61-80	•		•	•	•	4	80.00%
81-100	•		•	•	•	4	80.00%
Above 100	•		•	•		3	60.00%
Fluid Gravity							
0-10				•		1	20.00%
11-20	•		•	•	•	3	80.00%
21-30	•	•	•	•	•	5	100.00%
31-40	•	•	•	•	•	5	100.00%
41-50	•	•	•	•	•	5	100.00%
Above 50	•	•	•	•	•	5	100.00%
GOR							
0-100	•	•	•	•	•	5	100.00%
101-200	•	•	•	•	•	5	100.00%
201-300	•	•	•	•	•	5	100.00%
301-400	•		•	•		3	60.00%
401-500	•					1	20.00%
501-600	•					1	20.00%
Above 600	•					1	20.00%
Sands and Abrasives							
0-10	•	•	•	•	•	5	100.00%
11-20	•			•	•	3	60.00%
21-30	•			•		2	40.00%
31-40	•			•		2	40.00%
41-50	•			•		2	40.00%
Above 50	•					1	20.00%

Parameters	Artificial Lift Systems						Probability
	Gas Lift	ESP	SRP	PCP	HP	Total	
Corrosion Fluid Type							
Carbon dioxide	•				•	2	40.00%
Hydrogen Sulphide	•				•	2	40.00%
None	•	•	•	•	•	5	100.00%
Field Location							
Onshore	•	•	•	•	•	5	100.00%
Offshore	•	•		•	•	4	80.00%
Power Source							
Electricity	•	•		•	•	4	80.00%
Natural Gas	•				•	2	40.00%
Others			•		•	2	40.00%
Fluid Contaminants							
Scales		•				1	20.00%
Paraffin		•				1	20.00%
Salt		•				1	20.00%
None	•	•	•	•	•	5	100.00%
Pressure Maintenance Operations							
Gas Injection	•					1	20.00%
Water Injection	•	•	•	•	•	5	100.00%
Total	80	68	73	67	77		
Probability	80%	68%	73%	67%	77%		

4. Results and discussion

After a careful study of the selection criteria as shown in the table above, a decision matrix was designed as shown in table 1.

4.1. Description of decision matrix

The decision matrix is designed using Microsoft Excel 2007. Each option under each input parameter is represented on the matrix as it is programmed on the software. The bullets in each option for each input parameter signify that the option satisfies the criteria for the corresponding artificial lift system. For instance; the options under the input parameter "Production Rate". Looking at the bullets under the column for gas lift, it fills the options in the column from 30,001 - 45,000 to 0 - 10,000. This means that gas lift as an artificial lift system can only lift fluid volumes not greater than 45,000 bfpd. This same principle applies for the rest of the input parameters and their options.

Calculations

To determine the probability that a particular option will be selected for each artificial lift system: by dividing the total number of artificial lift system that satisfies that criteria to the total number of artificial lift system. Mathematically;

$$P_{os} = \frac{\text{Number of Artificial Lift System that Satisfies the Option}}{\text{Number of Artificial Lift System}} = \frac{P_{AO}}{N_A}, \text{ where:}$$

P_{os} = Probability that an Option will be Selected.

For example, the probability that the option a fluid viscosity of 61-80cp is chosen;

$$P_{os} = \frac{P_{AO}}{N_A} = \frac{3}{5} = 60\%$$

This calculation is repeated for all the options and the result is shown in the last column of the decision matrix.

Next step is to estimate the probability that a particular artificial lift system is selected amongst other artificial lift system. The calculation is done by dividing the total number of options that a particular artificial lift system satisfies by the total number of options. Mathematically;

$$P_{AS} = \frac{\text{Total Number of Options Satisfied}}{\text{Total Number of Options}} = \frac{N_{OS}}{N_O}$$

Let's take for instance, the probability that gas lift as an artificial lift system is selected amongst other artificial lift system.

$$P_{AS} = \frac{N_{OS}}{N_O} = \frac{80}{100} = 80\%$$

This calculation is repeated for all the artificial lift systems and the results are shown in the last row of the decision matrix.

5. Conclusion

Selection of artificial lift system which gives optimum production and economic benefit had been a great challenge in the petroleum industry. This is why an optimum and more suitable technology known as the Gas Lift has been discovered and established which has given rise to better oil recovery results in production over time. Historically, electric submersible pumps (ESP) have been associated with the production of large volumes of liquid; but electric pumps require too many steps for gas treatment and it often loses efficiency.

For gas lifts, the recovery ratio was higher than the recovery rate of the ESP. so an economic assessment was made that the capital cost for ESP was higher than that of gas lift systems. The operating costs of the ESP exceed the operating costs of the gas lift system.

Gas Lift has edge over other artificial lift because it is safer, flexible and reliable. It is 80% effective and efficient to give optimum production. It is highly recommended that Gas Lift should be used in the petroleum industry especially here in Nigeria to improve the production of crude oil to meet the demands of the consumers. On the other hand, it will boost the nation's economy.

Acknowledgement

The authors express their profound and sincere gratitude to Department of Petroleum Engineering, Covenant University, and the entire Management of Covenant University Canaan Land Nigeria; for their support and enabling environment to embark on this study.

References

- [1] Clegg JD, Bucaram SM, Heln J. Recommendations and comparisons for selection of Artificial Lift methods. *J. Petroleum Technol.*, 1993; 45(12): 1128 -1167.
- [2] Schlumberger (1999). Gas lift design and technology. Retrieved from <http://igs.nigc.ir/STANDS/BOOK/Gas-LiftTechnology.pdf> (accessed 9 March 2016).
- [3] Turner RG, Hubbard MG, and Dukler AE. Analysis and prediction of minimum low rate for the continuous removal of liquids from gas wells. *Journal of Petroleum Technology*, 1969: 1475-1482.
- [4] Neely B, Gipson F, Capps B, Clegg J, Wilson P. Selection of Artificial Lift method. Dallas, Texas, SPE#10337, 1981.
- [5] Hwang CL, Yoon K. *Multiple Attribute Decision Making: a state of the art survey*. Springer-Verlog 1981.
- [6] Valentine EP, Hoffman FC. OPUS: An expert adviser for Artificial Lift, IFP (1988) SPE#18184.
- [7] Clegg JD. High-rate Artificial Lift. *J. Petroleum Technol.* SPE#17638 1988.
- [8] Espin DA, Gasbarri S, Chacin JE, Intevep SA. Expert system for selection of optimum Artificial Lift method. Argentina, SPE#26967 1994.

To whom correspondence should be addressed: Dr. Emeka Emmanuel Okoro, Petroleum Engineering Department, Covenant University Ota, Nigeria, emeokaokoro@covenantuniversity.edu.ng

INSTANTANEOUS DETERMINATION OF BASIC RESERVOIR PROPERTIES IN NEAR WELLBORE WATER INJECTION USING ROUTINE INJECTION DATA

Mohammad Shadadeh, Mahdi Zeinali Hasanvand, Hassan Shokrollahzadeh Behbahani

Research Institute of Petroleum Industry, Tehran, Iran

Received February 6, 2018; Accepted April 27, 2018

Abstract

Planning for injection operation and determination of optimum time for acidizing an injection well require knowing the reservoir properties in the near wellbore. Conventional method to determine these properties is using two observation and one injection well, which is require ceasing the injection operation and spending more money and time. Based on performed studies, using daily production and injection data could be a proper solution to reduce expenses.

In this paper, it has been tried to determine essential near wellbore properties such as formation skin, radius of damage and permeability of damage area using daily injection data including: pressure, injection rate and injection time.

A new method to determine reservoir properties around the wellbore was devised by the application of injection process modeling. Finally, the developed method was applied to a real data of a water injection well in one of southern Iranian oil fields. In addition, the estimated data were validated comparing the real injection well conditions.

Keywords: Water Injection; Wellbore skin; Injection Rate; Injection Pressure; Hall plot; Hearn Plot; Injectivity.

1. Introduction

Water injection in different geological layers is aimed to pressure maintenance, EOR or associated produced water disposal [1]. Because of different dissolved solids in injecting water, injection usually encounter challenges. Some challenges include reservoir permeability reduction due to incompatibility between injection water and formation water, formation fracture due to a higher injection pressure than layer fracture pressure, determining maximum injection volumes in a specific formation and determining the injection depth to ensure not blending the injecting water with freshwater resources [2-7]. Due to the high salinity of associated produced water and the presence of radioactive elements in their solutions, environmentally, it is forbidden to release water on ground or to dispose it in rivers [8-9].

In order to timely dispose of producing water from an operation unit and determine the water movement in the injecting formation, it is necessary to know the compatibility of injecting and formation water, the amount and type of salt, and the exact determination of rock formation properties, such as permeability and porosity. In common ways of reservoir properties determination around the wellbore, two injection and monitoring wells are used, additionally it needs to stop injection process, then this takes time and causes extra costs. In addition, determine reservoir and well properties in this method requires bottom hole pressure gauges. Although this method has a great accuracy, it is defective due to the discontinuation of injection and high time consuming and expenses.

Different researchers have provided models and auxiliary diagrams for avoiding the problems of the falloff test by modeling the injecting fluid flow into well, which by their means, without having to discontinue the injection, only by using the basic variables such as the injected fluid volume, the injection time, and the wellhead pressure. These models have the

ability to obtain adequate information about the reservoir condition, skin effect, well injectivity and the presence of fracture around the well. These methods include Hall [10] and Hearn [11-12]

In this paper, it has been tried to investigate essential reservoir properties alongside the accuracy of proposed models by using the injection data and injecting and formation water compatibility, the geological characteristics of the injection well and the data related to injection operation in a real disposal water well, the main reservoir characteristics and skin effect, along with the performance of the proposed models. The defect of the Hearn and Hall methods is the simultaneously being unknown of the reservoir pressure, the damage radius of the well and the permeability around the well, which is resolved in the inventive method.

2. Modeling

2.1. Determination of reservoir properties by Hall method:

In the injection process, determination of the injectivity of the well is essential for determining the flow rate and injection pressure and the injection schedule. In case of reduction of the injectivity of well, determination of the amount of well damage is done through two falloff tests or direct method. The falloff test method compared to the direct method is time-consuming and costly and requires stopping of injection in both wells. In the direct method, the amount and the nature of injectivity drop is determined only by using the injection data of the well, without the need for an observation well.

Hall [10] presented a graph for analyzing the injectivity of wells. This graph, which is to be made on a monthly basis, includes the pressure at the time of injection versus the total injected volume in the same period of time. The analysis of the Hall graph before and after the well stimulation shows the amount of success of this operation. Generally, increasing the gradient of the curve shows a decrease in the injectivity. According to the Darcy relationship, in the cylindrical coordinates, the slope of pressure- versus rate will be equal to:

$$m = \frac{\mu_w B_w \ln(r_e / r_w)}{0.00707 k_w h} \quad (1)$$

The most important assumptions of this relationship are the constant pressure of the reservoir and the radius of injection. The concept of transmissibility is used to determine the amount of change in the injectivity and the effect of the skin. According to the definition of transmissibility:

$$Tm = \frac{k_w h}{\mu_w} \propto \frac{1}{m} \quad (2)$$

Based on this relation, with respect to the unit change from psi-month per barrel (P/Q) to mili Darcy-foot per centipoise (Kh/μ), the coefficient 29.2 is added to the relationship and the relation converted into the following equation:

$$Tm = \frac{4.884 B_w \ln(r_e / r_w)}{m} \quad (3)$$

Therefore, if the slope increases in the Hall diagram, there has indeed been a decrease in permeability in the porous medium. By having two different transmissibility values, mathematical analysis of relationships can be used to calculate the amount of the skin around the wellbore. Assume that the well has a skin and its permeability has decreased, in this case the average permeability will be equal to:

$$k_{avg} = \frac{k_a k_e \ln(r_e / r_w)}{k_a \ln(r_e / r_a) + k_e \ln(r_a / r_w)} \quad (4)$$

By using the definition of transmissibility in the above relation, and assuming that the reservoir thickness and viscosity of the fluid are constant over the radius of injection, we will have:

$$Tm_{avg} = Tm_2 = \frac{Tm_a Tm_1 \ln(r_e / r_w)}{Tm_a \ln(r_e / r_a) + Tm_1 \ln(r_a / r_w)} \quad (5)$$

From the above relation, assuming to have the value of damage radius, which is often about 3 feet [14]), the amount of Tm_a in the damage area is obtained. By having the value of Tm_a , the important variables for the injectivity, such as skin value, pressure drop in the skin region, damage ratio, Flow Efficiency, Damage Factor and minimum increase in the injection, are obtained from the following relationships:

$$S = \frac{(k_e - k_a)}{k_a} \ln(r_a / r_w) = \frac{(Tm_1 - Tm_a)}{Tm_a} \ln(r_a / r_w) \quad (6a)$$

$$\Delta P_a = \frac{q_{sc2} B_w S}{0.00707 Tm_1} \quad (6b)$$

$$P_e = P_{w1} - \frac{q_{sc2} B_w S}{0.00707 Tm_1} \quad (6c)$$

$$DR = \frac{P_e - P_w}{P_e - P_w - \Delta P_a} \quad (6d)$$

$$FE = 1/DR \quad (6e)$$

$$DF = 1 - FE \quad (6f)$$

$$I_{sr} = DR(q_{sc2}) \quad (6g)$$

Daniel Hawe [13] showed that the results obtained from the Hall diagram were more reliable than the results of the falloff test. The Hall plot is originally presented for the single-phase mode (water) under constant conditions and cylindrical flow of Newtonian fluid. This method is used assuming that the condition is stable, and since the data are investigated at weekly and monthly period, it is possible to determine the variation of the injection variables over time. Data acquisition is simple in the Hall method, and the only data that are used include the total injected volume and the injection pressure, which should eventually be converted to the bottom hole pressure. The dependence of the slope of the graph on both the skin factor (S) and transmissibility ($k_w h / \mu_w$) is the most important drawback of the Hall diagram method, which, to overcome the obstacle, the value of the skin radius is determined using estimate and error. (Radius ranging from 1 to 3 feet) [14].

2.2. Determination of reservoir properties by Hearn method:

This method is presented to estimate the permeability of the reservoir in the process of water injection into an oil layer. In this method, it is assumed that there is no gas phase in the porous medium, and the front between oil and water is piston-like. The Hearn method is actually a Muscat [15] corrected method for calculating a constant pressure well. Accordingly, the fluid flow relation around the wellhead is as follows:

$$q_w = \frac{0.00707 k_w h (P_w - P_e)}{\mu_w B_w (\ln(r_o / r_a) + M \ln(r_e / r_o))} \quad (7)$$

In which, $M = (k_w \mu_o / k_o \mu_w)$

The above equation is slightly changed to the following relation where the values of r_o and r_e are obtained using a mass balance.

$$q_w = \frac{0.01414 k_w h (P_w - P_e)}{\mu_w B_w (\ln(r_o^2 / r_a^2) + M \ln(r_e^2 / r_o^2))} \quad (8)$$

In which, $r_o^2 = FW_i$, $r_e^2 = CW_i$, $F = (5.615 / \pi h) \times \phi (\bar{S}_{wBt} - S_{wc})$ and $C = (5.615 / \pi h) \times \phi (1 - S_g - S_{wc})$

By manipulating the above relations we get the following relation

$$\frac{\Delta P}{q_w} = a \ln W_i + a \left(\ln \frac{F}{r_a^2} + M \ln \frac{C}{F} \right) a = \frac{\mu_w B_w}{0.01414 k_w h} \quad (9)$$

By plotting the reverse of injectivity versus logarithm of total injected fluid, we expect the

straight line with slope of a and intercept of $\left(\ln \frac{F}{r_a^2} + M \ln \frac{C}{F} \right)$, which is the same as the Hearn graph. Since, in the above-mentioned relation, mobility and saturation percentages are only present in the intercept part, the actual permeability of the reservoir can be calculated using the slope value.

In related industrial reports, four graphs are presented: 1) Flow rate and injection pressure versus time; 2) Hall diagrams; 3) Hearn diagrams; and 4) Injection rate and injectivity versus time. By analyzing the obtained diagrams, near wellbore reservoir properties and the existence of fracture are determined [12].

2.3. Innovative method

The problems of the Hall and Hearn method is that the number of unknown variables is greater than the equations. For this reason, in order to solve the relations and obtain the necessary values, some preset values should be considered using the initial guesses.

For example, in Hall's relation, the radius of damage is considered to be between 1 and 3 feet, and by assuming the value of this parameter, the value of the other variables (such as permeability, damage factor, etc.) are determined by solving the equations. In these methods, the amount of damage (S), the radius of damage (r_a), the pressure of the formation at the boundary (P_e) and the permeability of the reservoir (k_w) is unknown. Having three equations of skin (6a), slope of Hall plot (5), slope of Hearn plot (9) one more equation is needed to obtain all parameter without need to guess a value for damage radius. The missing equation is introduced in this innovative method.

As shown in Equation 9, the intercept of Hearn plot is a function of the dynamic and static properties of the reservoir around the well opening. This value is equal to:

$$a \left(\ln \frac{F}{r_a^2} + M \ln \frac{C}{F} \right) = a \left(\ln \frac{(5.615/\pi h) \times \phi (\bar{S}_{wBt} - S_{wc})}{r_a^2} + (k_w \mu_o / k_o \mu_w) \ln \frac{(1 - S_g - S_{wc})}{(\bar{S}_{wBt} - S_{wc})} \right) \quad (10)$$

Therefore, if we sure that no fracture has been created in the formation during the injection and acidizing process (the near wellbore static properties of the formation remain unchanged), the fourth equation can be calculated by subtracting the intercept of Hearn diagram before and after operation. Real data analysis shows that the slope of the Hearn graph is the same before and after the operation. Equation 10 is, in fact, the additional equation that can equate the multiplicity of equations and the unknown variables. Therefore, there is no need for the initial guess to calculate other variables. The method will be explained more in the follow.

3. Water injection case study

In this case study, associated producing water from Fahliyan Formation in one of Iranian southern oilfields is injected into Asmari Formation of the oilfield. The results of the pressure test in this formation indicate that in depth of 1443-1490 meters, the formation pressure changes from 2164 psi to 2241 psi, and this pressure gradient this layer confirms the presence of formation water.

Investigation of the chemical properties of injecting water and formation water as well as chemical equilibrium calculations show that Asmari Formation water has a high dissolved solid content (240 g/L) which is mainly made up from sodium and calcium chloride. The water produced from the Fahliyan reservoir is less salty than the Asmari Formation water. The solids

content of this formation in the two sub-layers is 75 and 150 g/L, which is mainly made up from sodium chloride and calcium chloride, respectively.

The compatibility analysis has been performed by SOLMINEQ88 PC / Shell software. In this analysis different ratios of Fahlyan member 2 and 3 formation water and Karun River as injecting water and Asmari formation water as target for injection has been considered. The results of the analysis show that two salt precipitation of barium sulfate and carbonate calcium has a chance to be formed in all water combination. Calcium carbonate (aragonite and calcite) is the most considerable salt precipitation in all water combinations. Fahlyan member 2 formation water at surface facilities and downhole will precipitate moderate amount of barium sulfate and calcium carbonate and Fahlyan member 3 formation water will precipitate large amount of calcium carbonate.

The formation of calcite deposition depends on the amount of alkaline ions in the water. By reducing the amount of these ions, the amount of carbonate deposits decreases. To this end, the continuous addition of alkali-reducing chemicals to surface facilities and downhole wells can reduce the sedimentation process.

Table 1. The highest amount of salt formed due to the incompatibility of injection and formation water (g/m³)

Chemical deposition	Water blend in surface facilities at 25°C and 73 Psi		Water blend in wellbore at 63°C and 2140 Psi		
	Karun River + Layer 2 Fahlyan	Karun River + Layer 3 Fahlyan	Asmari + Layer 2 Fahlyan	Asmari + Layer 3 Fahlyan	Asmari + Karun river
Barium sulfate (barite)	34	0	30	0	0
Calcium carbonate (aragonite and calcite)	26	700	20	900	443
Calcium sulfate (Anhydrite)	0	0	0	0	0
Strontium sulfate (Celestine)	0	0	0	0	0

To reduce damage around the wellbore during water disposal due to sedimentation, the process of water treatment is used before injection of water. The greater the amount of salt removal during this process, the lower the deposit in the reservoir conditions. However, due to the incompatibility of injected water and the formation water, damage in the injection wellbore is inevitable. During two years of water injection in Asmari formation four operation of acid treatment has been performed. To determine the properties of the formation during the water injection process and the success of acidizing operations, Hall and Hearn chart along with the history of water injections over two years has been plotted. In Figures 1 to 3, these operations are marked with a black, green, red and blue arrow line.

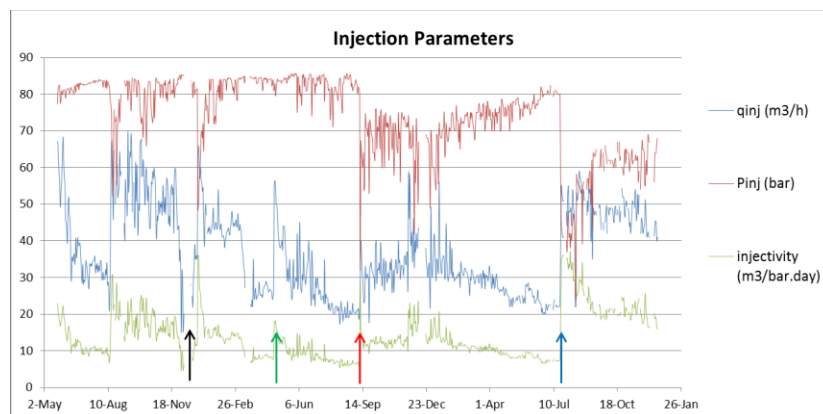


Figure 1. Water injection rate, injection pressure, and well injectivity over time

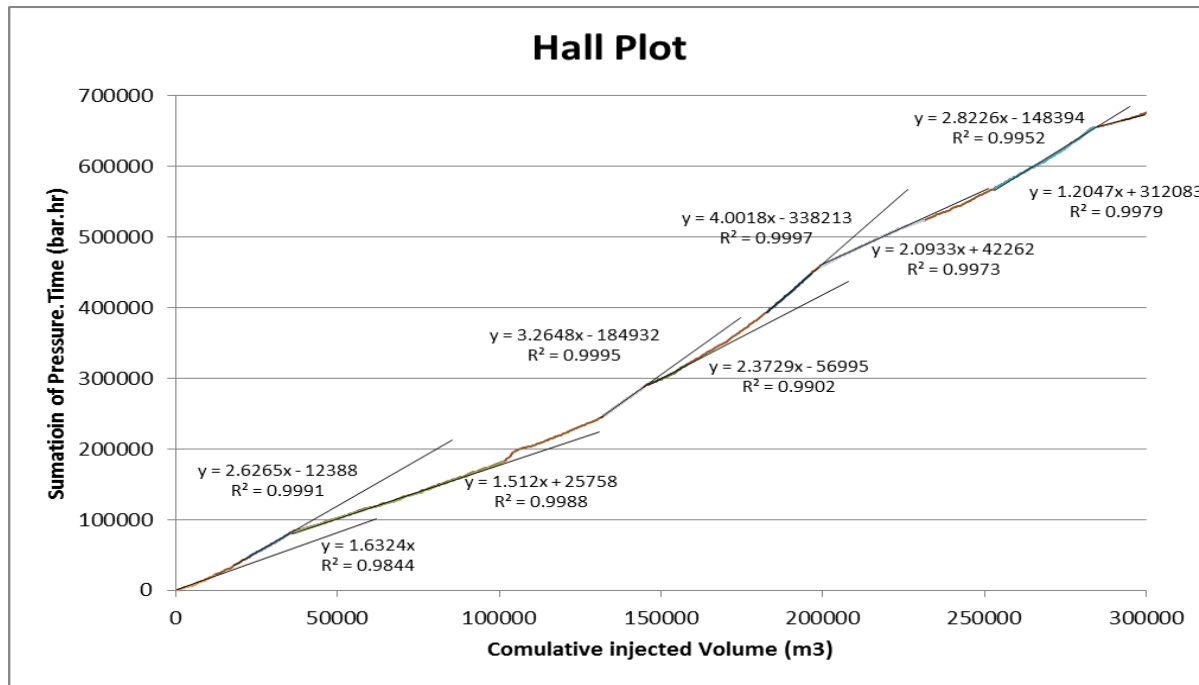


Figure 2. Hall plot for two years of injectable data

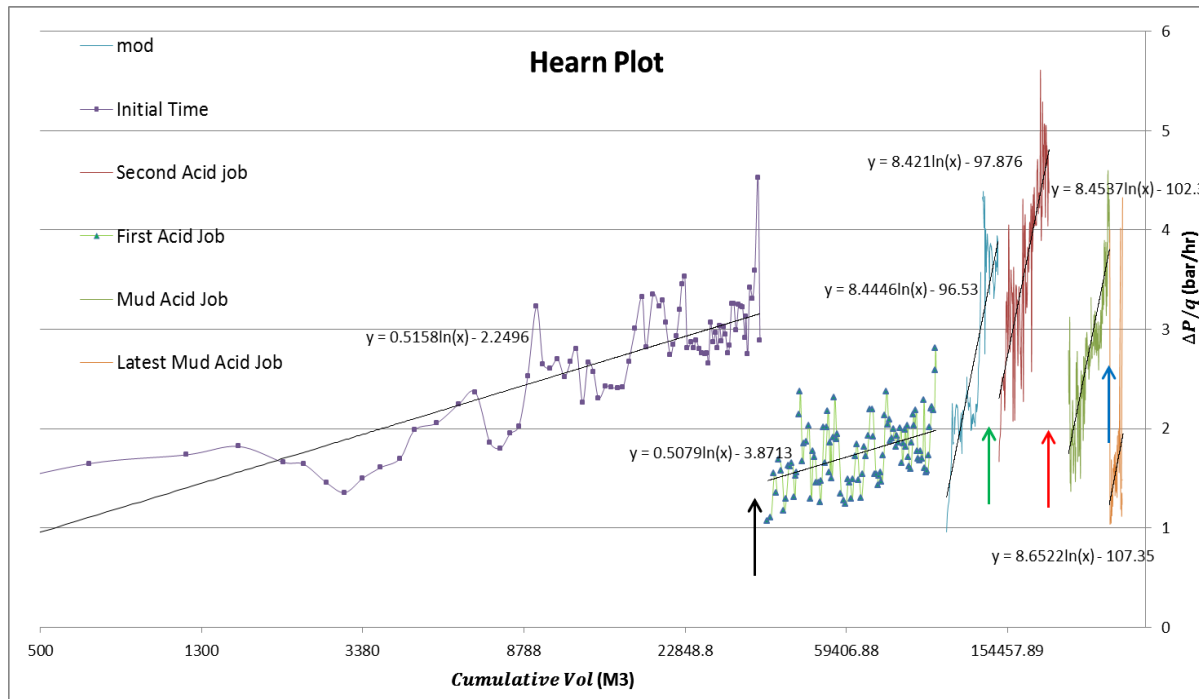


Figure 3. Hearn plot for two years of injectable data

According to the lines obtained from Hall and Hearn plots, the following table is presented to analyze the success of acidizing and determining the permeability of the reservoir.

Table 2. The results obtained from Hall and Hearn charts, include slope and intercepts

Acidizing operation #	Hall plot		Hearn plot		
	Slope before operation	Slope after operation	Slope before operation	Slope after operation	Interception difference
1	2.6	1.5	0.5	0.5	1.6-
2	3.2	2.3	8.4	8.4	1.3-
3	4	2	8.4	8.4	5.5-
4	2.8	1.2	8.4	8.6	5-

Regarding lower injection pressure compared to fracture pressure, the intercept change in Hearn plot after acidizing would be due to Skin removal in near wellbore which has a similar effect as fracture.

To determine precisely the amount of equivalent radius r_a and permeability near wellbore, the Hearn and Hall equations simultaneously is used. For this purpose, we obtain the value of the difference in intercept of the two graphs.

Using the equation 10 in water disposal wells, since both of the initial and injecting fluid are water, then mobility ratio M could be considered equal to one. In this case, given the fact that the coefficients F and C are constant before and after the acidizing operation (assuming complete removal of damage during the acid treatment operation), the difference in intercept will be equal to:

$$\text{Difference in intercept} = a \ln \frac{r_w^2}{r_a^2} = 2 a \ln \frac{r_w}{r_a} \quad (11)$$

The amount of viscosity and formation volume factor at the reservoir conditions are 0.48 cP and 1.01, in the studied well, the thickness of the formation is 36 ft. Using the equation 9 and having the slope 8.4 for Hearn plot, the mean permeability of the reservoir is equal to 882 md. Now, having the unknown value of the Hall relationship, i.e. the damage radius, we can calculate the skin coefficient and the permeability of the reservoir using equations 6a and 9. Based on this, properties around the wells, including permeability, skin, and damage radius during different operations are presented in Table 3.

The important point in this approach is that since the number of variables and the number of equations are equal, the obtained values are definite, and in fact, they can be considered as actual results of well testing. In Hall and Hearn methods, due to the assumption of some variables, the results should be verified using other methods, but in the new method, since none of the fundamental variables are assumed, the results are reliable. However, to verify this claim, well tests are helpful and can confirm the results.

Table 3. Near wellbore properties during different acidizing operations in the studied injection well

Acidizing operation #	Ln(rw/ra)	S	Ka (md)
1	0.8324	0.3522	682.06
2	0.6763	0.1902	781.46
3	2.8613	1.4307	173.15
4	2.6012	1.4864	181.23

4. Conclusion

In this paper, a direct method to determine reservoir properties such as reservoir pressure and reservoir permeability and near wellbore properties such as skin, damage radius and permeability of damage area has been presented. These properties were determined using only daily injection data such as pressure, flow rate and time. As a case study, daily injection data of one of the water disposal wells was investigated. The results show the success of operation of acidizing in removing salt deposition and treatment of near wellbore damage. The study and analysis of daily injection data by this method can show the behavior of sediments in injected water in damaging the wells. The information obtained from the direct method has

a high accuracy, and requires minimum time and cost, so this method is preferred to the traditional falloff test method.

In this method, there is no need to stop the injection for well testing, and only using the injection data the dynamic properties of the reservoir and near wellbore could be calculated. Unlike previous methods, which use guessing and error method to determining the dynamic properties near wellbore, because of providing an additional equation in the presented method none of the variables is previously assumed.

This results in precision and the conversion of this method into a permanent well test method. Another result from this study is the use of gas injection data in hydrocarbon reservoirs to determine the Instantaneous properties of the reservoir. Implementing this method for gas injection wells requires a more detailed study of well testing in gas injection wells, that will be tried to be investigated in the in a separate paper in near future.

References

- [1] Paige RW and Murray LR. Re-injection of produced water - Field experience and current understanding. Presented at the Rock Mechanics in Petroleum Engineering, Delft, Netherlands, 29-31 August 1994. SPE-28121-MS.
- [2] Barkman JH, Davidson DH. Measuring water quality and predicting well impairment. *Journal of Petroleum Technology*, 1972; 24(07): 865-873.
- [3] Eylander JGR. (1988). Suspended Solids Specifications for Water Injection from Core flood Tests. *SPE Res Eng.*, 1988; 3 (4): 1287-1294. SPE-16256-PA.
- [4] Sharma MM, Pang S, Wennberg KE, Morgenthaler LN. Injectivity decline in water-injection wells: an offshore Gulf of Mexico case study. *SPE Production & Facilities*, 2000; 15(01): 6-13.
- [5] van Oort E, van Velzen JFG, Leerlooijer K. Impairment by suspended solids invasion: testing and prediction. *SPE Production & Facilities*, 1993; 8(03): 178-184.
- [6] Wennberg KE, Sharma MM. Determination of the filtration coefficient and the transition time for water injection wells. In *SPE European Formation Damage Conference*. Society of Petroleum Engineers, 1997, January.
- [7] Shutong P, Sharma MM. A model for predicting injectivity decline in water-injection wells. *SPE Formation Evaluation*, 1997; 12(03): 194-201.
- [8] Christie C. Disposal of produced water from oil & gas exploration. Masters project. Duke University Durham 2012, NC
- [9] Pichtel J. (2016). Oil and gas production wastewater: Soil contamination and pollution prevention. *Applied and Environmental Soil Science*, 2016.
- [10] Hall HN. How to analyze waterflood injection well performance. *World Oil*, 1963; 157(5): 128-33.
- [11] Moffitt PD, Menzie DE. Well injection tests of non-newtonian fluids. In *SPE rocky mountain regional meeting* 1978, January. Society of Petroleum Engineers.
- [12] Jarrell PM, Stein MH. Maximizing Injection Rates in Wells Recently Converted to Injection Using Hearn and Hall Plots. In *SPE Production Operations Symposium*. Society of Petroleum Engineers 1991, January.
- [13] Hawe DE. Direct Approach Through Hall Plot Evaluation Improves The Accuracy Of Formation Damage Calculations And Eliminates Pressure Fall-Off Testing (1976).
- [14] Buell RS, Kazemi H, Poettmann FH. Analyzing injectivity of polymer solutions with the Hall plot. *SPE Reservoir Engineering*, 1990; 5(01): 41-46.
- [15] Muskat M. Physical Principles of Oil Production. McGraw-Hill Book Co. Inc., New York, 1949, pp.682-686.

To whom correspondence should be addressed: Dr. Mahdi Zeinali Hasanvand, Research Institute of Petroleum Industry, Tehran, Iran, hasanvand@put.ac.ir

LITHOLOGICAL VARIATIONS IN BLACK SHALES AND MUDSTONE FORMATIONS OF CENTRAL SARAWAK, MALAYSIA

Walaa Elnasir Ibrahim*, Abdul Ghani MD Rafeek and Ahmed Mohamed Ahmed Salim

Universiti Teknologi PETRONAS, Department of Geoscience, Perak Darul Ridzuan, 32610 Seri Iskandar, Tronoh- Malaysia

Received February 13, 2018; Accepted April 27, 2018

Abstract

This paper examines the Cretaceous – Upper Pliocene shale and mudstone outcrops in Central Sarawak. Related geological studies focused basically on sandstone and coals of Sarawak Basin, with no comprehensive outcrop study on lithological variations in the black shales and mudstone formations. Detailed lithological variations of these formations will allow us discretize potential shale gas intervals. Therefore, the aim of this study is to investigate the field geological characteristics of the Black shales and mudstone formations of Central Sarawak by using outcrop description, sedimentary log analysis, spectral gamma ray (SGR) data and geochemical characteristics (TOC %) of the selected mudstones and black shales. The study covers Nyalau, Tatau, Begrih, Liang and Belaga formations. Representative samples of the formations were subjected to detailed description in terms of lithology, structures and stratigraphy. Features such as laminations, sandstone intercalations, coal lenses, iron nodules, phyllite inclusions and fault structures were identified in the black shale and mudstone. The lowest U (ppm) was recorded for Belaga Formation, which can be attributed to the low grade metamorphism of the Formation, whereas the higher U (ppm) in Tatau and other formations is possibly due to their relatively higher clay content. The TOC values for all formations varied from 0.8% to 3.17%, suggesting they have fair to good hydrocarbon generative potential.

Keywords: Geological; Black shale; Mudstone; Central Sarawak.

1. Introduction

Shale is a fine-grained (grain size less than 4 microns in diameter) clastic sedimentary rock composed of mud and tiny fragments (silt-sized particles) of other minerals, particularly quartz and calcite [1]. Shale is distinguished by its fissility, which is the ability of a rock to break along parallel bedding or thin laminae less than one centimetre in thickness [2]. However, fissility is absent in mudstones [2-3]. Shale gas is a natural unconventional gas produced in shale rocks rich in organic matter [4]. The shale gas can be stored via two principal ways: (1) as chemically and/or physically adsorbed gas to/or within organic matter, and (2) as free gas in pore space and/or fractures [5].

A short field trip was carried out to study outcrops of black shales and mudstones in Central Sarawak. The study area covers Nyalau, Tatau, Begrih, Liang and Belaga formations in central Sarawak, Malaysia (Figures 1&2). The Sarawak Basin is considered Late Eocene to Recent in age [6]. It is a foreland basin developed from the collision of the Luconia block and West Borneo basement during Eocene times [7]. Basin modelling suggest a strike –slip origin due to the rapid subsidence in the early stages during Oligocene [8].

Sarawak Basin has a wide predominance of shale outcrops. However, previous studies have indicated that the source beds for hydrocarbon in Sarawak basin are coals and organic-rich clays of Oligocene to Lower Miocene age [9]. Rocks in the study area are considered the onshore analogue of the hydrocarbon-rich, offshore Balingian Province [10-11]. The rocks in the

area consists mainly of sandstone, mudstone and shale. The rock formations are Mesozoic to Cenozoic in age [12].

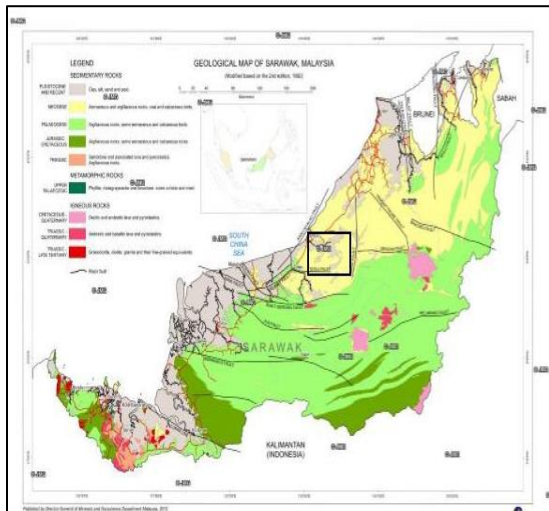


Figure 1. Location map of the study area [6]



Figure 2. Location map of the formations

Zin [13] discussed the tertiary tectonics and sedimentation history of Sarawak Basin. The Tatau Formation consists of a succession of sandstone, siltstone and shales with intercalations of marls, limestones and locally developed conglomerates. The sediments of this formation were deposited as submarine fan and slope deposits during the late Eocene-Oligocene times. The Liang Formation consists of shale, sandstone, conglomerates and abundant lignite, which were deposited during Middle Miocene to Upper Miocene in predominantly coastal plain with some influences of shallow marine deposition [13]. Nyalau Formation is a thick succession of friable sandstone, laminated clay, and coal seams.

Furthermore, Bakar, Madon *et al.* [15] documented the different facies types in deep-marine rocks of the Belaga Formation (Cretaceous-Eocene) in the Sibu-Tatau area, Sarawak, aged from Late Cretaceous to late Eocene. The lithology of the Belaga Formation consists of thin to thick, fine to medium grain interbedded bedded sandstone with argillaceous rocks, mudstone facies with dark grey carbonaceous shale intercalated with fine grained silty sand along Bintulu Sibu road [15-16]. Recently, Siddiqui, Rahman *et al.* [14] studied the textural characteristics of shallow marine sandstone (well-exposed outcrops) of the Nyalau Formation (Oligocene-Middle Miocene), Bintulu area, Sarawak. The sandstone layers of Miocene Nyalau Formation are 4.5-9 m thick and alternated with soft carbonaceous clays [14].

However, the above mentioned studies focused ONLY on sandstone. Moreover, there is no comprehensive outcrop study on lithological variations in black shales and mudstone formations of Sarawak Basin. Detailed study of the lithological variations of these formations will allow us discretize potential gas shale intervals. This current study employs the use of outcrop description, sedimentary logs analysis and spectral gamma ray data.

2. Materials and methods

Core and hand specimens of thirty two onshore samples were collected from Central Sarawak, Bintulu and Mukah city. The study focused on shale and mudstone samples from 19 locations. 13 shale and 19 mudstone samples were obtained from different formations (Table 1). Spectral gamma ray (SGR) readings of the outcrop were taken, as shown in Figure 3.

TOC analysis was carried out on powders of 6 onshore samples (labelled S1- S6) from different outcrop locations in central Sarawak formations. Total organic carbon (TOC%) measurement was carried out using the direct method proposed in an earlier study [17]. The weighed crushed samples were treated with 10% hydrochloric acid (HCl) to remove the inor-

ganic carbon. Carbonate minerals were also removed from the clays using HCl acid. Organic carbon content was reported on a dry weight basis [17].



Figure 3. Spectral Gamma Ray (SGR) reading of the outcrop

3. Results and discussion

3.1. Outcrop description

3.1.1. Nyalau Formation

Three outcrops of Nyalau Formation (Oligocene–Middle Miocene) are located at different sites in Bintulu area, Sarawak. The location coordinates of the outcrops range between Longitudes E 113° 05' 28.8" - E 113° 05' 51. 0" and Latitudes N 03° 09' 24. 1" - N 03° 11' 34.1". It consists of mudstones with iron nodules (Figure 4) and coal lenses (Figure 5), ferruginous reddish fine sandstone intercalated with mudstones, shale intercalated with thin layers of sandstones (Figure 6), fine to medium sandstones, sandy mudstones and laminated shale (Figure 7).



Fig.4. Mudstone with iron nodules from NY1-A outcrop



Figure 5. Mudstone with coal lenses from NY1-A outcrop

3.1.2. Tatau Formation

Four outcrops of the Tatau formation are located at different sites in Kampung Tatau Baru. The location coordinates of the outcrops range between Longitudes E 112° 50' 22.6" - E 112° 54' 40.7" and Latitudes N 02° 52' 18.6"- N 02° 59' 30.1". The lithology consists of mudstone, laminated mudstone interbedded with sandstone (Figure 8), fine sandstone interbedded with shale (Figure 9) and coal lenses (Figure 10).

3.1.3. Begrih Formation

There are three outcrops of Begrih Formation located at different sites. The location coordinates of the outcrops range between Longitudes E 112° 20' 23.0"- E 112° 20' 36.5" and Latitudes N 02° 45'23.7"- N 02° 49'44.5". The lithology of this outcrops consists of highly weathered mudstones interbedded with coal layers, gravel sandstones and fine sandstones (Figure 11).

Table 1 Number of shale and mudstone samples in the study area

Formation	Number of samples		
	Shale	Mudstones	Total
Nyalau Formation	3	6	9
Tatau Formation	3	6	9
Begrih Formation	0	3	3
Liang Formation	1	3	4
Belaga Formation	6	1	7
Grand Total	13	19	32



Figure 6. Shale intercalated with thin layers of sandstone from NY-2 outcrop

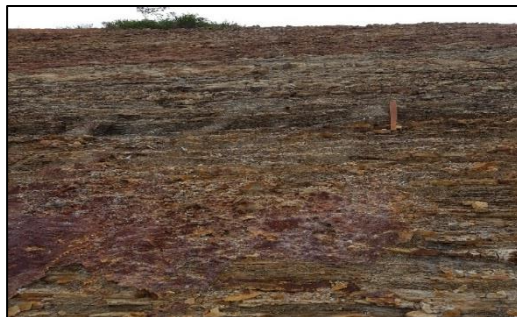


Figure 7. laminated shale formation from NY-2 outcrop



Figure 8. Laminated mudstone (red arrow) interbedded with sandstone (black arrow) from TA-2 Outcrop



Figure 9. Sandstones (red arrow) interbedded with shale (black arrow) from TA-3 Outcrop



Figure 10. Fine sandstone with coal lenses from TA-3 Outcrop



Figure 11. Mudstones (black arrow) with sandstone (red arrow) from BEG-3 outcrop

3.1.4. Liang Formation

Three outcrops of Liang Formation were identified at different locations. The location coordinates of the outcrops range between Longitudes E 112° 20' 16.0"- E 112° 20'43.4" and Latitudes N 02° 36'04.2"- N 02° 38'02.9". The lithology of the outcrop consists of shales, sandy mudstones and dark grey mudstones (Figure 12).

3.1.5. Belaga Formations

Six outcrops of Belaga Formation were identified at different locations. The location coordinates of the outcrops range between Longitudes E 112° 20' 16.0"- E 112° 20'43.4" and Latitudes N 02° 36'04.2"- N 02° 38'02.9". The lithology of the outcrops consists of dark grey

shale (example for sedimentological log Figure 15), highly fractured shale with quartz and phyllite inclusions (Figure 13) and lateral variation of black shales to sandstones to shales. Quartz veins were identified, indicating the outcrop is faulted. Another identified faulting structure is the alignment of the shale layer and sandstones at the same depth (Figure 14).

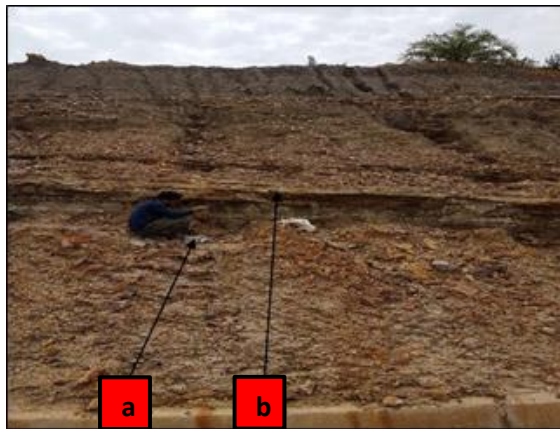


Figure 12. [a] Shale, and [b] sandy mudstones LI-1 outcrop



Fig. 13. Highly fractured shale with quartz and phyllite inclusions



Fig. 14. Fault structure indicated by the alignment of shale and sandstone at the same depth from BEL-3 outcrop

3.2. Uranium concentration

Natural gamma radiation provides information on the composition and lithology of a Formation. The spectral gamma-ray activity concentrations (uranium (U/ ppm) of the shale and mudstone outcrops of different formations are shown in Table 2. The uranium concentration in Nyalau Formation range from 12.87 - 18.55 ppm with an average of 16.12 ppm. Meanwhile, the Uranium concentration (ppm) of Tatau Formation range from 12.54 - 22.56 ppm with an average of 17.17 ppm. The uranium concentration in Begrih Formation ranges between 12.45-13.74 ppm with an average of 13.14 ppm. The uranium concentrations in Liang Formation vary between 10.34 - 14.60 ppm with an average of 12.46 ppm, whereas Belaga Formation exhibited a wider range between 2.49-19.21 ppm, with an average of 10.46 ppm. The lowest U/ ppm value was recorded for Belaga Formation, which can be attributed to the low grade metamorphism of the Formation, whereas the higher U (ppm) in Tatau and other formations is possibly due to their relatively higher clay content.

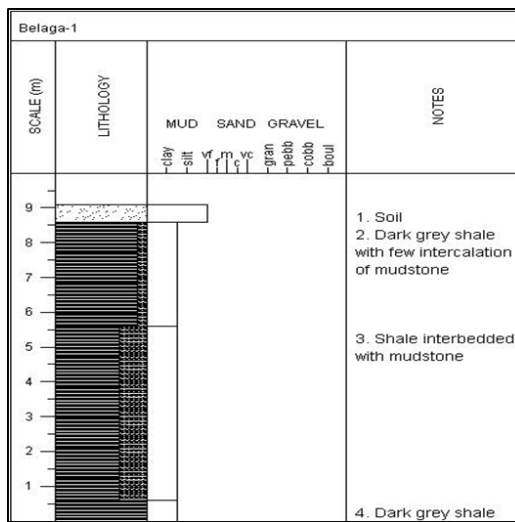


Figure 15. Sedimentological log for Belaga-1

Table 2. Uranium concentration of shale and mudstone in study area

Sample ID	Lithology	U/ppm	Sample ID	Lithology	U/ppm
NY1A-1	Mudstone	17.99	TA4-1	Shale	20.80
NY1A-2	Shale	18.27	TA4-2	Mudstone	15.88
NY1B-1	Shale	17.45	BEG-1	Mudstone	12.45
NY1B-2	Mudstone	18.55	BEG-2	Mudstone	13.23
NY1B-3	Mudstone	14.84	BEG-3	Mudstone	13.74
NY1B-4	Mudstone	12.87	LI1-1	Shale	12.91
NY1B-5	Mudstone	16.00	LI1-2	Mudstone	12.00
NY2-1	Shale	14.73	LI-3	Mudstone	14.60
NY2-2	Shale	14.41	BEL-1	Shale	3.79
TA1-1	Shale	13.00	BEL-2	Shale	2.49
TA1-2	Mudstone	12.65	BEL-3	Shale	4.73
TA-2	Mudstone	12.54	BEL4-1	Mudstone	11.62
TA3-1	Mudstone	19.48	BEL4-2	Shale	16.33
TA3-2	Shale	22.56	BEL5-A	Shale	15.02
TA3-3	Mudstone	17.37	BEL5-B	Shale	19.21
TA3-4	Mudstone	20.26			

3.3. Total Organic Carbon (TOC) % Analysis

The TOC values range from 0.8- 3.17 %, as shown in Table 3. Sample S1 (Begrih-1Formation) exhibited the highest TOC (3.17%), while S3 (Nyalau-1 Formation) has the least TOC (0.8%), indicating the shale and mudstone samples have fair to good hydrocarbon generative potential [18]. On the other hand, the Total carbon (TC) values range from 1.6 to 4.8% (Table 3). Sample S2 (Tatau-2 Formation) showed the highest TC of 4.8%, while S5 (Nyalau-4 Formation) exhibited the least TC (1.6%).

Table 3. TOC % and TC % values from study area

Formation	Lithology	Sample ID	TOC %	TC %
Begrih-1Formation	Shale	S1	3.17	3.19
Tatau-2 Formation	Mudstone	S2	1.2	4.8
Nyalau-1 Formation	Mudstone	S3	0.8	6.0
Belaga Formation	Shale	S4	1.1	3.3
Nyalau-4 Formation	Mudstone	S5	1.5	1.6
Nyalau-3 Formation	Mudstone	S6	1.3	1.7

4. Conclusion

Representative samples of various formations of mudstone and black shale were subjected to detailed description in terms of lithology, sedimentary structures and stratigraphy to improve the geological understanding of the area. Features such as laminations, sandstone intercalations, coal lenses, iron nodules, phyllite inclusions and fault structures were identified in the shale and mudstone. The lowest U (ppm) was recorded for Belaga Formation, which can be attributed to the low grade metamorphism of the Formation, whereas the higher U (ppm) in Tatau and other formations is possibly due to their relatively higher clay content. Based on the TOC% values from different formations (0.8-3.17%), this study predicts the black shale of the study area is a potential unconventional source of energy.

Acknowledgments

We thank Universiti Teknologi PETRONAS for providing the Graduate Research Assistantship Scheme (GRA) and shale gas grant.

References

- [1] Passey KMBQR, Esch W, Klimentidis R, and S. Sinha From Oil-Prone Source Rock to Gas-Producing Shale Reservoir – Geologic and Petrophysical Characterization of Unconventional Shale-Gas Reservoirs. Presented at the CPS/SPE International Oil & Gas Conference and Exhibition in China held in Beijing, China, China, 2010.
- [2] Blatt H, Tracy R, and Owens B. Petrology: igneous, sedimentary, and metamorphic. Macmillan. 2006.
- [3] Tucker M. Sedimentary petrology, an introduction to the origin of sedimentary rocks. Blackwells," ed: Oxford, RU, 1991.
- [4] Perry K, Lee J. Unconventional Gas Reservoirs—Tight Gas, Coal Seams, and Shales. [Working Documents of the NPC Global Oil and Gas Study]. 1-17. http://www.npc.org/Study_Topic_Papers/29-TTG-Unconventional-Gas.pdf.
- [5] Coveney R. Sphalerite concentrations in mid-continent Pennsylvanian black shales of Missouri and Kansas," Economic Geology, 1979; 74: 131-140.
- [6] Madon MBH. The petroleum geology and resources of Malaysia. PETRONAS, Malaysia: Petroleum Nasional Berhad (PETRONAS), 1999.
- [7] Madon M, Kim CL, and Wong R. The structure and stratigraphy of deepwater Sarawak, Malay-sia: Implications for tectonic evolution. Journal of Asian Earth Sciences, 2013; 76: 312-333.
- [8] Mathew M, Siddiqui N, and Menier D. An evolutionary model of the near-shore Tinjar and Balingian Provinces, Sarawak, Malaysia. Int. J. Pet. Geosci. Eng, 2014; 1: 81-91.
- [9] RD Nugraheni, Chow WS, Rahman AHA, and Nazor SNM. Tertiary coal-bearing heterolithic packages as low permeability reservoir rocks in the Balingian Sub-basin, Sarawak, Malaysia," Bulletin of the Geological Society of Malaysia, 2014; 60: 85-93.
- [10] Doust H. Geology and exploration history of offshore central Sarawak. 1981.
- [11] Hakimi MH, and Abdullah W. Liquid hydrocarbon generation potential from Tertiary Nyauau Formation coals in the onshore Sarawak, Eastern Malaysia. International Journal of Earth Sciences, 2013; 102: 333-348.
- [12] Hassan Baioumy YU, Nawawi M, Noor Akmal Anuar M. Black Shales Outcrops in Malaysia: Occurrence and Geological Setting. Presented at the 18th International Conference on Earth Science and Resource Engineering, 2015.
- [13] Mat-Zin I. Tertiary tectonics and sedimentation history of the Sarawak basin, east Malaysia. PhD theses, Durham University, 1996.
- [14] Hutchison CS. Geology of North-West Borneo: Sarawak, Brunei and Sabah. Elsevier, 2005.
- [15] Bakar ZAA, Madon M, and Muhamad AJ. Deep-marine sedimentary facies in the Belaga Formation (Cretaceous-Eocene), Sarawak: Observations from new outcrops in the Sibu and Tatau areas. Presented at the Geological Society of Malaysia, 2007.
- [16] Sia S-G, and Abdullah WH. Enrichment of arsenic, lead, and antimony in Balingian coal from Sarawak, Malaysia: Modes of occurrence, origin, and partitioning behaviour during coal combustion. International Journal of Coal Geology, 2012; 101: 1-15.
- [17] Dow WG and Pearson DB. Organic Matter In Gulf Coast Sediments. Presented at the offshore Technology Conference Dallas, Texas, USA, 1975.
- [18] Peters KE, and Cassa MR. Applied Source Rock Geochemistry: Chapter 5: Part II. Essential Elements. 1994.

To whom correspondence should be addressed: Walaa Elnasir Ibrahim, Universiti Teknologi PETRONAS, Department of Geoscience, Perak Darul Ridzuan, 32610 Seri Iskandar, Tronoh- Malaysia

SELECTING FEATURES OF MOTOR OILS FOR THE FACILITIES OPERATION IN ABNORMAL CONDITIONS

Andrey B. Grigorov¹, Irina A. Turkoman¹, Oleg I. Zelenskii², Elena Yu. Spirina²

¹ National Technical University «Kharkov Polytechnic Institute», 61002, 2 Kirpichova str., Kharkov, Ukraine

² Ukrainian State Coal-Chemistry Institute, 61023, 7 Vesnina Str., Kharkov, Ukraine

Received February 16, 2018; Accepted April 27, 2018

Abstract

The article deals with the features of selecting motor oils for the facilities operation in abnormal conditions, where the level of quality of lubricants must ensure the reliable operation of agricultural machinery. In this regard, the accumulation of the water in the oil SAE 10W-40, fuel and particles of incomplete combustion of fuel were simulated in the laboratory; the pollution significantly reduced the level of oil quality. It has been established that the accumulation of water in the oil under study leads to the elution of additives, as evidenced by a 45% decrease in the values of the alkaline number and sulfate ash by 50 %, from the initial value. With an increase in the concentration of soot particles to 10 %, the value of the dispersive stabilization capacity decreases to 0.67, the accumulation in diesel oil to 7.0 %, the flash point decreases by 73°C, and the kinematic viscosity by 34.16 %. The compatibility of motor oils was also studied using the example of oils SAE 10W-40 API CJ-4 and SAE 10W-40 API CI-4 which showed that as there was no oil turbidity, precipitation and discoloration then the oil data can be considered compatible. Based on the undertaken studies, it is possible to predict a change in the oil quality level during the facilities operation and to determine its residual life before replacement.

Keywords: motor oil; operating conditions; quality level; dispersive stabilization capacity; additives; compatibility of oils..

1. Introduction

It is known that one of the most abnormal conditions for the facilities operation is considered to be the field conditions during sowing and harvesting. Under the circumstances, there is considerable air pollution, difficult meteorological conditions, impassability of roads, as well as very high loads on the machinery, and therefore its reliable operation will be largely determined by the ability of lubricants, in particular motor oils, to maintain their operational properties throughout the lifetime until replacement.

2. The purpose and objectives of the research

The main purpose of the research is to create an investigation program, which will be characterized by the creation of severe, extreme conditions of the oils operation. Under the circumstances oils are able to show their properties to the maximum. In framework of the goal implementation, it is necessary to select the quality oil factors, which will reflect the qualitative state most adequately, and as a result it reflects on the reliable facilities operation. These indicators include alkali neutralization number, sulfate ash, indicator of dispersing and stabilizing properties, flash point and kinematic viscosity. Also, this series of indicators should be supplemented by studies in the field of oils compatibility. On the basis of information on the numerical values of these indicators, it is possible to predict the behavior of motor oil in emergency situations that may arise from the facilities operation in the field conditions, and

to justify the support system for those brands of motor oils, which are not available in the operation manual of the equipment.

3. Results and discussion

During the engine operation, motor oil loses its properties due to accumulation of such contaminants as water, dust, products of incomplete combustion and high boiling fuel fractions [1-3]. The most negative contamination of motor oil when it is transported, stored, pumped and refilled is water. The presence of water causes the hydrolysis of oil additives [4], increases the oxidation of oil and worsens its lubricity [5], contributes to the formation of deposits and engine corrosion [6]. In the presence of water, oil is foamed intensively and the mode of supplying the oil to the engine parts [7] is violated, which causes increased wear of the parts in the friction zone [8].

Therefore, to determine the effect of water on the oil it is necessary to conduct its flooding with the subsequent definition and comparison of the alkaline number and the sulfated ash of pure and watered oil, as these indicators characterize the presence of oil additives [9]. The oil was flooded in the laboratory in the following way: 50 cm³ of diesel semisynthetic oil SAE 10W-40 and 50 cm³ of distilled water were poured into a conical flask at a temperature of (60 ± 5°C) and then carefully mixed for 2 hours. The resulting emulsion was treated with a centrifuge at a separation factor of 3000 to separate the emulsion completely. From the upper part, a sample of oil was selected, and the alkaline number and sulfate ash were determined (Tab. 1).

Table 1 Alkaline number and the sulphate ash of the oil results

Indicator name	Pure oil sample	Watered oil sample
Alkaline number, mg KOH/g of oil	8,2	4,5
Sulfate Ash, % (mas.)	0,86	0,43

The obtained results showed that the number of impurities in the watered oil decreased in comparison with the pure oil, as evidenced by a decrease in the alkaline number by 45 % and a decrease in the value of sulfate ash by 50 %. However, these values of the indicators are not critical [10], but during the actual operation such amount of water never gets into the oil, then on the basis of this, it can be assumed that the oil was passed the flood test.

Then we will consider the effect on the dispersion and stabilization oil properties (DSP) of incomplete combustion products of diesel fuel - the soot particles that accumulate in the oil during the operation of a diesel engine [11-12]. The dispersion and stabilization oil properties are determined by the method of the drop test [13-14]. To do this, into the pure SAE 10W-40 diesel oil, soot particles were artificially injected and dispersed by ultrasound at a frequency of 50 Hz for 2 hours, and they were obtained by the thermal process [15]. Further, the sample of oil was applied to a filter paper to obtain the paper chromatograms, and the dispersion and stabilization oil properties were determined. Taking into account that the washing-dispersing oil additives begin to show their properties at a certain temperature [16], the following studies have been carried out to establish this temperature (Fig. 1).

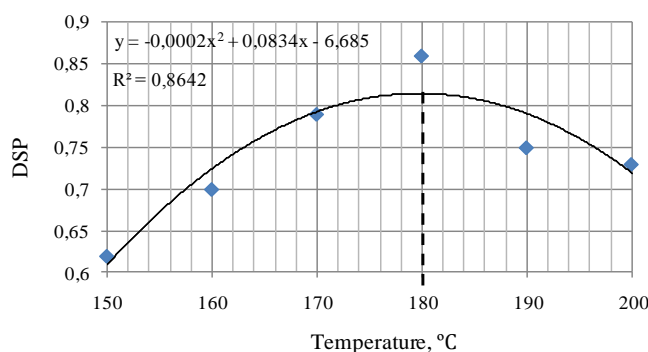


Fig.1. Dependence of the activity of the dispersion and stabilization oil properties on the temperature

According to Fig. 1, the maximum activity of the additive is observed at 180°C. Hence, further studies on the influence of the concentration of the soot particles on the dispersion and stabilization oil properties (Fig. 2) will be carried out at that temperature.

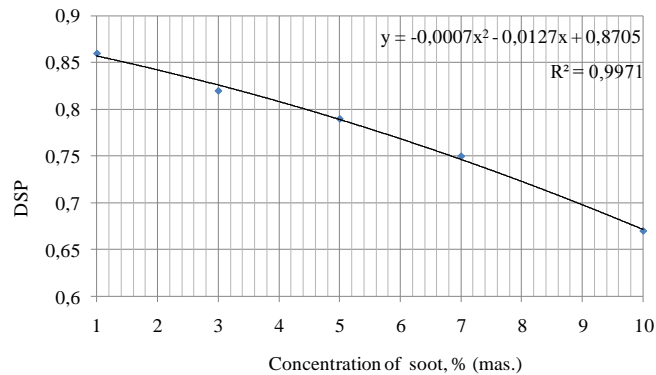


Fig. 2. Dependence of the activity of the dispersion and stabilization oil properties on the concentration of soot particles

It is clear that with an increase in the concentration of the pollutant (soot) from 1 to 10 %, the dispersion and stabilization oil properties deteriorate, and the numerical value decreases from 0.86 to 0.67. However, oil properties are considered unsatisfactory, and it should be replaced by new oil if the numerical value is equal to 0.3 standard units [17]. Therefore, in our case, we believe that the dispersion and stabilization oil properties are preserved when the oil concentration is up to 10 % of incomplete combustion products.

It is known that the presence of fuel in motor oil negatively affects its performance [18], and therefore, in accordance with [19], the influence of diesel fuel on the flash point in an open crucible (Fig. 3) and the kinematic viscosity of the oil at 100°C have been discovered (Fig. 4).

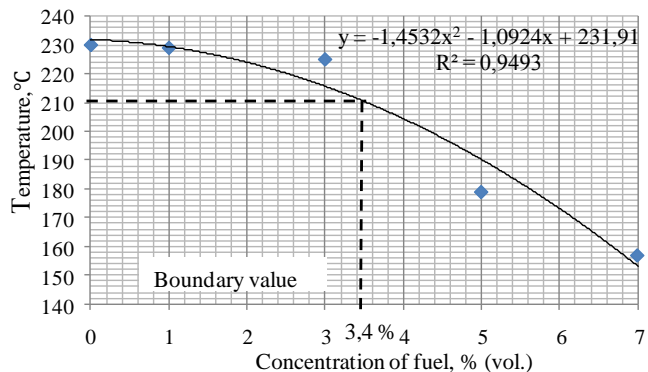


Fig. 3. Dependence of the flash point of the tested oil on the concentration of diesel fuel in it

It is obvious that when the concentration of diesel fuel in oil increases from 0 to 7 % (vol.), the flash point of the oil decreases from 230°C to 157°C, that is 73°C. A defective value for oil is the reduction of the flash point by more than 20°C [13]. And therefore, keep in mind that according to Fig. 3, the maximum allowable concentration of diesel fuel in the oil is equal to 3.4 % (vol.).

With increased concentration of the diesel fuel in the oil, its kinematic viscosity decreases from 14.05 mm²/s to 9.25 mm²/s, i.e., 34.16 %. Such a decrease in the kinematic viscosity is considered critical, and the oil should be immediately replaced by the fresh one. The initial stock of kinematic viscosity of the investigated oil allows observing the normal working capacity of the equipment at a decrease in viscosity by 25 % [20-21], that is, to the concentration of fuel in it up to 4 %.

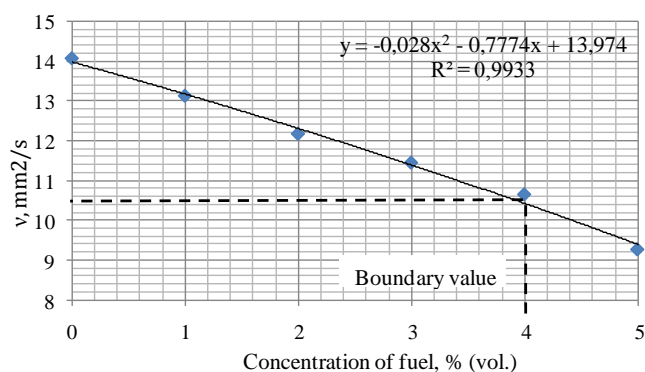


Fig. 4. Dependence of the viscosity of the tested oil on the concentration of the diesel fuel in it

In addition to the above-mentioned oil quality indicators, it is also possible to determine the compatibility of the studied oil with other ones. This is necessary to determine the principal possibility of the emergency extraction oil in the lubrication system of the engine instead of the system that has burnt or escaped. Basic oils must be mixed in one another, and the greatest danger when mixing oils of different grades is the additives added to the base. Each brand uses its own additive package, so when mixing motor oils, they can conflict with each other, which can lead to an increase in carbon content, foaming the mixture of oils, blush and color changes in oils, increasing the aging rate of oil in the engine [22].

To determine the compatibility of the oil, it was taken 50 cm³ of the semi-synthetic diesel oil grade viscosity SAE 10W-40 API CJ-4, which was added diesel oil SAE 10W-40 API CI-4, but another manufacturer. The resulting mixture was thoroughly mixed, warmed to a temperature of 100°C, and heated air was blown through the mixture for 2 hours. Next, the compatibility of the oils was determined visually by comparison with the pure oil. It was considered that the oils are not compatible if the mixture produces a precipitate, cloudiness and a change in color (Tab. 2).

Table 2. Results of the compatibility of oils determination

Oil №1, cm ³	Oil №2, cm ³	Impurity level, %	External features		
			Residue	Blush	Change in color
45	5	10	no	no	no
35	15	30	no	no	no
25	25	50	no	no	no

As a result of the study, it can be concluded that the tested oils are conventionally compatible, and gaining a complete understanding of compatibility it is necessary to conduct more detailed laboratory studies according to a clearly defined program [23].

4. Conclusion

Based on the results obtained, we can propose the following program, which will allow from the whole spectrum of motor oils presented in the Ukrainian oil market to select oils that can store their properties under abnormal operating conditions.

The proposed program at stage I involve the creation of extreme weather conditions, i.e. the addition of various contaminants that may fall into the oil, both in the normal operating conditions of the equipment and in an emergency. That is addition of water, creating a hydrolysis of oil additives; contamination of soot particles, which can form similar ointments, which complicate the supply of oil to the friction zone; contamination of high boiling fractions of the fuel, which promotes the oil dilution, thereby violating the hydrodynamic mode of friction of the engine parts.

At stage II, among the quality indicators, it is necessary to choose the most adequately describing the qualitative status of the oils and to determine the indicators in the laboratory.

These indicators include: alkaline number, sulfate ash, index of dispersing and stabilizing properties and kinematic viscosity.

Also, at this stage, it is necessary to determine the compatibility of the studied oils, which will provide information on the possibility of replenishing their volume in the lubricating system of the engine, in the field conditions without reducing the engine reliability.

Stage III involves the interpretation of the obtained numerical values of indicators and the construction of the mathematical models. That will allow to predict the change in the quality oil level during the facilities operation and determine its residual life to the replacement.

References

- [1] Francois Audibert. Waste engine oils: Re-refining and Energy Recovery; Elsevier, 2011; p 340.
- [2] Firas Awaja. Design aspects of used lubricating oil re-refining; Elsevier, 2006; p 122.
- [3] Speight JG, Exall DI. Refining used lubricating oil; CRC Press: Taylor & Francis Group, 2014; p. 460.
- [4] Alun L, Ken BT, Randy CB, Joseph VM. Large-scale dispersant leaching and effectiveness experiments with oils on calm water. *Marine Pollution Bulletin*. 2010; 60: 244–254.
- [5] Utaev S. Accumulation regularities of contaminants of motor oils during the engine operation. *Sovremennye materialy, tekhnika i technologii*. 2016; 5(2): 207-214.
- [6] Radushko AA. Methodology and the study results of motor oils for the presence of a mass water fraction. *Vestnik Bryanskoy gosudarstvenoy selskohozyaystvenoy academii*. 2014; 3: 72-74.
- [7] Ostrikov VV, Tupotilov NN. Lubricants and their change properties in the operation of agricultural machinery. Tambov: VNIITiN, 2002; p. 67.
- [8] Eachus A. The trouble with water, tribology & lubrication technology, Society of tribologists and lubrication engineers publishing. Ridge Park, IL, October 2005.
- [9] Grigorov AB, Naglyuk IS. Rational use of motor oils; Tochka: Kharkov, 2013; p. 179.
- [10] Naglyuk IS. The evaluation of the motor oil quality in the operation of passenger cars. *Avtomobilnuy transport*. 2011; 29: 184-186.
- [11] Kennedy IM. Models of soot formation and oxidation. *Prog. Energy Comb. Sci.* 1997; 23: 95–132.
- [12] Daido S, Kodama Y, Inohara T, Ohyama N, Sugiyama T. Analysis of soot accumulation inside diesel engines. *JSAE Rev.* 2000; 21: 303–308.
- [13] Reznikov VA. Engine diagnostics by analysis of engine oil. *Zhurnal RF «Gruzovik Press»*. 2005; 9: 27-33.
- [14] Yegorov AV, Zubova EV, Vakhrushev VV et al. The evaluation features of service properties of working motor oils. *APK of Russia*. 2015; 73: 49-57.
- [15] Clague AD, Donnet JB, Wang TK, Peng JCM. A comparison of diesel engine soot with carbon black. *Carbon*. 1999; 10(37): 1553–1565.
- [16] Guryanov YA. R.F. Patent RU2312344, 2007.
- [17] Itinskaya NI, Kuznetsov NA. Fuel, oil and technical fluids, 2nd ed.; Handbook; Agropromizdat: Moscow, 1989; p. 304.
- [18] Watrus M. Fuel property effects on oil dilution in diesel engines. *SAE Int. J. Fuels Lubr.* 2013; 6(3): 794-806.
- [19] Ljubas D, Krpan H, Matanovic I. Influence of engine oils dilution by fuels on their viscosity, flash point and fire point. *Nafta*. 2010; 61(2): 73-79.
- [20] Korneev SV. About the efficiency of motor oils. *Dvugonobuduvany*. 2004; 4: 36-38.
- [21] Guryanov YA. Quality indicators of working motor oils and methods of their determination. *Avtomobilna promuslovist*. 2005; 10: 20-23.
- [22] Shugarman A. Managing the risk of mixing lubricating oils. *Machinery Lubrication magazine*, September 2001, p. 3.
- [23] Denis J, Briant J, Hipeaux J. Lubricant properties analysis and testing; Editions Technip: Paris, 2000; p. 281.

To whom correspondence should be addressed: Dr. Andrey B. Grigorov, National Technical University «Kharkov Polytechnic Institute», 61002, 2 Kirpichova str., Kharkov, Ukraine, , grigorovandrey@ukr.net

IPR EQUATION OF CBM WELLS USING PALMER AND MANSOORI MODEL

Ratnayu Sitaressmi¹, Doddy Abdassah², Ryodi Hananda¹, Heri Susanto¹

¹ Petroleum Engineering, Faculty of Earth and Energy Technology, Universitas Trisakti, Indonesia

² Petroleum Engineering, Faculty of Mining and Petroleum Engineering, Institut Teknologi Bandung, Indonesia

Received February 28, 2018; Accepted April 27, 2018

Abstract

IPR equation is important in designing well completion, production optimization, nodal analysis and artificial lifts on CBM wells. The technique for producing gas of coalbed methane is different from conventional gas because the production initially was dominated by water. The gas will flow as the reservoir reaches the desorption pressure. Permeability is very sensitive to the pressure reflected in the phenomenon of cleat compression and the corresponding matrix shrinkage in the cleat and coal matrix. This phenomenon causes the conventional IPR curve is not applicable in CBM wells. This paper presents a dimensionless IPR curve for CBM wells considering the Palmer and Mansoori (P & M) model. The equation of IPR illustrates the change in permeability due to the compression phenomenon and the shrinkage of the matrix in the coalbed methane reservoir. The equation model of IPR produces a graph illustrating the increasing permeability when the coalbed methane reservoir pressure depleted. The six reservoir parameters included porosity (ϕ), drainage area (A_D), thickness (h), S_{wc} and two P & M parameters (Young modulus (E) and the Poisson ratio (ν) have been selected to make the IPR curve. Taking into account the P & M model in the development of the IPR curve, then the right method to predict the production performance of gas in coalbed methane will be obtained.

Keywords: Pressure; gas flow rate; methane; IPR; CBM.

1. Introduction

Coalbed methane (CBM) is a methane gas formed along with the establishment of coal. The gas is trapped and absorbed (adsorbed) inside the coal. The production of methane gas from the CBM reservoir is unique and different from the production process in the conventional reservoir (Fig. 1). In the early stages of production, when reservoir pressure is above the critical desorption pressure (CDP), usually only water flows from the cleats. After pressure reaches CDP, water and gas are produced simultaneously. When desorption pressure is reached, methane gas is released from the surface of the coal matrix and then begins to dominate the flow rather than water until it reaches the peak flow rate of gas (Fig. 2). As the gas flow rate reaches the peak, then the water production will reach zero so that only gas is produced.

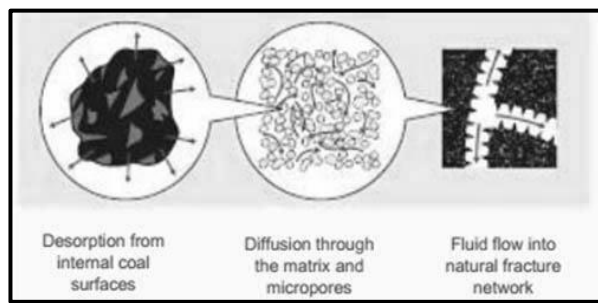


Fig. 1. Flow mechanism in CBM reservoir [11]

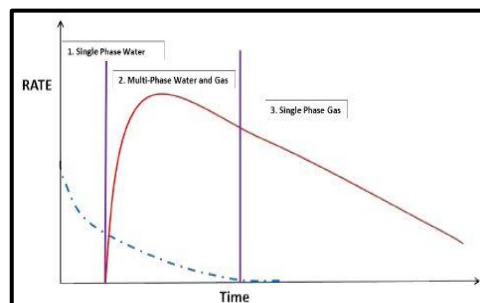


Fig. 2. Production profile of CBM well [11]

Palmer *et al.* [3] illustrate that the permeability of the CBM reservoir may change as it is influenced by changes of porosity due to the decrease of reservoir pressure. When reservoir pressure decreases, the overburden pressure forcing the cleat so that the cleat volume decreases resulting in a decrease in permeability. This phenomenon is referred as cleat compression (Fig. 3). But when reservoir pressure reaches below CDP, the gas is desorbed out from the coal matrix. This causes the volume of coal matrix will be reduced, but the cleats volume were enlarged so that the value of permeability increases (Fig. 4). Both these phenomena influence each other during pressure drop occurs.

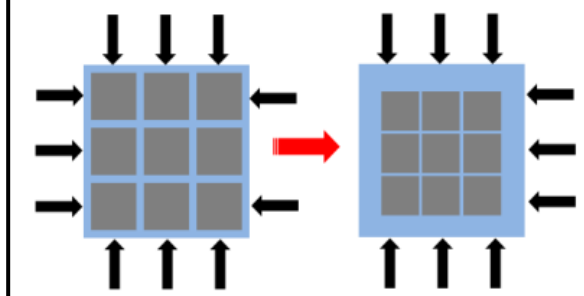


Fig. 3. Cleats compression (Zulkarnain [9])

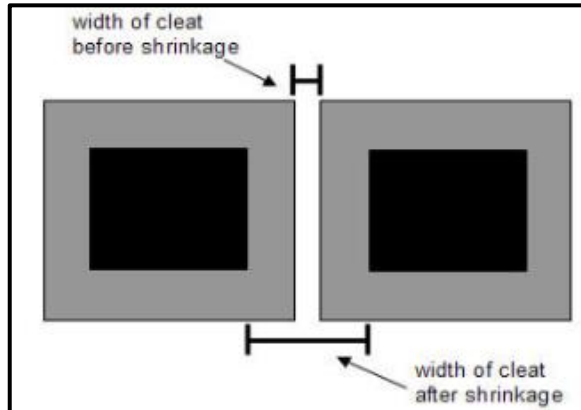


Fig. 4. Matrix shrinkage (Zulkarnain [9])

Palmer and Mansoori model [3] arranged the following equation:

$$\frac{\phi}{\phi_i} = 1 + \frac{c_m}{\phi_i} (p - p_i) + \frac{c_o}{\phi_i} \left(\frac{K}{M} - 1 \right) \left(\frac{Bp}{1+Bp} - \frac{Bp_i}{1+Bp_i} \right) \quad (1)$$

where Modulus axial constraint constant comes from :

$$M = \frac{(1-\nu)E}{(1+\nu)(1-2\nu)} \quad (2)$$

Poisson's ratio (ν) states the change in the shape of material if force is applied in one direction. The Young Modulus (E), also known as the elastic modulus, is expressing the magnitude of the failure or the change of shape of material when the material is subjected to force. When expressed in cm and the relation of K/M is expressed by the following equation:

$$\frac{K}{M} = \frac{1}{3} \left(\frac{1+\nu}{1-\nu} \right) \dots \quad (3)$$

then the Palmer and Mansoori equation can be written as follows :

$$\frac{\phi}{\phi_i} = 1 + \frac{(1+\nu)(1-2\nu)}{(1-\nu)E\phi_i} (p - p_i) + \frac{c_o}{\phi_i} \frac{2(1-2\nu)}{3(1-\nu)} x \dots \quad (4)$$

$$\left(\frac{P_i}{P_i + P_L} - \frac{P}{P + P_L} \right). \quad (5)$$

The center part of the above equation shows porosity change due to the effects of stress on coal, while the last part shows the influence of shrinkage porosity against the matrix.

Assuming the change of permeability depends on the value of the porosity, then obtained the equation as follows:

$$\frac{k}{k_i} = \left(\frac{\phi}{\phi_i} \right)^3 \dots \quad (6)$$

As discussed earlier, permeability is very sensitive to the effective stress (reservoir pressure). Palmer and Mansoori [3] (Fig. 5) show a phenomenon of permeability change as a function of effective stress. A decrease in pressure at the early of production will cause the effective stresses on cleats start to increase so that the cleats will be compressed and cause a decrease in permeability. In the next stage, the effect of effective stress on cleats will diminish so the permeability tends to increase.

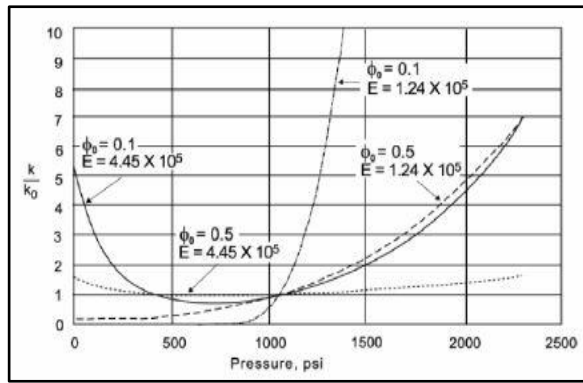


Fig. 5. Effect of stress on the permeability of Palmer & Mansoori model [3]

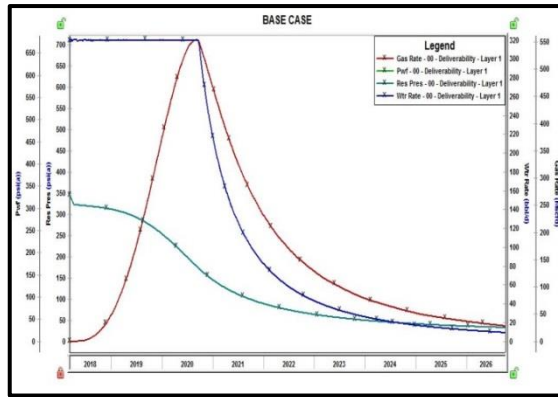


Fig. 6. The relationship of P_r , Q_g , and Q_w

This phenomenon affects the gas production of reservoir CBM because permeability increases one to four times greater than initial permeability. This should be increasing of gas recovery.

2. Material and methods

2.1 Development of IPR equation

Method of producing gas of coalbed methane is different from the conventional gas reservoir. In the beginning, production is dominated by water where the gas will flow when the pressure reaches a critical point. In addition, the permeability is very sensitive to the pressure indicated by the phenomenon of cleat compression and shrinkage of the matrix. Therefore, conventional IPR methods cannot be used for CBM wells.

Vogel's IPR [8] is well known and commonly used to describe fluid flow in oil wells. Vogel's IPR is performed by using simulations of single wells for various characteristics of gas and oil reservoirs. IPR for coalbed methane was initially developed with the assumption of conventional gas wells. Seidle and Erickson [6] used Vogel's IPR to construct IPR for gas of coalbed methane. Furthermore, there is a general form of Vogel's IPR equation developed by Richardson and Shaw [4].

$$\frac{Q}{Q_{max}} = 1 - V \frac{P_{wf}}{P_r} - (1 - V) \left(\frac{P_{wf}}{P_r} \right)^2. \quad (7)$$

Shaw [4] develops the same equation as Vogel's IPR by using the variable Vogel coefficient denoted by V . The IPR equation needs to be adjusted to the CBM reservoir characteristics. The new IPR equation is needed to provide the CBM wells performance more accurately than Vogel IPR.

2.2. Reservoir data

In this research, Fekete F.A.S.T CBM software is used to develop a reservoir model. This study uses vertical good models where the pressure response is a rectangular, homogeneous or double porosity reservoir. The hypothetical under saturated reservoir model is used with the assumption of 1 layer reservoir, homogeneous isotherm, no water entry, 100% water saturation in cleats, the abandon pressure 20 psia and the composition of the gas methane 100%. It is also assumed that the A_D value is 80 acres. The following is the data used for base case model of wells T-01.

The effect of the shrinkage matrix of P & M model was tested first with a reservoir simulation. In the simulation, the shrinkage parameter of the Poisson ratio matrix (ν), Young's modulus (E) is recommended parameter as the input, and greatly affects the shrinkage of the matrix.

Table 1. The Base data of well T-01

Layer		1	Moisture content (Wc),	%	38.8
Initial pressure (Pi),	psia	714	Ash content (a),	%	4.43
Langmuir volume (VL),	scf/ton	258.6	Bulk density (pb),	gr/cc	1.31
Langmuir pressure (PL),	psia	492.89	Skin damage (Sd)		0
Temperature reservoir (TR)	°F	110	Permeability		84.5
Gas saturation (Sg),	%	10	Well radius (rw),	ft	0.3
Connate gas saturation (Sgc),	%	1	Φi,	(%)	1.9
Connate water saturation (Swc),	%	20	AD assumption	Acre	80
Thickness (h),	ft	62.4	Pabd assumption	Psia	20
Initial water saturation (Swi),	%	1			

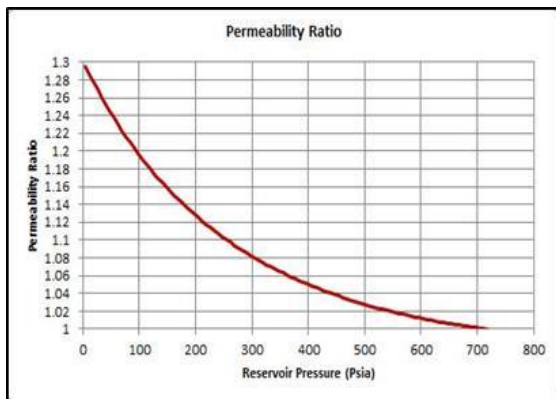
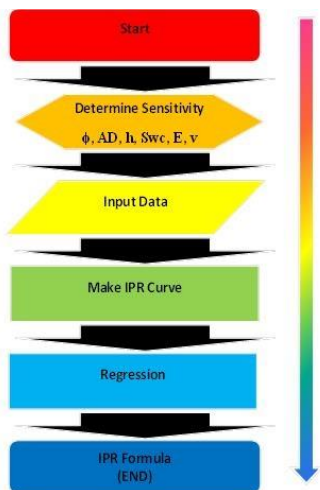


Fig. 7. Permeability ratio of P&M model

The value of Poisson's ratio (ν) is set at 0.35, and young's modulus (E) is 350,000 psi. After the data is inputted into the simulator, the Langmuir desorption pressure graph shows a value of 321 psia. The effects of desorption pressure can be seen in the profile of production rates as shown in the Fig. 6.

Fig. 7 shows that a decrease in pressure will cause the permeability to increase, even when pressure below the critical desorption pressure. The shrinking of the coal matrix will lead to cleat opening so that the permeability increase will be greater.

2.3. Methodology



IPR curve is defined as the relationship of flowing bottom hole pressure versus gas flow rate. The flowing bottom hole pressure are measured simultaneously with the gas flow rate under the conditions of pseudo steady state (PSS). In developing of IPR curve for gas of coalbed methane can be done by first specifying the constant flow rate. Furthermore, the flowing bottom hole pressure is calculated when it reaches the pseudo steady state condition. The calculation is done by sensitivity to several variables of coalbed methane reservoir. The relationships of flowing bottom hole pressure against the production rate are then changed into the form of a dimensionless variable of $\frac{p_{wf}}{P_r}$ vs $\frac{Q}{Q_{max}}$. The flowchart of development the dimensionless IPR for gas coalbed methane is shown in Fig. 8.

Fig. 8. Flowchart for the development of a dimensionless IPR curve

In the first stage, the sensitivity analysis of parameters ϕ , A_D , h , Swc , ν and E is conducted. The data is then inputted into the simulator which includes sorption data model, shrinkage of matrix and deliverability. The water flow rate constraint is set to constant at 320 bbl/d. The results of simulation show that in the second year of production time, the reservoir pressure reaches critical desorption and gas begin to flow.

The predicted result of gas production rate (Q_g) and flowing bottom hole pressure (P_{wf}) is taken to create the IPR curve (Fig. 9). Furthermore, based on these data, it is used to create the dimensionless IPR equation for T-01 well.

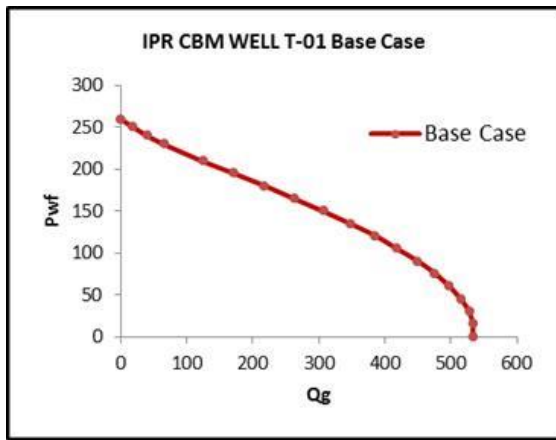


Fig. 9. Inflow performance relationship curve of base case

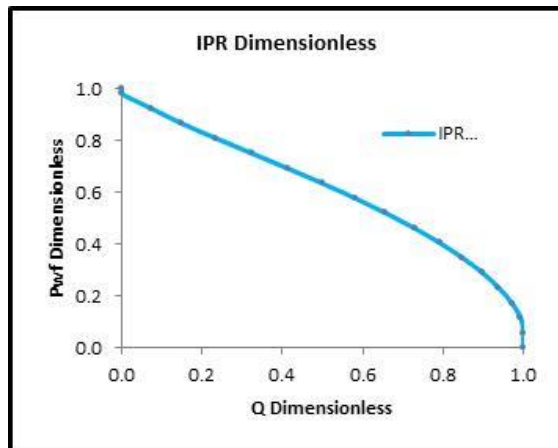


Fig. 10. Dimensionless IPR curve of base case

As discussed earlier, the sensitivity analysis of input parameters ϕ , A_D , h , S_{wc} , v and E is conducted in the simulation. Sensitivity analysis of Langmuir Volume (VL) parameters, Langmuir Pressure (PL) and Reservoir Pressure (P_i) cannot be performed because these three parameters influence one with the other. Changing one variable will change the other parameter. Sensitivity analysis was conducted on various parameters such as following:

Table 2. Sensitivities analysis data

ϕ_i (%)	1 : 3 : 5 : 9
A_D (Acre)	60 : 80 : 100 : 120
E (Psia)	100000 : 200000: 300000: 400000
v	0.35 : 0.4 : 0.45
h	50 : 60 : 70 : 80
S_{wc}	10 : 20 : 30 : 40

Based on the sensitivity analysis of these six parameters (Table 2), the dimensionless IPR curve and IPR equation for coalbed methane are obtained (Fig. 10).

3. Result and discussion

3.1. Sensitivity analysis and IPR curve

Six reservoir parameters such as porosity (ϕ), drainage area (A_D), thickness (h), S_{wc} , young modulus (E) and poisson's ratio (v) are selected to construct the IPR curve. The value of porosity 1.9 % is chosen as base of porosity. Furthermore, the sensitivity test for porosity of 1, 3, 5 and 6 % was performed. The resulting IPR curve can be seen in Fig. 11. Fig. 11 shows the effect of porosity to gas production rate. The larger porosity will result in lower gas production rates compared to lower porosity. The next sensitivity analysis was conducted for the drainage area. The base value of the drainage area used is 80 acres. While the sensitivity analysis carried out for the drainage area 60, 80, 100 and 120 acre. The resulting IPR curve is shown in Fig. 12. Fig. 12 shows the effect of the drainage area on the gas production rate. The larger drainage areas will result in larger gas production rates. The sensitivity test for thickness indicates that rate of gas production is linear with reservoir thickness (Fig. 13). The thicker the reservoir thickness will result in a larger of gas production rate.

The sensitivity analysis of residual water saturation (S_{wc}) shows that the greater the value of S_{wc} , the greater the gas production rate (Fig. 14). Another sensitivity analysis is to test the matrix shrinkage parameters of young's modulus (E) and Poisson's ratio (v). The base value of 300,000 psi is used as an assumption of the young's modulus. The sensitivity analysis was performed for the value of young's modulus of 100,000, 200,000 300,000 and 400,000 psi.

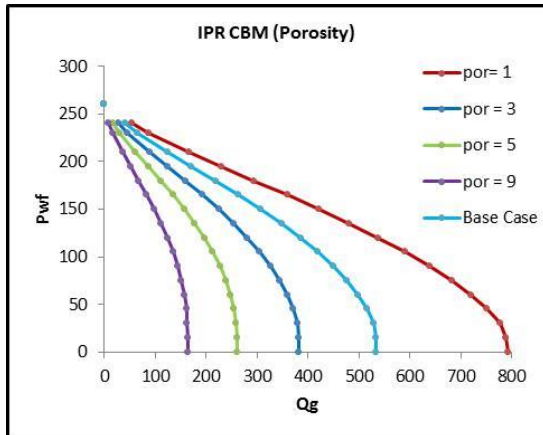


Fig. 11. The influence of porosity on IPR curve

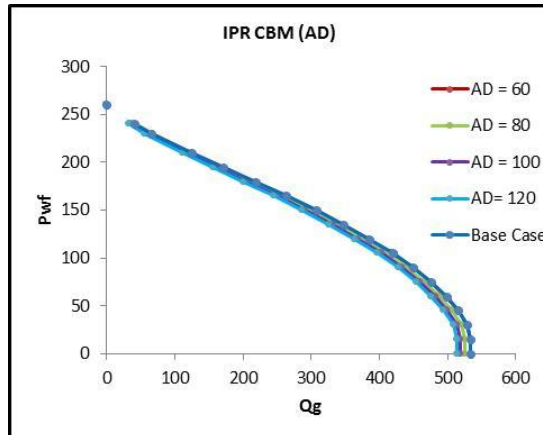


Fig. 12. The influence of drainage area on IPR curve

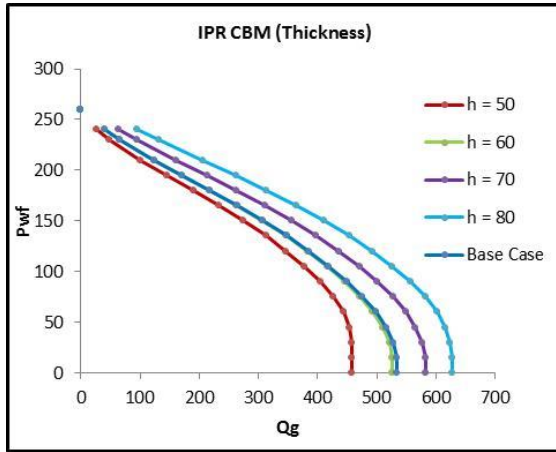


Fig. 13. The influence of reservoir thickness on IPR curve

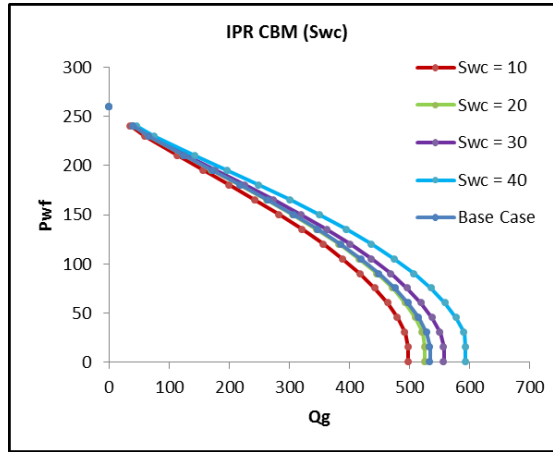
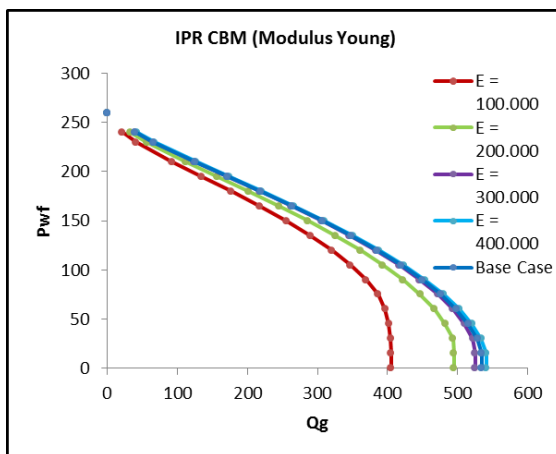
Fig. 14. The influence of S_{wc} on IPR curve

Fig. 15. The influence of Young's Modulus on IPR curve

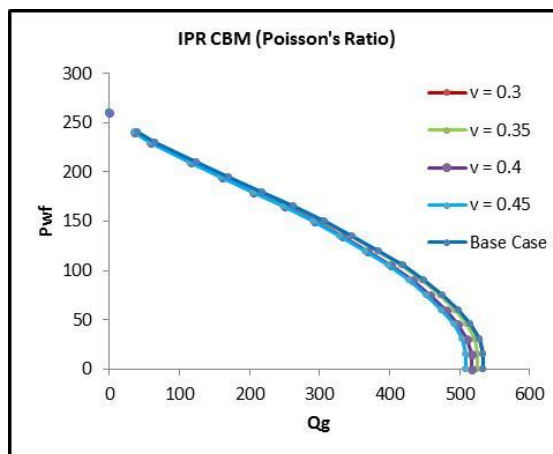


Fig. 16. The influence of Poisson's Ratio on IPR curve

Fig. 15 shows that the greater the young's modulus, the greater the gas production rate. In contrast, the sensitivity of Poisson's ratio indicates that decreasing the Poisson's ratio will provide greater gas flow rate (Fig. 16). As we know, Palmer and Mansoori show that young's modulus, Poisson's ratio, and porosity are part of the matrix shrinkage phenomenon. Thus,

these three parameters will have the greatest impact on the gas production rate. In the event of shrinkage of the matrix, the permeability of the coalbed methane reservoir increases as the pressure falls below the critical desorption pressure. At that time, there will be shrinkage of cleats so that porosity fissures (cleats) filled by water also shrinking. The lower porosity indicates that less water fills the cleats, so the gas permeability is getting enlarged. In addition, gas production may increase due to young's modulus and Poisson's ratio; the greater the young's modulus and the smaller Poisson's ratio, the more difficult the coal to be compressed.

3.2. Dimensionless IPR curve of coalbed methane

The dimensionless IPR curve equation is developed by combining the IPR curve resulting from the sensitivity analysis. The sensitivity analysis of six CBM reservoir parameters such as porosity (ϕ), drainage area (A_D), thickness (h), S_{wc} , young modulus (E) and Poisson's ratio (ν) yields 1 dimensionless IPR curve for each parameter. The six curves are then combined to obtain a dimensionless IPR curve equation (Fig. 17).

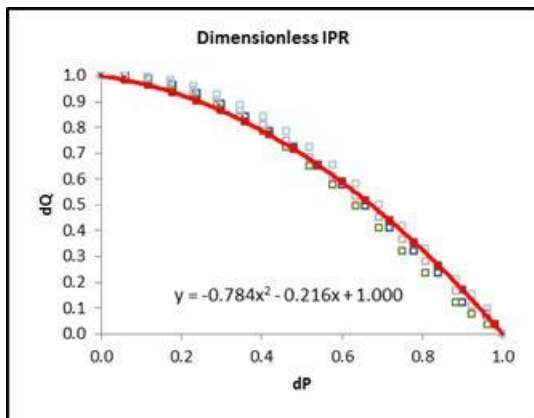


Fig. 17. The polynomial regression of dimensionless IPR curve

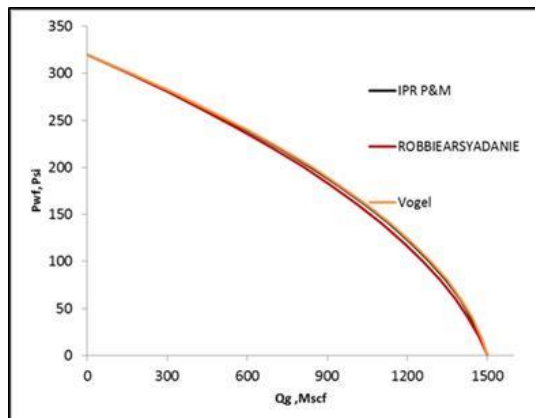


Fig. 18. Comparison of the IPR of P & M, Vogel and Robbie Arsyadanie

To obtain the general equation of the dimensionless IPR curve is done by using the second order polynomial regression method as follows:

$$\frac{Q}{Q_{max}} = 1 - 0.216 \frac{P_{wf}}{P_r} - 0.784 \left(\frac{P_{wf}}{P_r} \right)^2. \quad (8)$$

Fig. 18 shows the comparison of IPR for CBM derives by using the P & M method (eq. 7), Robbie Arsyadanie's methode and Conventional Vogel IPR. The IPR curve derives by using the P & M method is relatively similar to Vogel IPR but more optimistic than IPR of Robbie Arsyadanie's because the IPR P & M is considering the permeability changes in CBM reservoir. Thus the P & M IPR curve will be appropriate when applied to predict the gas production performance of coalbed methane.

4. Conclusion

1. The dimensionless IPR equation has been successfully arranged and provides accurate prediction results of IPR curve. This equation can be used to estimate the peak gas production rate of CBM wells.
2. The matrix shrinkage has a major impact on the permeability of CBM reservoir. The effect of matrix shrinkage can increase permeability up to 2 times than before.
3. The changes in permeability were strongly influenced by the reservoir pressure in dewaterring stage when matrix shrinkage effect is taking the role after reservoir pressure reached CDP.
4. Porosity is the most influential parameter to the IPR curve of CBM reservoir.

5. Recommendation

1. Need to consider the influence of other variables that may affect the deliverability of CBM reservoir.
2. It is necessary to validate this dimensionless IPR equation in the field to verify its accuracy.

List of symbols

c_m	$1/M, \text{ psia}^{-1}$	Pr	reservoir pressure, psia
c_o	volumetric strain coefficient, psia^{-1}	P_i	initial pressure, psia
B	reciprocal of Langmuir pressure, psia^{-1}	TR	reservoir temperature, F
M	constrained axial modulus, psia	S_g	gas saturation, fraction
K	bulk modulus, psia	S_{gc}	connate gas saturation, fraction
ν	Poisson's ratio, fraction	S_{wc}	connate water saturation, fraction
E	modulus Young, psi	h	thickness, ft
ϕ	porosity, %	Sw_i	initial water saturation, fraction
ϕ_i	initial porosity, %	W_c	moisture content, fraction
P_L	Langmuir pressure, psia	a	ash content, fraction
V_L	Langmuir volume, scf/ton	ρ_b	bulk density, gr/cc
Q_w	water flow rate, bbl/d	rw	well radius, ft
Q_g	gas flow rate, mscf	AD	drainage area, acre
P_{wf}	well flowing bottom hole pressure, psia	P_{abd}	abandonment pressure, psia

References

- [1] Arsyadanie and Robbie: IPR Sumur pada reservoir coalbed methane, Petroleum Engineering Department, Institut Teknologi Bandung, 2008.
- [2] Feng Q, Shi H, Zhang X, Du P. New inflow performance relationship for coalbed methane wells, Society of Petroleum Engineers, SPE-152163-MS, 2012.
- [3] Palmer I, and Mansoori J. How permeability depends on stress and pore pressure in coalbeds: a new model, Society of Petroleum Engineers, SPE-36737-PA, 1998.
- [4] Richardson JM, and Shaw AH. Two-rate IPR testing a practical production tool, The journal of Canadian Petroleum, PETSOC Journal, 1982: 57-60.
- [5] Rogers RE. Coalbed methane: principles and practice, Prentice Hall Petroleum Engineering Series, 1994.
- [6] Seidle JP, and Erickson DJ. Use of Vogel's inflow performance relation for coal wells, SPE, 26201-MS, 1993.
- [7] Blasingame TA. Semi-analytical rate relations for oil and gas flow, Texas A & M University, 2005.
- [8] Vogel JV. Inflow performance relationship for solution gas drive wells, Journal of Petroleum Technology, 1986; 20(01).
- [9] Zulkarnain I. Simulation study of the effect of well spacing, effect of permeability anisotropy, and effect of Palmer and Mansory model on coalbed methane production, Texas A & M University, 2005.
- [10] http://fekete.com/SAN/TheoryAndEquations/WellTestTheoryEquations/Vertical_Model.htm, Accessed March 2007.
- [11] petrowiki.org/Coalbed_methane, Accessed March 2007.

To whom correspondence should be addressed: Dr. Ratnayu Sitaresmi, Petroleum Engineering, Faculty of Earth and Energy Technology, Universitas Trisakti, Indonesia, rsitaresmi@trisakti.ac.id

STATIC AND DYNAMIC LOAD RESPONSES OF 304 STAINLESS STEEL IN CHLORIDE SOLUTION AT LOW TEMPERATURES

Saad R. Ahmed

Mechanical Engineering Department, Tikrit University, Tikrit, Iraq

Received March 11, 2018; Accepted April 27, 2018

Abstract

The cryogenic properties of metal alloys have received great attention with new developments in petrochemical processes that require operation at low temperature. This paper presents the evaluation of 304 stainless steel under static and dynamic loading at extreme temperatures after being immersed in chloride solution. An environmental chamber was used to test the influence of sub-zero process temperatures on the tensile and corrosion properties of the specimens. Each specimen requiring pre-immersing in chloride solution was subjected to low temperature thermal cycling. The results show that with the decrease in temperature the mechanical properties of the immersed 304 stainless steel specimens under both static and dynamic loadings decreases as compared to dry specimens. However, the mechanical properties of the immersed specimens still acceptable since the decreases in mechanical properties were with 25% change for one low temperature, and they are close to the properties of dry specimens at most of the examined temperature. Microstructure examination of the immersed specimens reveals low ductility at low temperatures.

Keywords: 304 stainless steel; low temperature, dynamic load, static load, tensile test; microstructure analysis.

1. Introduction

Austenitic Stainless Steel (ASS) 304L is Fe-Cr alloys with sufficient nickel and manganese (and sometimes nitrogen) to stabilize austenite, a face-centered cubic (FCC) phase. The most typical austenitic stainless steels are variations of the 18Cr-9Ni alloy. Although none of the commercial alloys were specifically developed for low-temperature service, several of them have been widely used in a variety of cryogenic applications [1]. Cryogenic engineering has a particular need for the evaluation of the performance of materials at very low temperatures. Materials tend to become stiff and brittle at low temperatures; therefore, reasonable concerns are raised about their safety and reliability in such harsh environment. On the other hand, advanced and lighter materials and products for engineering applications, especially the structures, and systems are speedily replacing the typical and heavier materials and parts. There is an expanding need to assess these materials at extremely low temperatures to utilize them in engineering applications such oil production and other energy production [2].

This steel is being extensively used in the field of defense, nuclear science and cryogenic applications due to its excellent corrosion. This property of ASS 304L is due to the presence of chromium, which prevents chloride corrosion. Austenitic stainless steels are subjected to stress corrosion cracking (SCC) in solutions that contain chlorides [3-9]. In magnesium chloride solution, the scenarios of climate-induced corrosion cracking of austenitic stainless steels can be either hydrogen embrittlement (HE) or SCC, determined by the environment temperature [4-5]. A reasonable amount of cold work may reduce the SCC tendency of austenitic stainless steels, whereas too much cold work invert that trend [10-11]. The worked 304L SS showed an obvious increase in SCC tendency in comparison with the unmachined, cold worked and solution-annealed, unmachined samples [12-13].

The alloy steels that are used at cryogenic temperatures are tailored to combine high structural strength with good fracture toughness. For particular applications, they may also be required to meet other criteria, such as good fatigue resistance, weldability, low thermal expansion or low magnetic permeability. The steels that have been most often proposed for use in cryogenic structures can be conveniently divided into three categories: (1) Ferritic steels that contain 5-9Ni and are heat treated to have good combinations of strength and toughness at 77K. These are attractive because of their relatively low cost. (2) 300-series austenitic stainless steels, including particularly the low-carbon, high-nitrogen modifications, 304LN and 316LN, which combine high strength and toughness at 4K with good weldability. These alloys are metastable austenitic steels that transform under strain at 4K. (3) High-strength, stable austenitic alloys that have specifically developed for structural use at 4K. These include Fe-Ni-Cr N alloys (e.g., JN1: 15Ni-25Cr-4Mn-0.4N-0.3Si-0.01C) and Fe-Mn-Cr-N alloys (e.g., OCR Output JK1: 22Mn-13Cr-5Ni-0.2N-0.02C-0.5Si) [14].

It is generally known that chloride stress corrosion cracking (CLSCC) starts from sites of potential pitting or crack corrosion [15] and as a sequence, cracks are estimated to grow in the concentrated chloride, strongly acidic, semi saturated solution that develops at active sites of localized corrosion. A theory [16] assumed that CLSCC only possible when a crevice grows more rapidly than the speed of material removal by pitting corrosion from the base of a crack or pit; in other words, it is a matter of competition between the speed of CLSCC growth and the speed of localized corrosion. Crack growth is also limited to the electrochemical potential that is determined by an upper limit where removal of materials exceeds crack growing and a lower limit determined by re-passivation. This proposition has been considered by Tsujikawa to demonstrate a temperature dependency of CLSCC since crevice growth increases more quickly with temperature than the speed of pitting corrosion. Stress corrosion study carried out by Tsujikawa and another work carried at HE [17] have proven that it is very tricky to initiate CLSCC on smooth and bare specimens under test conditions when pitting corrosion of the surface under stress is missing. The tendency of austenitic stainless steels to CLSCC determined by a range of environmental parameters that include temperature, pH, and chloride concentration. Temperature is the most effective environmental variable based on numerous studies. Cold regions material problems are many, and it is basically known that several alloys which show ductile behavior at room temperature face to become brittle under extreme conditions of low temperature or high rate of deformation [2]. The temperature range of practical interest for most of the cryogenic application is -60 and 0°C (Exploration and production of oil and gas have begun to take place in climates down to -60°C). At present, the knowledge necessary to prevent brittle fracture, which is fatal in engineering application, is far from complete. There is an obvious lack of data on the mechanical behavior of austenitic stainless steels in chloride solutions at the extreme cold environment. Most of the available information regarding the corrosivity induced by chloride solutions are at high temperatures [18]. The aim of the work is the study of the rate of growth of stress corrosion cracking of traditional 304L austenitic stainless steels exposed to extremely low temperatures in chloride solutions.

2. Material

The steel specimens were prepared, using 30 mm thick plates of 304 L austenitic stainless steel. Table 1 shows the chemical composition properties of the specimens

Table 1. Chemical composition steel specimen

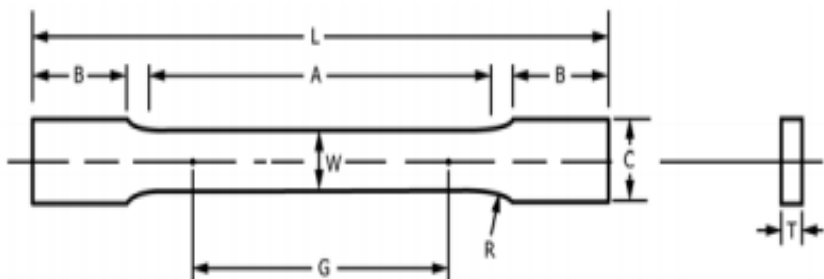
C	Mn	A P	S	Si	Cr	Ni	Cu	Mo	Pb	Ca	Sn	
%wt.	0.052	0.084	0.021	0.01	0.49	18.25	9.51	0.21	0.18	<0.001	0.11	0.006

3. Method

Many experimental techniques can be used to determine, thermal, static and dynamic properties of materials under very low temperatures, like drop weight, tension, thermal con-

ductivity, etc. in this study the impact of exposure to very low temperatures on mechanical properties of 304 stainless steel are studied under a tensile load. To maintain the desired temperature, all tests were conducted in an environmental chamber supplied with a temperature controller used to adjust the flow rate of liquid nitrogen, and the data were acquired and analyzed at each temperature.

The cryogenically treated specimens were immersed in deaerated 1 M NaCl solution in an open circuit potential cell for 1 hour. The specimens were dried kept in a desiccator until used for testing. Fig. 1 shows the stranded shape of tension specimen.



G—Gauge length: 50 mm; W—Width 12.5 ± 0.2 mm; T—Thickness of material 0.5 mm; R—Radius of fillet, 12.5 mm; L—Overall length, 200 mm; A—Length of reduced parallel section, 57 mm; Length of grip section, 50 mm; C—Width of grip section, 20 mm

3.1. Tensile test

Universal testing machines (100 Series Universal Test Machines, Testresources, US, loads up to 10 kN (2,250 lbf)). This series includes five load frames, four actuators, two controllers, three software levels and load cells to the test requirements. Fig. 2 shows the experimental equipment used for tensile stress tests.



Fig. 2. Tension-compression equipment

Displacement control was applied to the tensile test at all temperatures, and a quasi-static strain rate of 2×10^{-3} /s was applied. In this process, liquid nitrogen is used for extreme cooling in an environmental chamber. In this chamber, liquid nitrogen is passed over the shaped specimens for 90 minutes to reduce the temperature from room temperature to 0, -15, -30, -45 and -60 °C. The chamber will be maintained at the desired temperature for 10 hours and leave for getting back to ambient temperature naturally. The specimens of 16 cm^2 area immersed in the solution, were used to obtain the data of electrochemical noise. The second group of specimens was used to collect the electrochemical noise data during localized corrosion; those were with 22 cm^2 surface area immersed in the chloride solution under tension conditions. The data of signals created by electrochemical noise were acquired at 4 Hz frequency. The reference electrode was used in this test represented by calomel electrode.

4. Results and discussion

4.1. Dynamic load-displacement behavior

Figure 3 shows the dynamic load –displacement results of the immersed specimens at different low temperatures to determine the effect of high loading rates on 304 SS performance. It is observed that the behavior at low temperatures is completely different from that at ambient and high temperatures that have been studied earlier [19-22]. The effect of temperature on dynamic load–displacement curves of 304 SS obtained during instrumented impact experiments is oscillatory. Fig. 3 showed overlap fluctuation of the load signal due to the typical dynamic effects of tension loading [23]. It also shows that the highest displacement occurs is 0.17 mm at 0°C with the loading of 40,000 N. The displacement becomes less at lower temperatures because of brittleness behavior [24]. At higher temperature, it becomes more ductile and displacement increases due to the expansion of 304 SS.

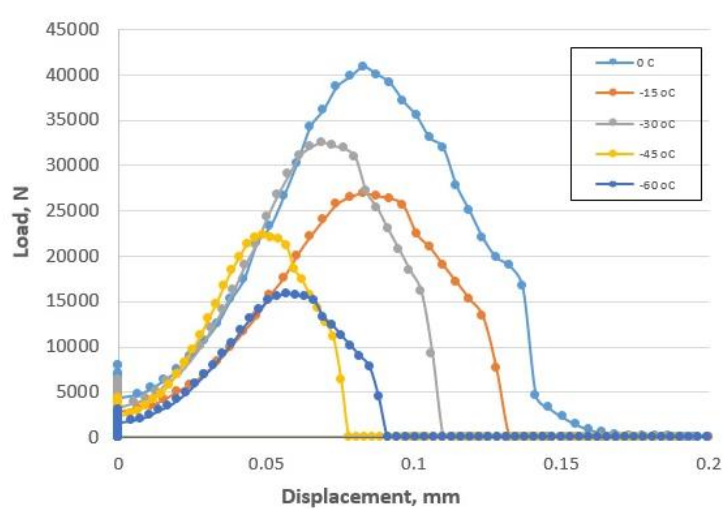


Fig. 3. Dynamic load vs. displacement curves for immersed 304 SS at different low temperature

Fig. 4 shows the effect of temperature on dynamic load-displacement curves for the dry 304 SS specimens.

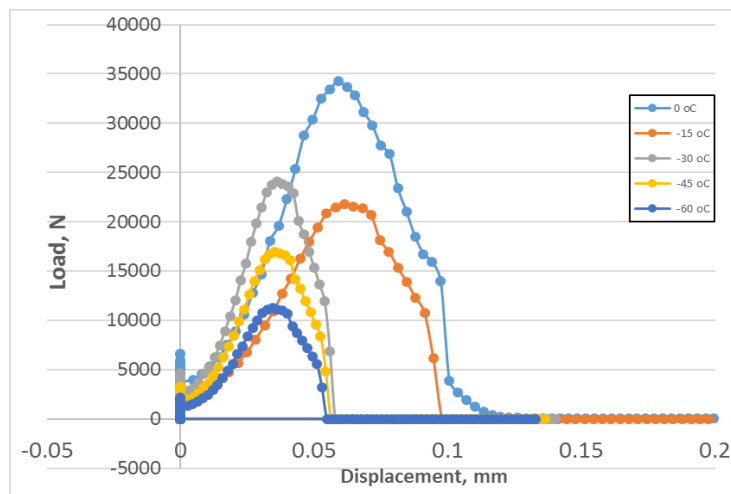


Fig. 4 Dynamic load vs. displacement curves for dry 304 SS at different low temperature

The metal strength and modulus can degrade with increasing temperature [25]. However, testing at low temperature revealed high strength and modulus. Figure 4 shows less oscillation in load-displacement curves and the lowest displacement, 0.05 mm, at -60°C. Although the 304 SS creeps under a sustained load, it can be designed to perform satisfactorily. The fiber itself is regarded as an isotropic material and has a lower thermal expansion coefficient than that of steel [26].

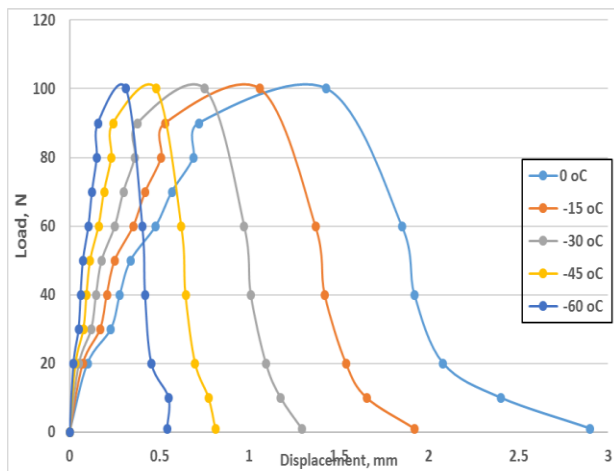


Fig. 5. Static load vs. displacement curves for immersed 304 SS at different low temperature

4.2. Static load-displacement behavior

Response to the static load applied on immersed 304 SS is shown in Figure 5, which represents load-displacement curves obtained by the impact tester at different low temperatures. It is evident that response to static load is more stable than the response to dynamic load. All curves have similar trends and exhibit the highest displacement, 2.9 mm, at 0°C.

The behavior follow fourth order polynomial as follow:

$$D = a + bl + cl^2 + dl^3 + el^4 \quad (1)$$

where D: Displacement, mm and l is static load, N.

The numeric values of polynomial coefficients are listed in Table 2:

Table 2. Polynomial coefficients of static load-displacement curves for immersed 304 SS at different low temperatures

Temperature	a	b	c	d	e	R ²
0°C	2.216	129.28	30.401	80.865	18.973	0.9675
-15°C	5.334	118.84	233.85	366.57	110.33	0.9831
-30°C	5.4175	164.59	479.42	1050.4	447.37	0.9825
-45°C	5.1102	269.51	1084.3	3834.4	2565.7	0.9811
-60°C	5.8474	367.1	3102.8	-15755	16181	0.979

Fig.6 shows the static load-displacement behavior at different low temperatures for the dry 304 SS. As for the dynamic response, the displacement due to applying the static load is much less than the immersed metal. This is due to shrinkage of the structure and transformation from ductile to brittle metal. Table 3 lists the polynomial coefficients of equation 2 for dry 304 SS.

Table 3. Polynomial coefficients of static load-displacement curves for the dry 304 SS at different low temperatures

Temperature	a	b	c	d	E	R ²
0°C	18.089	230.05	96.935	47.677	21.122	0.9746
-15°C	1.4285	336.73	346.27	20.15	64.81	0.9134
-30°C	1.3708	387.59	227.25	-787.65	588.19	0.9542
-45°C	4.7264	896.95	2959.8	3001.1	846.97	0.9219
-60°C	-4.781	1383.2	-7040.5	11038	4849.9	0.921

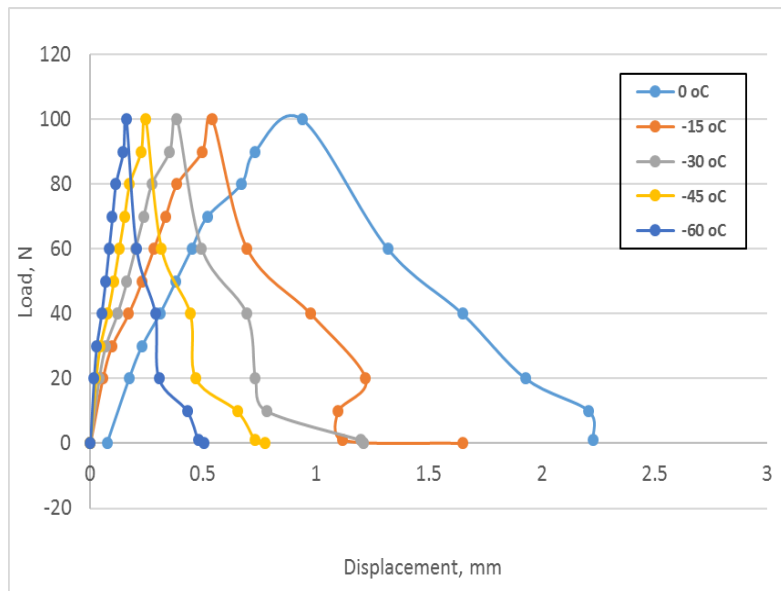


Fig. 6. Static load vs. displacement curves for dry 304 SS at different low temperature

4.3. Stress corrosion cracking

A microstructure study was conducted on the failed immersed specimens loaded with 10 kN. Several small cracks have been observed that resulted in specimen failure. Most of the fracture is brittle as shown in Figure 7 that is account for 70% of the fracture, whereas the rest of the surface fracture was ductile as shown in Figure 8 due to applying the load at 10 kN.

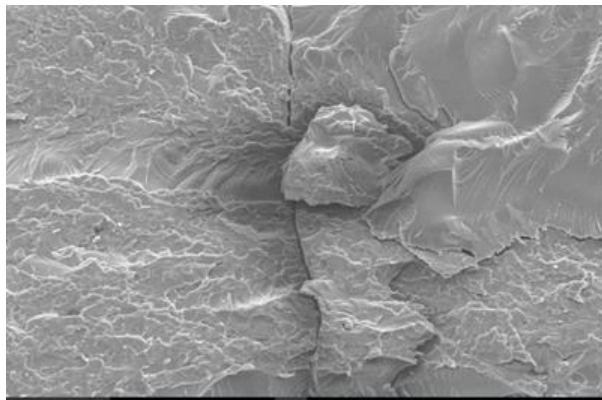


Fig. 7. Brittle part of fracture for the immersed 304 SS at -60°C

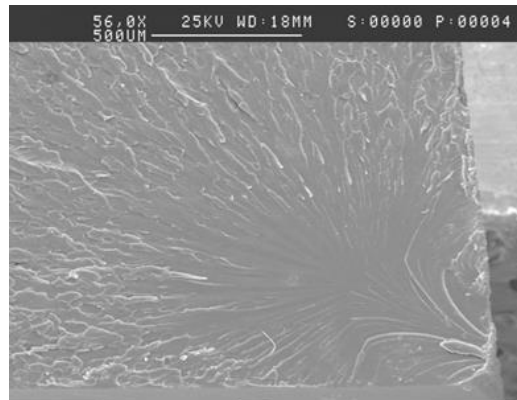


Fig. 8. Ductile part of fracture for the immersed 304 SS at -60°C

5. Conclusions

The mechanical characteristics of 304 stainless steel immersed in chloride solutions under static and dynamic loading have been investigated through tensile tests by various sub-zero temperatures and SEM characterizations in the present study. Immersion of the tested specimens in chloride solution reduces the tensile strength by approximately quarter at zero temperature under static loading. Also the ductile properties were reduced however, the tensile elongation was maintained at extreme low temperatures. Under dynamic loading, tensile elongation was enhanced by immersion in chloride solution for all sub-zero temperatures examined. It is likely to be more effective at sub-zero. However, the results of microstructure showed that immersion in chloride solutions has a significant impact of immersion on ductility. It showed major reduction in ductility that resulted in brittle failure.

Declarations**Authors' contributions**

Saad Ahmed made substantial contributions to the present study specifically in the conception, experimental works, and data analysis. He also administrates the SEM test of the failed specimens and prepared them for testing. Since he is the principal author of the manuscript, he was involved in the drafting of the manuscript, reading and approved the final manuscript.

Competing interests

The author declare that they have no competing interests.

Funding

This work was funded by University of Tikrit, Iraq.

Availability of supporting data

Data will not be shared during the current study because of an agreement with the funder.

References

- [1] McHenry HI. The properties of Austenitic Stainless Steel at Cryogenic Temperatures. Fracture and Deformation Division National Bureau of Standards. Boulder, Colorado. 1987
- [2] Part 1: Program rational and test plan. The behavior of Materials at Cold Region Temperatures. Special Report July 1988.
- [3] Alyousif OM, Nishimura R. Stress corrosion cracking and hydrogen embrittlement of sensitized austenitic stainless steels in boiling saturated magnesium chloride solutions. *Corros. Sci.*, 2008; 50: 2353–2359.
- [4] Alyousif OM, Nishimura R. The stress corrosion cracking behavior of austenitic stainless steels in boiling magnesium chloride solutions. *Corros. Sci.*, 2007; 49: 3040–3051.
- [5] Alyousif OM, Nishimura R. The effect of test temperature on SCC behavior of austenitic stainless steels in boiling saturated magnesium chloride solution. *Corros. Sci.*, 2006; 48: 4283–4293.
- [6] Lai CL; Tsay LW; Kai W; Chen C. Notched tensile tests of cold-rolled 304L stainless steel in 40 wt. % 80 _C MgCl₂ solution. *Corros. Sci.*, 2009; 51: 380–386.
- [7] Lai CL; Tsay LW; Ka, W; Chen C. The effects of cold rolling and sensitisation on hydrogen embrittlement of AISI 304L welds. *Corros. Sci.*, 2010; 52: 1187–1193.
- [8] Li WJ, Young MC, Lai CL, Ka W, Tsay LW. The effects of rolling and sensitization treatments on the stress corrosion cracking of 304L stainless steel in the salt-spray environment. *Corros. Sci.*, 2013; 68: 25–33.
- [9] Raman R, Siew W. Stress corrosion cracking of austenitic stainless steel in nitrite-containing chloride solutions. *Materials* 2014; 7: 7799–7808.
- [10] García C, Martín F, Tiedra PD, Heredero JA, Aparicio ML. Effects of prior cold work and sensitization heat treatment on chloride stress corrosion cracking in type 304 stainless steels. *Corros. Sci.*, 2001, 43, 1519–1539.
- [11] García C, Martín F, Tiedra PD, Alonso S, Aparicio ML. Stress Corrosion Cracking Behavior of Cold-Worked and Sensitized Type 304 Stainless Steel Using the Slow Strain Rate Test. *Corrosion*. 2002; 58(10): 849–857.
- [12] Ghosh S, Kain V. Effect of surface machining and cold working on the ambient temperature chloride stress corrosion cracking susceptibility of AISI 304L stainless steel. *Mater. Sci. Eng. A*, 2010; 527: 679–683.
- [13] Ghosh S; Kain V. Microstructural changes in AISI 304L stainless steel due to surface machining: Effect on its susceptibility to chloride stress corrosion cracking. *J. Nucl. Mater.*, 2010; 403: 62–67.
- [14] Morris JW Jr. Steels: For Low Temperature Applications. Report. December 1993
- [15] Newman RC, Whitney WR. Understanding the Corrosion of Stainless Steel. *Corrosion*, 57(12): 1030–104.

- [16] Che-sheng chen P, Shinohara T, and Tsujikawa S. Applicability of the Competition Concept in determining the Stress Corrosion Cracking Behaviour of Austenitic Stainless Steels in Chloride Solution. *Zairyo-to-Kankyo*, 1997; 46: 313-320.
- [17] Geary EA. Peening and Stress Corrosion Cracking in Stainless Steel. HSL Report MM/07/03, March 2009.
- [18] Kasri R. Olive JM, Puiggali M, Desjardinse D. Stress corrosion cracking of austenitic stainless steels in H_3BO_3 + NaCl solutions between 100°C and 200°C. *Corrosion Science*, 35; 1-4: 1993, 443-

To whom correspondence should be addressed: Dr. Saad R. Ahmed, Mechanical Engineering Department, Tikrit University, Tikrit, Iraq

BIODIESEL PRODUCTION FROM KITCHEN LARD VIA TRANSESTERIFICATION BY MAGNETIC SOLID BASE CATALYST

Sen Qiao^{1,2}, Rui Wang^{1,2*}

¹ School of Environmental Science and Engineering, Shandong University, No. 27 Shanda South Road, Jinan 250199, China

² Suzhou Research Institute of Shandong University, No. 388 Ruoshui Road of Industrial Park, Suzhou, 215123, China

Received March 17, 2018; Accepted May 11, 2018

Abstract

A magnetic solid base catalyst ($K/CeO_2-Fe_2O_3$) was successfully synthesized by sol-gel method which was used to catalyze transesterification of stable kitchen lard and methanol to produce biodiesel. The main components of kitchen lard were analyzed by gas chromatography-mass spectrometer (GC-MS) and the catalysts were characterized by Brunauer-Emmett-Teller (BET), Fourier transform infrared spectroscopy (FT-IR), scanning electron microscope with energy dispersive X-ray (SEM-EDX) and vibrating sample magnetometer (VSM). Results demonstrated that the catalyst had granular nano-structures and superparamagnetism. The optimum conditions for transesterification were found as follows: reaction temperature of 60°C, methanol/oil molar ratio of 6:1 and catalyst amount of 1.5 wt%, corresponding to a maximum biodiesel yield of 92.02% in reaction time of 3 h. Recovery experiment results indicated that the magnetic catalyst maintained high activity after four times' use with a biodiesel yield of more than 84.53%, which would provide the possibility of a potential application to produce biodiesel from waste cooking oil.

Keywords: biodiesel; magnetic recovery; transesterification; kitchen lard.

1. Introduction

As a potential substitute of petroleum diesel, biodiesel whose essential component is long chain fatty acid methyl esters (FAME) has stood out in recent decades [1]. Due to its high oxygen content, high flash point, little of sulfur and aromatic content, biodiesel is a kind of renewable, clean, non-toxic and efficient fuel [2]. At present, the main method for industrial production of biodiesel is transesterification of renewable feedstocks like oils and animal fats with methanol or ethanol under the action of the catalyst [3-4]. The transesterification behavior is divided into three synchronous reversible reactions, in which glycerol is collected as byproduct with the production of biodiesel [5].

Generally speaking, the current feedstocks for commercial production of biodiesel are pure refined edible oils such as soybean, canola, sunflower, palm, castor and peanut oil. However, their high price and the threat to worldwide food reserves and safety are major impediments in commercialization of biodiesel [6]. As novel and less costly oily feedstocks, the non-edible oils, microalgae, waste cooking oil, animal fats, and other sources can take place of edible oils for biodiesel production [7-8].

Previously, homogeneous acids and bases including HCl, H_2SO_4 , NaOH, and CH_3ONa were used as catalysts for the transesterification reaction, and they have already been conducted on a commercial scale using [9]. Unfortunately, there are many problems for these homogeneous catalysts such as high corrosiveness, difficulty for recovery and large amount of wastewater production [10]. In contrast, heterogeneous catalysts used for biodiesel production by transesterification reactions have been found to be easily separated from the reaction system,

thereby simplifying the production process [11]. Liu *et al.* [12] used CaO as a solid base catalyst for transesterification from soybean oil to biodiesel. Under optimal conditions, the biodiesel yield could exceed 95% at 3 h. Shu *et al.* [13] synthesized a solid acid catalyst from sulfonation of an incompletely carbonized organic compound, and the maximum conversion rate reached 94.8% after 4.5 h.

As a basic catalyst, cerium oxide (CeO_2) is not active in transesterification reactions, but it is a good candidate as carrier for homogeneous acid or base catalysts to improve the catalytic efficiency because of its larger specific surface with plenty of active sites and high catalytic activity [14]. Wong *et al.* [15] synthesized solid base $\text{CaO}-\text{CeO}_2$ mixed oxide catalysts via transesterification from palm oil to produce biodiesel. The biodiesel yield could achieve 95% by this catalyst under the optimum reaction conditions. Similarly, Ca-doped Ce-SBA-15 catalyst was successfully synthesized by using direct synthesis of Ce-incorporated SBA-15 followed by impregnation of CaO for biodiesel production [16]. However, the studies on transesterification process using $\text{KOH}-\text{CeO}_2$ catalyst are scarce.

In this paper, the fat pork was used to refine lard which was to simulate stable waste cooking oil to be used as the raw material for transesterification. And the magnetic solid base catalyst $\text{K}/\text{CeO}_2-\text{Fe}_2\text{O}_3$ was synthesized by sol-gel method to catalyze this reaction. The transesterification of kitchen lard with methanol to biodiesel using KOH loaded on magnetic ceria as solid base catalyst has been studied by investigating the role of reaction time, catalyst dosage and ethanol-to-oil molar ratio. The main components of kitchen lard were analyzed by gas chromatography-mass spectrometer (GC-MS) and the synthesized solid base catalysts were characterized by Brunauer-Emmet-Teller method (BET), fourier transform infrared (FT-IR) spectra, scanning electron microscope-energy dispersive X-ray (SEM-EDX) and vibrating sample magnetometer (VSM). The characterization results demonstrated that the mesoporous CeO_2 which was magnetized by Fe_2O_3 and loaded by KOH was successfully synthesized. The effect of its separation and reuse was remarkable. The studies showed that the biodiesel yield could reach 92.02% under the optimal preparation and reaction conditions. The catalyst could be recycled and used more than 4 times with high efficiency.

2. Materials and methods

2.1. Materials

Fat pork was obtained from supermarket (Jinan, China). Polyoxyethylene ether (Brij35) was purchased from Macklin (Shanghai, China). Ceric ammonium nitrate ($\text{Ce}(\text{NH}_4)_2(\text{NO}_3)_6$), ethanol, methanol, n-hexane, ammonia solution (25 wt%), potassium hydroxide (KOH), ferrous chloride tetrahydrate ($\text{FeCl}_2 \cdot 4\text{H}_2\text{O}$) and six hydrated ferric chloride ($\text{FeCl}_3 \cdot 6\text{H}_2\text{O}$) were procured from Sinopharm (Shanghai, China). Heptadecanoic acid methyl ester, hexadecanoic acid methyl ester, oleic acid methyl ester, octadecanoic acid methyl ester, 11-octadecenoic acid methyl ester and 9, 12-octadecadienoic acid methyl ester were purchased from J&K (Beijing, China). All the chemicals were analytical reagent and used without further purification. Deionized water was used for dissolution and dilution of chemical solutions.

2.2. Preparation of catalyst

The CeO_2 carrier was synthesized by soft template method [17]. Brij35 and $\text{Ce}(\text{NH}_4)_2(\text{NO}_3)_6$ were mixed with a molar proportion of 2:1 and dissolved into 50% ethanol solution. Then, 25 wt% ammonia was added drop-wise into the solution to regulate pH to 10.0. The resultant solution was filtered and washed with ethanol and deionized water twice respectively. Then it was stirred for 3 h and statically aged for 2 d. The collected residue was dried in a vacuum oven at 80°C for about 6 h and then calcined at 350°C in a muffle furnace.

The $\text{K}/\text{CeO}_2-\text{Fe}_2\text{O}_3$ catalyst was obtained by sol-gel method. The obtained CeO_2 carrier was dissolved into deionized water. The solution was stirred for 2 h and treated by sonication for 0.5 h. The $\text{FeCl}_3 \cdot 6\text{H}_2\text{O}$ and $\text{FeCl}_2 \cdot 4\text{H}_2\text{O}$ with a mole ratio of 2:1 were simultaneously added into the above CeO_2 solution with constantly stirring by polytetrafluoroethylene agitator for about 1 h. The ammonia was added into the above solution at room temperature until the pH of the

solution was maintained at about 11.0. After 1 h of strong stirring, the resultant solution was aged for 2 h. Then it was dialyzed over deionized water until the washing solution became neutral. After being freeze-dried and shattered, magnetic carrier $\text{CeO}_2\text{-Fe}_2\text{O}_3$ was synthesized. The $\text{CeO}_2\text{-Fe}_2\text{O}_3$ was dipped into aqueous solutions of KOH with loading amount of 40% and subsequently vacuum dried at 120 °C for 12 h. After being crushed into powder with a mortar, the dried material was calcined in a muffle furnace at 300°C for 3 h to obtain the final magnetic solid base catalyst $\text{K/CeO}_2\text{-Fe}_2\text{O}_3$.

2.3. Transesterification reaction

In this article, kitchen lard was used to simulate stable waste cooking oil. Raw material was refined from the fat pork in a pan. The kitchen lard was filtered to remove the impurities of fat pork after the frying process. Before production of biodiesel, the filtered lard was pre-treated by heating at a 90°C water bath pot for about 2 h. The process of transesterification was carried out in a 250 mL neck flask with a certain proportion of lard, methanol and catalyst. The neck flask was put into a water bath equipped with a stirrer and a water-cooled condenser at certain temperature for transesterification. The solution was stirred for 4 h, and the upper liquid phase was sampled every 0.5 h. After rotary evaporation and centrifugation, the collected samples became biphasic. The purified biodiesel was produced in the upper phase transformed from kitchen lard.

After transesterification process was completed, the magnetic catalyst was separated and recycled from the mixture by a permanent magnet. Then, the recycled catalyst was cleaned by methanol and dried in an oven at 70°C for about 5 h. Finally, it was put into a desiccator for further use.

The products was dissolved into n-hexane and analyzed by a gas chromatograph (GC, SP-6800) equipped with a capillary column (AT-FFAP: 30 $\text{m}\times\Phi$ 0.32 mm \times 0.33 μm) and a flame ionization detector (FID) detector. The yield of fatty acid methyl ester (FAME) can be calculated by using the following equation:

$$Y_{\text{FAME}} = \frac{\sum f_e A_e}{A_i} \times \frac{m_i}{m_e} \times 100\%$$

where, Y_{FAME} is the yield of fatty acid methyl ester, f_e is the correction factor of each fatty acid methyl ester that biodiesel contains, A_e is the peak area of corresponding fatty acid methyl esters, A_i is the peak area of the internal standard, m_i is the mass of internal standard and m_e is the mass of fatty acid methyl esters.

The recovery of the catalyst is described as follows:

$$R_c = \frac{w_1}{w_2} \times 100\%$$

where, R_c is the recovery of catalyst, w_1 is the weight of the recovery catalyst and w_2 is the weight of the added catalyst.

2.4. Biodiesel sample analysis

Gas chromatography-mass spectrometer (GC-MS) method was used to determine the main components of biodiesel. The samples were analyzed by a GCMS-QP2010Plus (Shimadzu, Japan) equipped with a flame ionization detector (FID) and an Rxi-Wax capillary column (30 $\text{m}\times\Phi$ 0.25 mm \times 0.25 μm). The total flow rate of carrier gas (helium) was maintained at 44.0 mL/min. The final product was injected at 250°C with a split ratio of 1:44. At the same time, the temperature of detector was also 250°C. At first the oven temperature was fixed at 160°C for 1min. Next, the temperature was increased to 200°C at 5°C /min and then kept for 1 min. Last, it was increased to 230°C at 2°C /min and then held it for 5 min.

2.5. Catalyst characterization

The specific surface area was calculated from the adsorption curve by the Brunauer-Emmett-Teller (BET) method using ASAP2020 (Micromeritics, USA). The mesoporous volume and pore size distribution were calculated according to the Barrett-Joyner-Halenda (BJH)

method from the desorption branch of the isotherm. FT-IR spectra of the samples were carried out with ALPHA-T Fourier transform infrared spectrometer (BRUKER Corp, Germany). Scanning electron microscope with energy dispersive X-ray (SEM-EDX) analysis was performed to examine the surface structure and morphology of the catalyst with JSM7610F (Hitachi, Japan). Magnetization curves were measured on a vibrating sample magnetometer (VSM) on a LDJ9500 instrument (USA) with a magnetic field of 10,000 Oe.

3. Results and discussions

3.1. Analysis and characterization

3.1.1. GC-MS of biodiesel

The main components of biodiesel detected by GC-MS are presented in Fig.1. Table.1 shows main components and their content. They were hexadecanoic acid methyl ester, oleic acid methyl ester, octadecanoic acid methyl ester, 11-octadecenoic acid methyl ester, 9, 12-octadecadienoic acid methyl ester respectively and a small amount of other fatty acid methyl esters.

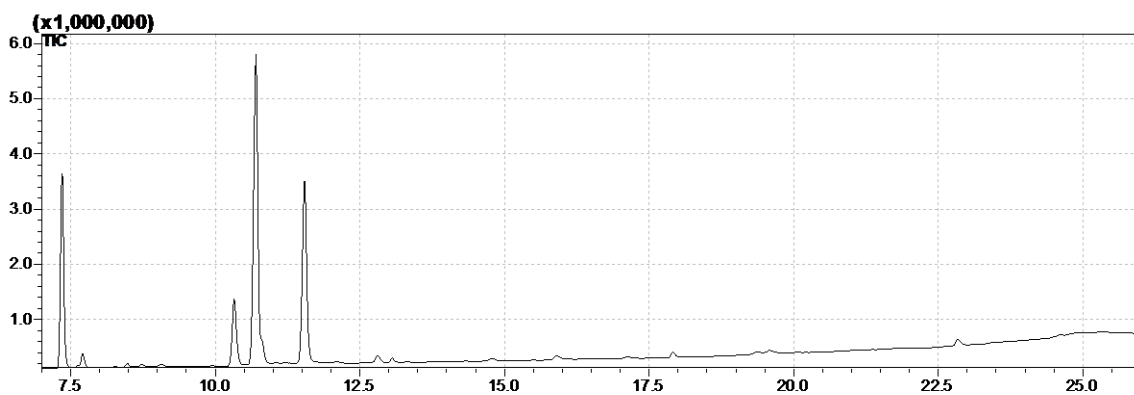


Fig.1 GC-MS spectrum of produced biodiesel

Table.1 GC-MS date of the produced biodiesel

Peak no.	Retention time (min)	Identified methyl esters	Corresponding fatty acids	Composition (%)
1	7.36	Hexadecanoic acid methyl ester	C16:0	19.59%
2	7.77	Oleic acid methyl ester	C18:1	1.53%
3	10.32	Octadecanoic acid methyl ester	C18:0	8.62%
4	10.69	11-Octadecenoic acid methyl ester	C18:1	42.75%
5	11.55	9,12-Octadecadienoic acid methyl ester Other fatty acid methyl esters	C18:2	23.77%
				3.74%

3.1.2. BET

The specific surface area, pore volume and pore size of CeO_2 before and after calcination are presented in Table 2. This carrier has the specific surface area of $169.98 \text{ m}^2/\text{g}$, pore volume of $0.078 \text{ cm}^3/\text{g}$ and average pore diameter of 3.24 nm .

The N_2 adsorption-desorption isotherms and pore diameter distributions of the CeO_2 carrier are shown in Fig.2. According to the IUPAC classification, the N_2 adsorption-desorption isotherms belong to type IV with an H2 hysteresis loop which is associated with the capillary

condensation of typical mesoporous materials [18]. The main pore diameters are mainly distributed in the range of 0-10 nm. This also proves that the synthesized CeO₂ is mesoporous.

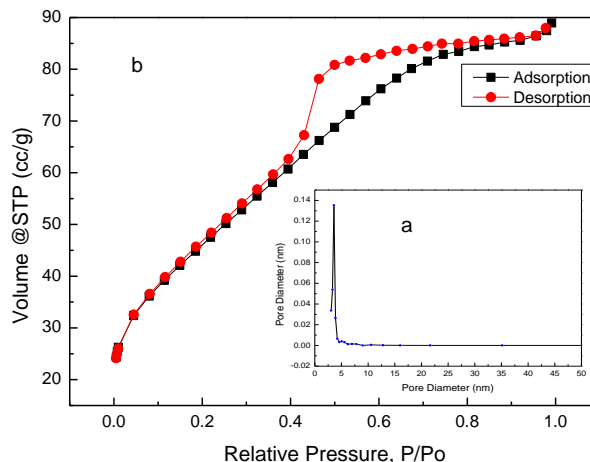


Fig.2. CeO₂ after being calcinated at 350°C (a) pore size distribution curves, (b) nitrogen adsorption-desorption isotherm

Table.2 Physical properties of CeO₂ before and after calcination

Type	Specific surface area (m ² /g)	Pore volume (cm ³ /g)	Most probable pore size (nm)	Average pore width (nm)
Before calcination	163.759	0.068	3.067	3.09612
After calcination	169.98	0.078	3.31	3.24

3.1.3. FT-IR

The functional groups of the materials are elucidated by FT-IR absorption spectra of in Fig.3. All samples show characteristic absorption band at 3447 and 1625 cm⁻¹, which represent the stretching vibration and bending vibration of O-H, respectively. The broad bands at 1120 and 1385 cm⁻¹ be attributed to the presence of C-O and C-H. The existence of the peak at 515 cm⁻¹ is the telescopic vibration of Ce-O. The characteristic bands of Fe-O-Fe stretching vibration can be found around 600 cm⁻¹, which indicates the catalyst contains magnetic components. The peak at 487 cm⁻¹ can be seen as the lattice vibration of the metal oxide KO_x produced from the decomposition of KOH [19].

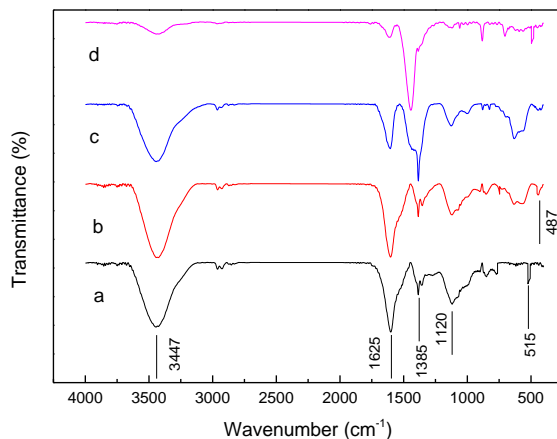


Fig.3. FT-IR absorption spectra of (a) CeO₂, (b) magnetic CeO₂, (c) precursor, (d) magnetic catalyst of K/CeO₂-Fe₂O₃

3.1.4. SEM-EDX

Fig.4a and Fig.4b show the surface micrographs of CeO_2 and $\text{K}/\text{CeO}_2\text{-Fe}_2\text{O}_3$. Fig.4c and Table.3 are the EDX image and analysis of $\text{K}/\text{CeO}_2\text{-Fe}_2\text{O}_3$.

The micrograph of CeO_2 exhibited massive structure and $\text{K}/\text{CeO}_2\text{-Fe}_2\text{O}_3$ displayed cluster shape particles of mutual accumulation evenly. The surface element contents of catalysts are listed in Table.3. O, K, Ce, Fe and some minor components can be seen in the EDX spectra. The contents indicated that the K and Fe were well loaded on the surface of CeO_2 .

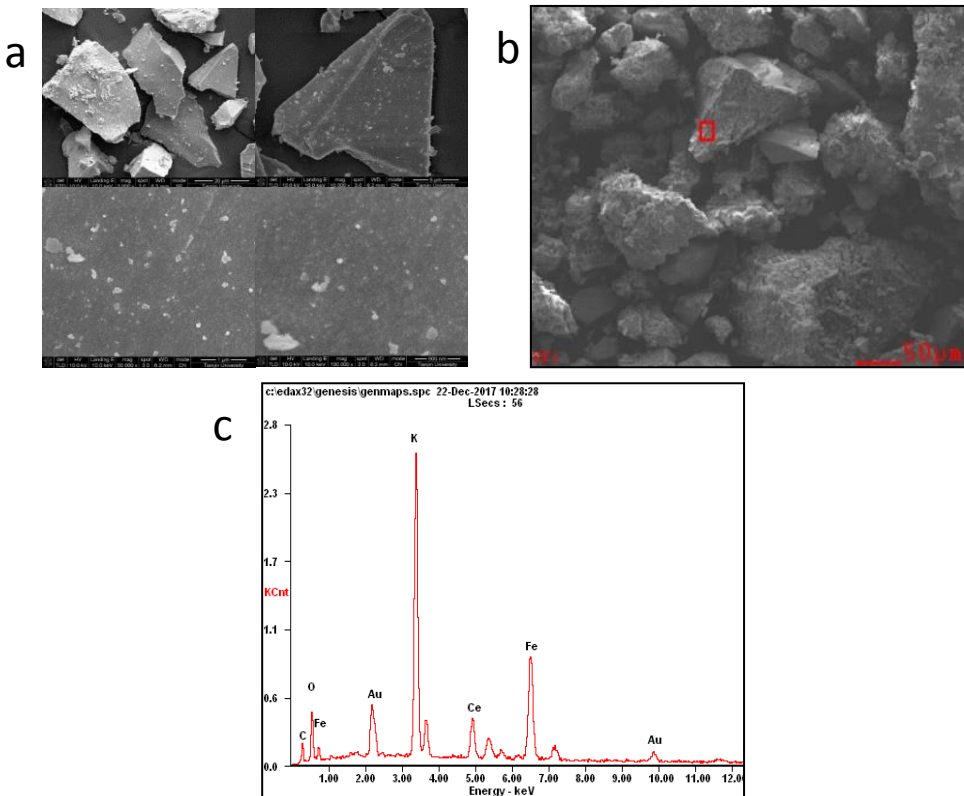


Fig.4 SEM of images of (a) CeO_2 , (b) magnetic catalyst of $\text{K}/\text{CeO}_2\text{-Fe}_2\text{O}_3$ and EDX image of (c) magnetic catalyst of $\text{K}/\text{CeO}_2\text{-Fe}_2\text{O}_3$

Table.3 EDX analysis of $\text{K}/\text{CeO}_2\text{-Fe}_2\text{O}_3$

Element	Wt %	At %
O	10.46	29.06
K	30.63	34.82
Ce	22.50	7.14
Fe	36.41	29.98

3.1.5. VSM

The magnetic properties of $\text{K}/\text{CeO}_2\text{-Fe}_2\text{O}_3$ were measured using VSM and the resulting magnetization curves are presented in Fig.5 which shows the magnetic hysteresis loops for different recovery times. It can be concluded that these catalysts possessed ferromagnetic characteristic and exhibited superparamagnetism, because all curves go through the zero point. As the number of recovery increases, the saturation magnetization becomes weaker, and the saturation magnetization changed from 10.73 emu/g to 7.29 emu/g after four times' recycle, which might be the loss of the magnetic substrates.

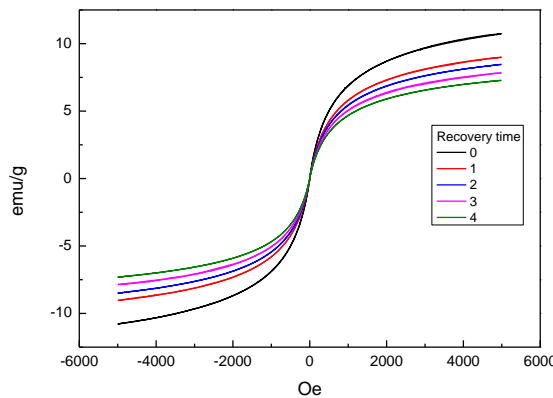


Fig.5 VSM images of different recycle time

3.2. Influence of reaction parameters

3.2.1. Effect of the transesterification conditions

To determine the effect of transesterification conditions, three main factors: reaction temperature, methanol/oil molar ratio and catalyst amount were investigated. Fig.6. exhibits the effect of the transesterification conditions under the optimum preparation conditions of catalyst.

The variations of biodiesel yield after 3h under different reaction temperature are shown in Fig.6a with methanol/oil molar ratio of 6:1 and catalyst amount of 1.5%. It can be seen that with the increment of reaction temperature from 50°C to 60°C, the yield of biodiesel rise from 82.41% to 92.02%. However, as reaction temperature increased continuously, the biodiesel yield decreased significantly because the methanol bubbles out at 64.7°C. Hence, the optimum reaction temperature for the transesterification is 60°C.

Fig.6b shows the variations of biodiesel yield of different methanol/oil molar ratio with catalyst amount of 1.5% under 60°C after reacting for 3h.

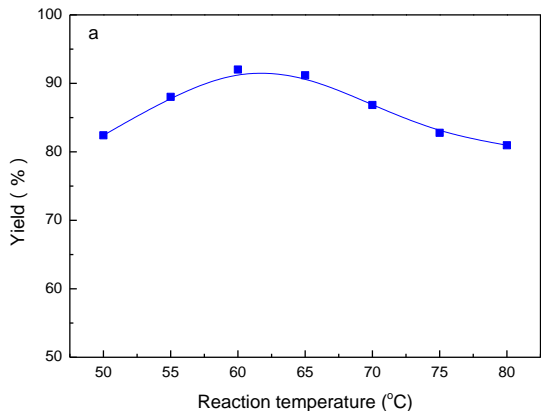


Fig.6. Effect of (a) reaction temperature on yield

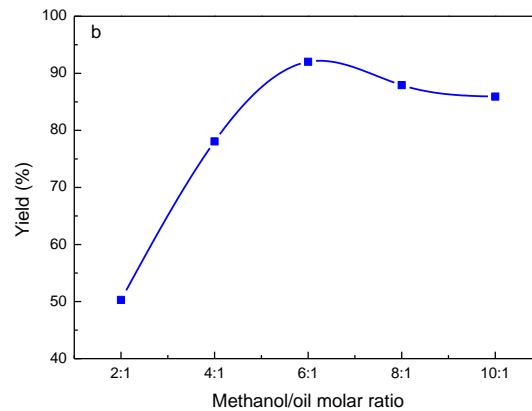


Fig.6. Effect of (a) reaction temperature, (b) methanol/oil molar ratio on yield

The biodiesel yield rose from 50.29% to 92.02% with the methanol/oil molar ratio increased from 2:1 to 6:1. However, the yields decreased gradually when the methanol/oil molar ratio rose to 8:1 and 10:1. Because the transesterification reaction is a reversible reaction, excessive methanol/oil molar ratio more than theoretical value of 3:1 is necessary to promote the reaction. The equilibrium of the reaction moves forward with the methanol/oil molar ratio improved to 6:1. Excessive use of methanol will dilute the whole reaction system, causing the deactivation of catalyst and reducing the contact area of oil and catalyst. Besides, too much amount of methanol might make it difficult to separate biodiesel and glycerol. Thus, the optimum methanol/oil molar ratio was determined as 6:1.

The biodiesel yield under different catalyst dosage is presented in Fig.6c with methanol/oil molar ratio of 6:1 under 60°C after reacting for 3h. The yield of biodiesel increased from 33.64% to 92.02% with the increment of the catalyst dosage from 0.5wt% to 1.5wt%. While the amount of catalyst was 1.5wt%, the highest yield of biodiesel was reached. Further increase on the catalyst amount will cause the decrease of the yield of biodiesel, because excessive catalyst brings out saponification which will pollute the biodiesel and make it difficult to recover the catalyst. Therefore, the optimum catalyst amount was determined as 1.5wt%.

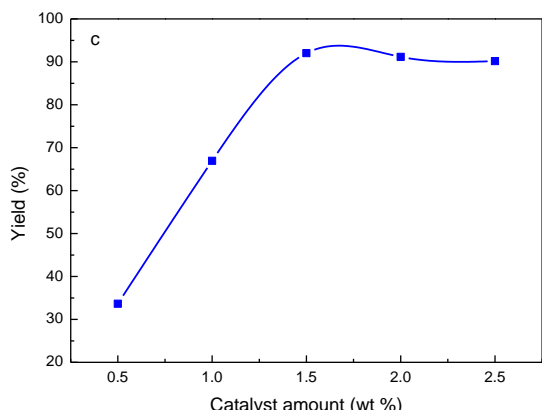


Fig.6. Effect of (c) catalyst amount on yield

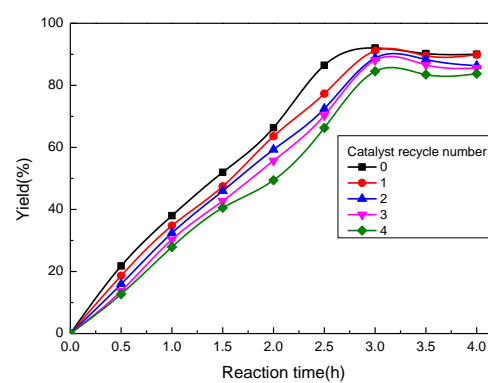


Fig.7. Effect of catalyst cycle number on yield

3.2.2. Reusability of magnetic catalyst

Fig.7 displays the change of biodiesel yield among four times' recycles. It can be seen that the biodiesel yield slightly reduced because of the loss of active components of the catalyst with the number of recycling increased during the processes of reaction and separation. Thus, this magnetic solid base catalyst was proved to maintain considerable catalytic activity after recovery.

4. Conclusions

A magnetic solid base catalyst K/CeO₂-Fe₂O₃ was successfully prepared by sol-gel method and used to convert kitchen lard to biodiesel via transesterification. Kitchen lard was used to simulate stable waste cooking oil to explore the catalytic performance and recyclability of the magnetic solid base catalyst. Based on our experiments, the maximum biodiesel yield of 92.02% was achieved after 3 h under the optimum conditions as follows: reaction temperature of 60°C, methanol/oil molar ratio of 6:1, catalyst amount of 1.5 wt%. After being recycled for four times, the biodiesel yield was maintained more than 84.53% due to its high activity and unique magnetic properties. In summary, K/CeO₂-Fe₂O₃ is a solid base catalyst with high catalytic activity and remarkable recyclability, which make it an ideal substitute for the traditional catalysts.

Acknowledgements

This work was supported by the Scientific & Technological Development Program of Suzhou City, China, under project number SYN201520.

References

- [1] Hassan SZ, Vinjamur M. Chem. Eng. Sci. 2014; 110: 94-104.
- [2] Patil PD, Deng S. Fuel, 2009; 88(7): 1302-1306.
- [3] Meher L C, Sagar D V, Naik S N. Renew. Sust. Energ. Rev., 2006; 10(3): 248-268.
- [4] Kondamudi N, Mohapatra S K, Misra M. Appl. Catal. A-Gen. 2011; 393(1-2): 36-43.
- [5] Verma P, Sharma MP. Renew. Sust. Energ. Rev 2016; 62: 1063-1071.
- [6] Yadav M, Singh V, Sharma YC. Energ Convers. Manage. 2017; 148: 1438-1452.
- [7] Cheng J, Qiu Y, Huang R. Bioresour. Technol. 2016; 221: 344-349.

- [8] Liu K, Wang R. Pet. Coal, 2013, 55(1): 68-72.
- [9] Lee A F, Wilson K. Catal. Today. 2015; 242: 3-18.
- [10] Fattah IMR, Masjuki HH, Kalam MA. Energ Convers. Manage. 2014; 79: 265-272.
- [11] Liu K, Wang R, Yu M. RSC Adv. 2017; 7(82): 51814-51821.
- [12] Liu X, He H, Wang Y. Fuel, 2008; 87(2): 216-221.
- [13] Shu Q, Gao J, Nawaz Z. Appl. Energ., 2010; 87(8): 2589-2596.
- [14] Yu X, Wen Z, Li H. Fuel, 2011; 90(5): 1868-1874.
- [15] Wong YC, Tan YP, Taufiq-Yap YH. Fuel, 2015; 162: 288-293.
- [16] Thitsartarn W, Maneerung T, Kawi S. Energy 2015; 89: 946-956.
- [17] Zhao X, Luo L, Liu C. Chem. Res. & Appl., 2007; 19 (8): 858-862.
- [18] da Conceição L R V, Carneiro L M, Giordani D S, et al. Renew. Energ., 2017; 113: 119-128.
- [19] Al-Abadleh H A, Al-Hosney H A, Grassian V H J. Mol. Catal. A: Chem. 2005; 228(1-2): 47-54.

To whom correspondence should be addressed: prof. Rui Wang, School of Environmental Science and Engineering, Shandong University, No. 27 Shanda South Road, Jinan 250199, China, ree_wong@hotmail.com

PREDICTION OF RESERVOIR CHARACTERISTICS IN WESTERN GHANA OILFIELD (TANO BASIN)

Prince Appiah Owusu¹, Liu Dehua², Robert Derry Nagre³

¹ Department of Civil Engineering, Kumasi Technical University, Kumasi, Ghana-

² College of Petroleum Engineering, Yangtze University, Wuhan, 430100, China;

³ Department of Chemical Engineering, Kumasi Technical University, Kumasi, 00233, Ghana

Received February 28, 2018; Accepted May 11, 2018

Abstract

The Tano Basin is one of the prospective oil fields in Western part of Ghana. Geographically, the area lies 4°46' north of latitude and about 3° west of longitude. The study dwells on the evaluation of the Petrophysical parameters of the reservoir through the modification of the extended Archie's model by Pickett. Through the technique, the reservoir Petrophysical parameters such as specific surface per unit volume, permeability, capillary pressure, bulk volume and height above free water surface have been established. The procedure uses existing resistivity model which is a function of water saturation and porosity. Resistivity is expressed as an additional function of permeability, specific surface per unit volume, capillary pressure, bulk volume and height above free water surface through the embedded water saturation model. Additionally, saturation exponent n , porosity exponent m and tortuosity factor a were evaluated in the process. The study presents a useful model of the extended Archie's model which provides a quick integration of formation Petrophysical parameters which is very significant for reservoir interpretation, prognostication and appraisal

Keywords: Tortuosity; water saturation; Capillary pressure; Resistivity; Porosity; permeability.

1. Introduction

Hydrocarbon reserves inundation is a key function in formation estimation and by large extent reserves capacity evaluation. It equally offers a lead variable in reservoir formation development and modeling. Several characteristics are employed in the evaluation of reservoirs and reserve inundation. These include water saturation, porosity, permeability, specific surface per unit volume, capillary pressure, height above free surface and bulk volume. Pickett plot presents a log-log relationship between porosity and resistivity [1]. The Petrophysical parameters indicated above are superimposed via the Pickett plot and determination of reservoir parameters of the six exploratory well in the Western Tano Basin are established. Sanyal and Ellithorpe [2] showed that Pickett plot which is combines the Archie's models results in a linear plot with the slope representing porosity exponent (m). The study presents a well work out plot embracing all the Petrophysical parameters such as water saturation, porosity, permeability, specific surface per unit volume, capillary pressure, height above free surface and bulk volume in a single plot. The combination of these parameters in a single plots presents one time simplified important information for evaluation of the reservoir.

2. Study area

In this study, three wells namely 1S-1X, 1S-3AS, 1S-4AX, ST-05, ST-06 and ST-7H were studied, Fig1. The studied wells are located in the Western Basin (Tano Basin), a sub-basin of Cape Three Point. It forms part of the larger Ivory Coast Basin in the Gulf of Guinea of West Africa. Geographically, the area lies 4°46' north of latitude and about 3° west of longitude,

east-west onshore-offshore structural basin [3]. It is precisely 35km offshore of Ghana and occupies about 3000km² Figure 1.

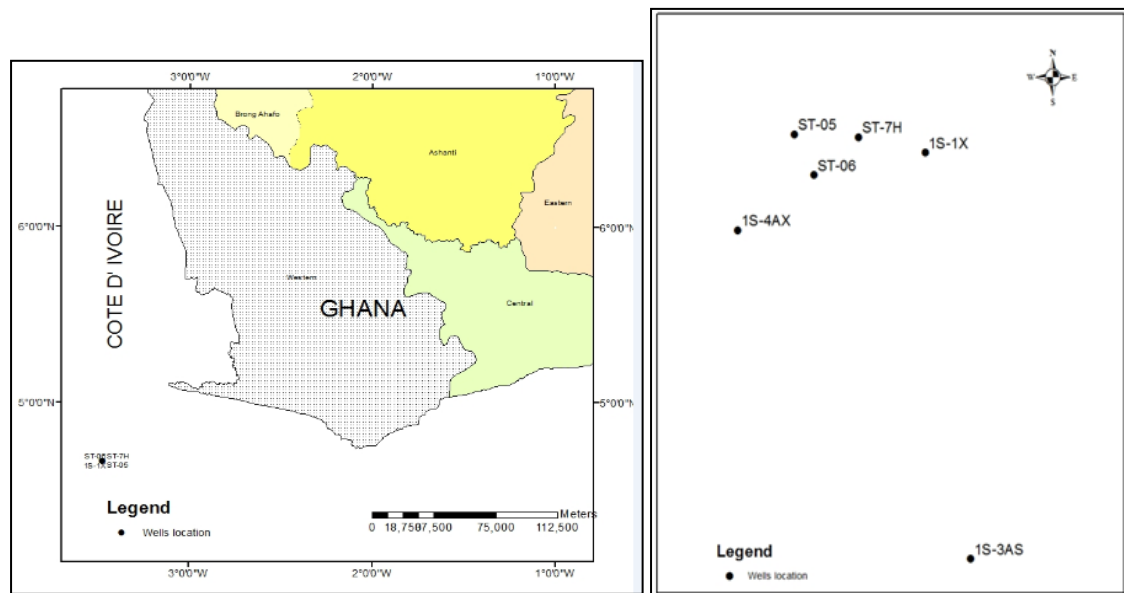


Figure 1. Location of studied wells

3. Theory of resistivity model

As mentioned earlier, cementation factor, m , saturation exponent, n , and tortuosity factor, a , are key variables in the Archie's model. A conservative value of 2 has been assumed for cementation factor. For saturation exponent, it is reported in literature to be between 2 (strongly water-wet rocks) and 25 (strongly oil-wet rocks) [4]. A value of unity is usually assumed for tortuosity, a . It is certain that wrong assumption of these variables has an effect on the reliability of the saturation estimates. Archie's model was initiated based on two experimental connections where resistivity index (RI) and formation factor (F). The resistivity index and formation factor are expressed as in Equation 1 and 2

$$RI = \frac{R_t}{R_o} = \frac{1}{S_w^n} \quad (1)$$

$$F = \frac{R_o}{R_w} = \frac{a}{\phi^m} \quad (2)$$

where, R_t is the true resistivity of the rock saturated with both formation water and hydrocarbons; R_o is the resistivity of a 100% water (brine)-saturated sandstone; S_w water saturation in fraction and n is the saturation exponent, R_w is the water (brine) resistivity; and m is the cementation factor, a is a tortuosity factor, ϕ rock porosity in fraction.

Combination of Eqs. (1), and (2) leads to Eq. (3)

$$S_w = \left(\frac{1}{RI} \right)^{\frac{1}{n}} = \left(\frac{F \times R_w}{R_t} \right)^{\frac{1}{n}} \quad (3)$$

Rearranging Eq. (3) gives expression to true resistivity

$$R_t = a \times \phi^{-m} \times R_w \times S_w^{-n} \quad (4)$$

Applying logarithm rules to Eq. 4 yields (7);

$$\log R_t = \log(aR_w) - m\log\phi - n\log S_w \quad (5)$$

This is the theory underlying the Pickett's plot. Eq. (5) leads to a straight line plotting on a log-log paper with a slope of (- m). The slope is determined by measuring distance on the R_t axis and expressing as a ratio of corresponding distance on porosity axis [5]. The intercept at where porosity axis equals to unity corresponds to (aR_w) which lends to determine a when R_w is known and vice versa. According to Pickett [6] saturation exponent, n , approxi-

mates porosity exponent, m . since no data on water resistivity at the study area was available, an apparent water resistivity R_{wa} was estimated. Additionally, Winsauer [7] evaluated the formation factors and porosities on some 29 sandstones of North America. They concluded that for rocks studied, an expression of the form Eq. 2 described their experimental work.

They evaluated tortuosity a and cementation m to be 0.62 and 2.15 respectively. Since Tano Basin, the study area is sandstone formation the tortuosity value of 0.62 was adopted for this work. Figure 2 presents the Pickett plots for the six exploratory wells of the Western Tano Basin as an instance. The resultant Petrophysical exponents for the geological domain for all the exploratory wells are equally determined in Table 1.

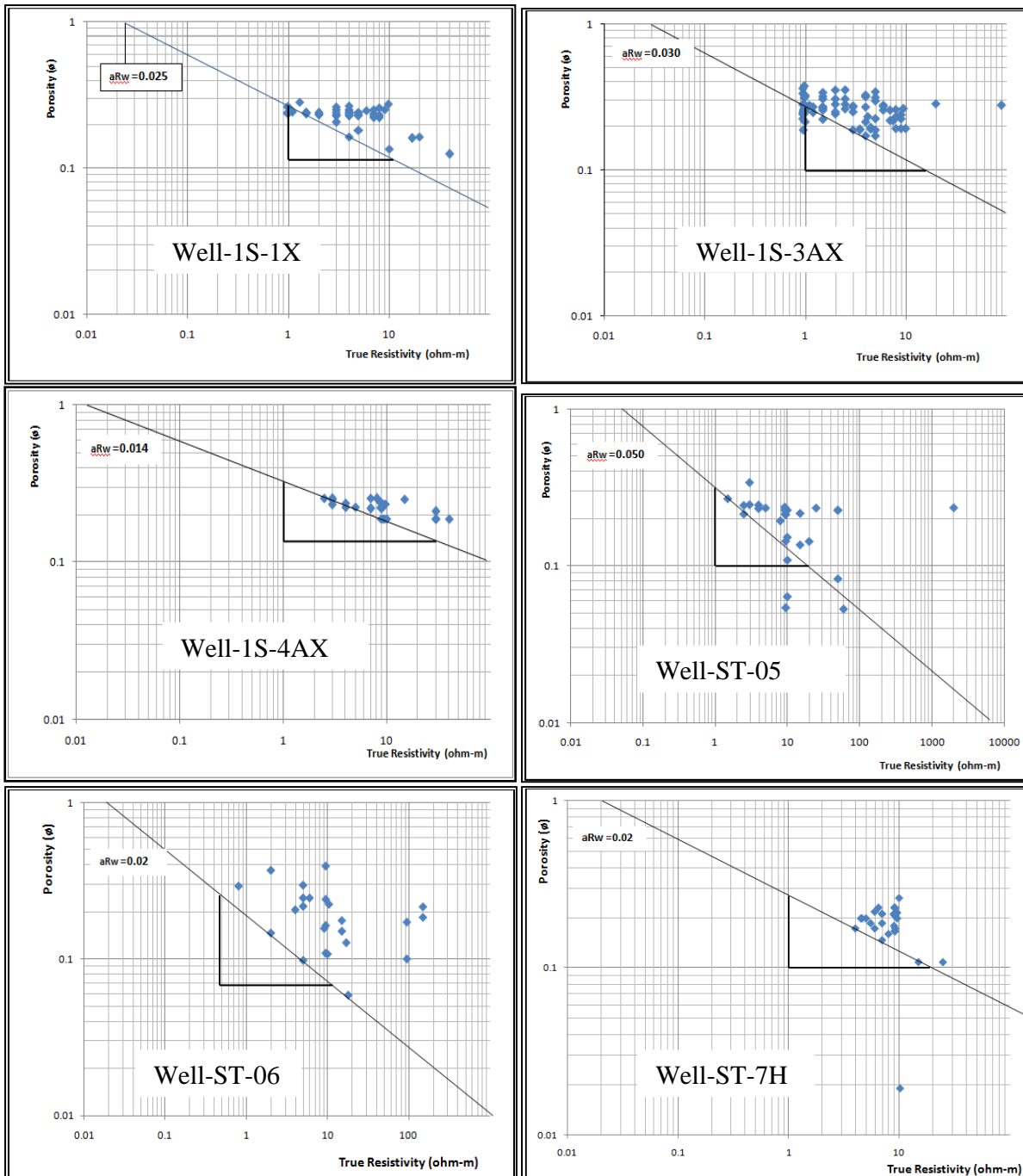


Figure 2. Pickett's plot for the exploratory wells in the western Tano Formation

Table 1. Petrophysical exponents and characteristics of the Western Tano Basin

Well name	aR_w	R_{wa}	m	Δ of S_w	Δ of S_v	Δ of K	Δ of P_c	Δ of B_{vw}
1S-1X	0.025	0.040	1.93	0.52	-4.83	-7.72	3.50	0.00
1S-3AS	0.030	0.048	1.94	0.52	-4.85	-7.76	3.52	0.00
1S-4AS	0.014	0.023	2.69	0.37	-6.73	-10.76	4.88	0.00
ST-05	0.050	0.081	1.21	0.89	-3.03	-4.84	2.19	0.00
ST-06	0.02	0.032	1.36	0.74	-3.40	-5.44	2.47	0.00
ST-07	0.02	0.032	1.97	0.51	-4.93	-7.88	3.57	0.00

3.1. Effect of specific surface per unit solid volume on Archie model

The specific surface of a porous material is the total area exposed within the pore space per unit volume. The unit volume may be the solid material framework, in which case the specific surface is represented by S_v . The specific surface is a key Petrophysical parameter for an understanding of the physics and relationships of porous media. Many practical models have been developed to relate relative permeability with porosity and specific surface of the porous material. One such empirical model is one developed by Kozeny and Carman [8].

$$K = \frac{\phi^3}{f \times a \times S_v^2} \quad (6)$$

where f is the shape factor, a is the tortuosity and S_v is the specific surface per unit surface area to rock volume.

Morris and Biggs [9] also developed an empirical equation to relate permeability as a function of porosity and irreducible water saturation.

$$K = \left(250 \frac{\phi^3}{S_{wir}^2} \right)^2 \quad (7)$$

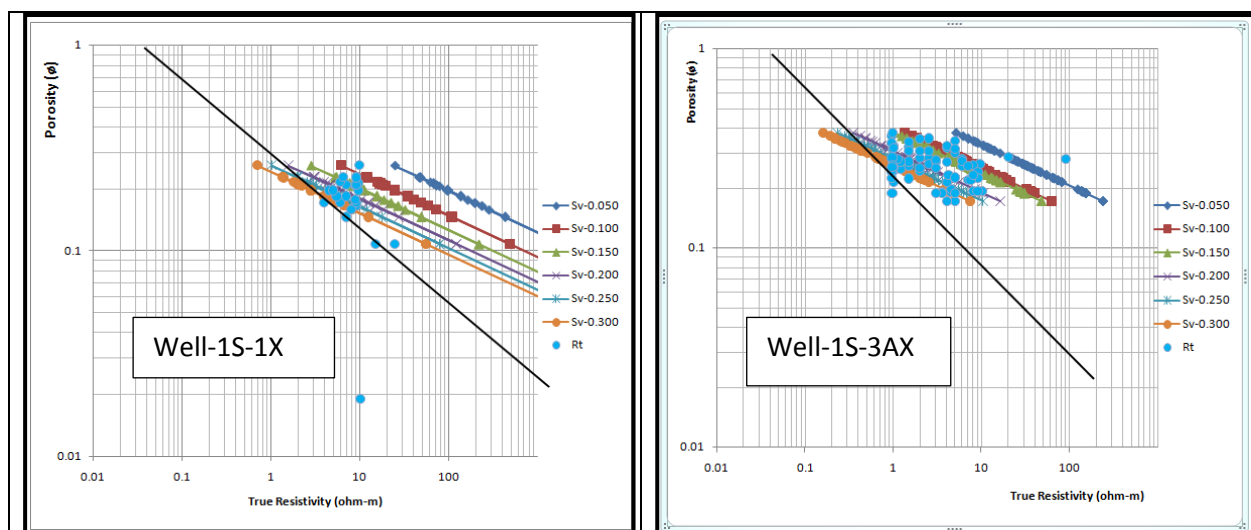
Equating Eq. (6) and (7) leads to an expression for irreducible water saturation

$$S_{wir} = \left(250 \times \phi^3 \times S_v^2 \times f \times a \right)^{1/2} \quad (8)$$

Substituting Eq. 8 into Eq. 4 yields

$$R_t = a \times \phi^{-m-1.5n} \times R_w \times \left(250 \times S_v^2 \times f \times a \right)^{-0.5n} \quad (9)$$

By plotting R_t against ϕ on a log-log coordinate using Eq. (9) should generate straight line with a slope equal to $(-m-1.5n)$ with constant specific surface per unit solid volume. Parallel lines of constant specific surface per unit solid volume Eq. (9) are determined via the determination of R_t and the resultant plots are shown in Figure 3 incorporating the specific surface from 0.050 to 0.30.



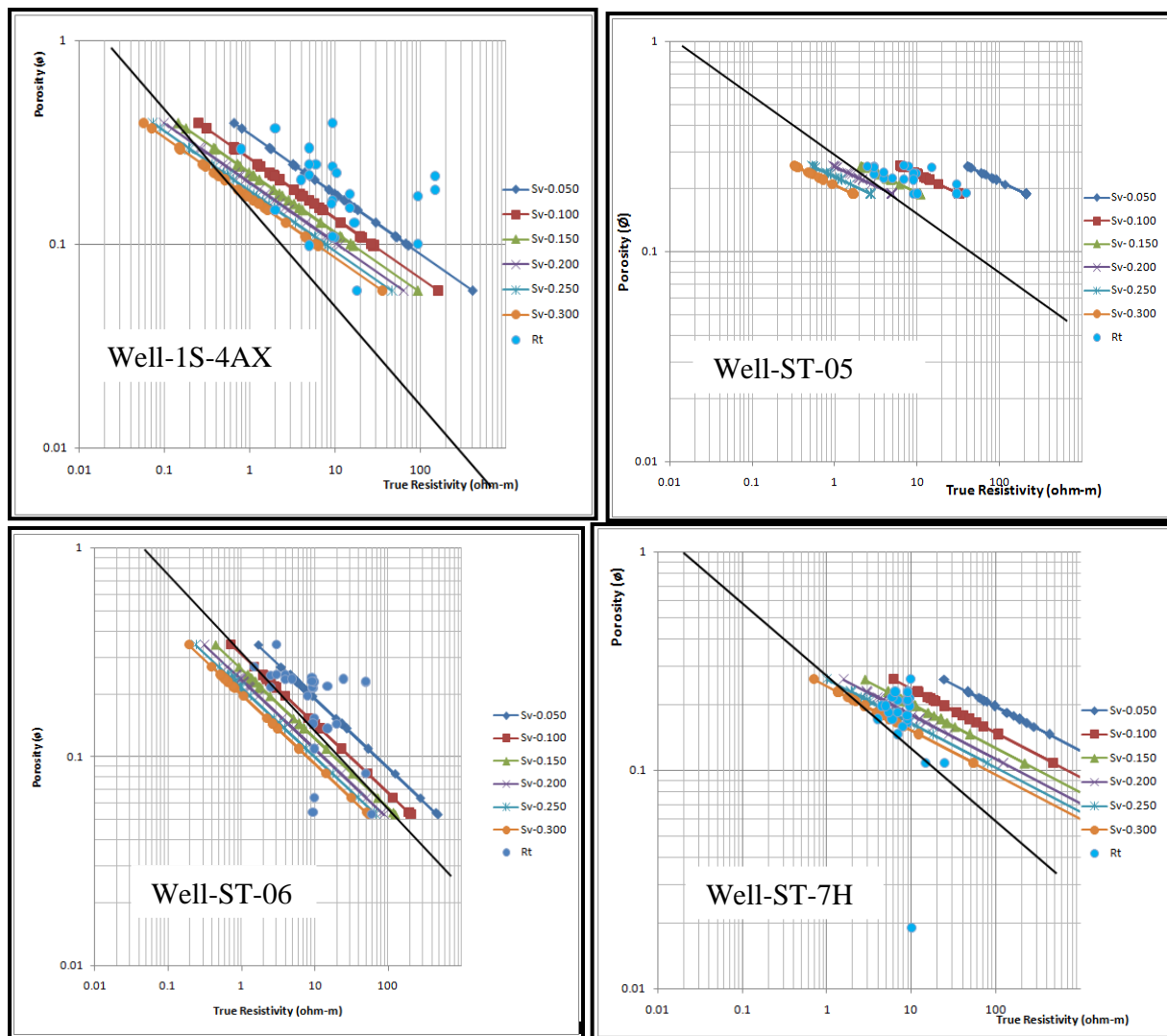


Figure 3. Pickett's plot for the exploratory wells in the western Tano Formation integrated with the specific surface

3.2. Effect of permeability on Archie Model

Permeability is an important Petrophysical parameter which indicates the reservoirs ability to allow fluid to pass through the effective voids. The effect of permeability on the model was investigated. According to Wyllie and Rose [10], permeability is a direct function of porosity and inversely related to irreducible water saturation, Eq. 10.

$$K = \left(250 \frac{\phi^3}{S_{wir}} \right)^2 \quad (10)$$

$$S_{wir} = \left(250 \frac{\phi^3}{K^{1/2}} \right) \quad (11)$$

According to El-Khadrgy *et al.* [5], the irreducible water saturation (S_{wir}) relates to the water saturation (S_w) as shown in Eq. 12.

$$S_{wir} = \frac{\phi_t \times S_w}{\phi_{eff}} \quad (12)$$

Incorporating Eq. 12 into Eq. 4 yields

$$R_t = a \times \phi^{-3n-m} \times R_w \times \left(\frac{250}{K^{1/2}} \right)^{-n} \quad (13)$$

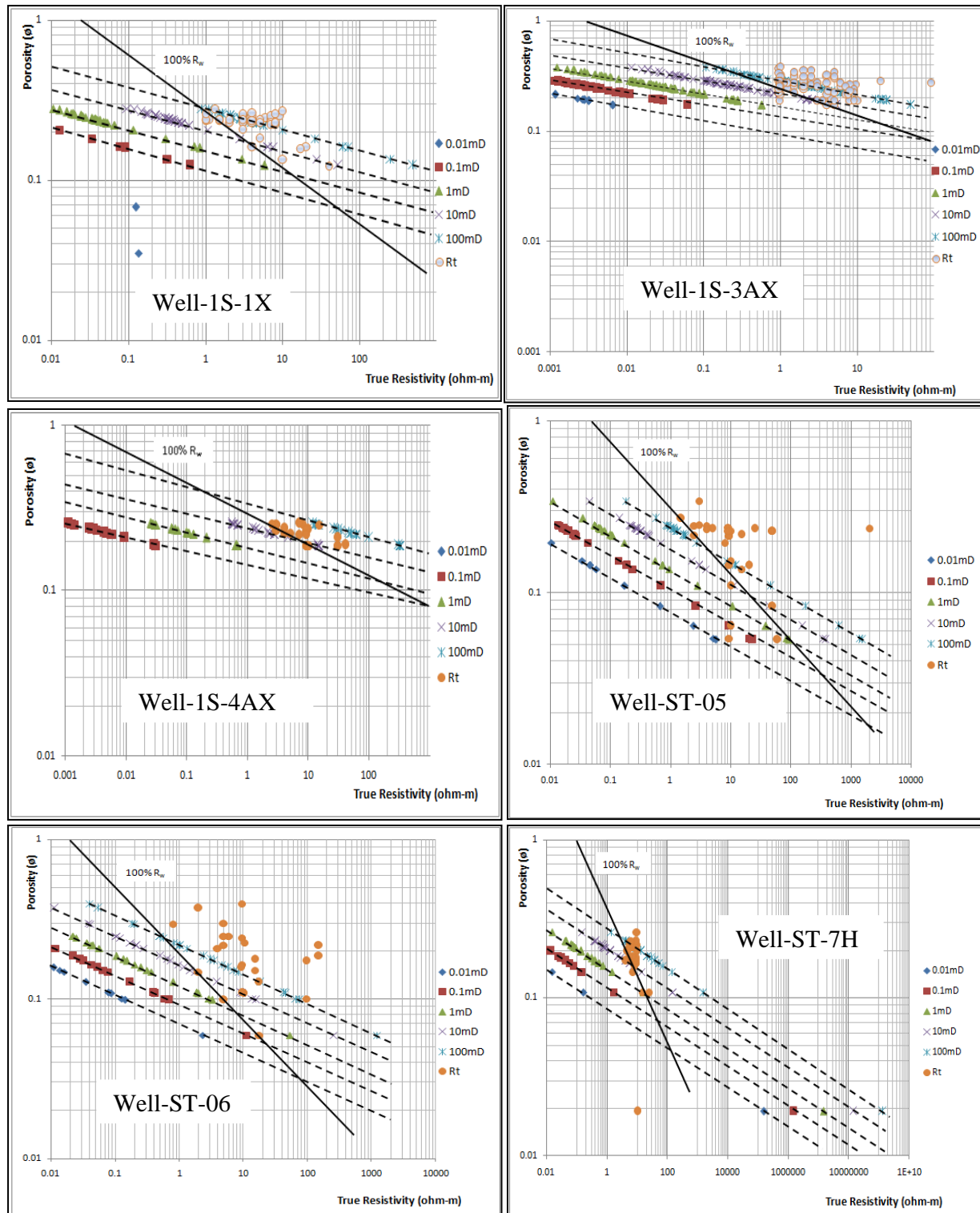


Figure 4. Pickett's plot for the exploratory wells in the western Tano Formation integrated with permeability

Applying logarithm to both sides gives

$$\log R_t = (-3n - m) \times \log \phi + \log \left[a R_w \times \left(\frac{250}{K^{1/2}} \right)^{-n} \right] \quad (14)$$

Plotting R_t against \emptyset on a log-log coordinates results in a linear relation with the slope equal to $(-3n - m)$ with permeability been constant. Parallel permeability lines of different permeability values are drawn using Eq. 13 with the intercept on the true porosity line representing $(aR_w (250/K^{1/2})^{-n})$ Figure 4 shows the effect of permeability from 0.01 to 100md.

3.3. Effect of capillary pressure on Archie model

The equally important Petrophysical parameter in the characterization of the reservoir is capillary pressure. It is the measure of the pressure difference between two different fluids at equilibrium. Know, and Pickett's [11] generated a model for capillary pressure as a function of rock permeability and porosity as in Eq. 15.

$$P_c = A \left(\frac{K}{10000\emptyset} \right)^{-B} \quad (15)$$

Know, and Pickett's [11] found out that for most rocks A is a constant and lies between 151.35 and 22.91. It was also found out that for B is approximately 0.45. A further correlation of A against water saturation (S_w) approximates Eq. 16.

$$A = 19.5S_w^{-1.7} \quad (16)$$

Combining Eq. 10, Eq. 16 and Eq. 15 yields Eq. 17:

$$P_c = 3.033(S_w^{-0.8} \times \emptyset^{-2.25}) \quad (17)$$

Rearranging Eq. 17 gives an expression for water saturation (S_w), Eq. 18:

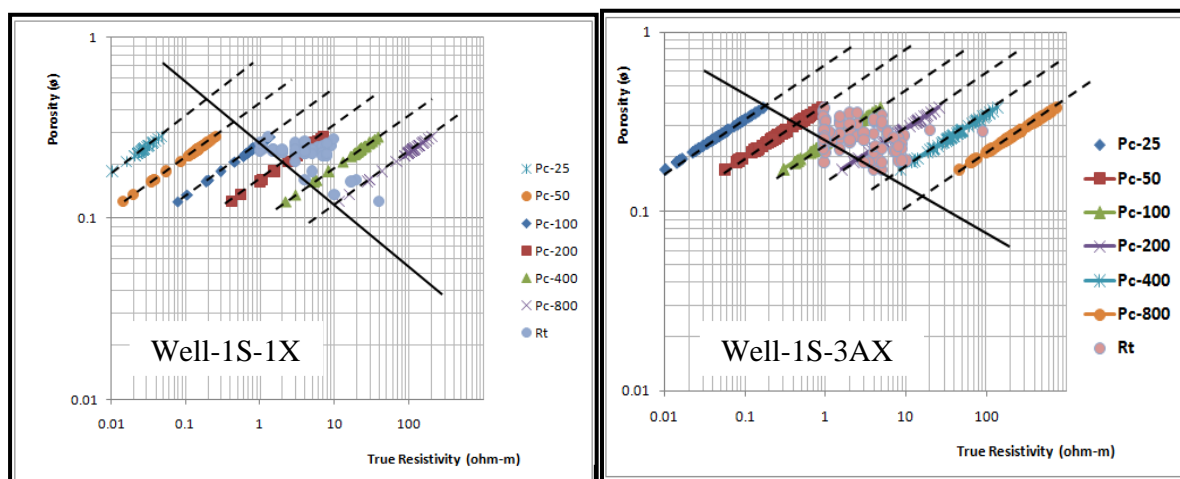
$$S_w = \left(\frac{P_c}{3.033 \times \emptyset^{-2.25}} \right)^{-1.25} \quad (18)$$

Substituting Eq. 18 into Eq. 4 and applying logarithm to both sides

$$R_t = a \times \emptyset^{2.8125n-m} \times R_w \times \left[\left(\frac{P_c}{3.033} \right)^{-1.25} \right]^{-n} \quad (19)$$

$$\log R_t = (2.8125n - m) \times \log \emptyset + \log [aR_w \times (4.0026 \times P_c^{-1.25})^{-n}] \quad (20)$$

Plotting Eq. 19 on a log-log coordinate with a constant (aR_w) and varying capillary pressures leads to a linear relationship with a slope equal to $(2.8125n - m)$ and the intercept on the true porosity line represents $[aR_w \times (4.0026 \times P_c^{-1.25})^{-n}]$. Figure 5 shows the effect of constant capillary pressure values from 25 psi to 800 psi incorporated into the model.



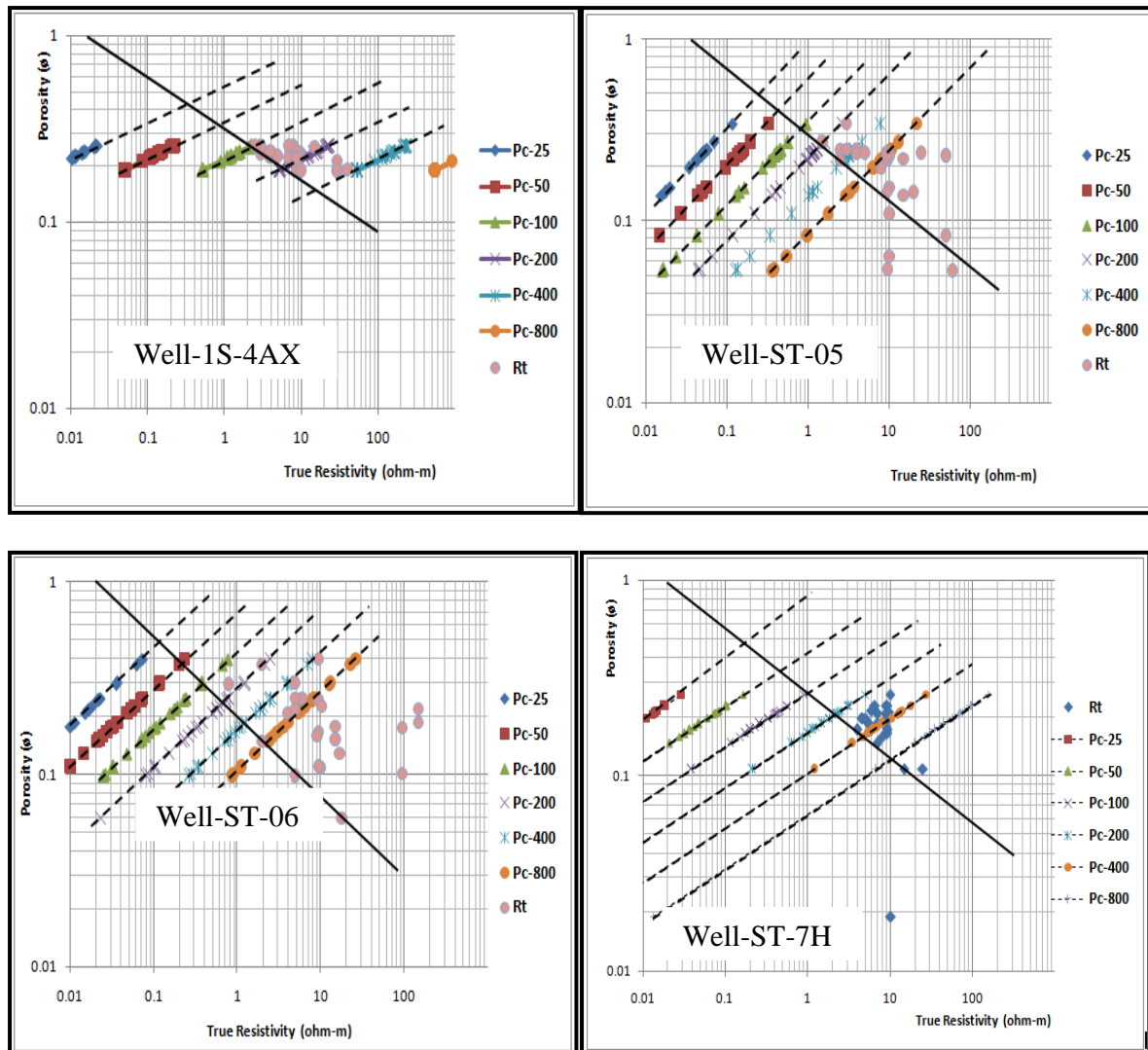


Figure 5. Pickett's plot for the exploratory wells in the western Tano Formation integrated with capillary pressure

3.4. Effect of bulk volume of water

The volume per unit mass of a dry material plus the volume of the air between its particles is referred to as a bulk volume. It is expressed as the product of formation water saturation (S_w) and its porosity (ϕ).

$$B_{vw} = S_w \times \phi \quad (21)$$

$$S_w = \frac{B_{vw}}{\phi} \quad (22)$$

Substituting Eq. 22 into Eq. 4

$$R_t = a \times \phi^{n-m} \times R_w \times (B_{vw})^{-n} \quad (23)$$

According to Sanyal and Ellithorpe [2], log-log plots of R_t and ϕ produces straight lines with slope equal to $(n-m)$ which is also corroborated by both Doveton *et al.* [12] and Buckles [13]. Figure 6 illustrates the effect of bulk volume of water on Archie's model. The plots have zero slope this is due to the fact that n is equal to m as explained earlier. Hence $(n-m)$ is equal to zero leading to vertical lines. The intercept of the vertical on the true porosity plot correspond to $[aR_w \times (B_{vw})^{-n}]$.

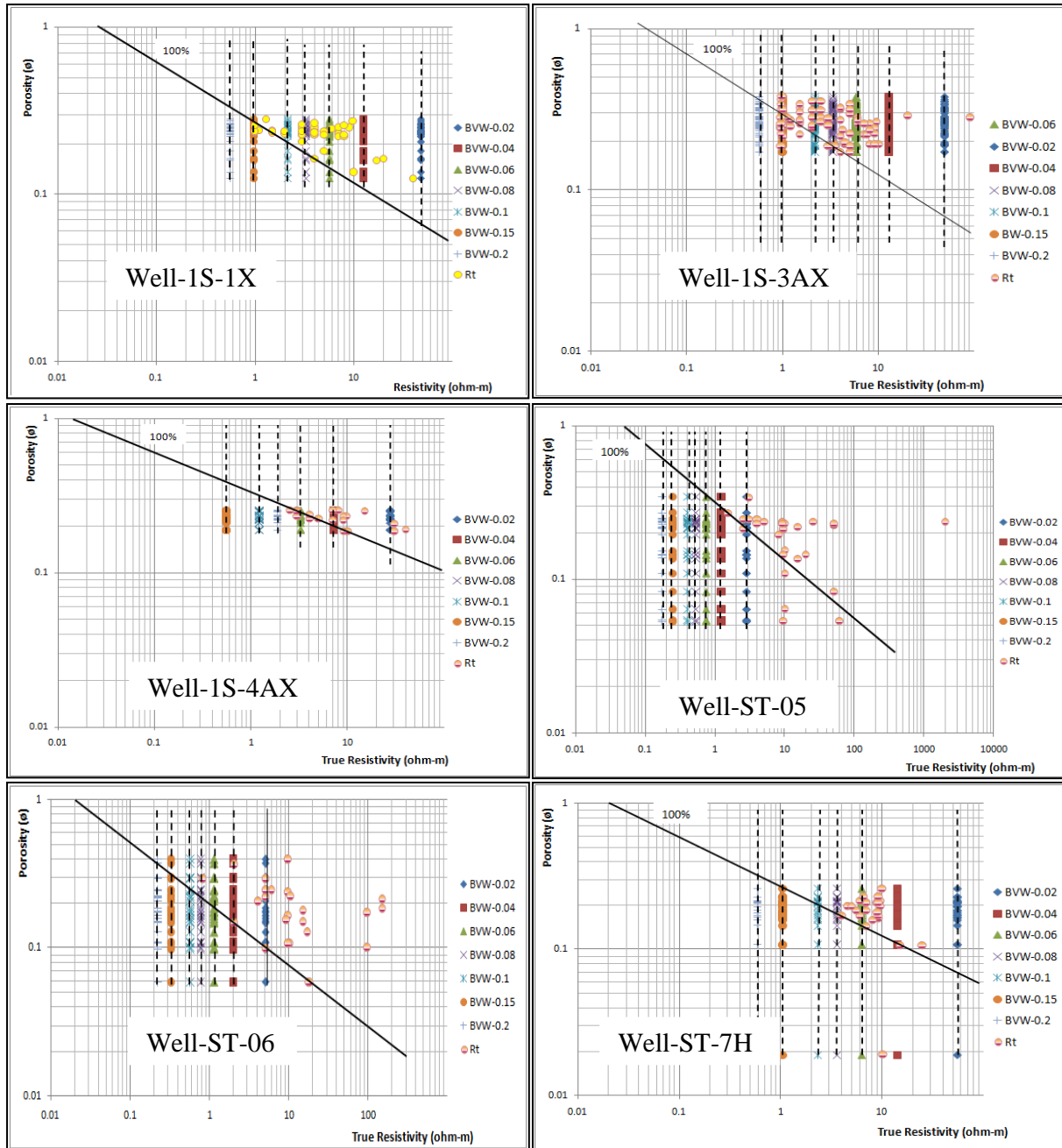


Figure 6. Pickett's plot for the exploratory wells in the western Tano Formation integrated with the bulk volume of water

3.5. Effect of height above the free water surface

Reservoir rock usually contains immiscible fluids which exist in phases: oil, water, and gas. The forces which keep these fluids at equilibrium with each other and the medium is known as capillary forces. The pressure difference existing across the interface separating the fluids is referred to as capillary pressure [14-18]. Accordingly, the height of hydrocarbon column above the free water surface can be expressed as a linear function of the capillary pressure existing between the fluids as

$$h = \frac{P_c}{0.433(\rho_w - \rho_{hc})} \quad (24)$$

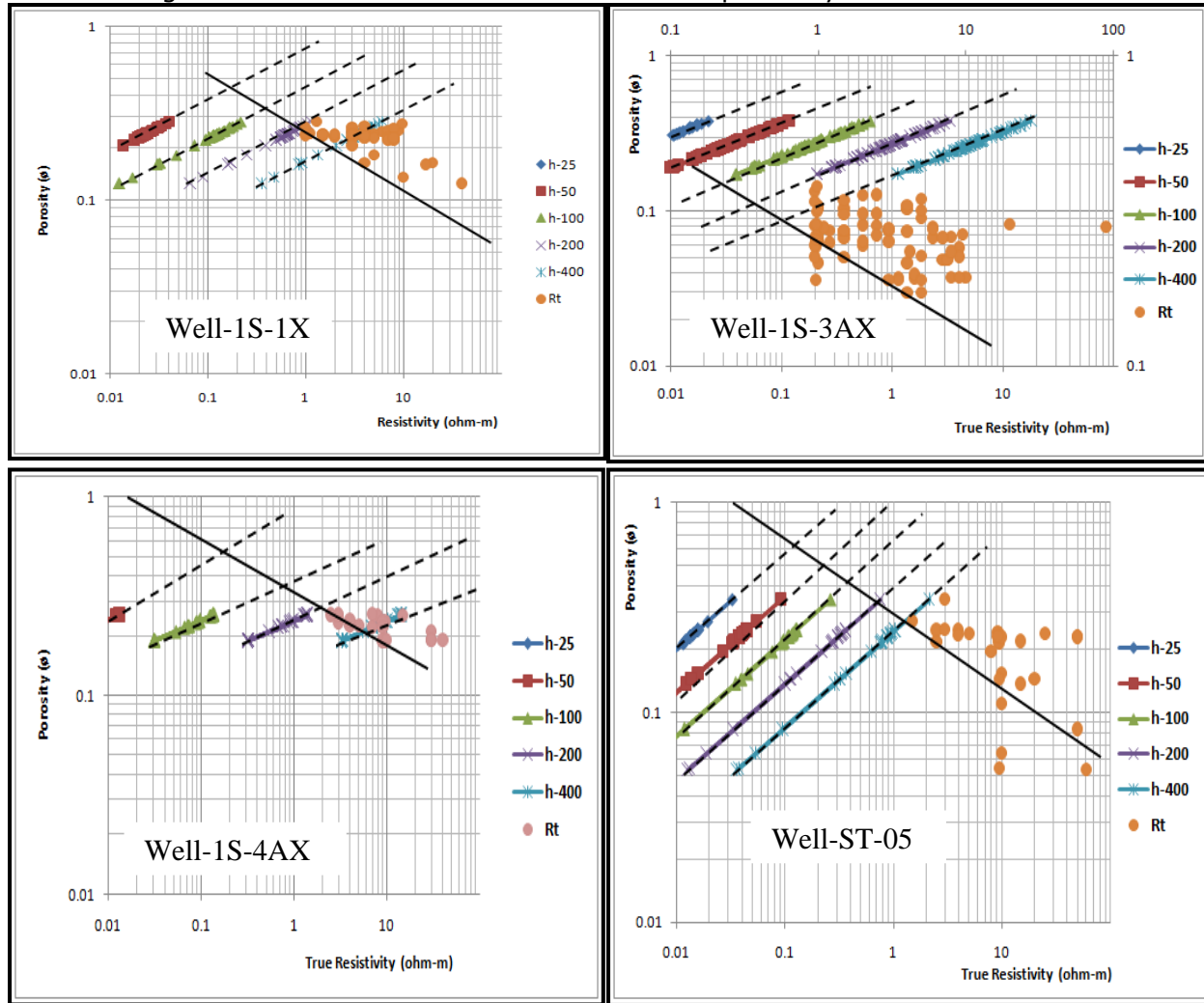
where subscripts w and hc denote wetting phase and non-wetting phases, respectively, ρ_w and ρ_{hc} are densities of the respective phases, and h is height above the free water level.

Rearranging and substituting Eq. 24 into Eq. 19 and applying logarithm to both sides leads to the form;

$$R_t = a \times \emptyset^{2.8125n-m} \times R_w \times \left[\left(\frac{0.433 \times h (\rho_w - \rho_{hc})}{3.033} \right)^{-1.25} \right]^{-n} \quad (25)$$

$$\log R_t = (2.8125n - m) \times \log \emptyset + \log \left[a R_w \times \left(\left(\frac{0.433 \times h (\rho_w - \rho_{hc})}{3.033} \right)^{-1.25} \right)^{-n} \right] \quad (26)$$

Eq. 23 presents a straight line with a slope corresponding to $(2.8125n - m)$ with constants aR_w , ρ_w , ρ_{hc} , and height above the free water surface. The intercept of the straight line on the true porosity plot correspond $\left[aR_w \times \left(\left(\frac{0.433 \times h (\rho_w - \rho_{hc})}{3.033} \right)^{-1.25} \right)^{-n} \right]$. Figure 7 exhibits the effect of height above free water surface for the exploratory wells in the Tano formation.



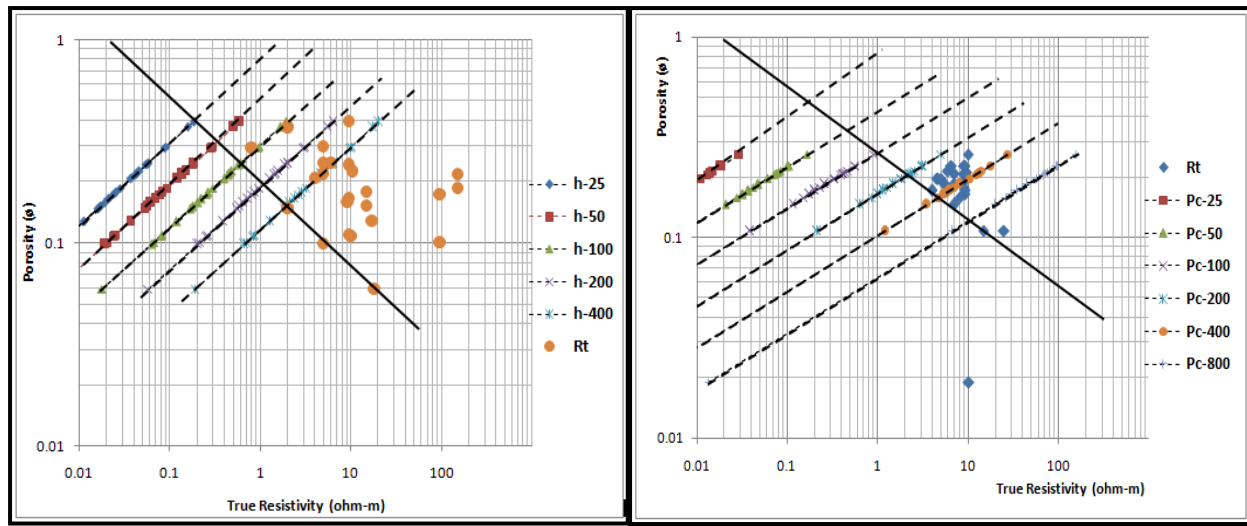


Figure 7. Pickett's plot for the exploratory wells in the western Tano Formation integrated with height above the free water surface

3.6. The relationship between water saturation and petrophysical parameters

Accurate hydrocarbon reserve in a reservoir formation is very crucial for reservoir economics. One key variable in the determination of the reserve is water saturation amount. Proper evaluation of water saturation leads to adequate reserve estimation. The study compares the relationship of water saturation with Petrophysical parameters such as the bulk volume of water, capillary pressure, and permeability for the exploratory wells used for the study.

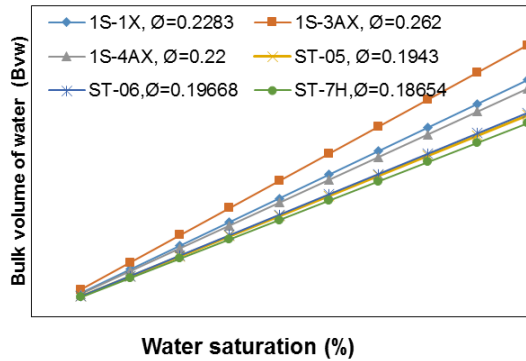


Figure 8. Correlation between the bulk volume of water and water saturation for exploratory wells

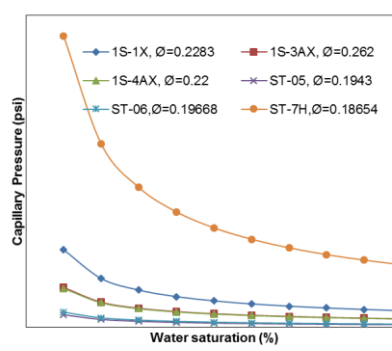


Figure 9. Correlation between capillary pressure and water saturation for exploratory wells

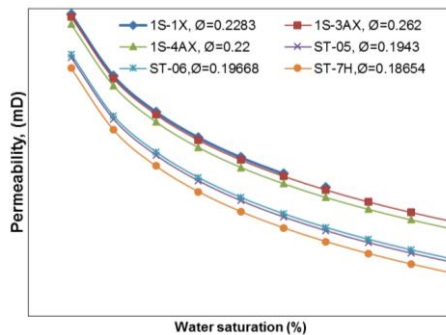


Figure 10. Correlation between permeability and water saturation for exploratory wells

As expected, bulk volume of water is found to be proportional to water saturation and that bulk volume of water increases as water saturation increases, Figure 8. Additionally, as water saturation increases, the pore space within the reservoir gets filled up with water, and this has a reduction effect in both permeability and capillary pressure, Figure 9 and Figure 10.

4. Results and discussions

An approach which integrates the Petrophysical constants of the Tano formation has been established via the Pickett's resistivity and porosity model. The approach incorporates in the Pickett's models such Petrophysical parameters as specific surface per unit pore, permeability, capillary pressure, bulk volume of water and height above the free water surface.

The specific conclusions are as follows:

The study shows different results and effects of the various Petrophysical parameters considered which depend on the log-log plots of resistivity and porosity. For a given resistivity, porosity decreases with increasing permeability, capillary pressure, and height above the free water surface.

Resistivity approximates zero slopes with specific surface per unit volume and bulk volume of water the slope being affected by the porosity of different exploratory wells. There is, however, the marginal increasing effect of specific surface per unit solid volume and bulk volume of water. The slopes of all the plots are affected by the saturation and porosity exponents. These exponents as wells apparent water resistivity for the formation have been determined.

Finally, it is observed that water saturation has an inverse relation with both capillary pressure and permeability but a direct relation with the bulk volume of water.

References

- [1] Archie GE. (1942) The theoretical resistivity log as an aid in determining some reservoir characteristics: American Institute of Mining and Metallurgical Engineers, Transactions, 1942; 146: 54-61.
- [2] Sanyal SK, Ellithorpe JE. A generalized resistivity-porosity crossplot concept, Society of Petroleum engineers in California. Regional meeting, SPE paper 7145, 1978, 8pp.
- [3] Davies DW. The Geology and Tectonic Framework of the Republic of Ghana and the Petroleum Geology of the Tano Basin, Southwestern Ghana. Internal Report 1986, G.N.P.C.
- [4] Ara TS, Talabani S, Atlas B, Vaziri HH, Islam MR. In-Depth Investigation of the validity of the Archie Equation in Carbonate Rocks, paper SPE 67204, 2001.
- [5] El-Khadragy AA, Ghorab MA, Shazly TF, Ramadan M, and El-Sawy MZ. Using of Pickett's plot in determining the reservoir characteristics in Abu Roash Formation, El-Razzak Oil Field, North Western Desert, Egypt. Egyptian Journal of Petroleum, 2014; 23: 45-51.
- [6] Pickett GR. Pattern recognition as a means of formation evaluation, in Society of Professional Well Log Analyst 14th Annual Logging Symposium Transactions Paper A, 1973, pp A1-A21.
- [7] Winsauer WO, Shearin HM, Jr, Masson PH, Williams M. Resistivity of Brine Saturated Sands in Relation of Pore Geometry. Published in 1952 in the Bulletin of the AAPG.
- [8] Kozeny J. (1927) Ober kapillare Leitung des Wassers in Boden: Sitzungsbericht der Wiener Akademie, Abteilung IIa, 1927; 136: 271
- [9] Morris RL, Biggs WP. Using log-derived values of water saturation and porosity: Society of Professional Well Log Analysts Annual Logging Symposium 1967, 26 p.
- [10] Wyllie MRJ, Rose WD. Some Theoretical Considerations Related to the Quantitative Evaluation of the Physical Characteristics of Reservoir Rock from Electric Log Data, Trans., AIME, 1950; 189: 105.
- [11] Know BS, Pickett GR. A new pore structure model and pore structure interrelationship, in: Socioety of Professional Well Log Analysis, 16th Annual Logging Symposium, 1967, 26pp.
- [12] Doveton JH, Guy WJ, Watney WL, Bohling GC, Ullah S, Adkins-Heljeson D. Log Analysis of petrofacies and flow units with microcomputer spreadsheet software; Kansas Geological Survey, University of Kansas, Lawrence, Kansas, 1996.
- [13] Buckles RS. Correlating and averaging connate water saturation data. J. Can. Petrol. Technol., 1996; 5: 42-52.

- [14] Leverett MC. Capillary behavior in porous solids: American Institute of Mining and Metallurgical Engineers, Transactions, 1941; 142: 152-169.
- [15] Brooks RH, Corey AT. Properties of porous media affecting fluid flow: Journal of Irrigation and Drainage Division, Proceedings of the American Society of Civil Engineers, 1966; 92(IR 2):.61-88.
- [16] Dullien FAL. Porous media: fluid transport and pore structure, 2nd edition: Academic Press 1992, San Diego, 574 p.
- [17] Vavra CL, Kaldi JG, Sneider RM. Geological applications of capillary pressure: a review: AAPG Bulletin, 1992; 76: 840-850.
- [18] Smith DA. (1966) Theoretical considerations of sealing and non-sealing faults: AAPG Bulletin, 1966; 50: 363-374.

To whom correspondence should be addressed: Dr. Prince Appiah Owusu, Department of Civil Engineering, Kumasi Technical University, Kumasi, Ghana

IMPACT OF SMALL - SCALE HETEROGENEITY ON POTENTIAL RECOVERY IN SELECTED RESERVOIR SANDSTONES FROM WEST BARAM DELTA, OFFSHORE, SARAWAK

I. Yusuf, E. Padmanabhan

Department of Geosciences, Faculty of Geosciences and Petroleum Engineering, Universiti Teknologi PETRONAS, postcode 32610, Seri Iskandar, Perak, Malaysia

Received February 10, 2018; Accepted April 27, 2018

Abstract

Small - scale sedimentary heterogeneity in reservoir description is required for reliable recovery. West Baram Delta was selected as a case study because of the ongoing residual oil phase recovery in the area. This paper investigates effects of different small - scale sedimentary structures on permeability variation of selected reservoir sandstones using an integrated approach combining cores, thin sections, mercury injection capillary pressure data and tiny spot air permeameter. Two main sandstone lithofacies; namely massive fine grained and massive coarse grained sandstone lithofacies were identified to exhibit small-scale heterogeneity. The result indicates in massive fine grained sandstones characterized by fining-up grains with fossil shell fragments, *Ophiomorpha* burrows and faint lamination structures measured air permeability values along host sample accounted for 50% of varying air permeability from 79 mD to 648 mD and attributed to poor interconnectivity of pores resulting from grain packing and volume matrix content, as along coarse - fine boundary permeability varies between 249 mD to 1124 mD accounted for 50% permeability ascribed to variation in grain sorting and embedded shell fragments. Also along *Ophiomorpha* burrows, air permeability vary from 298 mD to 794 mD accounted for 45% permeability, but along host sediment permeability varies from 75 mD to 368 mD accounted for 55% increase. The measured permeability along lamina structure, values vary between 123 mD to 738 mD accounting for 55.6% also ascribed to grains topology that facilitates pore interconnectivity. But however, along host sediment air permeability varies from 89 mD to 448 mD accounted for 44.4% increase. In massive coarse grained sandstones characterized by faint lamination and bioturbation, air permeability vary from 533 mD to 819 mD along lamina accounted for 60% and varies from 828 mD to 1188 mD along host sample, along biotubated spots permeability vary from 78 mD to 93 mD and is attributed to decrease in grain isotropy and sorting within region. It shows that the massive fine grained sandstones hold higher fluid flow potential advantage over massive coarse grained sandstone lithofacies in the delta. Furthermore, prior knowledge of small-scale sedimentary structure will give insight on potential recovery variations within different reservoir sandstone lithofacies as they either enhance or reduce permeability

Keywords: Small - scale sedimentary heterogeneity; permeability variation; reservoir sandstone; pore diameter; oversize pores.

1. Introduction

The measure of the ability of the rock to transmit fluids is known as permeability [1-2]. The goal of reservoir characterization is to generate models that allow the accurate prediction of future well performance and characterization of permeability heterogeneity to accurately understand flow behavior in reservoirs [3]. In petroleum reservoir modeling however, researchers acknowledge small - scale sedimentary structures plays an important role in oil recovery, perhaps incorporating knowledge of small - scale sedimentary heterogeneity in reservoir description is required for reliable prediction of oil production [3-6] for it significantly contributes to reservoir complexity. However, failure to adequately evaluate or take account of such variation and complexities in reservoir results in failure to optimize hydrocarbon production [6] in many fields. West Baram Delta is most prolific matured West Baram Delta field [7] is among

enlisted for an EOR process [7-9] to maximize oil production from some of the existing more than 170 production wells. This study is challenged to investigate the variable small – scale sedimentary structures in reservoir sandstone lithofacies that poses to impact fluid flow behavior of the reservoir. These because lateral continuity and connectivity of reservoir lithofacies are one of the high-ranking heterogeneities that are often ignored and difficult to predict [3] as they describe rock properties that potentially influence dynamic permeability measurement of the reservoir. In addition, permeability values obtained from outcrops are not very reliable [3], because they are not true representatives of reservoirs rock. This study is performed on cores from producing hydrocarbon reservoir to evaluate it dynamic permeability measurement. However, till date accurate estimation of permeability still remains challenge [10] in many fields.

2. Study area

The Baram Delta is mature field, and one of seven geological provinces, situated offshore, Sarawak, Malaysia (Figure 1). It is the most oil and gas prolific of all the geological provinces in the basin [11-12]. The oil-in-place in multiple stacked sandstone reservoirs were estimated to contain more than 0.48×10^8 m³ in a shallow offshore environment as at 1969 when the delta were discovered. More than eight fields have been found in Baram Delta, with more than 30 years production history, and presently with an average recovery factor of about 30% [12,27]. The offshore formations of the Baram Delta include coastal to coastal-fluviomarine sands deposited in a northwestward prograding delta since the Middle Miocene (from Cycle IV onwards), in which the Cycle V (Middle to Upper Miocene) to Cycle VII (Upper Pliocene) are the most developed [11-13]. Each cycle develops in a coastal plain environment to the south dominated by deposition of sands, silts and clays, and grades northwards into holomarine neritic to bathyal environments with deposition of mainly clays, silts, minor sands and, in places turbidites [14]. The sandstone core samples were taken from some wells in West Baram delta, which has obvious primary sedimentary heterogeneities feature in the form laminations, bioturbation and cross-beddings which are apparently distinguishable from the several sandstone lithofacies [11,15] in the study area.

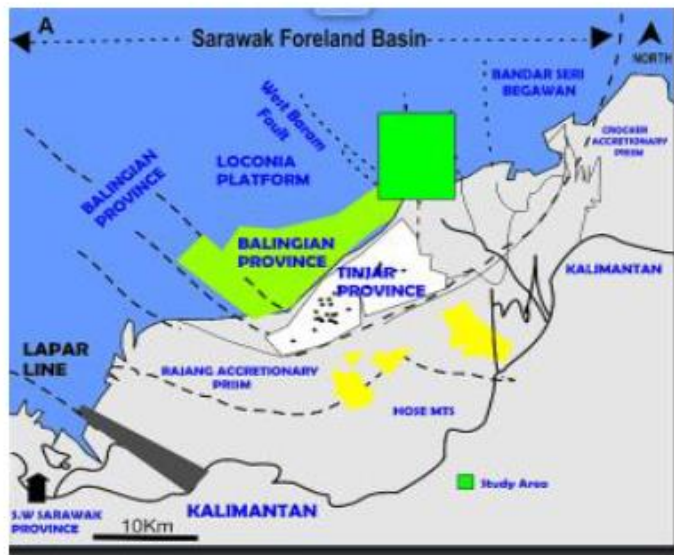


Figure 1. Location of the Sarawak basin and the study area

3. Materials and methods

The total of ninety-seven (97) core samples from exploratory wells within the Middle-Upper Miocene age within the Cycle IV and V lithological sequences were characterized into (5) five major lithofacies facies based on visible textural and sedimentary structures varying from

poorly stratified sandstone, low angle/parallel to crossed-bedding sandstone, biotubated sandstone. Tan [11] were identified and others reported are ripple cross - laminated sandstone, fining upward laminated, flaser bedded sandstones, massive coarse sandstone in the study area. Forty (40) sizeable hand core specimen samples, thin sections, mercury injection capillary pressure (MICP) and spot air-probe permeameter were integrated in this investigation.

The sandstone lithofacies and identification of sedimentary structures were carried out by conventional core logging with emphasis on texture and sedimentary structure [16-18]. The lithofacies description was complimented with thin section studies for pore sizes and textural composition analysis. Pore size was measured using a scaled petrographic image analyzer (JMicroVision 1.2.7), as obtained datasets in micrometers (μm) are converted to microns (μ) scale for matching the value ranges on mercury graphs generated from mercury injection capillary pressure (MICP). A gridded 1cm X 1cm line is drawn over the variable identified sedimentary heterogeneities on sandstone slab samples (Figure 2) as readings were taken at cross-spots (P). The 1cm X 1cm cube for air-probe permeability was measured using NER's Tiny Perm which is a portable hand-held air permeameter used for measurement of rock matrix permeability on outcrops and at the macro scale (3cm-3m). The permeability measurement range varies from approximately 10 millidarcys to 10 Darcys. The response function of the sample-instrument system is computed, and key characteristics of the response are displayed on the liquid crystal display (LCD). The results are then computed using the theoretical relation of the response function to permeability, the matrix permeability is determined from the calibration charts and tables provided with the instrument. In order to ensure the accuracy of the displayed measured values, reading was taken 4 -5 times at sample grid spot such the average was recorded before the conversion.

3.1. Petrography: Lithofacies description and pore sizes distribution

The faintly cross-stratified sandstone (Figure 2a) contains about 50.33 % coarse to medium grains, moderate to well sorted monocrystalline and polycrystalline quartz grains size ranging between 27-259 μm with an average grain size of 104 μm (Figure 3a). While matrix composition made up 30.25%, with an overall porosity of 19.42%. The variable measured pore sizes from thin section vary from 24931nm to 249980nm at an average of 96886nm constituted within overall porosity. This oversize pore [19] are indicated by low pressure region on the mercury bimodal (figure 4a) and will serve as a conduit for fluid flow [20]. Within the matrix filling intergranular space (see Figure 4a) measured pore size from thin section also vary from 1460nm to 39957nm at an average of 9083nm corresponding to the region of higher mercury pressure [20]. Furthermore, suggested inclusive within, are pores varying from 7.25nm – 99 nm ascribe altered to clay minerals and within 100nm to 1100 nm are ascribed to have resulted from dissolution pore cavities of feldspar mineral in the framework.

In the laminated, finning up sandstone with shell fragment sandstone lithofacies (Figure 2b), is a poorly sorted framework characterize by mottled structure appearance (Figure 3c & d). The grain size varies from 13.42 μm to 139.3 μm at an average value of 34.25 μm having a total porosity of 7.67%. The embedded preserved fossil fragments during early deposition facilitated visible intragranular pores (figure.3d). It also comprises predominantly monocrystalline quartz grain and few polycrystalline grains at 24.58% proportion (Figure 3c & d) having 67.75% of matrix content.

The mercury unimodal graph shows pore size (figure 4c) correspond to measure shell cavities pores varying between 620 nm to 98992 nm with an average of 42080 nm. The unmarked pore sizes are resulting matrix within the range 6.25 nm-60 nm and 61nm-619nm all below thin section resolution.

In the cross stratified sandstone, bioturbation with trace fossils (Figure 2c), grain size varies from 46.01 μm to 262.2 μm with an average of 133.6 μm dominant monocrystalline quartz grain and few polycrystalline grains at 63.25%. It contains a matrix of 24.67% with a total porosity of 12.08% (Figure 3f). This lithofacies comprise of oversize pores [19] associated with changes in the energy of the depositional environment [21-22]. The measured pores from thin

section vary from 35286 nm to 112791nm at an average of 64895 nm correspond to the region of low pressure values in mercury bimodal (Figure 4e).

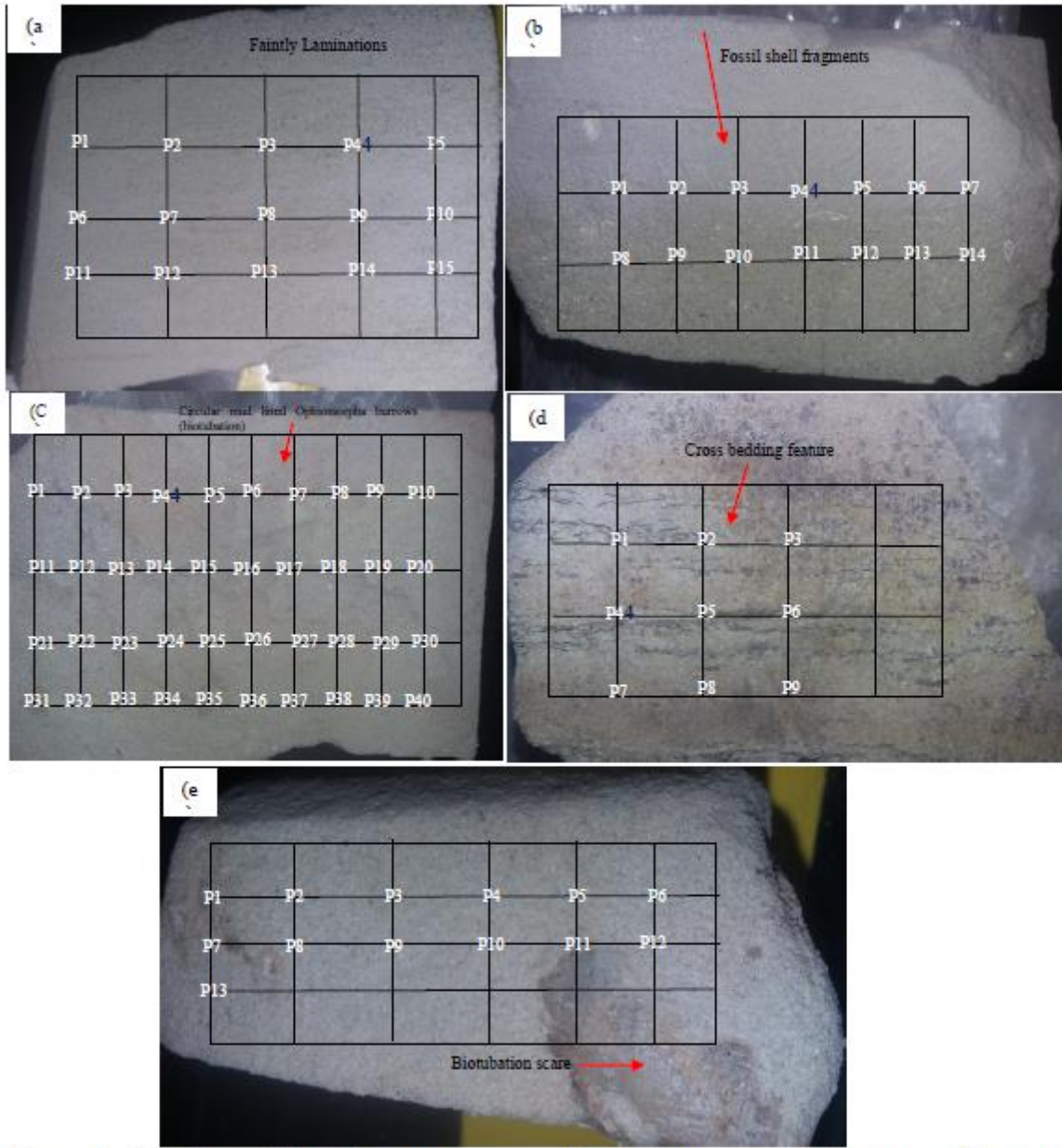


Figure 2. Showing variable sedimentary structures (a) Faintly cross-stratified sandstone with no trace fossils (b) laminated, finning up sandstone with shell fragments (c) cross stratified sandstone, circular mud lined Ophiomorpha burrows (bioturbation) presence of high content of iron oxides and clay (d) cross laminated sandstone with no bioturbation features (e) coarse bioturbation sandstone lithofacies

The sedimentary cross laminated structured sandstone lithofacies (Figure 2d) has a porosity of about 4.08% with matrix content of 50.08% composition. The monocrystalline grain size varies from $67.7\mu\text{m}$ to $316.6\mu\text{m}$ averaging to $172.7\mu\text{m}$, but little polycrystalline quartz totaling to 45.83% (Fig 3g) composition. The developed oversize (Fig. 3h) measured from microphotographs pore vary from 42238 nm to 135635 nm at an overall average of 74151 nm as indicated in mercury bimodal (Figure 4d)

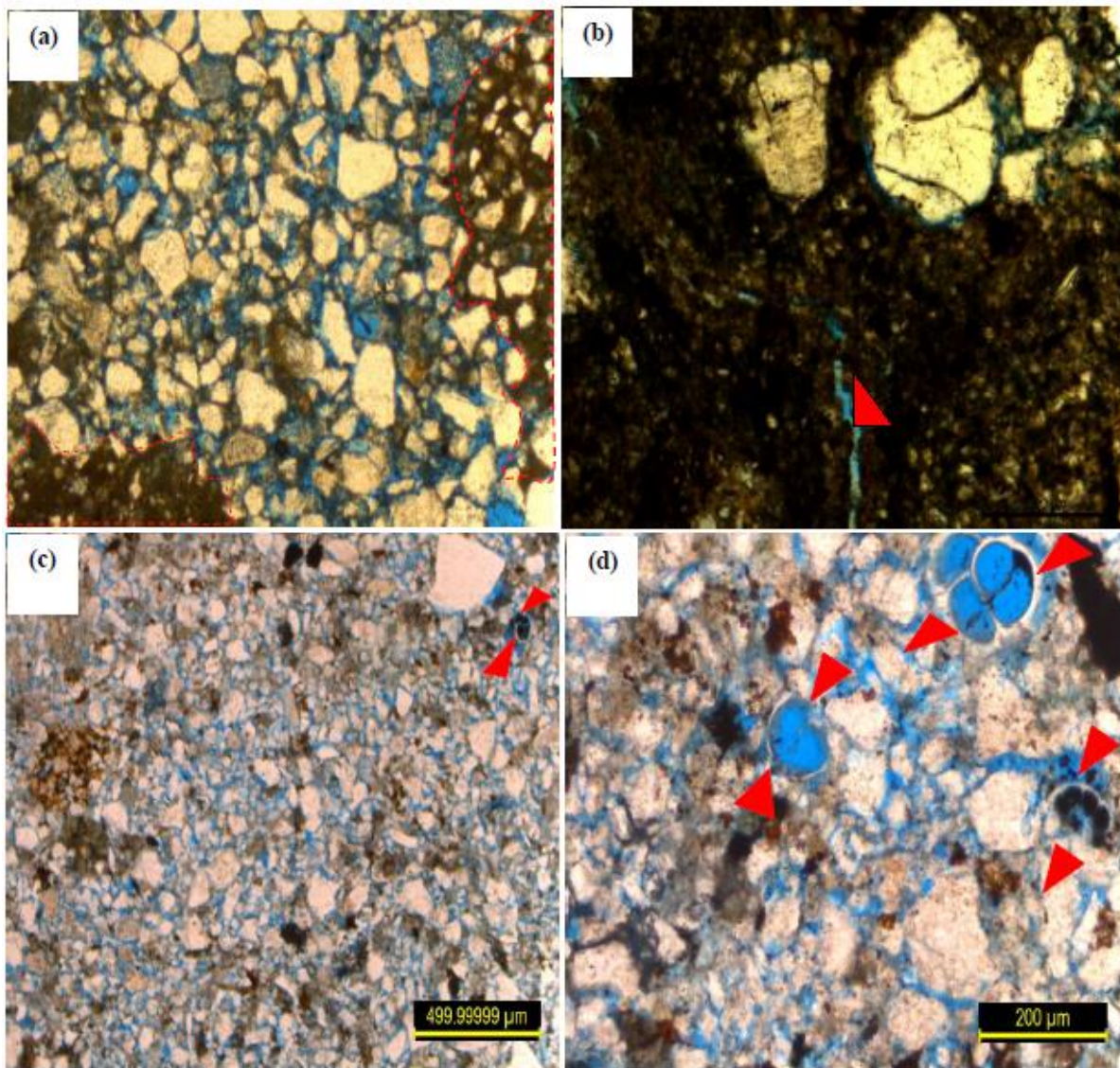


Figure 3. Showing thin section (A) faintly cross-stratified sandstone with random matrix filling (indicated with red dotted line) and (B) pore space within matrix indicated with red arrow (C) laminated, finning up sandstone with shell fragment facies (D) indicating intra pores within shell fragment cavities depict with red arrows

The coarse bioturbation sandstone lithofacies (figure 2e), is texturally matured with moderately to well-sorted grain. It comprises of 44.17% monocrystalline and polycrystalline quartz grains. The sub-matured sandstone is having loosely (figure 3e) intergranular oversize pores [19] totaling to 11.05% porosity, and a matrix of 44.33%. The measured pore sizes from a thin section within it matrix (as depicted in figure 3a) varying from 168 nm to 119656 nm with an average of 18749 nm and 91319 nm are intergranular pores as indicated in mercury bimodal (see Figure 4e).

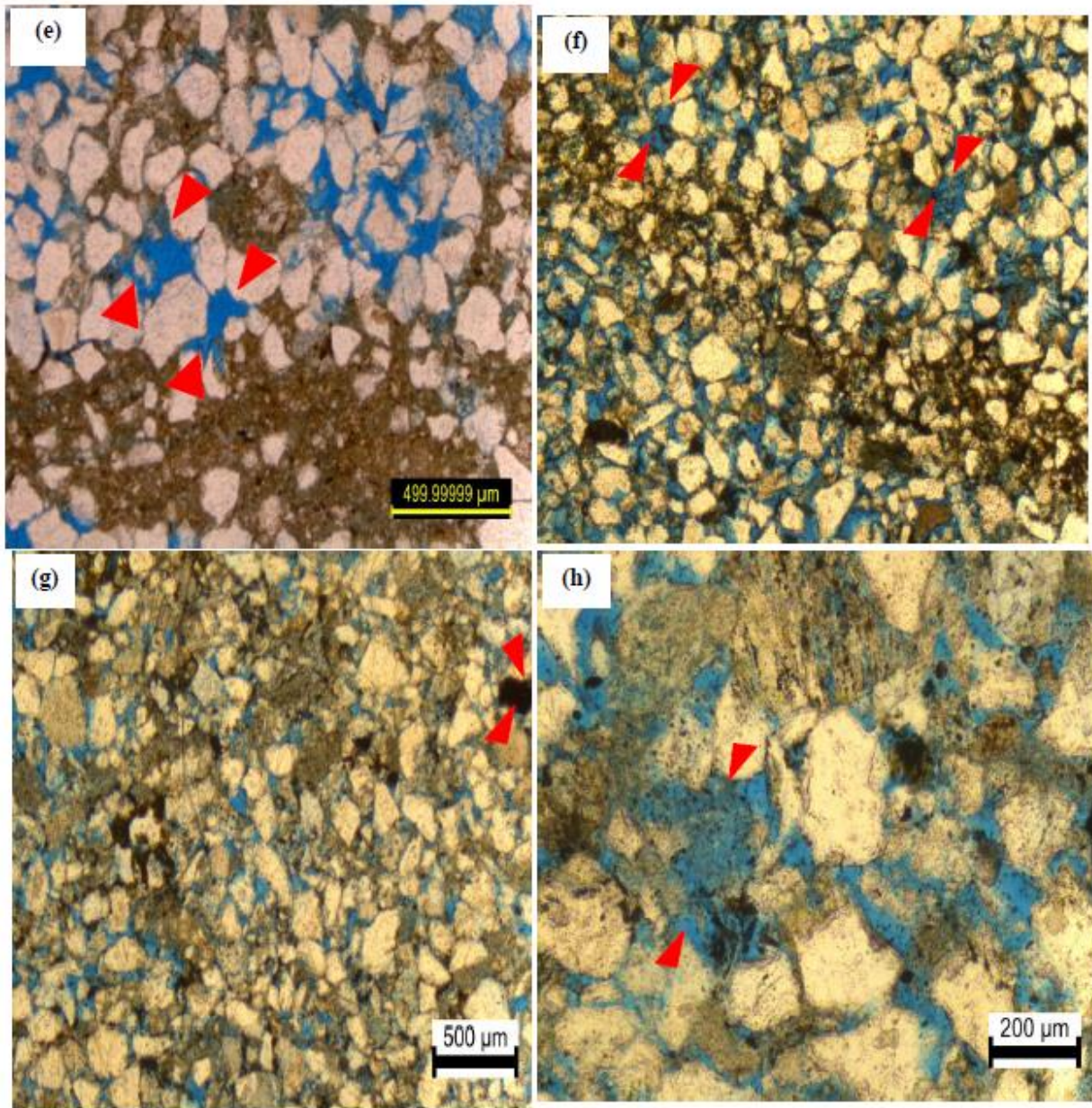


Figure 4 (e). Matrix in fill and oversize pores indicated with red arrows (f) pore cross stratified sandstone, biotubulated sandstone facies indicated by red arrow (g) cross laminated sandstone facies with oversize pore indicated (h) with red arrows

4. Results and discussion

4.1. Impact of small-scale heterogeneities on permeability variations

The variable internal textural compositional suites and distributions in faintly cross stratified, laminated fining up, cross laminated and cross stratified with circular mud line *Ophiomorpha* burrows sedimentary structured sandstone lithofacies excluding coarse biotubulated lithofacies suggest to contain both coarse-and fine foreset laminae [23-24].

These inhomogeneous internal configuration, differences in origins and distribution of pore types (Figure a; c; e; g & i) reveal to have different effects on permeability measurement [25-26]

at every crossed-points (P1-Pn) on gridded variable sedimentary structure, Figure 2a – e presented in Figure 4(b; d; f, h & j) and Table 1-5.

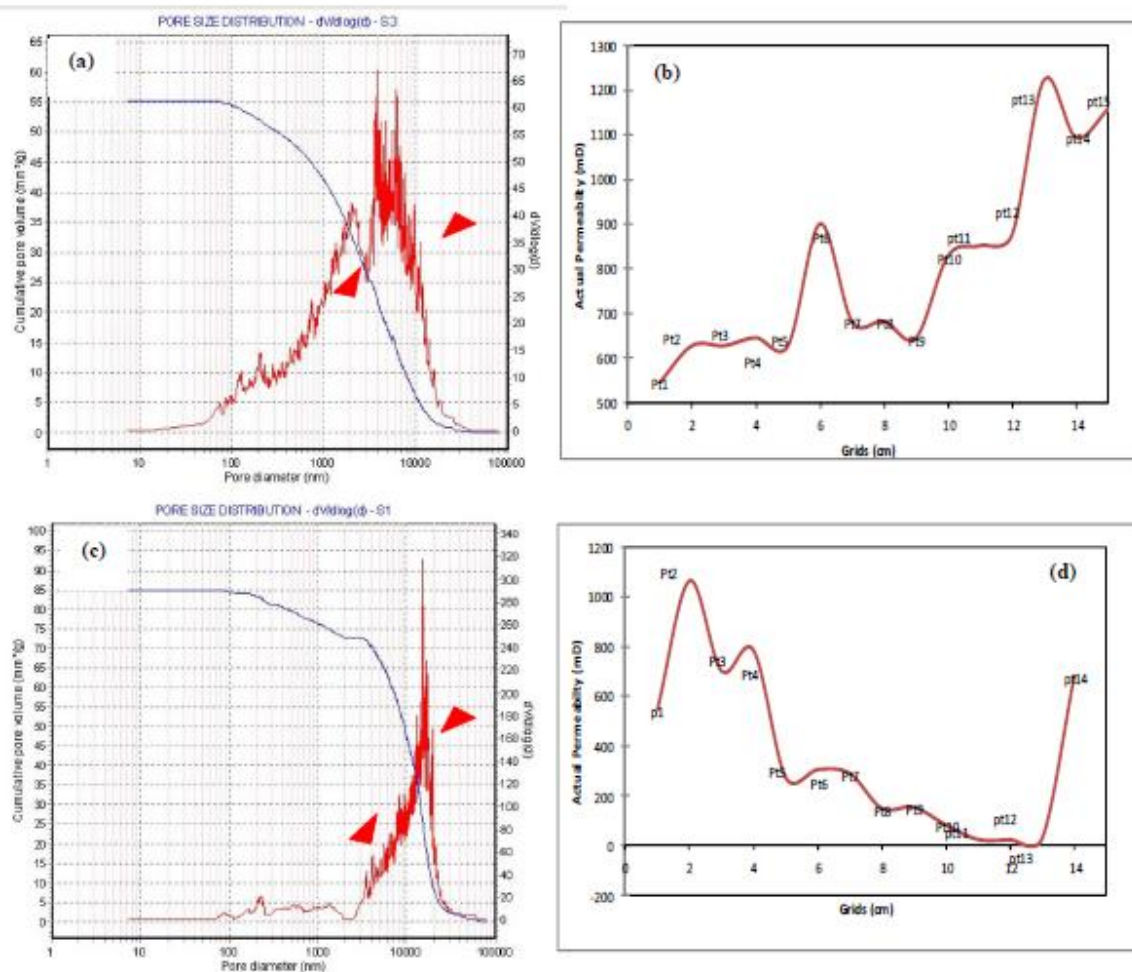


Figure 5 (a). Showing corresponding pore sizes in mercury bimodal (nm) indicated with red arrows (b) impact of small-scale heterogeneity at point spots on permeability in cross-stratified sandstone (c) corresponding pore sizes in mercury bimodal (nm) indicated with red arrows (d) impact of small - scale heterogeneity at point spots on permeability in laminated, finning up sandstone lithofacies

Table 1. Permeability distribution in the faintly laminated cross stratified sandstone lithofacies

Point number	Permeability $10^{-3} \mu\text{m}^2$	Point description	Point number	Permeability $10^{-3} \mu\text{m}^2$	Point description
P1	533	Lamina structure	P9	618	Lamina structure
P2	635	Lamina structure	P10	819	Lamina structure
P3	628	Lamina structure	P11	828	Host sample
P4	618	Lamina structure	P12	910	Host sample
P5	592	Lamina structure	P13	1188	Host sample
P6	893	Host sediment	P14	1120	Host sample
P7	682	Lamina structure	P15	1140	Host sample
P8	693	Lamina structure			

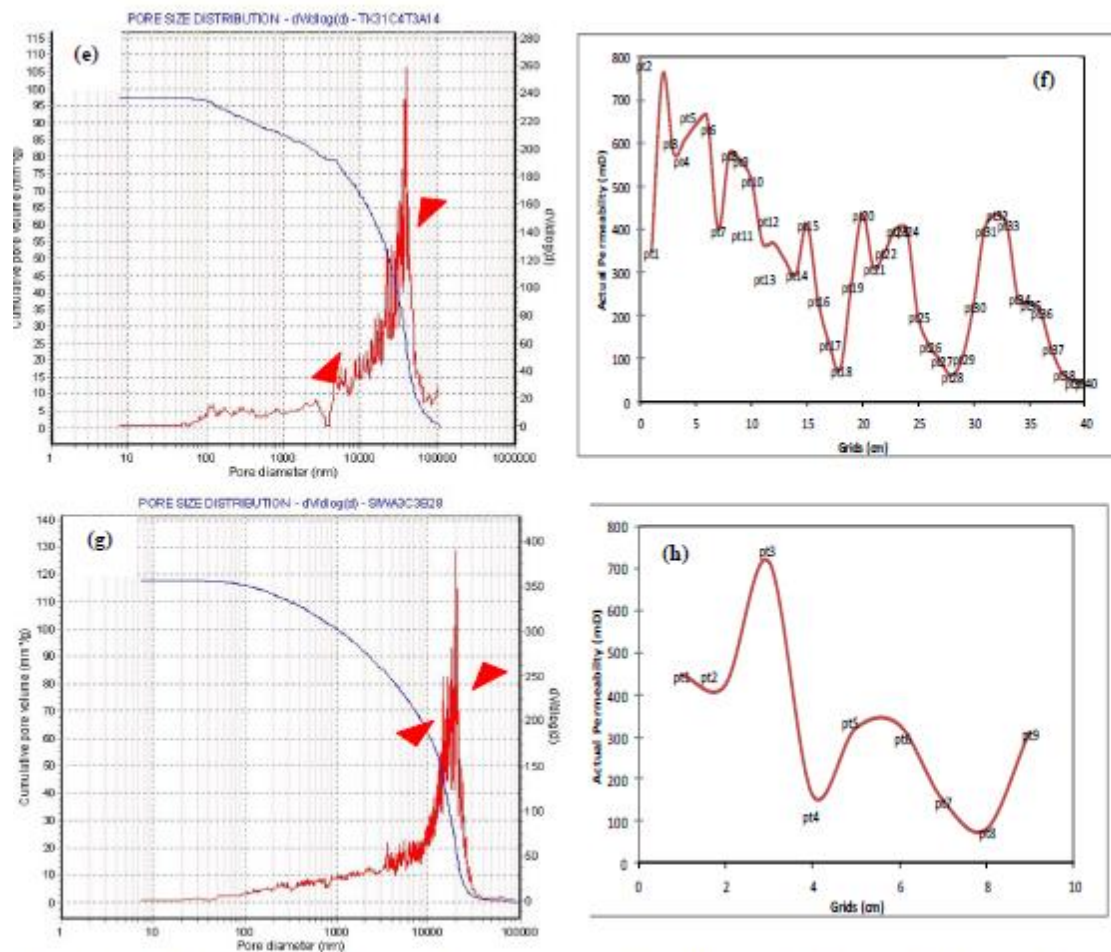


Figure 5 (e). Showing corresponding pore sizes in mercury bimodal (nm) indicated with red arrows (f) impact of small-scale heterogeneity at point spots on permeability in cross laminated sandstone (g) corresponding pore sizes in mercury bimodal (nm) indicated with red arrows (h) impact of small - scale heterogeneity at point spots on permeability in coarse biotubated sandstone lithofacies

Table 2. Permeability distribution in laminated, finning up sandstone with shell fragment lithofacies

Point number	Permeability/ $10^{-3} \mu\text{m}^2$	Point description
P1	498	Host sample (fining section)
P2	1124	Host sample (boundary between coarse -fining section)
P3	726	Host sample (boundary between coarse -fining section)
P4	793	Host sample (boundary between coarse -fining section)
P5	253	Host sample (boundary between coarse -fining section)
P6	234	Host sample (boundary between coarse -fining section)
P7	249	Host sample (boundary between coarse -fining section)
P8	168	Host sample (coarsening up section)
P9	171	Host sample (coarsening up section)
P10	121	Host sample (coarsening up section)
P11	118	Host sample (coarsening up section) with fossil
P12	98	Host sample (coarsening up section)
P13	79	Host sample (coarsening up section)
P14	648	Host sample (coarsening up section)

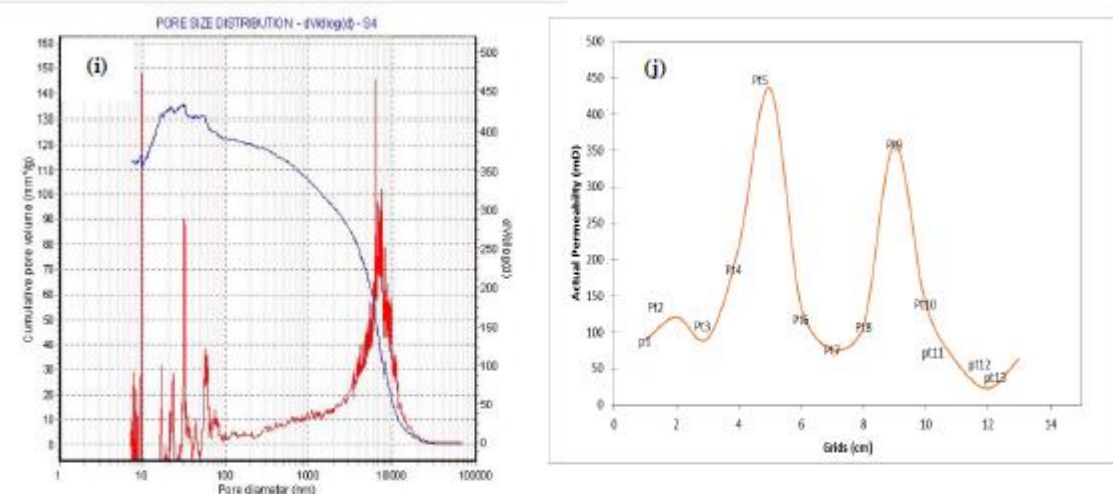


Figure 5 (i). Showing corresponding pore sizes in mercury bimodal (nm) indicated with red arrows (j) impact of small- scale heterogeneity at point spots on permeability in cross laminated sandstone

Table 3. Permeability distribution in cross stratified sandstone, *circular mud lined Ophiomorpha burrows* (bioturbation) lithofacies

Point number	Permeability $10^{-3} \mu\text{m}^2$	Point description	Point number	Permeability $10^{-3} \mu\text{m}^2$	Point description
P1	348	Ophiomorpha burrows scare	P21	301	Host sediment
P2	794	Ophiomorpha burrows scare	P22	368	Host sediment
P3	598	Ophiomorpha burrows scare	P23	398	Ophiomorpha burrows scare
P4	564	Ophiomorpha burrows scare	P24	378	Ophiomorpha burrows scare
P5	645	Ophiomorpha burrows scare	P25	179	Host sediment
P6	631	Ophiomorpha burrows scare	P26	144	Host sediment
P7	398	Host sediment	P27	186	Ophiomorpha burrows scare
P8	567	Ophiomorpha burrows scare	P28	73	Host sediment
P9	558	Ophiomorpha burrows scare	P29	118	Host sediment
P10	512	Host sediment	P30	219	Host sediment
P11	355	Host sediment	P31	368	Ophiomorpha burrows scare
P12	410	Ophiomorpha burrows scare	P32	411	Ophiomorpha burrows scare
P13	310	Host sediment	P33	352	Host sediment
P14	298	Ophiomorpha burrows scare	P34	216	Host sediment
P15	416	Ophiomorpha burrows scare	P35	218	Ophiomorpha burrows scare
P16	242	Host sediment	P36	197	Host sediment
P17	143	Host sediment	P37	112	Host sediment
P18	75	Host sediment	P38	87	Host sediment
P19	268	Host sediment	P39	82	Host sediment
P20	448	Ophiomorpha burrows scare	P40	51	Host sediment

Table 4. Permeability distribution in cross bedding sandstone lithofacies

Point number	Permeability $10^{-3} \mu\text{m}^2$	Point description
P1	448	Host sediment
P2	398	Host sediment (lamina structure)
P3	738	Host sediment (lamina structure)
P4	128	Host sediment (lamina structure)
P5	309	Host sediment
P6	298	Host sediment (lamina structure)
P7	123	Lamina structure
P8	89	Host sediment
P9	300	Host sediment

Table 5. Permeability distribution in coarse bioturbation sandstone lithofacies

Point number	Permeability $10^{-3} \mu\text{m}^2$	Point description
P1	93	Host sediment (biotubated scare)
P2	128	Host sediment
P3	89	Host sediment (biotubated scare)
P4	189	Host sediment
P5	438	Host sediment
P6	113	Host sediment
P7	78	Host sediment (biotubated scare)
P8	111	Host sediment
P9	370	Host sediment
P10	119	Host sediment
P11	76	Host sediment (biotubated scare)
P12	48	Host sediment (biotubated scare)
P13	52	Host sediment (biotubated scare)

However, bioturbation either enhances permeability due to a different degree of burrowing activity and burrow fillings or perhaps reduces permeability [12] because of grain reworking and resorting. However, in faintly cross-stratified sandstone the consequential increase permeability values (see Figure 2a) suggest due to oversize pores in fabric framework (see Figure 3a & b) as it reveals measured average pore diameter to vary from 9083 nm to 96886 nm marked in mercury injection graph. In the laminated, finning up sandstone with shell fragments sandstone facies (figure 2b), have a porosity of 7.67%. The measured intrapores preserved within the framework by variable shell cavity sizes at an average of 42080 nm embedded grandmas matrix of 67.75%. These, however, suggest responsible for the increase in permeability values at some cross-points (figure 4d), while decrease at some cross-points are attributed to the impact of coarse - and fine foreset [23-24] composition varying pore sizes.

Furthermore, in the cross stratified sandstone, *circular mud lined Ophiomorpha burrows* (bioturbation); Figure 2c, the variability in permeability value are attributed the discrete coarse-fine grains making up the 12.08% total porosity. The measured pore diameters from thin section average at 64895 nm indicated also in mercury bimodal (figure 4e) by a decrease in pressure [25]. The variation in permeability values (figure 4h) in the cross laminated sandstone with no bioturbation features (figure 2d) having a low porosity of 4.08% (Figure 3g). The measured pore size diameter (Figure 3h) from thin section average at 74151 nm as indicated in mercury bimodal (Figure 4g). In coarse bioturbation sandstone (figure 2e), having matrix content of 44.33% composing intergranular oversize [19] pore diameter at an average of 913159 nm amounting to 11.05% porosity as indicated in mercury bimodal (Figure 4i). However, measured intra pore diameters within the matrix in fill (see figure 3b) vary from 168 nm to 119656 nm suggest variations in permeability values at the cross points in figure 4j.

5. Conclusion

The result concluded that small - scale sedimentary heterogeneities have a potential impact on permeability [3-6] variation in all studied sandstone lithofacies as indicated in spot air permeameter values. These variabilities are attributed to the internal textural compositional suites and distributions containing both coarse - and fine foreset laminae [21,23-24], as bioturbation also either enhances permeability due variable degree of burrowing activity and burrow fillings or perhaps reduces permeability [12] because of grain re-sorting. The inhomogeneity in the internal configuration resulting from the pattern visible primary structures contribute to having variable effects on pore sizes distribution, fluid flow unit [3] and permeability measurement [25-26] at every crossed-points (P1- Pn) on the gridded variable sedimentary structure in studied sandstone lithofacies. Thus, acknowledging and understanding the variable effect of small – scale sedimentary heterogeneities at macroscale

(3cm – 3m's thick) would be useful as requirements for reliable prediction of fluid flow in hydrocarbon production and oil recovery during reservoir modeling.

Acknowledgment

Thanks to PETRONAS for core samples and PhD scholarship opportunity given to carry out this work

References

- [1] Tiab D and Donaldson EC. *Petrophysics: theory and practice of measuring reservoir rock and fluid transport properties*. Gulf Professional Publishing, 2015.
- [2] Ben-Awuah J and Padmanabhan E. *Porosity and Permeability Modifications by Diagenetic Processes in Fossiliferous Sandstones of the West Baram Delta., Offshore Sarawak*, 2014.
- [3] Mikes D. Sampling procedure for small-scale heterogeneities (crossbedding) for reservoir modelling. *Marine and Petroleum Geology*, 2006; 23: 961-977.
- [4] Morton K, Thomas S, Corbett P and Davies D. Detailed analysis of probe permeameter and interval pressure transient test permeability measurements in a heterogeneous reservoir. *Petroleum Geoscience*, 2002; 8: 209-216.
- [5] Willis BJ and White CD. Quantitative outcrop data for flow simulation. *Journal of Sedimentary Research*, 2000; 70: 788-802.
- [6] Huysmans M, Peeters L, Moermans G and Dassargues A. Relating small-scale sedimentary structures and permeability in a cross-bedded aquifer. *Journal of Hydrology*, 2008; 361: 41-51.
- [7] Latief AI, Ridzuan AI, Faehrmann PA, MacDonald AC, Arina W and Rahman G. An Innovative Static Modeling Approach to handle a Complex Giant within a Compressed Timeframe; A Case Study of Baram Oil Field, Offshore Sarawak, East Malaysia. in *SPE Asia Pacific Oil and Gas Conference and Exhibition*, 2012.
- [8] Khatib H. IEA world energy outlook 2011—A comment. *Energy policy*. 2012; 4: 737-743.
- [9] Abdullah R. Oil & Gas Industry—Opportunities and Challenges Ahead. Retrieved on February. 2012; 3: 47-61.
- [10] Ben-Awuah J and Padmanabhan E. An enhanced approach to predict permeability in reservoir sandstones using artificial neural networks (ANN). *Arabian Journal of Geosciences*, 2017; 10: 173-183.
- [11] Tan D, Rahman A, Anuar A, Bait B, and Tho CK. West Baram Delta. *The Petroleum Geology and Resources of Malaysia*, Petroliam Nasional Berhad (PETRONAS), Kuala Lumpur, 1999. 291-341.
- [12] Ben-Awuah J and Eswaran P. Effect of bioturbation on reservoir rock quality of sandstones: A case from the Baram Delta, Offshore Sarawak, Malaysia. *Petroleum Exploration and Development*, 2015; 42: 223-231.
- [13] Hutchinson Jr C, Dodge C and Polasek T. Identification, classification and prediction of reservoir nonuniformities affecting production operations. *Journal of Petroleum Technology*, 1961; 13: 223-230.
- [14] Rijks E. Baram Delta geology and hydrocarbon occurrence. *Geol. Soc. Malays. Bull*, 1981; 14: 1-8.
- [15] Abdulrahman AH, Menier D, and Mansor YM. Sequence stratigraphy modeling and reservoir Architecture of the shallow marine succession of Baram Field, West Baram Delta offshore Sarawak, East Malaysia. *Mar. and Petrol. Geol.*, 2014; 4: 687-703.
- [16] Pettijohn F, Potter P, and Siever R. *Sand and Sandstone*. New York/Heidelberg/Berlin, 1973.
- [17] Tucker ME. *Sedimentary rocks in the field*. John Wiley & Sons, 2003.
- [18] Boggs S. *Petrology of sedimentary rocks*. Cambridge University Press, 2009.
- [19] James RA. Application of petrographic image analysis to the characterization of fluid-flow pathways in a highly-cemented reservoir: Kane Field, Pennsylvania, USA. *Journal of Petroleum Science and Engineering*, 1995; 13: 141-154.
- [20] Ehrlich R, Prince C, and Carr MB. Sandstone reservoir assessment and production is fundamentally affected by properties of a characteristic porous microfabric. in *SPE Annual Technical Conference and Exhibition*, 1997.
- [21] Evans RC. An investigation into the influence of common sedimentary structures and diagenesis on permeability heterogeneity and anisotropy in selected sands and sandstones. 1987.
- [22] Martinus AW, Howell J, Steel R, and Wonham J. *From Depositional Systems to Sedimentary Successions on the Norwegian Continental Margin (Special Publication 46 of the IAS)*: John Wiley & Sons, 2014.

- [23] Hurst A, and Rosvoll KJ. Permeability variations in sandstones and their relationship to sedimentary structures. in *Reservoir Characterization II*, ed: Elsevier, 1991: 166-196.
- [24] Hartkamp-Bakker CA. Permeability heterogeneity in cross-bedded sandstones: impact on water/oil displacement in fluvial reservoirs. TU Delft, Delft University of Technology, 1993.
- [25] McCreesh CA, Ehrlich R, and Crabtree SJ. *Petrography and Reservoir Physics II: Relating Thin Section Porosity to Capillary Pressure, the Association Between Pore Types and Throat Size (1)*. AAPG Bulletin, 1991; 75: 1563-1578.
- [26] Passey QR, Bohacs K, Esch WL, Klimentidis R, and Sinha S. From oil-prone source rock to gas-producing shale reservoir-geologic and petrophysical characterization of unconventional shale gas reservoirs. in *International Oil and Gas Conference and Exhibition in China*, 2010.
- [27] Abu Bakar M, Chong YY, Nasir E, Din A, Chai CF, Fui CC, Agarwal B, Valdez R, Adamson GR. EOR Evaluation for Baram Delta Operations Fields, Malaysia. in *SPE Enhanced Oil Recovery Conference*, Indonesia 2011, SPE 144533.

To whom correspondence should be addressed: I. Yusuf, Department of Geosciences, Faculty of Geosciences and Petroleum Engineering, Universiti Teknologi PETRONAS, postcode 32610, Seri Iskandar, Perak, Malaysia

SULPHUR: NATURE, TECHNOLOGY, APPLICATION, WORLD PRODUCTION AND CONSUMPTION, AND ITS OUTLOOK

Javad Alaei Kadijani¹, Sahar Sirani², Amirmasoud Zolfaghari²

¹ Research Institute of Petroleum Industry (RIPI), Gas Department (Tehran- Iran)

² Islamic Azad University, Science and Research Branch (Tehran- Iran)

Received March 11, 2018; Accepted May 11, 2018

Abstract

This article aims at reviewing sulphur by presenting its nature, traditional and new technologies of extraction, removal or recovery, and introducing its most common applications. In the article, global sulphur production and consumption rate are presented as well. Moreover, sulphur balance, logistics and outlook are addressed.

Keywords: Elemental sulphur; sulphur modified materials; sulphur fertilizer; sulphur concrete; Lithium/Sulfur battery.

1. Introduction

Sulphur is one of the world's common chemical elements that occur naturally in its native form, a solid crystal substance, or extracted mainly from petroleum refineries and natural gas processing, thus creating a global surplus of sulphur [1]. Sulphur as a non-metals is capable of combining essentially with all chemical elements and form various compounds; such as sulphuric acid, produced as a by-product of ferrous and non-ferrous metal smelting. Other compounds, such as sulphur dioxide, come from the emission from petroleum products used in cars and coal generating electricity. Its other properties include low thermo- and electro-conductivity and low water solubility.

Elemental sulphur (Brimstone): This refers to sulphur produced in its elemental form, that is, sulphur mined by processes such as Frasch or as native refined sulphur, or recovered from gas and oil production [2]. Elemental sulfur is mostly used in the production of sulfuric acid for the preparation of fertilizers. In addition, it has been also employed as a concrete additive and more recently, lithium-sulfur batteries and polymeric materials [3].

Lime sulphur: Lime sulphur, a mixture of calcium and sulphur (calcium polysulfide), has been used as a pesticide to control diseases in a wide range of plant species for over a century in both floriculture and horticulture. Firstly, lime sulphur dips are used in veterinary industry to cure dogs, cats, puppies and kittens suffering from non-specific dermatoses and parasites [4].

Sulphur in other forms (SOF): The forms other than brimstone or pyrites, where sulphur is produced in the form of sulphuric acid or other sulphur compounds without prior refining to brimstone. SOF, mainly, originates from the smelting of non-ferrous metals, led by copper, followed by zinc, lead, and nickel [5].

Sulphur in all forms: The aggregate of brimstone, the equivalent sulphur content of pyrites, and the equivalent SOF [5].

Discretionary (voluntary) and non-discretionary (non-voluntary) sulphur: where there is an economic case for producing, Sulphur can also be classified as discretionary sulphur which normally includes Frasch, native sulphur, and pyrites. Non-discretionary sulphur has to be recovered, regardless of the economics of sulphur recovery, either for environmental/regulatory or process reasons. Recovered sulphur and SOF are almost always non-discretionary [5].

The oil and gas industry must look at sulphur as a primary product and manage its production, and a large quantity of sulfur is obtained from the current environmental restrictions regarding the petroleum and gas refining processes, coal processing, and refining of copper in the mining sector. Thus, the interest appeared regarding the application of sulphur in different fields, and extensive research programs initiated with the focus on various properties of the material. Sulphur is utilized in many fields the most important of which are agriculture, construction and energy source industries.

2. Extraction, removal or recovery

Natural gas which contains varying amounts of CO_2 and H_2S is called sour natural gas. Hydrodesulphurization or natural gas sweetening is a process for H_2S removal from natural gas. Hydrodesulphurization of natural gas with subsequent sulphur recovery is mainly performed in amine and Claus plants. For as for large quantities of sulphur (> 50 ton/day), these processes are most economical. However, in case of H_2S removal from smaller gas fields, the gas is generally treated by liquid redox processes, or, alternatively, by amine treatment followed by incineration or re-injection of the acid gas in an empty well. There are some new technologies in the field as well. All these processes have their strengths and weaknesses [\[6\]](#).

2.1. The Frasch process

The Frasch process developed in the 1890's by chemist Herman Frasch. Sulphur is extracted from underground deposits by the Frasch process until the end of the 20th century. It is carried out by putting three concentric tubes into the sulphur deposit. Then, superheated water and hot air are put into the tubes, so the sulphur is pushed up to the surface. This kind of recovered sulphur is usually very pure, but if contaminated by organic compounds there is no need to purify it.

2.2. Amine process

The most common gas treating process is the amine process in which acid gases react chemically. The 'rich' amine solution is heated under low pressure to regenerate the liquid by forcing off the acid gases. In this process, several different amine solutions can be used such as: methyl di-ethanol amine (MDEA), mono-ethanol amine (MEA) and di-ethanol amine (DEA). For each of the amine solutions listed, the sweetening process is similar. The type of solution used in the process depends upon the type and quantity of acid gas contained in the sour gas stream and the volume of sour gas to be treated [\[7\]](#).

2.3. The Claus process

Nowadays, the standard process used to extract sulphur via petroleum and gas sources is the Claus process developed in the 1880's by chemist Carl Friedrich Claus. For quantities of sulphur greater than 50 ton/day, this process is considered economical. In this kind of sulphur needs to be processed to remove it from the natural gasses that are mixed with it. In the Claus processing, the sulphur compounds in the gas are converted into elemental sulphur, and the hydrogen sulphur is extracted from the gas. Sulphur recovered this way may be in a solid or a liquid form.

Hauwert [\[8\]](#) reviewed four processes for small-scale sulphur recovery from sour associated gas, including liquid reduction/oxidation (redox), Thiopaq O&G, CrystaSulf, and direct catalytic oxidation. He described the processes for removal of sulphur quantities ranging from 1 ton per day to 20 tons per day, for direct treatment of high-pressure natural gas and low-pressure associated petroleum gas, and for sulphur recovery from low-pressure acid gas.

2.4. Liquid redox

The liquid redox processes are suitable for recovery when the sulphur load is too small for the Claus process. In Redox methods an alkaline solution with high-valent metal ions is used, such as vanadium (Stretford process) and iron (LoCat and SulFerox processes). The metal

ions convert the dissolved H_2S into elemental sulphur. Then, it is regenerated by oxidation with air. The sulphur content is generally 80% by weight (dry) and can be upgraded to 99.5% by washing and smelting. plugging and foaming may occur and cause operational problems due to the process solution is aqueous with hydrophobic (i.e., repel water) solid sulphur particles [8].

2.5. Thiopaq O&G

Thiopaq O&G process, developed in the 1990s by Paques for desulphurization of biogas, was modified by collaboration with Shell Global Solutions for application at high pressure in oil and gas environments. The first commercial Thiopaq O&G unit was built in 2002. It is a biotechnological process which removes H_2S from gaseous streams by absorption into a mild alkaline solution followed by the oxidation of the absorbed sulfide to elemental sulphur by naturally occurring microorganisms. offers a replacement for liquid redox processes or amine treating, Claus recovery and tail gas treatment; minimal chemical consumption, high turndown ratio, gas treatment as well as sulphur recovery, H_2S removal to below 4 ppmv, essentially 100% conversion of sulfide in the bioreactor with 95-98% selectivity to S, no need to replacement of the biocatalyst. Application to H_2S concentrations of 100 ppmv to 100 vol.% and pressures from 1-75 bar(g). Thus, direct treatment of either the sour gas or the amine off-gas is possible [6]. This process is shown in Figure. 1.

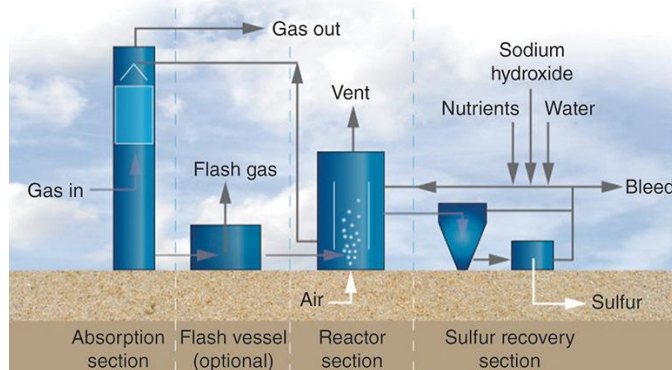


Fig. 1. The Thiopaq O&G desulfurization process uses naturally occurring *Thiobacillus* bacteria to oxidize hydrogen sulfide to elemental sulfur. Source: Paqell

In this processing method, in comparison to traditional removal processes such as the Amine/Claus process the following advantages are recognized: no practically free H_2S available anywhere downstream of the scrubber inlet leading to very safe and easy to operate unit; very simple line-up requiring little control and supervision; no complex control loops; a relatively large volume of (cheap) solvent leading to very slow changes in solvent composition and performance of the unit and more robust process [6].

2.6. CrystaSulf

In the 1990s, The Gas Research Institute developed the process for H_2S removal from high-pressure gas in which a non-aqueous hydrocarbon solvent which contains sulphur dioxide is used similarly to a liquid-phase Claus process. When the solution comes into contact with the gas containing the H_2S , elemental sulphur and water are formed, the sulphur dissolves in the solvent and is precipitated in a scraped-surface crystallizer to decrease plugging and foaming. The amount of H_2S is reduced to ppmv levels, and for associated gas applications, no foaming or negative effects from hydrocarbon condensation are expected. However, the solvent can be costly for large, low-pressure gas flows with limited H_2S content [8]. Figure. 2 illustrates the CrystaSulf process.

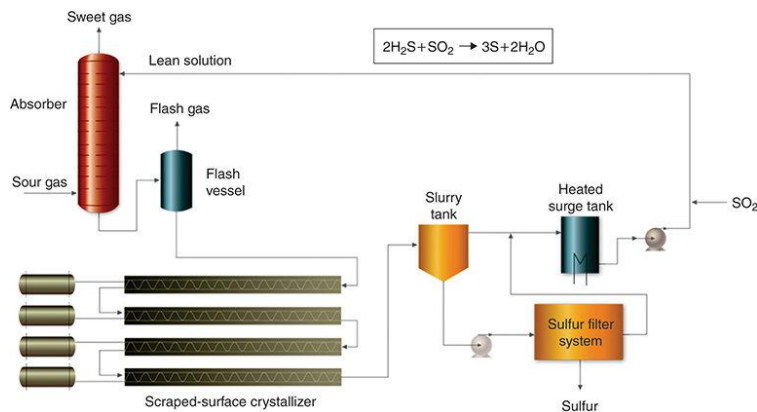


Fig. 2. The CrystaSulf process uses a non-aqueous solvent that contains sulfur dioxide. When the solution comes into contact with hydrogen sulfide, elemental sulfur and water are formed. *Source: GTC Technology*

2.7. Direct catalytic oxidation

This process was developed by TDA Research, which is licensed by GTC Technology. the process (Figure 3)which is applicable to lean acid gas streams, converts H₂S directly into sulphur by using a catalyst. As the company said, it is effective for sulphur recovery ranging from 0.1 ton per day to 200 tons per day and that the sulphur conversion efficiency is approximately 90% in a single pass [8].

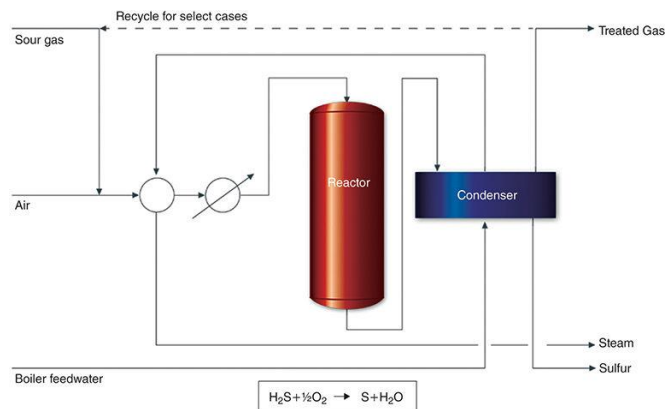


Fig. 3. The direct catalytic oxidation process is applicable to lean acid gas streams and converts hydrogen sulfide directly into sulfur by using a catalyst. *Source: GTC Technology*

3. Application

There was a remarkable investment in clean air and against discharge of sulphur into the atmosphere during the 1960s. This made sulphur a surplus commodity on the market, particularly in the United States and Canada. Therefore, the interest appeared regarding the application of sulphur in different fields, and extensive research programs initiated with the focus on various properties of the material.

Most elemental sulphur is converted into sulphuric acid (H₂SO₄) which is used in the industrial production of chemicals and in the sulphur-iodine cycle to obtain hydrogen. The largest use of sulphuric acid is for the manufacture of primary phosphates, nitrogen, potassium, and sulphate fertilizers. Sulphuric acid often used to manufacture numerous products including industry chemicals, construction materials, paints, rubber products, medicines, fibers, sugar, plastics, paper, lead-acid batteries, non-ferrous metals, pigments, hydrofluoric acid, carbon disulphide, water treatment, caoutchouc, dyestuffs, drilling muds, in petrochemical and pulp and steel pickling, fungicides, pesticides, and pharmaceuticals.

3.1. Sulphur in agriculture: fertilizer

For many years, the focus of fertilizer industry has been on nitrogen, phosphorus, and potassium; however, that attention is expanding to include plant nutrient sulphur as sulphate. Sulphur is typically considered the fourth major nutrient in terms of total volume requirements for plant growth [9]. Sulphur is necessary for plant growth and nutrition. it contributes to an increase in crop yields in different ways: it provides a direct nutritive value; it provides indirect nutritive value as soil amendments; and it improves the use efficiency of other essential plant nutrients, particularly nitrogen and phosphorus.

Sulphur contained fertilizers are of two primary kinds; sulfate fertilizers where the sulphur is in sulfate form and readily available for crops to intake, and elemental sulphur fertilizers which need to be oxidized into sulfate before plants are able to uptake it [10].

The traditional fertilizers containing sulphate includes single superphosphate, ammonium sulphate, and potassium sulphate. The emerging fertilizers containing sulphate are ammonium phosphate-sulphate, potassium magnesium sulphate, various micronutrient sulphate salts, ammonium nitrate-sulphate, sulphate-NPK compound fertilizers and urea-ammonium sulphate [11].

The sulphur formed from the THIOPAQ desulphurization plant is ideal for use as a fertilizer due to having a small particle size which helps in the oxidation of sulphur into sulfate, the effluent sludge from the THIOPAQ process contains sodium salts, sulfate and carbonate, which are all useful nutrients [12].

Worldwide sulphur deficiencies (Figure 4) are increasing due to a reduction in traditional S-containing materials, cleaner air programs and intensified agriculture increasing crop demand which leads Sulphur to gain prominence as a major nutrient [11]. It also provides an opportunity to advance carbon sequestration through the removal of a primary constraint to biomass production.

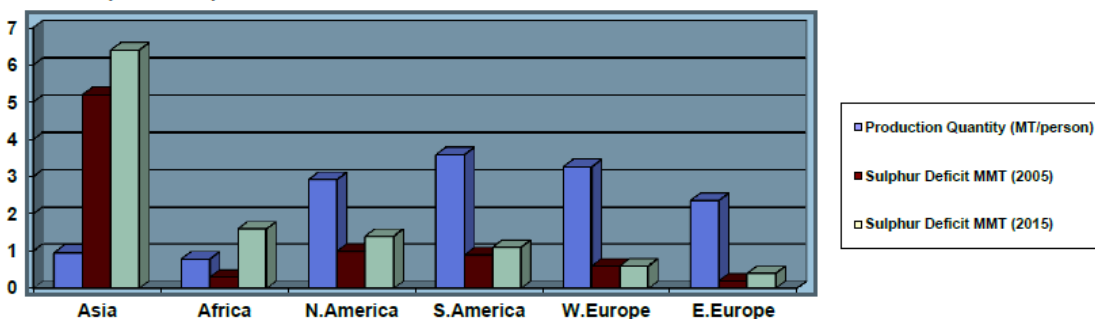


Fig. 4. Regional plant nutrient Sulphur deficit worldwide. Source: TSI

3.2. Sulphur in construction

In recent years, sulphur is increasingly used in road construction because the most significant consumers of sulphur surplus can be construction and road-building industries. Construction materials such as sulphur concrete and sulphur asphalt is receiving more attention since they are environmentally friendly and cost-effective. Many research [12-13] proved that in order to obtain composite resistant to chemical aggression, the sulphur could be used as a bond in the sulphur concrete. granular form is preferred for this area because it is more technological and creates no dust.

3.2.1. Sulphur concrete

Sulfur concretes is the mixtures of mineral aggregate and modified sulfur (*sulphur-polymer*) as a binder. The study of sulphur concrete began in the 70-ies of the 20th century, and its first application was for building ship anchors. In 1921, Bakon and Davis [14] introduced sulphur properties and its application in the production of construction materials.

The primarily produced sulphur concretes had several disadvantages - low resistance to high temperatures (this drawback has remained till now, and it is caused by the fact that sulphur melting temperature is 120°C), low fire resistance and cracking during hardening of large sulphur concrete volumes. Technology development allowed to eliminate the majority of the drawbacks. Thus it was determined that addition of plasticisers (especially polysulfides) to sulphur binders would not only improve plasticity of the solution but also decrease cracking, while the addition of stabilizers including dicyclopentadiene would increase fire and atmospheric conditions resistance of sulphur concrete. Moreover, the addition of Fire-retardants and Antiseptics decrease sulphur composition combustibility and increase the biological stability of sulphur concretes, respectively [9]. Figure 6 illustrates the technological scheme for sulphur concrete manufactures production.

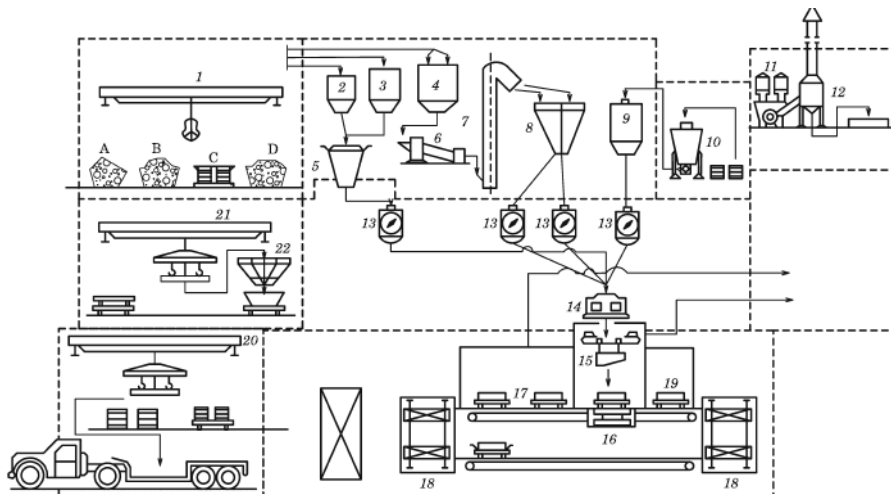


Fig. 5. Technological scheme for sulphur concrete manufactures production: A – gravel, B – sand, C – additives, D – sulphur, 1 – compounds storehouse, 2, 3, 4 – tanks (silos), 5 – sulphur modification reactor, 6 – rotary dryer, 7 – feeder, 8 – sand and gravel's silo, 9 – extender's silo, 10 – extender's feeder, 11 – cyclone, 12 – filter, 13 – feeder, 14 – mixer with heater, 15 – forming device, 16 – vibration station, 17, 18 – mobile forms, 19 – chamber for heating up the forms, 20 – storehouse for finished manufactures, 21, 22 – recycling station. Source: Ciak 2007, cited in Ciak 2013 [15]

Sulphur concrete has many advantages such as: frost resistance, high strength, stability in corrosive medium, low water permeability, high corrosion resistance, fast strength development, utilisation possibility of most of the harmful substances including radioactive wastes, and recycling possibility [15]. One of the key advantages of sulphur concrete is the little time it takes to harden that propitiates a kind of application in which it can offer a great advantage in repairing rigid (concrete) pavements, and urgent repairs in big industries [16]. In Table 1. the comparative characteristics of sulphur concrete and Portland cement concrete is presented [9].

Table 1. Comparative characteristics of sulphur concrete and Portland cement concrete

Properties	Sulphur concrete	Concrete
Moisture resistance	1	0.8
Chemical resistance (to acids)	84%	23%
Frost resistance (at 100% humidity)	300	50
Attrition resistance, %	3%	17%
Compression strength, MPa	55-65	15-25
Bending strength, MPa	10-15	6-9
Tensile strength, MPa	5-7	3-4
Time of strength development, hr	0.3	24

Utilization of sulphur-polymer materials is most efficient in some fields including: 1) Chemical industry: building vessels for chemically active substances (including chemical wastes), foundations for chemical vessels, concrete floors for chemical facilities, containers for chemical product storage, etc.; 2) Hydrotechnic construction building: manufacturing pipes for gravity and pressure sewer systems; pipelines for corrosive and toxic waste waters; facing slabs for canals; collector rings; drainage pipes; 3) Hazard waste disposal: Sulphur polymer materials allow to solve a problem of disposal of solid toxic wastes (mercury-containing wastes, radioactive wastes, overdue medical substances, dry pesticides) [9].

3.2.2. Sulphur asphalt

Bitumen, which is hard to obtain as a raw material, can be replaced by sulphur which is an abundant and practical raw material. Sulphur asphalt (SA) which is sometimes called sulphur bitumen or sulphur extended asphalt (SEA), is an alternative for asphalt road binder, a process in which sulphur is used to extend asphalt materials as a means of energy conservation by minimizing asphalt demand [5].

Commercial development of sulphur asphalt road paving materials started during the oil embargo in the 1970s. early attempts in sulphur enhanced asphalt showed positive improvements in the asphalt properties; however, it suffered from the formed H₂S during the manufacturing of the asphalt. New interest in using sulphur as a construction material has led to the development of sulphur enhanced asphalt with much better quality than standard asphalt [17]. Sulphur asphalt can create additional markets for the sulphur surplus and extend the overall asphalt products market.

3.3. Lithium/sulfur batteries

Recent decades witness worldwide attention towards new energy sources due to the impact of CO₂ emissions on global warming effect. In this regards, electrochemical energy storage systems, and most particularly batteries, play a crucial role in current and next generation applications. one such promising technology is lithium/sulfur (Li/S) systems with the potential for extremely high gravimetric energy [18]. The interest in Li-S is driven by the advantages it has over the existing Li-ion technologies. Many research teams are focused nowadays on the development of Li/S technology, fundamental understanding and modeling, and application-based control algorithm development [19], and at present, there are two start-up companies-Sion Power [20] in the USA and OXIS Energy [21] in the UK - on the market.

The Li-S battery's working mechanism is complex; however, Fotouhi [19] summarizes the working principle as follows.

"In a fully charged state, a Li-S cell consists of a cathode usually containing sulfur, a carbon-based material and a binder. The anode is lithium metal and is separated from the cathode by a polymer separator and an organic-solvent based electrolyte. During operation (discharge), solid sulfur from the cathode dissolves into the electrolyte, forming S_{8(l)}. Liquid S₈ is then electrochemically reduced at the cathode to form intermediate products, so called lithium polysulfide species (Li₂S_x) with accompanying oxidation of Li metal to Li⁺ ions at the anode. The polysulfides species (Li₂S_x 2 < x ≤ 8) are soluble in the liquid electrolyte and diffuse out from the cathode to the electrolyte/separator side. When the discharge proceeds, the length of the polysulfide chain is getting reduced, which in turns affects the viscosity, mobility and solubility of Li₂S_x compounds. At the end of discharge, S₈ is fully reduced to S²⁻ (Li₂S), and the anode is fully stripped of Li metal. This process is demonstrated schematically in Figure 1. During charge, the reverse reactions occur, with Li⁺ ions depositing at the anode as Li metal and low-order polysulfides oxidizing from S²⁻ up to S²⁻⁸ and eventually S_{8(s)}."

By developing state of the art in modeling, it is envisaged that it will be possible to explore state-of-the-art techniques for rapid online execution of spatially distributed models [22]. Auger [23] represents a possible road map (Figure 6), including contributions by control engineers follow developments in fast-executing electrochemical models.

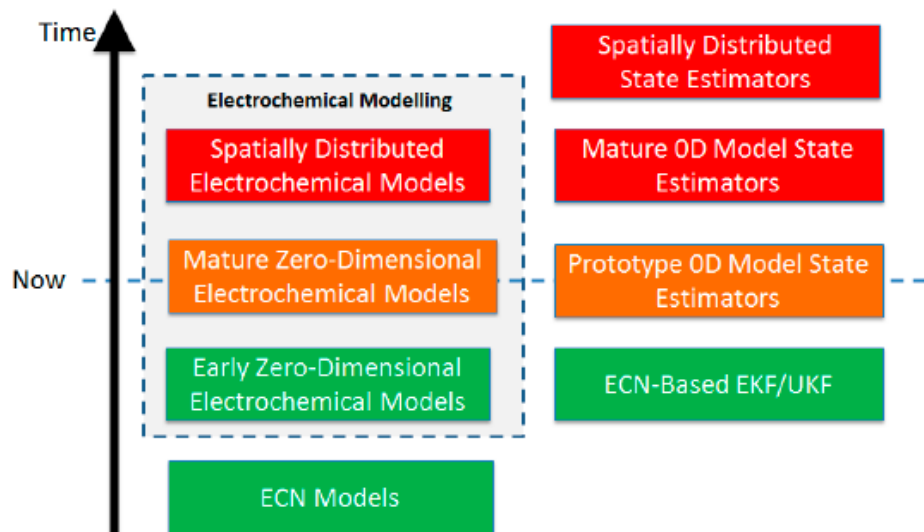


Fig. 6. Expected road map for state estimation in Li-S: colors are a 'traffic light' indication of technology readiness, with green representing most ready, and red representing furthest off

3.3.1. Advantages and limitations

One of the key advantages of the Li-S battery is the higher specific energy, predicted to be 2–3 times higher than the excited li-ion batteries. another advantage is that sulphur is cheap, abundant and non-toxic and environmentally friendly. Other advantages of Li-S batteries include low cost and availability of sulfur; intrinsic protection mechanism from overcharge, providing safety; wide temperature range of operation; possibility of long cycling [19–24]. In addition, the Li-S battery can be operated over a wide temperature range, especially at low temperature, which is a good power source in cold environments, such as battery systems for electric vehicles, as well as some aeronautical applications [25].

Despite the advantages of the Li-S battery technology, it suffers from some limitations as well. The complex reaction mechanism involved in the conversion of elemental sulfur (S_8) to the final reduction product, lithium sulfide (Li_2S) is a major difficulty in Li-S materials and cell development [22]. It also suffers from limitations such relatively low practical specific energy (200– 300 W h/kg) against expected values of 450–650 W h/kg; rapid decrease in capacity during cycling (0.1–0.4% per cycle); high self-discharge rates, high self-discharge and short cycle life, particularly in the presence of high discharge currents [19–24]. This problem arises from the following reasons: insulating nature of sulphur and Li-S; dissolution of lithium polysulfide intermediates that occur during battery charge and discharge; large volume change during intercalation processes due to a reduction from elemental sulphur to Li-S; use of Li metal electrode; shuttle effect and self-discharge [26].

3.3.2. Application

Current applications of Li-S battery technology is limited to low power and cycle life requirements such as high altitude long endurance unmanned aerial vehicles (HALE UAVs). Future applications of the Li-S battery were then discussed in three areas, the need for more cycle life, the need for more power, and the need for both [27].

4. World production and consumption

Over the last two decades, sulphur production has changed from a mining industry to almost a co-product of the oil and gas industry. over 25% of elemental sulphur all over the world originates from the desulphurization of fossil fuels, and alone in Europe, it is already 38.6% Elemental sulphur, accounts for over 97% of world elemental sulphur output , while mined

sulphur is in retreat. production via the Frasch process ceased in the United States in 2000 and is in decline elsewhere [9]. In 2017, the world production was 83000 m/t, and the largest producers were China, USA, Russia, UAE, Canada and Saudi Arabia, respectively [28].

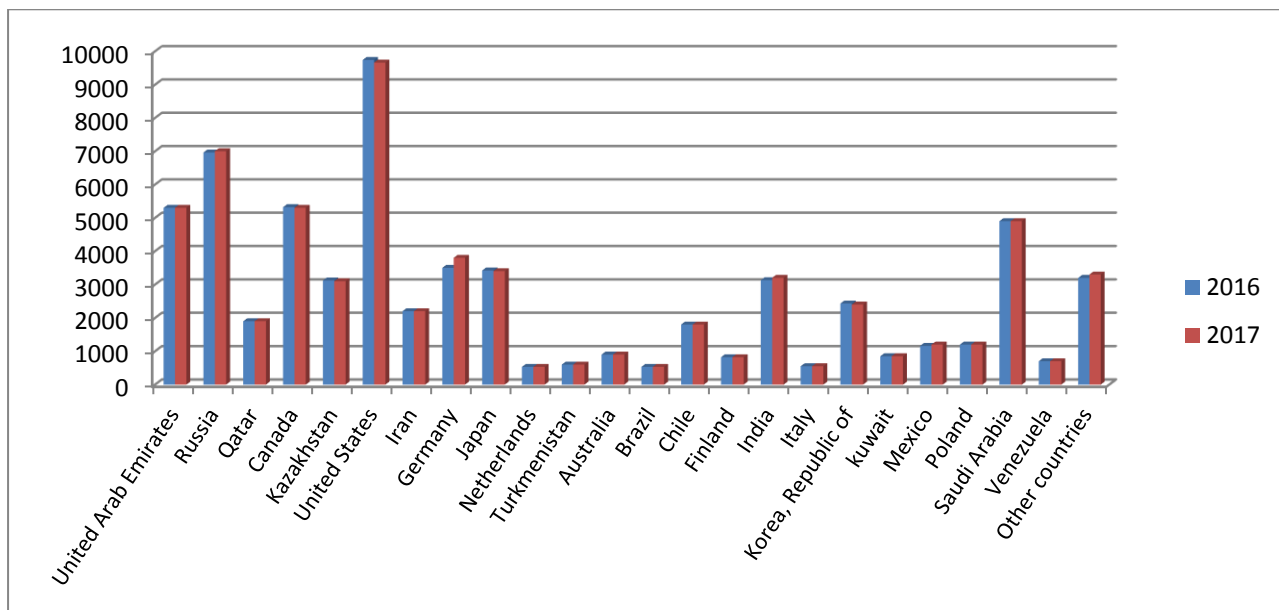


Fig. 7. World Sulphur Production in 2016 and 2017. Source: OEC

In the developed world, much of the additional sulphur from clean fuels has already occurred; however, potential production from the developing world due to stricter regulations limiting sulphur content looms large. A large source of sulphur output is regulations restricting sulphur content in marine bunker fuels [9]. In 2016, the International Maritime Organization (IMO) has set a global limit for sulphur in fuel oil used on board ships of 0.50% m/m (mass by mass) from 1 January 2020. The current global limit for the sulphur content of ships' fuel oil is 3.50% m/m (mass by mass). That means refineries will have to be configured to strip out excess sulphur [29].

Over the last decade, sulphur consumption has also increased in the world. China is the leading consumer with demand across fertilizer and other sectors representing over a quarter of global consumption. However, its attempt in development of domestic production will reduce China's dependence on foreign supply. In 2017, the largest consumers were China, Cuba, Australia, Chile, South Africa, Congo, respectively [28].

In terms of lime sulphur demand, the largest and fastest growing region for lime sulphur is the Asia Pacific. North America is also anticipated to boost the market growth of lime sulphur in the market. Other regions expected to boost market demand for lime sulphur are Europe, Latin America and Middle East & Africa during the forecast period [4].

5. Balance, logistics and outlook

Increased supply leads to elemental sulphur inventories rise, and prospective surpluses (figure 7) will further add to it and stocks are expected to play increasing roles in world sulphur markets. Increased development of sour gas reserves and refining of sour crudes combined with growing government restrictions requiring sulphur removal from fuels leads to sulphur outputs. Thus, the sector will face serious unbalance problems in the near future unless consideration is given to the increased supply streams [9]. At the end of 2016, some experts [30] reported that global market is facing oversupply and forecasted it continues till 2020.



Fig. 8. Oversupply of sulphur in the global market. Source: Argus

The main functions of sulphur logistic concept include: procurement, production, distribution and disposal. The changing nature and dynamics of sulphur production and consumption always are having great effects on sulphur logistics worldwide. The non-voluntary nature of today's production coupled with still cyclical demand industries has interfered with logistical sulphur structures, particularly on the production side. With the implementation of IMO's 0.5 per cent sulphur cap, the costs and logistics of compliance are at the forefront of discussions for professionals across the industry. It is necessary that operators and suppliers work together to ensure fuel availability past the cutoff point [31] and the shipping industry will have to consider a switch to alternative fuels, such as marine gas oil (MGO), or install scrubbers, a system that removes sulphur from exhaust gas emitted by bunkers [32].

According to Heffer and Prud'homme [33], a new supply of exportable sulphur in 2016 in West Asia and EECA Global sulphur production will grow by 4% p.a. compared with 2015, reaching 72 Mt S in 2020. during the next five years, the largest increases in production will occur in the sulphur exporting regions of West Asia and EECA, each at 6% p.a. Moderate growth of global sulphur demand will occur in the near term, but the current balance is shifting to potential surpluses. Global consumption of elemental sulphur will grow at an annual rate of 3% compared with 2015, reaching 69 Mt S in 2020 and the global supply/demand situation will shift from a near equilibrium condition in 2015 to the emergence of growing surplus towards 2020.

6. Summary

In the last decades, sulfur availability has considerably grown in many countries as a by-product of the petroleum industry, mainly due to the current environmental restrictions regarding the petroleum and gas refining processes, which limit the maximum quantity of sulfur present at combustibles. In the past oil and gas companies were primarily by-product suppliers, they are now the primary producers.

Sulphur has applications in different fields, the most important of which are agriculture, construction, and energy source industries. Sulphur is becoming an important fertilizer nutrient, with soil deficiencies reported in many regions of the world. Sulphur consumption for industrial uses is likewise showing some exciting changes. sulphur asphalt and sulphur concrete seem to be more employed as construction materials. Electrochemical energy storage systems, and most particularly batteries, play a crucial role in current and next generation applications. Thus, lithium/sulfur (Li-S) systems are one such promising technology with the potential for extremely high gravimetric energy.

Over the last two decades, sulphur production has changed from a mining industry to almost a co-product of the oil and gas industry, and sulphur production and consumption have also increased in the world. In 2017, the largest producers were China, USA, Russia, United Arab Emirates, Canada and Saudi Arabia, respectively. The largest consumers of sulphur are China, Cuba, Australia, Chile, South Africa, Congo, respectively.

The development of necessary and flexible logistical chains to match evolving production and consumption is very important to the sulphur marketplace. These issues need to be addressed by producers and consumers to remove uncertainty, discontinuity and possible refinery shutdowns.

References

- [1] Rauchfuss T. Under sulfur's spell. *Nat. Chem.* 2011; 3: 648.
- [2] Learn More About Sulphur, The Sulphur Institute. www.sulphurinstitute.org/learnmore.
- [3] Sang Hyun J, Onur B, Daeok K, Ali C. Direct Utilization of Elemental Sulfur in the Synthesis of Microporous Polymers for Natural Gas Sweetening. *Chem.* 2016; 1(3): 482-493.
- [4] Report. Lime Sulfur Market By End User (Horticulture Industry and Veterinary Industry)-Growth, Share, Opportunities, Competitive Analysis, and Forecast 2015 - 2022. Jul 2016. Report Code: 57976-07-16. Available from: <http://www.credenceresearch.com/report/lime-sulfur-market>.
- [5] Sulfur institute. Glossary. 2015. Available from: <http://www.sulphurinstitute.org/learnmore/glossary.cfm>.
- [6] Cline C, Hoksberg A, Abry R, Janssen A. Biological process for H₂S removal from gas streams the SHELL-PAQUES/THIOPAQ gas desulfurization process. Paper for the LRGCC, , Norman, Oklahoma, USA. February 2003. Available from: <http://www.environmental-expert.com/Files%5C587%5Carti-cles%5C5529%5Cpaques6.pdf>
- [7] Norrie. Gas Dehydration by Low Temperature Separation (L.T.S). 2010. Available from: <http://articles.compressionjobs.com/.../2711-gas-dehydration-lts-hydrates-sweetening-amine>.
- [8] Hauwert P. Sweetening and Sulfur Recovery of Sour Associated Gas and Lean Acid Gas in the Middle East. SPE Paper 172058-MS, International Petroleum Exhibition and Conference. Abu Dhabi, UAE: Society Petroleum Engineers. 2014.
- [9] Kopylov A. Unpublished Report. 2004.
- [10] Järvensivu R. Reuse Possibilities for Elemental Sulfur Sludge. A thesis submitted to Helsinki Metropolia University of Applied Sciences for the degree of Bachelor of Art. Department of Environmental Engineering. Helsinki, Finland. 2015.
- [11] Messick D. Agricultural Demand for Sulphur - The Challenges, The Future. The Sulphur Institute. TFI- FIRT's Outlook and Technology Conference. Savannah, Georgia, USA. November 2014. .
- [12] Loov RE, Vroom AH, Ward MA. Sulfur concrete-a new construction material. *PCI*. 1974; 19(1): 86-95.
- [13] Malhotra VM. Sulphur Concrete and Sulphur Infiltrated Concrete. Properties, Applications and Limitations. Canada Centre for Mineral and Energy Technology, Mineral Sciences in Ottawa, Ont. Canmet Report, 1979; 79-28: 26.
- [14] Bacon, RF, Davis HS, Recent Advances in the American Sulfur Industry, *Chem. Metallurgical Eng.* 1921; 24 (2): 65.
- [15] Ciak N, Harasymiu J. Sulphur concrete's technology and its application to the building industry. *Technical Sciences*, 2013; 16(4),323-331.
- [16] Gracia V, Vázquez E, Carmona S. Utilization of by-produced sulfur for the manufacture of unmodified sulfur concrete. International RILEM Conference on the Use of Recycled Materials in Buildings and Structures. Barcelona, Spain. November 2004.
- [17] McBee WC, Sullivan TA, Fike HL. Sulfur construction materials. 1985. Available from: <http://digicoll.manoa.hawaii.edu/techreports/PDF/USBM-678.pdf>.
- [18] Walus S. Lithium/Sulfur batteries: development and understanding of the working mechanisms. A thesis Submitted to Université Grenoble Alpes, 2015.
- [19] Fotouhi A, Auger D, O'Neill L, Cleaver T, Walus S. Lithium-Sulfur Battery Technology Readiness and Applications—A Review. *Energies*, 2017;10(12): article number 1937.
- [20] OXIS Energy. Available from: <http://www.oxisenergy.com>.
- [21] SION Power. Available from: <http://www.sionpower.com>.

- [22] Bizeray AM, Zhao S, Duncan SR, Howey DA. Lithium-ion battery thermal-electrochemical model-based state estimation using orthogonal collocation and a modified, extended Kalman filter. *Power Sources*. 2015; 296: 400–412.
- [23] Auger DJ. Using Ideas from Control Theory in the Modelling and Management of Lithium-Sulfur Batteries; lecture University of Oxford. Oxford, UK, February 2017.
- [24] Kolosnitsyn VS, Karaseva EV. Lithium-sulfur batteries. Problems and solutions. *Russian Journal of Electrochemistry*, 2008; 44(5): 506–509.
- [25] Mikhaylik YV, Akridge JR. Low Temperature Performance of Li/S Batteries. *Journal of The Electrochemical Society*. 2003; 150 (3): A306-A311.
- [26] Yermukhambetova A. Development of lithium sulphur battery and insights into its failure mechanism. A thesis submitted to University College London for the degree of Doctor of Philosophy. Department of Chemical Engineering. Torrington Place, WC1E 7JE. May 2017.
- [27] Euromines Industrial Materials - Sulphur. Available from http://www.euromines.org/im_sulphur.html
- [28] The Observatory of Economic Complexity (OEC). Available from: <https://atlas.media.mit.edu>
- [29] The 2020 global sulphur limit. IMO. Available from: http://www.imo.org/en/MediaCentre/HotTopics/GHG/Documents/FAQ_2020_English.pdf
- [30] Argus FMB Monthly Sulphur Outlook, Argus consulting services Report. 2016; 16-10
- [31] ExxonMobil supports industry leaders in preparation for change. Available from: <https://www.exxonmobil.com/en/marine/technicalresource/news-resources/marine-fuel-cap-implementation>
- [32] Hong Liang L. What you need to know: The 2020 IMO fuel sulphur regulation. Seatrade Maritime News. Available from: http://www.seatrade-maritime.com/images/PDFs/SOMWME-whitepaper_Sulphur-p2.pdf
- [33] Heffer P, Prud'homme M. Fertilizer Outlook 2016-2020. International Fertilizer Industry Association (IFA). 84th IFA Annual Conference. Moscow, Russia. May- June 2016.

To whom correspondence should be addressed: Sarah Sirani, Islamic Azad University, Science and Research Branch (Tehran- Iran)

STUDY THE EFFICIENCY OF SOME ESTERS AS SYNTHETIC LUBRICATING OIL

Amal M. Nassar, Nehal S. Ahmed and, Rasha S. Kamal

Department of Petroleum Applications, Egyptian Petroleum Research Institute, Nasr City, P.O. Box 11727, Cairo, Egypt

Received January 12, 2018; Accepted April 27, 2018

Abstract

Polyolesters (POE) were the strongest candidates to replace the traditional mineral oil. It have good miscibility with the new alternative refrigerants and possess good electrical insulation that is important in hermetic compressors where the electrical motor is exposed to the lubricant. In the present work, the different mixed esters were prepared by reaction of trimethylol propane with different ratio of valeric, heptanoic and octanoic acids. Structure of the prepared compounds was confirmed by study the physico-chemical properties as (Infra-Red spectroscopy, Nuclear Magnetic Resonance, Thermo Gravimetric Analysis, Total Acid Number, the Molecular Weights Determination, Density, Reflective Index, Specific Gravity and Flash Point) for all the prepared compounds were determined. The efficiency of the prepared compounds were investigated as synthetic refrigeration lubricating oil. It was found that the prepared compounds have low temperature properties (pour point), high viscosity index (VI) and the rheological behavior is a simple Newtonian fluid.

Keywords: *Synthetic lubricant; mixed ester; viscosity index; pour point and rheology.*

1. Introduction

Lubrication is the operation by which friction and wear are reduced between contact surfaces of solids moving in relation to each other by applying a substance with appropriate characteristics. Well-applied lubrication brings significant economic benefits in the form of energy-saving, conservation of materials, reduction in maintenance operations, and also positive effects on environmental impact [1]. A lubricant is a substance introduced between two moving surfaces to reduce the friction between them, improving efficiency and reducing wear [2-3]. Synthetic lubricants do not originate from crude oil like conventional mineral oil. Instead, synthetic lubricants not only have high-performance base stock but usually also benefit from premium additive systems. In fact, many of the benefits that are commonly attributed to synthetic lubricants actually come from the additives with which they are formulated [4].

The lubricant industry generally treats synthetic esters as a monolithic class of Group V base oils with well-defined properties. It is not difficult to find a chart that lists esters as having "fair" hydrolytic stability, "good" biodegradability, "very good" lubricity, "excellent" oxidative stability and so on. Sometimes diesters and polyol esters are listed separately, but there is seldom further differentiation. However, the nature of esters defies such over simplification. There are endless varieties of esters that can be built from commonly available acids and alcohols, so almost anything is possible [5]. Esters are another class of synthetic base, typically used for motor transport vehicles; these are polar compounds and for this reason are generally used in mixtures with PAOs. Depending on the type of acid and alcohol used in the synthesis, it is possible to give the base the desired rheological and performance characteristics. Thanks to their lubricating capacity and, when required, their pronounced biodegradability, esters are widely used in oils for two-stroke engines. Other classes of synthetic bases are used in particular lubricating sectors [1]. Esters are a broad and diverse family of synthetic lubricant base stocks which can be custom designed to meet specific physical and performance

properties. The inherent polarity of esters improves their performance in lubrication by reducing volatility, increasing lubricity, providing cleaner operation, and making the products biodegradable. A wide range of available raw materials allow an ester designer the ability to optimize a product over a wide range of variables in order to maximize the performance and value to the client. They may be used alone in very high temperature applications for optimum performance or blended with PAOs or other synthetic base stocks where their complementary properties improve the balance of the finished lubricant. Esters have been used in synthetic lubricants for more than 60 years and continue to grow as the drive for efficiency make operating environments more severe. Because of the complexity involved in the designing, selecting, and blending of an ester base stock, the choice of the optimum ester should be left to a qualified ester engineer who can better balance the desired properties [7-14].

In the present work we prepared some synthetic lubricant based on mixed esters by esterification of trimethylol propane with valeric acid, heptanoic acid and octanoic acid, then study the physico-chemical properties and rheological properties of the prepared compounds.

2. Experimental

2.1. Preparation of mixed ester

Reaction of trimethylol propane with different ratio of valeric acid C₅, heptanoic acid C₇ and octanoic acid C₈. The reactions were carried out in a resin kettle flask in presence of 1wt % a catalyst and xylene as a solvent. The esterification reactions were carried out under a slow stream of deoxygenated nitrogen; the reactions were agitated using mechanical stirrer at 500 rpm. The reactants which were mixed with an equal weight of xylene then heated gradually from room temperature to 170° C ± 0.5° C using a well controlled thermostat. The extent of reaction was followed by monitoring the amount of liberated water to give products A, B, C, D, E, F, G and H as given in the part 3.1.

2.2. Purification of prepared esters

The prepared esters were purified according to the following procedures:

- Filtrate it from the catalyst which washed with methanol and used it again
- Take the filtrate and washed it by 10% sodium carbonate solution in separating funnel and shaked well.
- The entire process was repeated several times to ensure complete removal of unreacted acid.
- The purified ester was then washed several times with distilled water to remove any traces of sodium carbonate then the ester was left overnight on calcium chloride anhydrous for drying.
- The anhydrous calcium chloride was then removed by filtration and the xylene was removed by rotary evaporator.

2.3. I.R. spectroscopic analysis

I.R. spectra of the prepared compounds were determined by using FTIR spectrometer Model Type Mattson Infinity Series Top 961.

2.4. ¹H NMR Spectroscopic analysis

The ¹H NMR spectra of prepared compounds were measured by Magnet: 400 Megahertz, console (Spectrometer): Varian model Mercury plus, probe: Varian 5 millimeter.

2.5. Determination of the molecular weights

The molecular weights of the prepared ester were determined by using GC- MS Agilent technologies Model Type 5977A MSD, 7890B GC system, column DB- 5MS (0.25nm x 30cm, 0.1μm film) and flame ionization detector. Pure nitrogen was used as a carrier gas. The oven temperature program was varied from 40-320°C at a fixed rate of 20°C/min. The temperature of the injector detector was 300°C.

2.6. Thermal analyses

Thermo gravimetric analyses (TGA) were performed to study the structural changes of the prepared samples with thermal treatment. A 10 mg of sample was heated up to 700°C, with a heating rate of 10°C min⁻¹ in an (air or N₂) flow at a rate of 100 ml min⁻¹ on SDTQ-600 (TA-USA) thermo balance instrument.

2.7. Total Acid Number (TAN)

The total acid number (TAN) of prepared compounds were determined according to ASTM D664 by using Model Type Mehrshom CLO-05.

2.8. Density

Density at 15°C (g/mL) of the prepared compounds were determined by using Standard Test Method for Density according to ASTM D1298

2.9. Refractive index

The refractive index of prepared compounds were determined according to ASTM D1747

2.10. Specific gravity

Specific Gravity at 15°C of the prepared compounds were determined by using Standard Test Method for Specific Gravity according to ASTM D4052 by using Model Type Metler Toledo DEUO Density meter

2.11. Flash point

The flash point of prepared compounds were determined according to ASTM D 92 by using Cleveland open cup tester

2.12. Measure viscosity index

The kinematic viscosity of the prepared esters were determined at 40°C and 100°C. Then viscosity index were calculated according to ASTMD 22-70

2.13. Measure pour point

The pour point of the prepared compounds were determined according to the ASTM-97-93. The instrument used for measuring the pour point was the Cold Filter Plugging Point Automatic Tester (CFPPA-T), model 1st CPP97-2.

2.14. Study rheological properties

The rheological properties of prepared compounds were studied by using Model Type the Modular Compact Rheometer 502 (Anton Paar).

3. Results and discussions

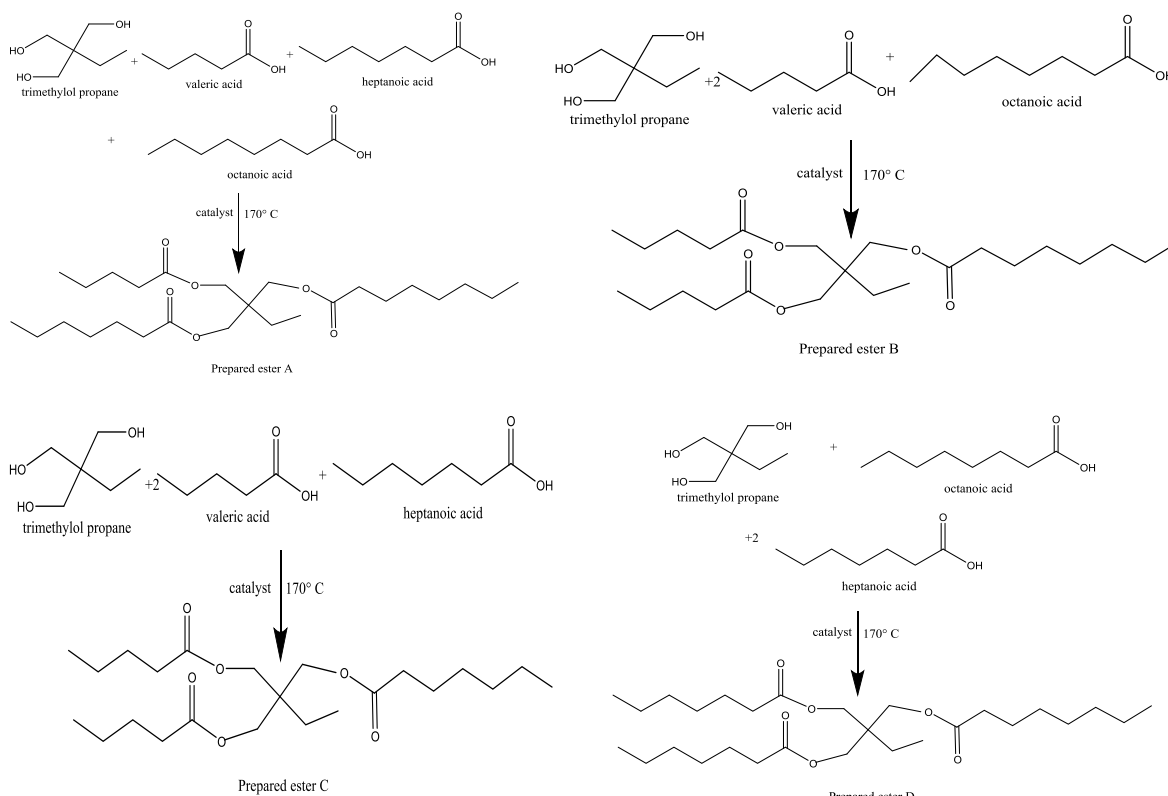
3.1. Preparation of mixed ester

Reaction of 1 mole of trimethylol propane with 1 mole of valeric acid C₅ , 1 mole of heptanoic acid C₇ and 1 mole of octanoic acid C₈. The esterification reactions were carried out and the extent of reaction was followed by monitoring the amount of liberated water to give product A.

Reaction of 1 mole of trimethylol propane with 2 mole of valeric acid C₅ and 1 mole of octanoic acid C₈. The esterification reactions were carried out and the extent of reaction was followed by monitoring the amount of liberated water to give product B

Reaction of 1 mole of trimethylol propane with 2 mole of valeric acid C₅ and 1 mole of heptanoic acid C₇. The esterification reactions were carried out and the extent of reaction was followed by monitoring the amount of liberated water to give product C.

Reaction of 1 mole of trimethylol propane with 2 mole of heptanoic acid C₇ and 1 mole of octanoic acid C₈. The esterification reactions were carried out and the extent of reaction was followed by monitoring the amount of liberated water to give product D.

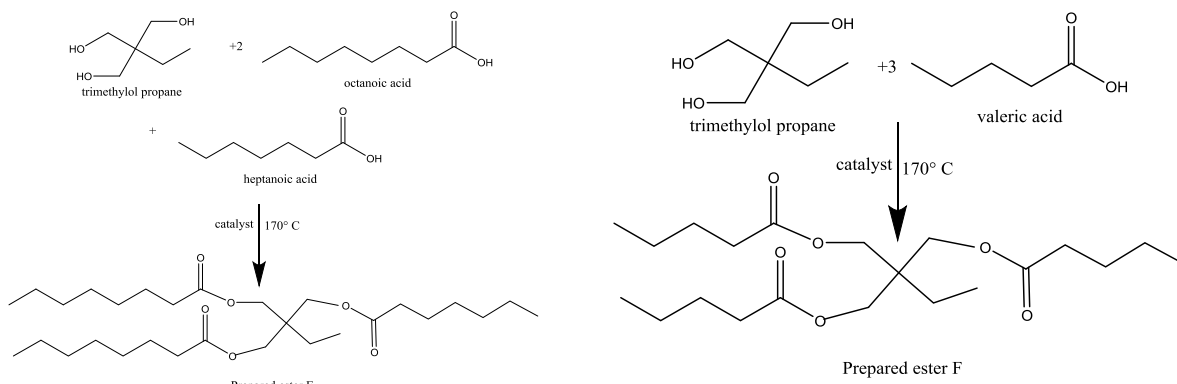


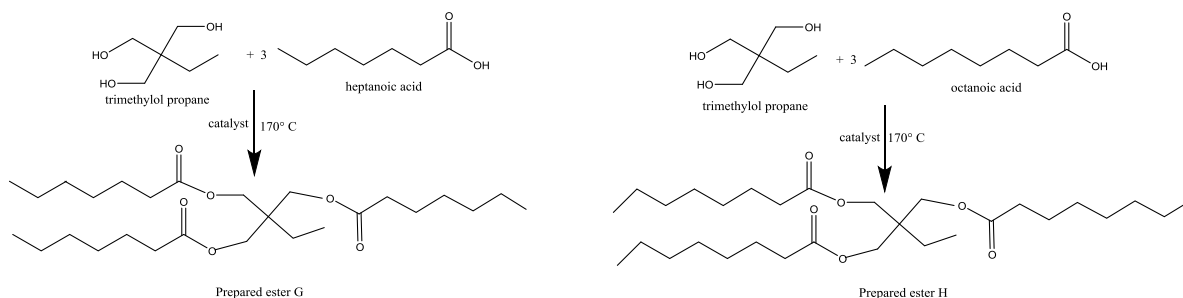
Reaction of 1 mole of trimethylol propane with 1 mole of heptanoic acid C₇ and 2 mole of octanoic acid C₈. The esterification reactions were carried out and the extent of reaction was followed by monitoring the amount of liberated water to give product E.

Reaction of 1 mole of trimethylol propane with 3 mole of valeric acid C₅. The esterification reactions were carried out and the extent of reaction was followed by monitoring the amount of liberated water to give product F.

Reaction of 1 mole of trimethylol propane with 3 mole of heptanoic acid C₇. The esterification reactions were carried out and the extent of reaction was followed by monitoring the amount of liberated water to give product G.

Reaction of 1 mole of trimethylol propane with 3 mole of octanoic acid C₈. The esterification reactions were carried out and the extent of reaction was followed by monitoring the amount of liberated water to give product H.





I.R. spectroscopy was used to elucidate the completion of the esterification reactions. All esters afford similar I.R. spectrum, I.R. spectrum of them are given in Figures (1-8) which indicate the following: absence of strong absorption band at 3200cm^{-1} of aliphatic (-OH) group, the characteristic absorption bands of the carboxylic acids. These bands are broad peak extending from 3300cm^{-1} to 2500cm^{-1} due to hydrogen bonded (-OH) and the (C-H) stretching vibrations. Appearance of the ester group bands at $1740\text{ cm}^{-1} \pm 10\text{ cm}^{-1}$ and $1280\text{ cm}^{-1} \pm 100\text{ cm}^{-1}$ due to (C=O) and (C-O-C) stretching respectively. The band for (C-H) aliphatic appear near 2850cm^{-1} & 2950cm^{-1} . This indicates that the esterification process is carried out successfully.

The chemical structures of the prepared compounds can be proved from ^1H NMR analysis, which is represented in Figures (9-16). In this respect, the signal at 3.9 ppm (which is assigned to O-CH₂ groups), the signal at 2-2.5 ppm (which is assigned to O=C-CH₂ groups) and the signal at 1.5-2 ppm (which is assigned to aliphatic protons) were selected to determine the esterification of the prepared compounds [15].

The mean molecular weights of prepared compounds by using gas chromatography are given in Table 1, as shown the theoretical and experimental mean molecular weight are equal for all prepared compounds. Finally compound H is the largest molecular weight while compound F is the smallest one. Mass spectra for prepared compound are given Figures (17 and 24).

Table 1. The mean molecular weight of prepared compounds

Designation of the prepared esters	Molecular formula	Mean molecular weight (g/mole)	
		Theoretical	Experimental
A	C ₂₆ H ₄₈ O ₆	456.66112	455
B	C ₂₄ H ₄₄ O ₆	428.60736	428
C	C ₂₃ H ₄₂ O ₆	414.58048	414.2
D	C ₂₈ H ₅₂ O ₆	484.71488	484.2
E	C ₂₉ H ₅₄ O ₆	498.74176	495.5
F	C ₂₁ H ₃₈ O ₆	398.622	396
G	C ₂₇ H ₅₀ O ₆	470.688	469.5
H	C ₃₀ H ₅₆ O ₆	512.6864	513.5

3.2. Thermal analyses

Thermal stability of the prepared compounds was studied using thermal gravimetric analysis "TGA". TGA is a technique which the thermal properties of a material are determined as a function of temperature [16]. The thermal tests measure the change of weight and enthalpy as the sample is heated. TGA has been extensively used for measurement of degradation as we see in Table 2. (T₁) is the temperature when primary degradation step occurs with weight loss % (W₁) and (T₂) is the temperature when major degradation step occurs with weight loss % (W₂).

TGA analysis, the thermo gravimetric study has shown a good thermal stability for the prepared compounds, as in these compounds the temperature at when the primary degradation step occurs ranging from 243.68 to 308.86°C and weight loss ranging from 12 to 19%, and the temperature when the major degradation step occurs ranging from 299 to 366°C and

the weight loss ranging from 98 to 99%, and this confirms the suitability of using the prepared compounds as synthetic lubricating oil as it can be used at high temperature without degradation, which is represented in Figures (25-32).

Table 2. The thermal stability of prepared compounds

Synthetic lube oil designation	T ₁ (°C)	W ₁ (%)	T ₂ (°C)	W ₂ (%)
A	249.73	12.97	315.25	99.0726
B	252.59	19.74	309.28	98.922
C	245.65	15.44	305.58	99.0699
D	279.84	18.66	338.93	98.3359
E	288.25	16.25	352.53	98.143
F	234.68	17.32	299.69	99.7509
G	269.22	13.2	334.95	98.19
H	308.86	19.84	366.09	98.333

3.3. Measuring the viscosity index

The VI increases with increasing the mean molecular weight of the prepared compounds compared with the mineral oil as shown in Table 3 & Figure (33) [17]. The increase in VI means that these oil can be used at a wide range of temperature.

Table 3. Kinematic viscosity and viscosity index of tested esters

Designation of the prepared esters	Kinematic viscosity at 40°C, mm ² /s	Kinematic viscosity at 40°C, mm ² /s	Viscosity index
A	16.81774	3.686596	104
B	6.22026	1.946054	94
C	8.75444	2.415356	93
D	10.3671	2.7649	109
E	11.97976	3.047594	112
F	11.74938	2.764947	62
G	8.0633	2.349952	108
H	17.50888	3.877282	115
Mineral oil	86.16212	9.766988	90

3.4. Measuring the pour point

The pour point is defined as the lowest temperature at which the oil will pour or flow when it is chilled without disturbance under prescribed conditions [18]. A pour point in synthetic lubricating oil is lower than the mineral oil due to absence of crystal formed interlocking growth restricts the pour of oil. and pour point decrease according to decrease in the molecular weight of the prepared synthetic lubricating oil [19]. The pour point of all the prepared compounds A. B. C. D. E. F. G and H is lower than- 45°C. This means that these oil can be used at low temperature.

Table 4. The physico-chemical properties of prepared esters

Properties	A	B	C	D	E	F	G	H
TAN, (mg KOH/g)	0.0376	0.0202	0.0475	0.0101	0.0112	0.044	0.027	0.0196
Density at 20°C, (g/cm ³)	0.9638	0.9672	0.9680	0.9516	0.9481	0.9692	0.9601	0.9372
Refractive index at 28°C	1.4669	1.4668	1.4569	1.4789	1.4879	1.4479	1.4787	1.4978
Flash point (COC), °C	255	248	248	276	289	234	276	303

3.5. Study rheological properties

The rheological behavior of oils and their products is generally simple Newtonian fluid (viscosity is independent of shear rate). Shear rate is a measure of the rate of shear deformation [20-21]. Shear Stress is an applied force per unit area needed to produce deformation in a fluid. A Newtonian liquid is one that flows immediately on application of even

the smallest force. and for which the rate of flow is directly proportional to the force applied. All the prepared synthetic lubricating oil is Newtonian fluid behavior as shown in Figure (34- 42).

3.6. Comparison of the physical properties between the prepared esters and the commercial turbo engine oil (Turbo Nycoil 13B) specifications

The comparative study indicates that the prepared esters could be considered as synthetic base oil and may be used in formulations for turbo engine according to Air specification 3514 as illustrated from the comparison with commercial turbo engine oil (Turbo Nycoil 13B) [22].

Table 5. Properties of the commercial engine oil Turbo Nycoil 13B

Properties	Turbo Nycoil 13B
Kinematic viscosity at 40°C, mm ² /s	13.35
Kinematic viscosity at 100°C, mm ² /s	3.30
Viscosity index	124
Pour point, °C	-63
TAN, (mg KOH/g)	0.03
Density at 20°C, g/cm ³	0.940
Refractive index at 28°C	1.4534
Flash point (COC), °C	218

4. Conclusion

- The mixed ester were prepared by reaction of trimethylol propane with different ratio of valeric acid. heptanoic acid and octanoic acid.
- Study the physicochemical properties (Fourier transform infrared spectroscopy FTIR. proton nuclear magnetic resonance ¹HNMR. determination of the molecular weights. Thermo gravimetric analysis TGA. total acid number TAN. density. reflective index. specific gravity and flash point) were determined for the prepared compounds.
- Evaluation of the prepared esters as synthetic lubricating oil by measuring viscosity index. pour point and study rheological properties. It was found that the prepared compounds have low temperature properties (pour point). high viscosity index (VI) (except F) and the rheological behavior is simple Newtonian fluid.
- Comparative study between the commercial turbo engine oil (Turbo Nycoil 13B) and the prepared ester indicates that the prepared esters could be considered as synthetic base oil

Figures

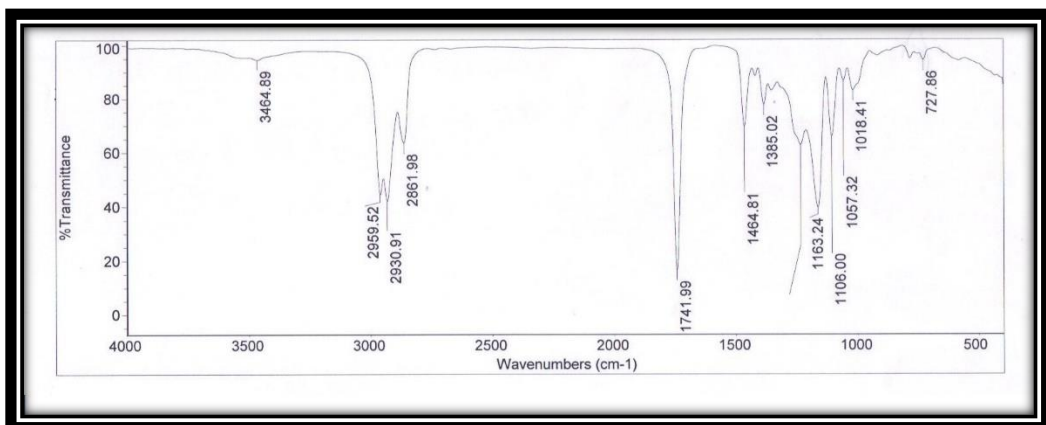
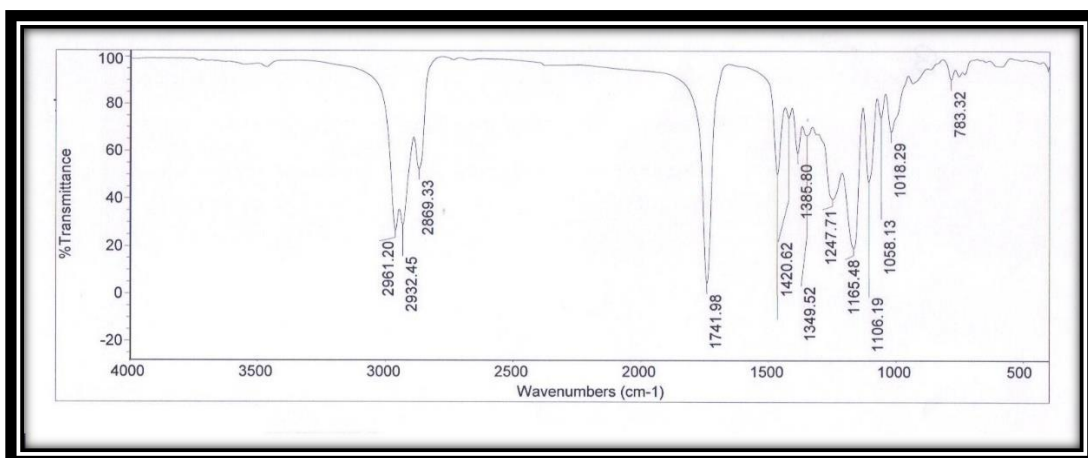
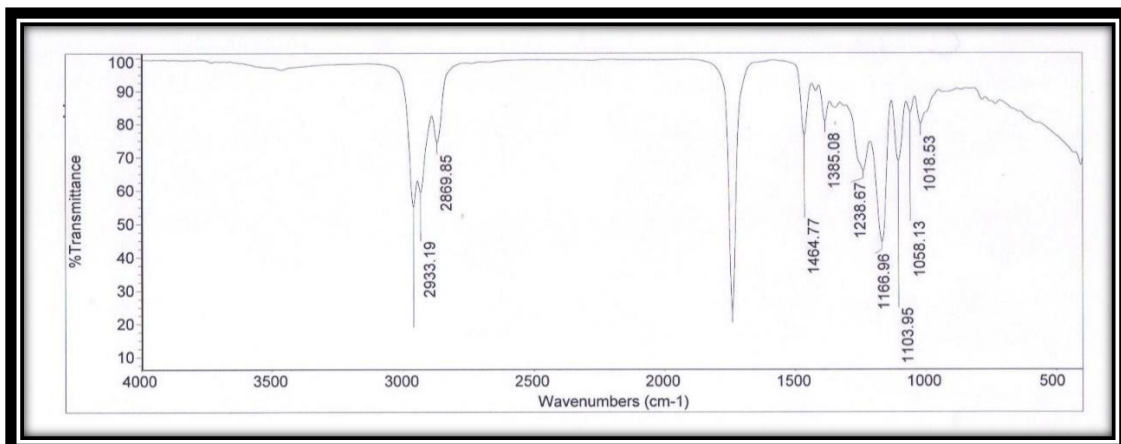


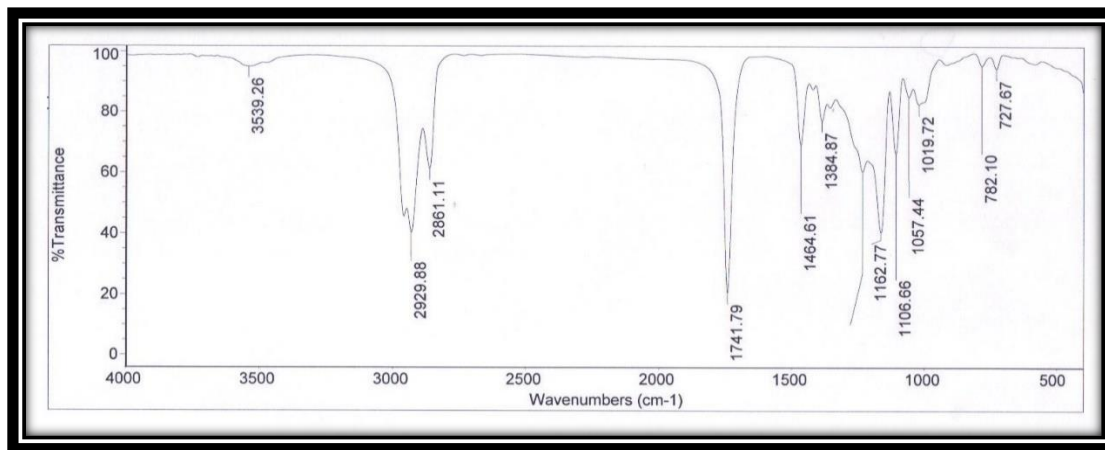
Figure 1. IR spectrum of the prepared compound (A)



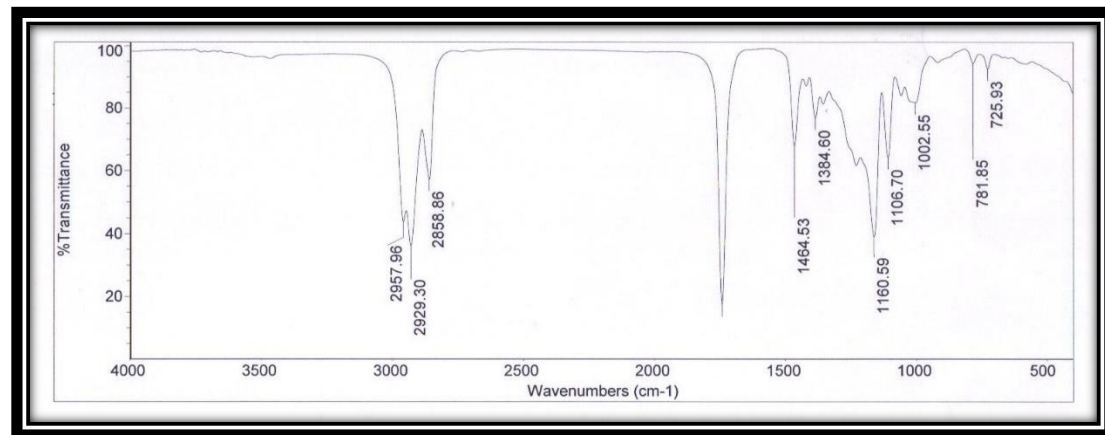
• Figure 2. IR spectrum of the prepared compound (B)



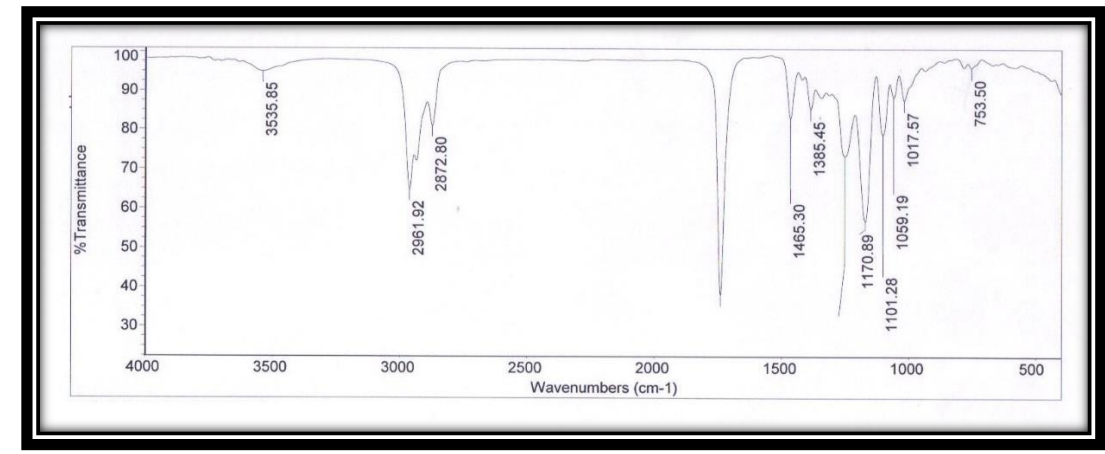
• Figure 3. IR spectrum of the prepared compound (C)



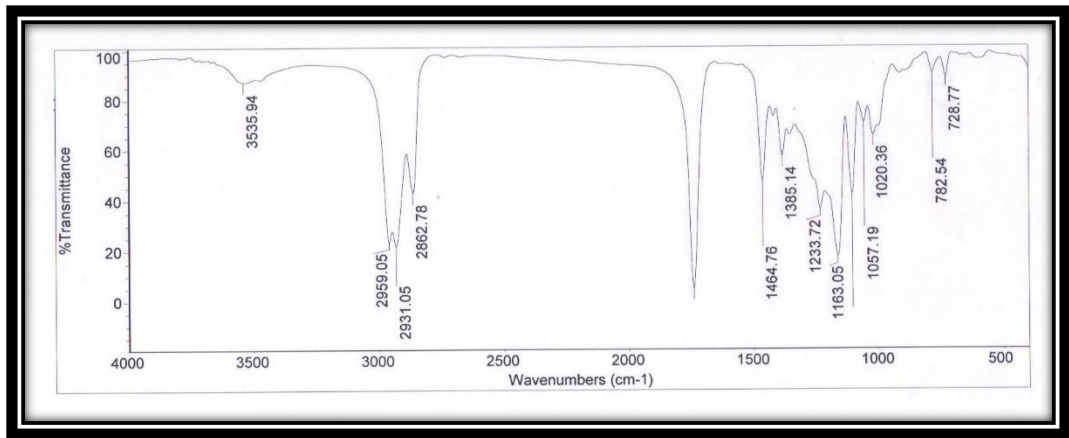
• Figure 4. IR spectrum of the prepared compound (D)



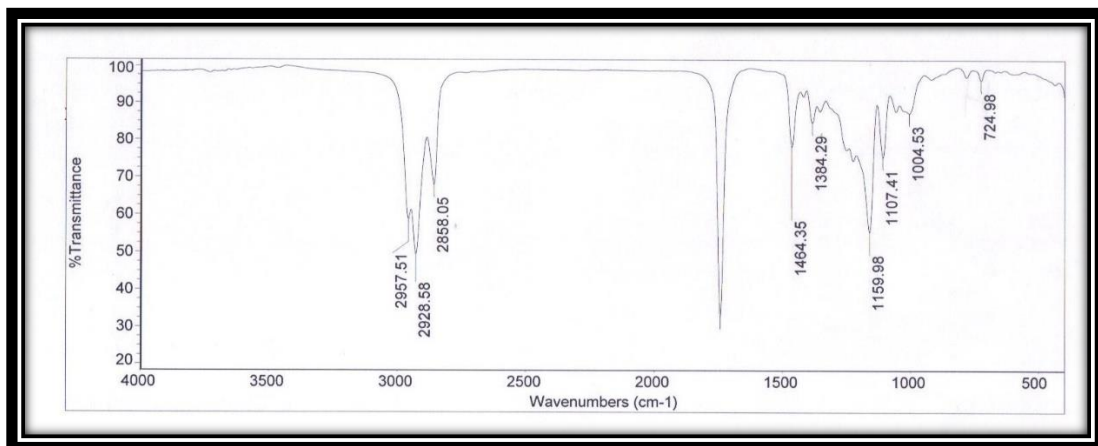
• Figure 5. IR spectrum of the prepared compound (E)



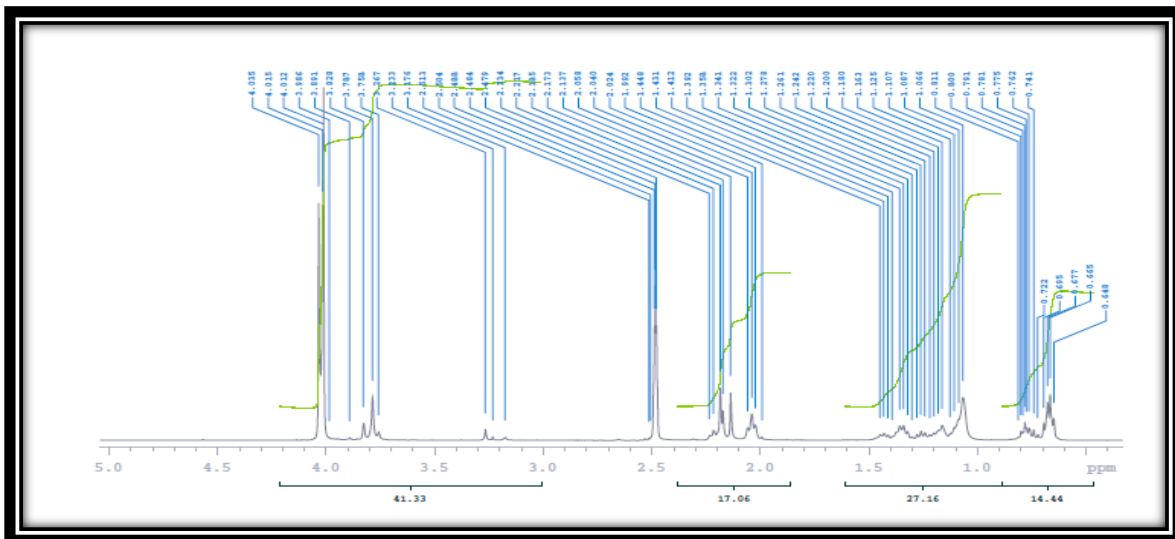
• Figure 6. IR spectrum of the prepared compound (F)



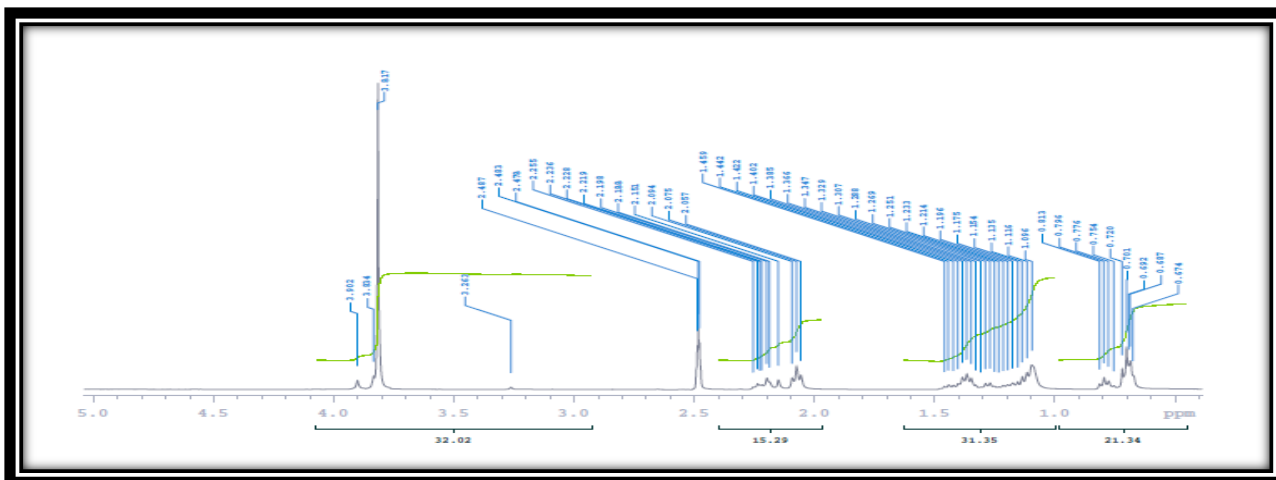
- Figure 7. IR spectrum of the prepared compound (G)



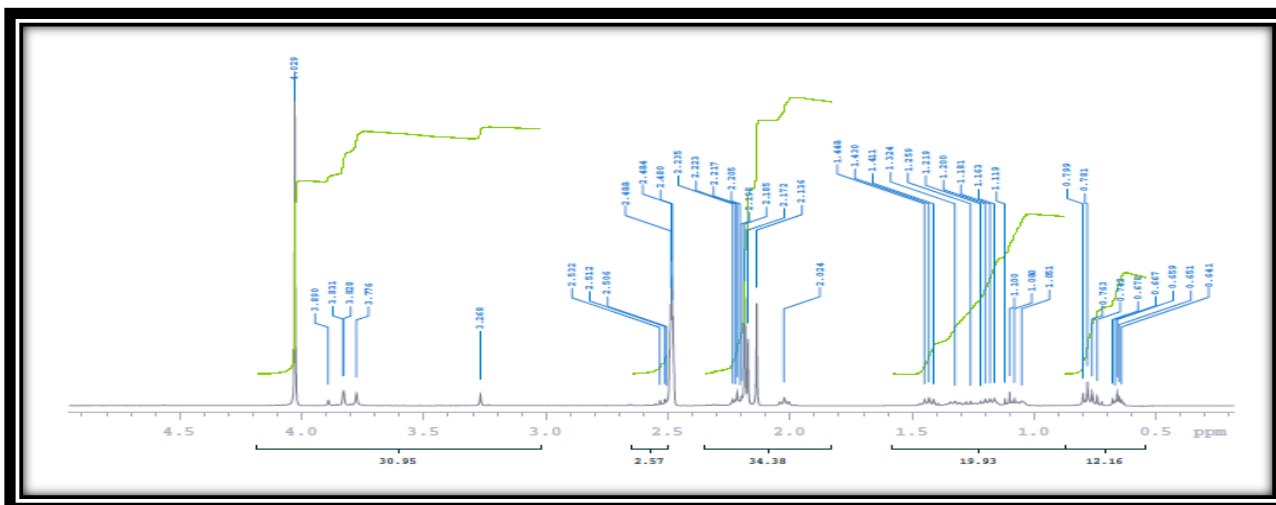
- Figure 8. IR spectrum of the prepared compound (H)



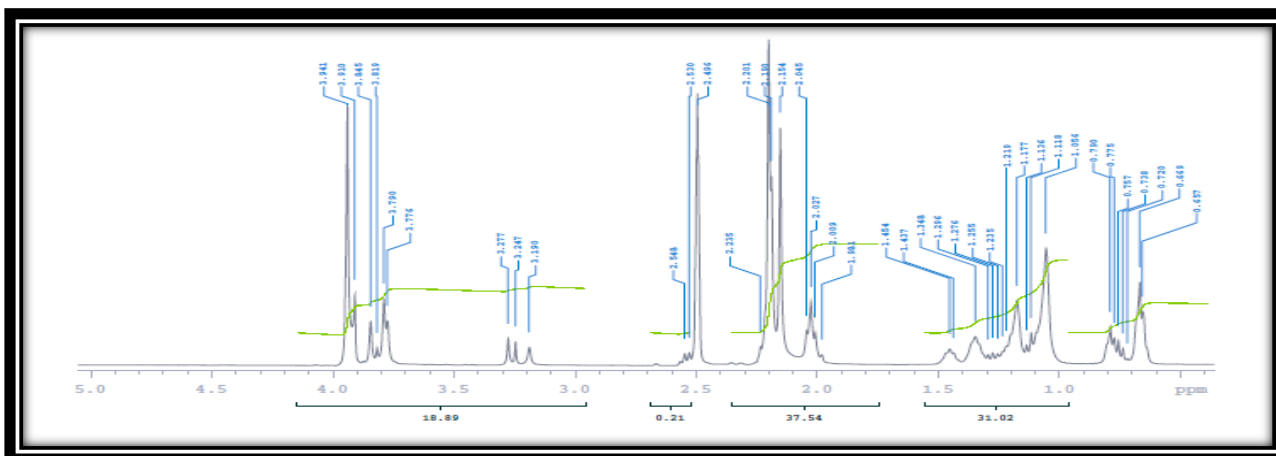
- Figure 9. ^1H NMR spectrum of the prepared compound (A)



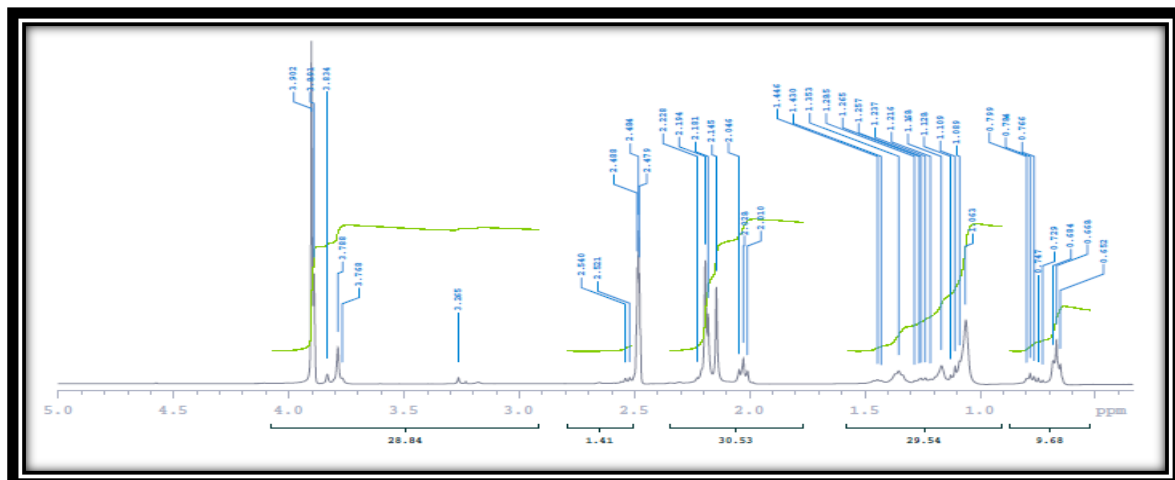
• Figure 10. ^1H NMR spectrum of the prepared compound (B)



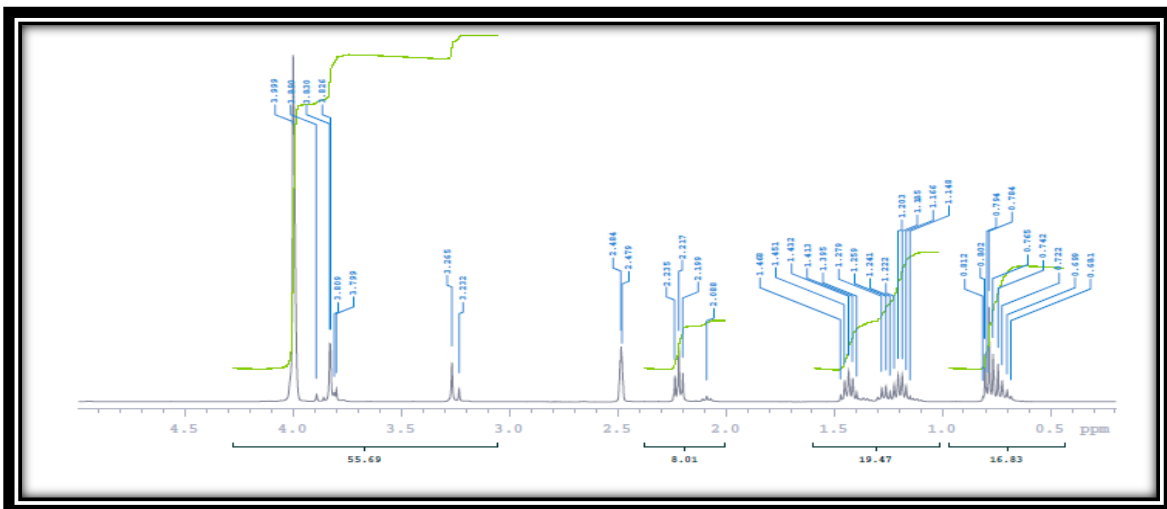
• Figure 11. ^1H NMR spectrum of the prepared compound (C)



• Figure 12. ^1H NMR spectrum of the prepared compound (D)



- Figure 13. ^1H NMR spectrum of the prepared compound (E)



- Figure 14. ^1H NMR spectrum of the prepared compound (F)

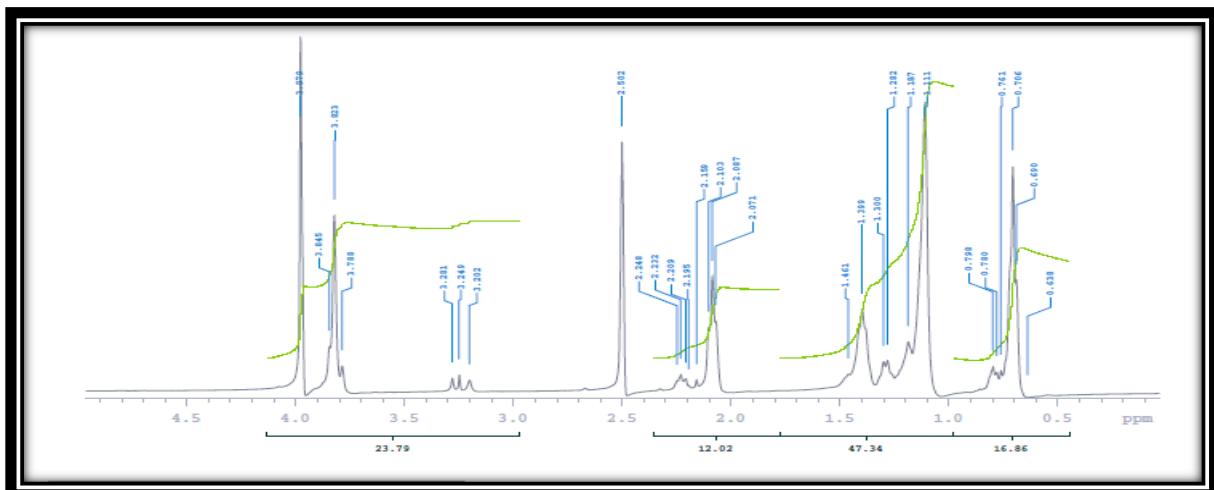
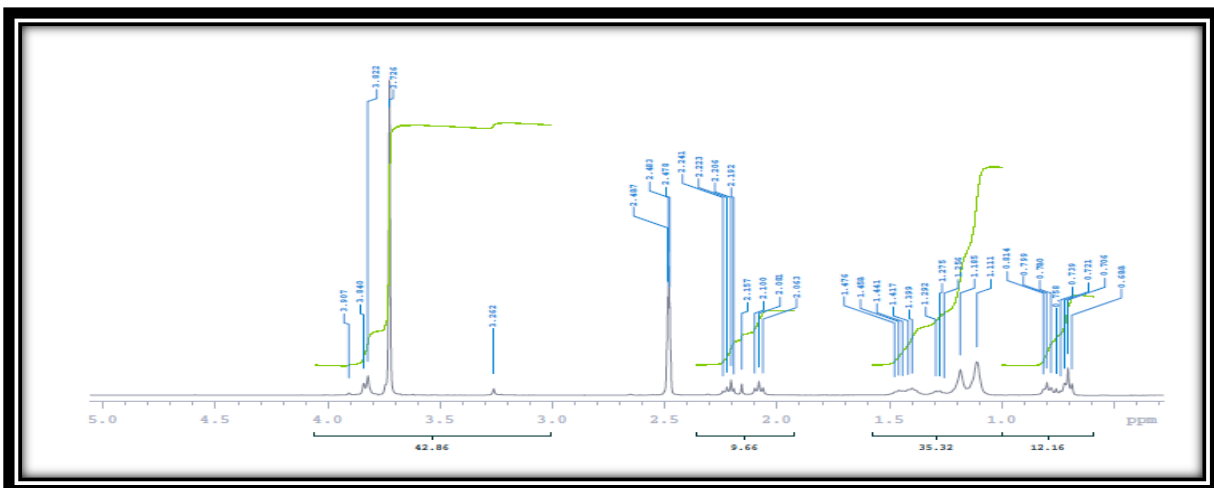
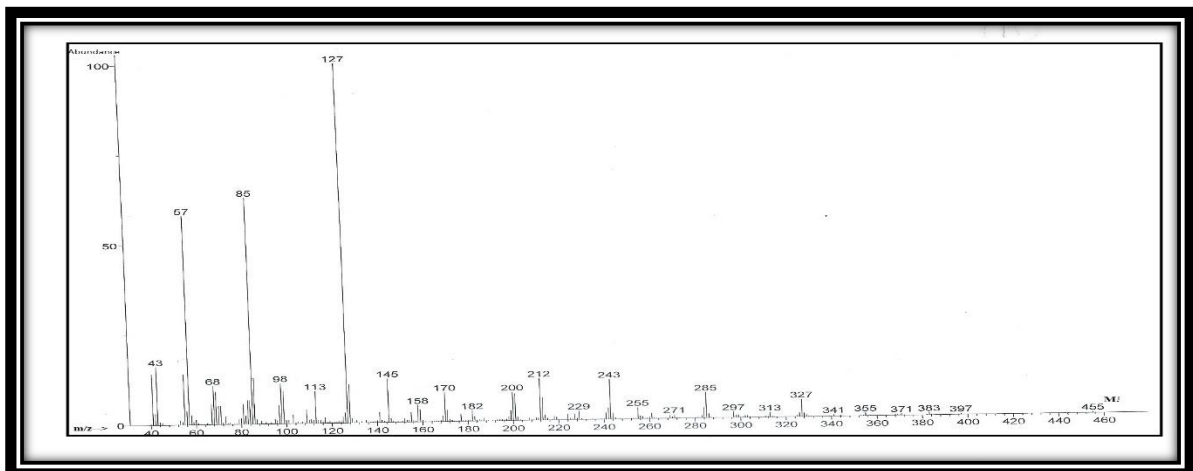


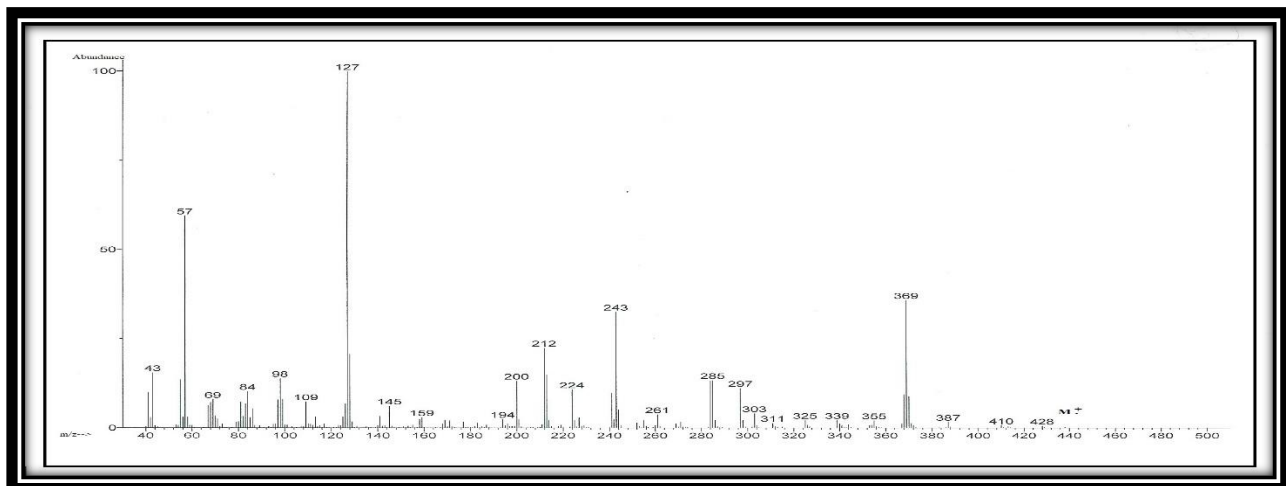
Figure 15. ^1H NMR spectrum of the prepared compound (G).



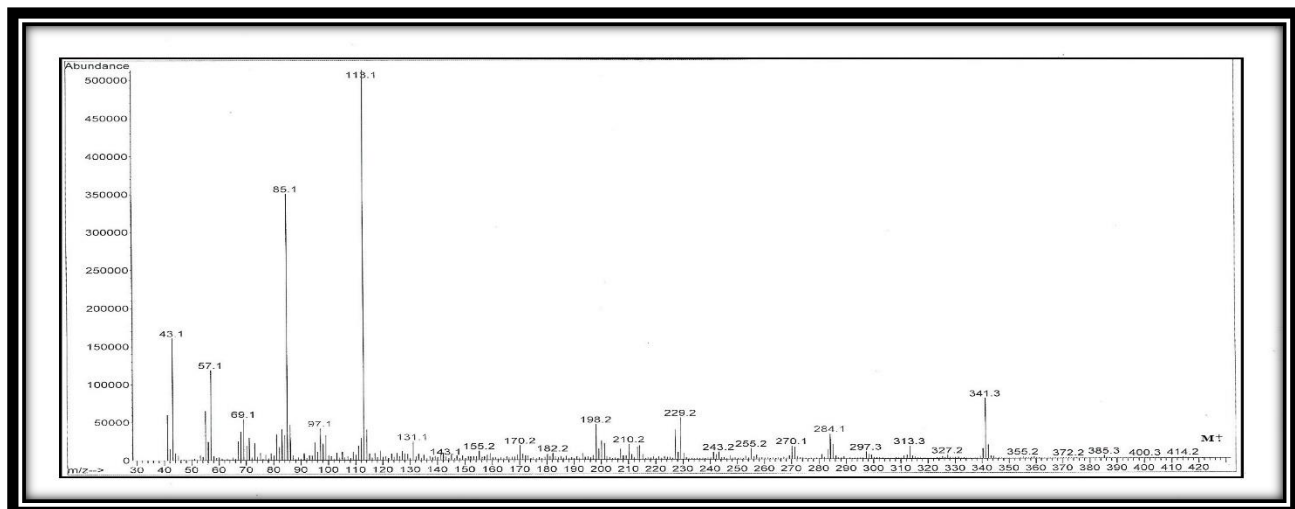
- Figure 16. ^1H NMR spectrum of the prepared compound (H)



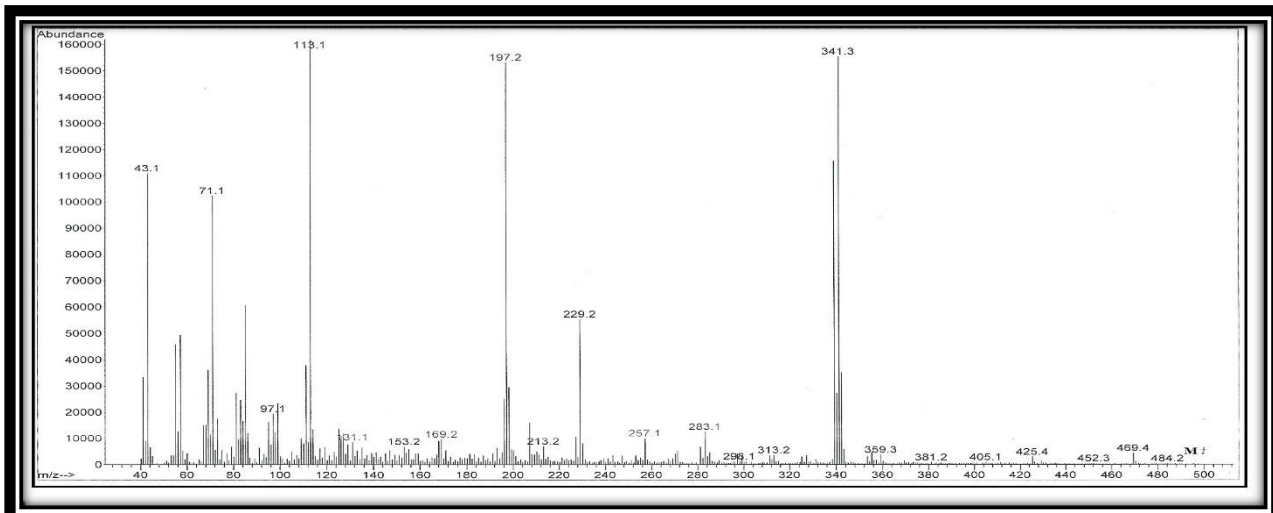
- Figure 17. Mass spectra of the prepared compound (A)



- Figure 18. Mass spectra of the prepared compound (B)



• Figure 19. Mass spectra of the prepared compound (C)



• Figure 20. Mass spectra of the prepared compound (D)

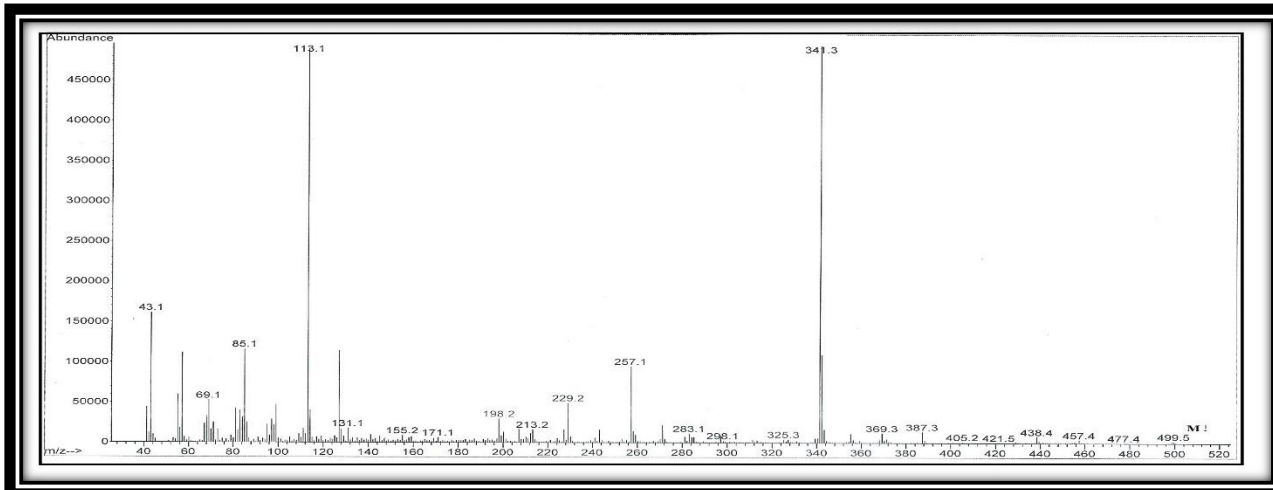
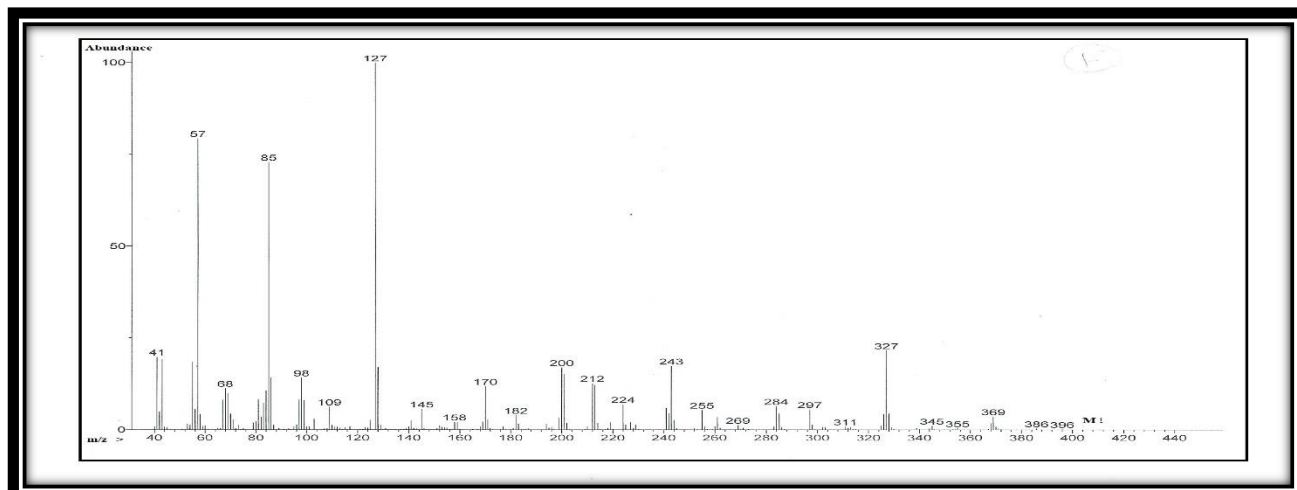
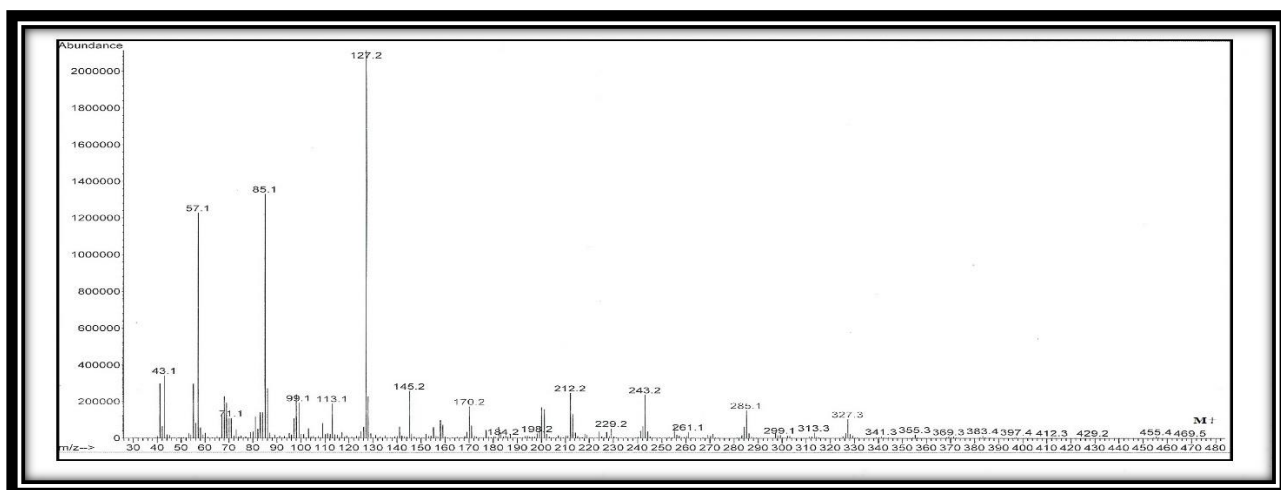


Figure 21. Mass spectra of the prepared compound (E)



• Figure 22. Mass spectra of the prepared compound (F).



• Figure 23. Mass spectra of the prepared compound (G)

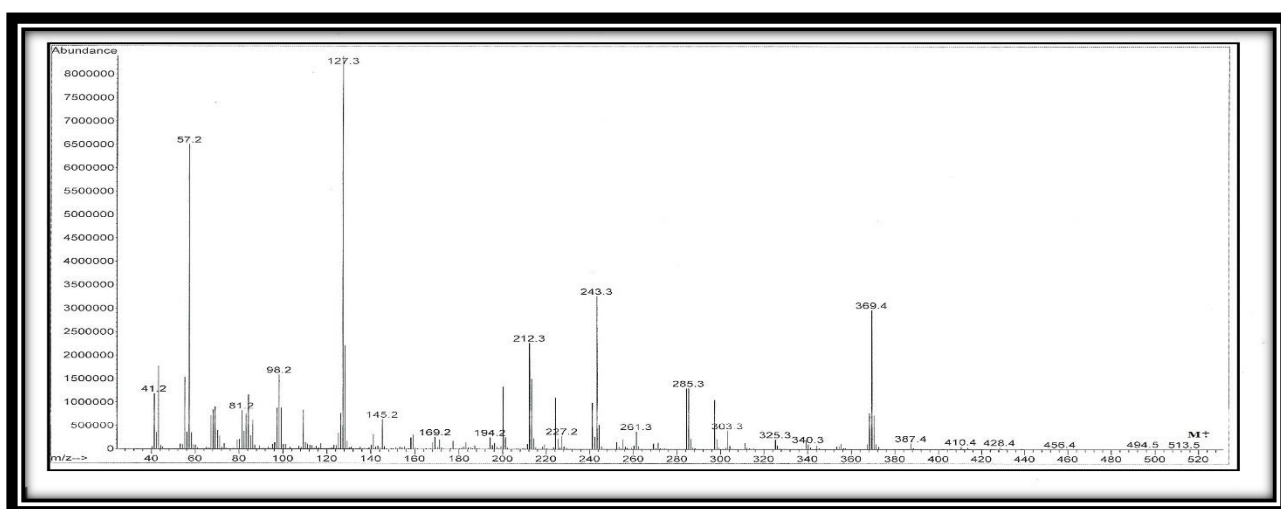
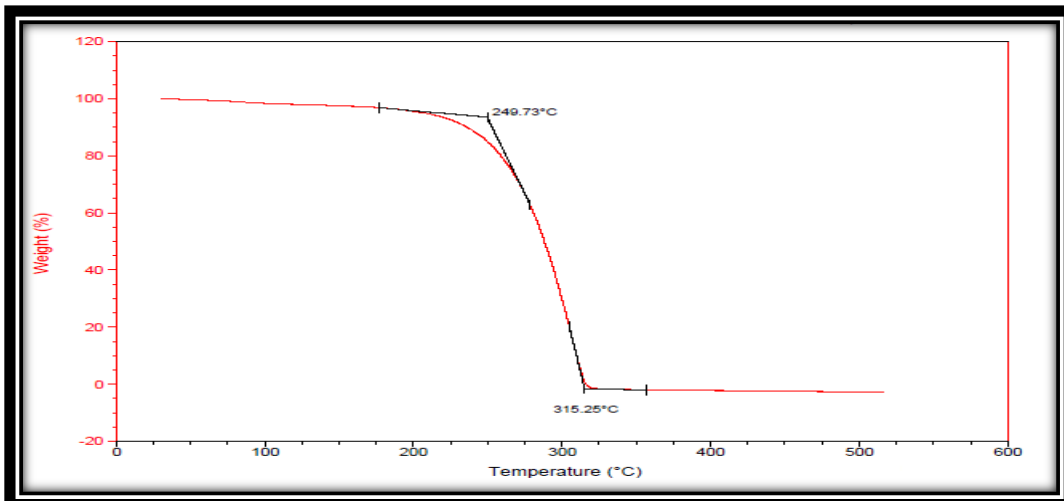


Figure 24. Mass spectra of the prepared compound (H)



• Figure 25. TGA analysis of the prepared compound (A)

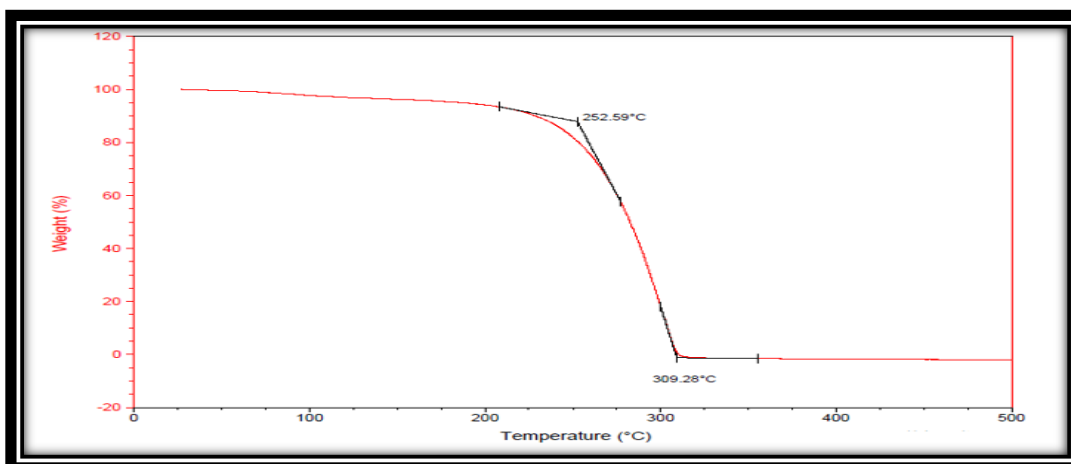


Figure 26. TGA analysis of the prepared compound (B)

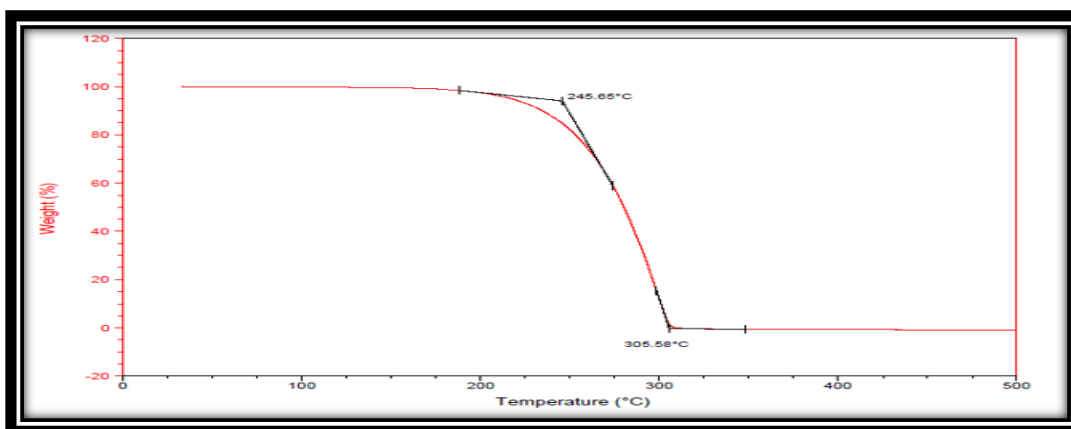
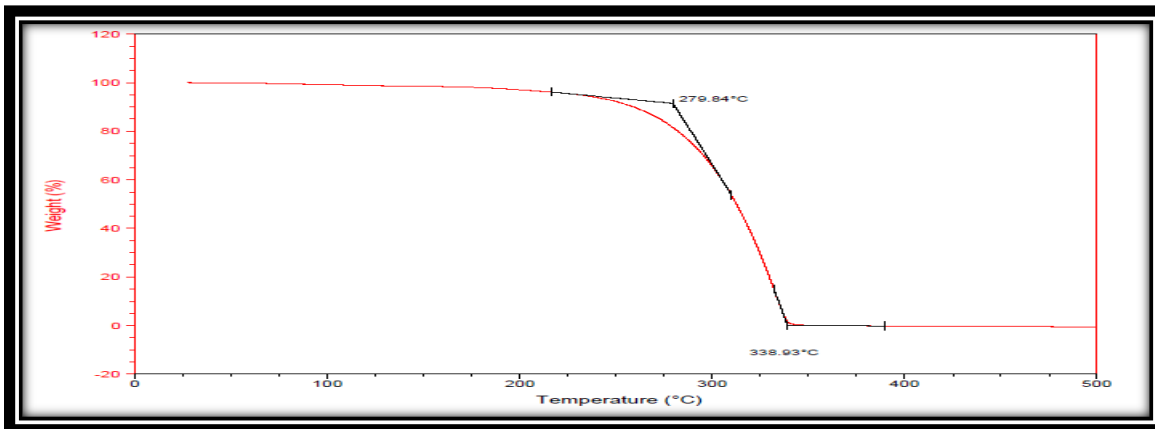


Figure 27. TGA analysis of the prepared compound (C)



• Figure 28. TGA analysis of the prepared compound (D)

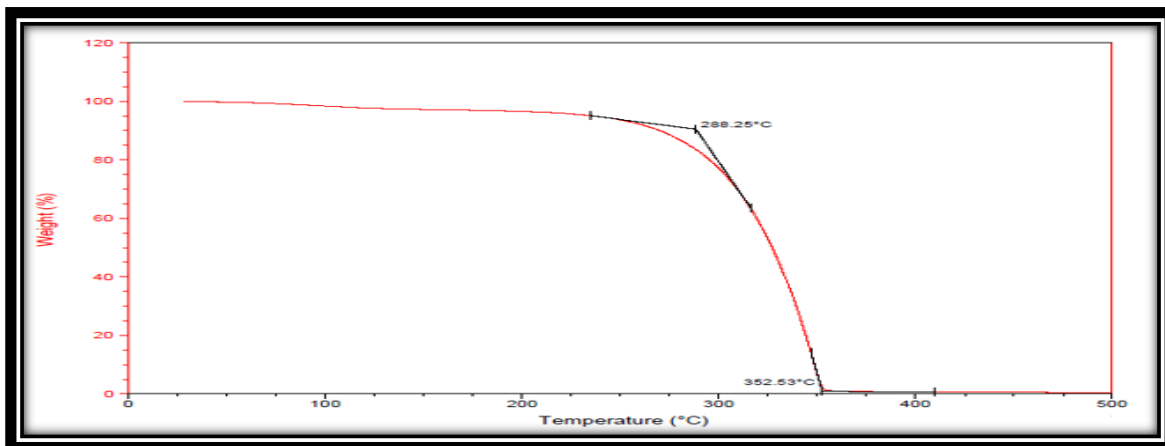


Figure 29. TGA analysis of the prepared compound (E)

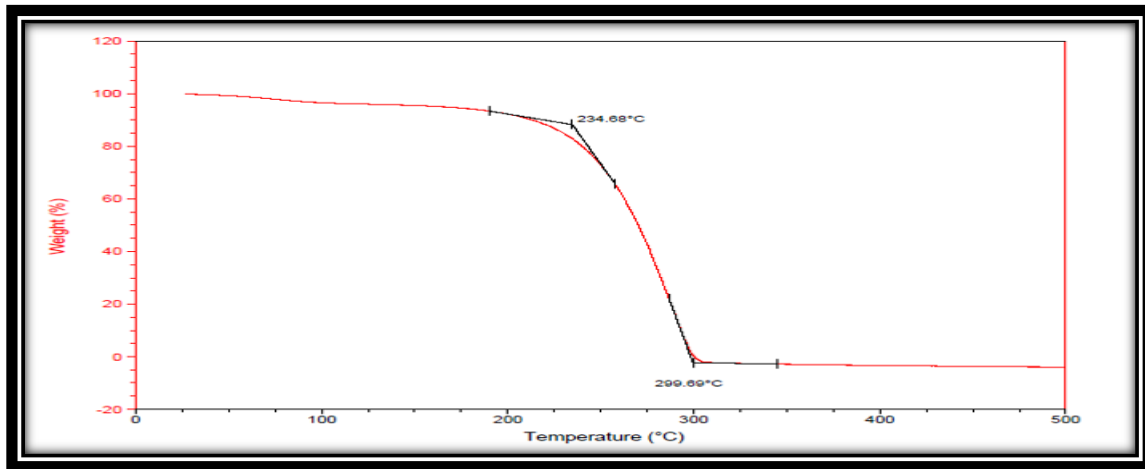
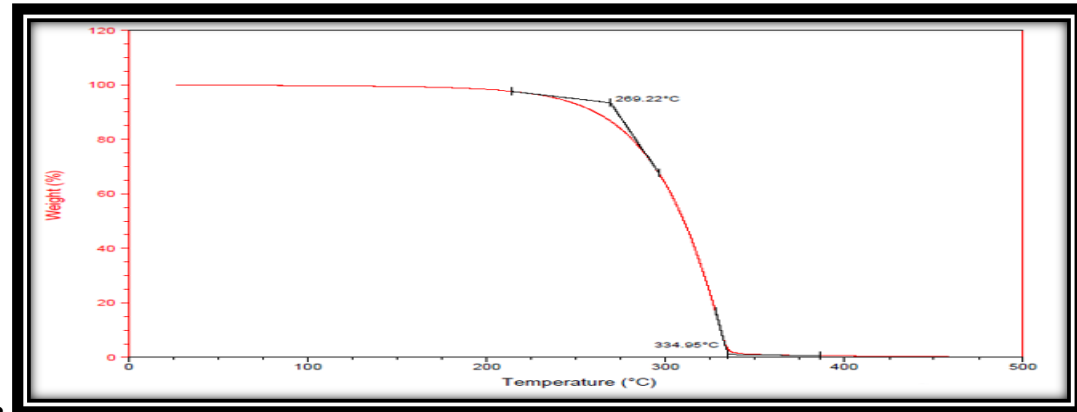
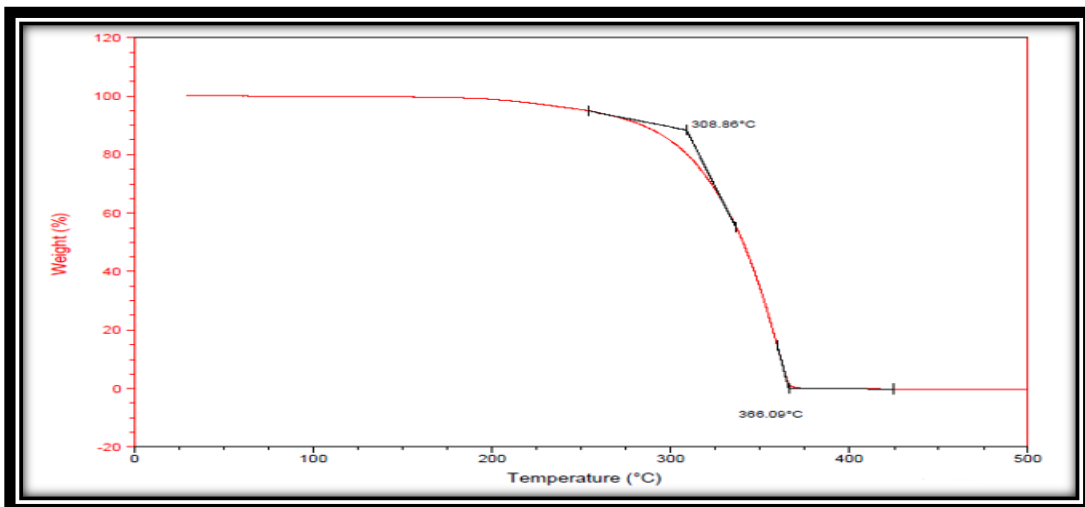


Figure 30. TGA analysis of the prepared compound (F)



• Figure 31. TGA analysis of the prepared compound (G)



• Figure 32. TGA analysis of the prepared compound (H)

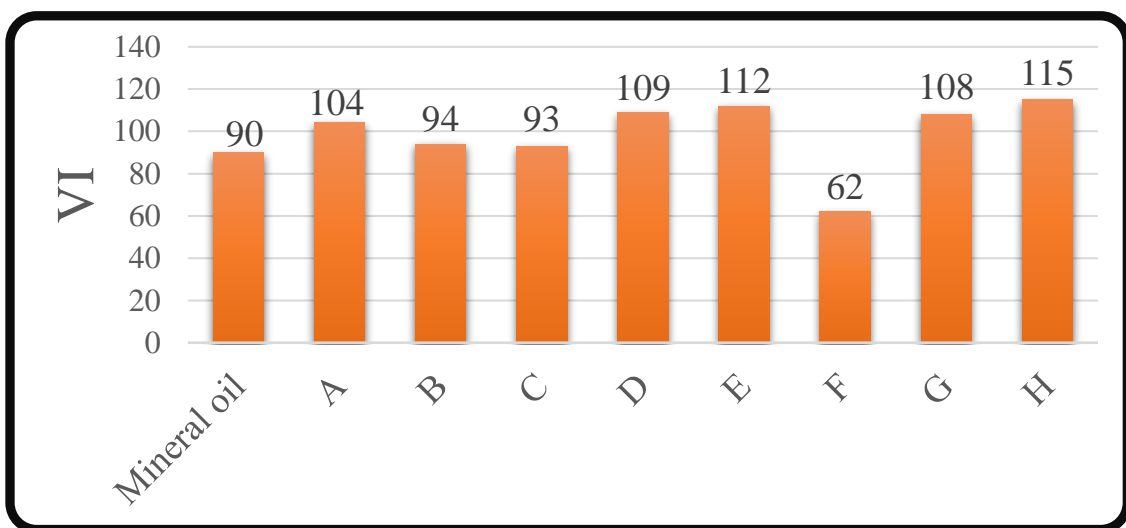
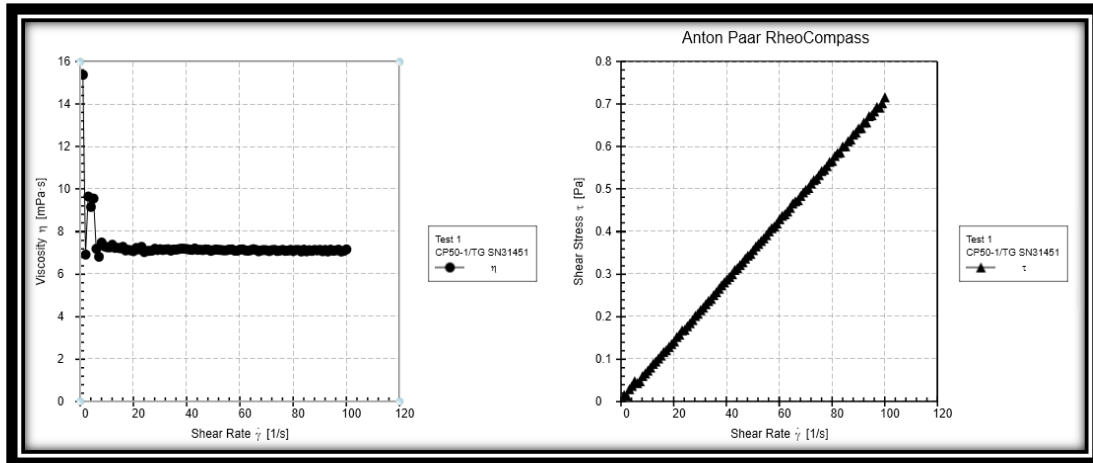
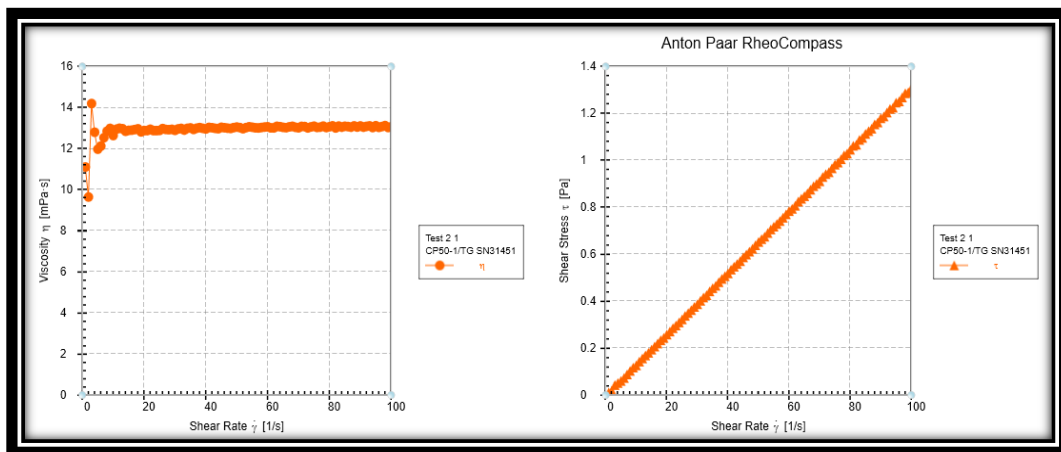


Figure 33. Dependence of VI on the mean molecular weight of synthetic lubricating oils
(A. B. C. D. E. F. G and H).



• Figure 34. The rheological behavior of synthetic lubricating oil (A)



• Figure 35. The rheological behavior of synthetic lubricating oil (B)

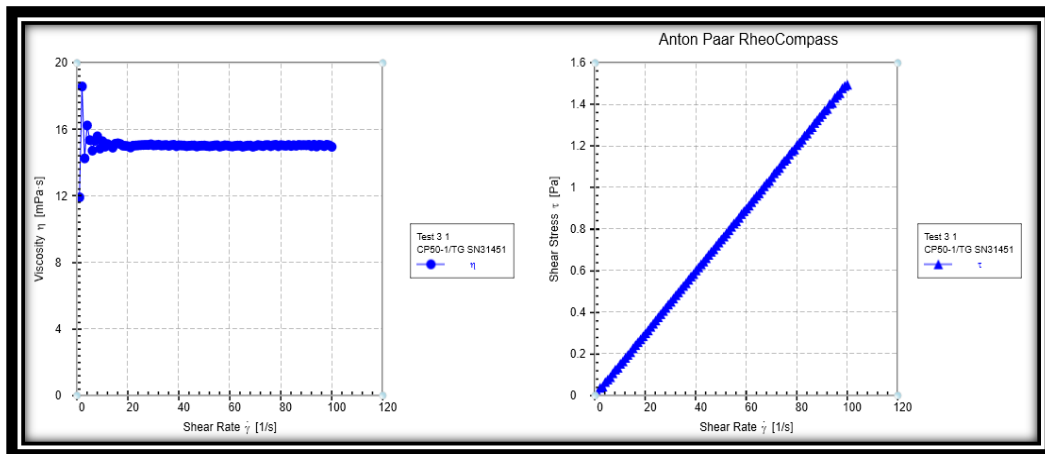
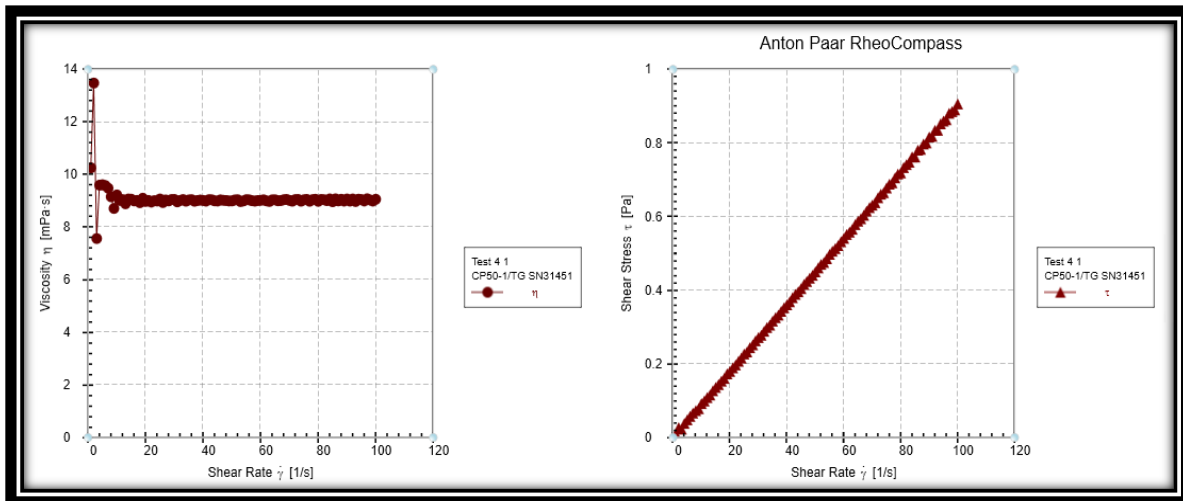
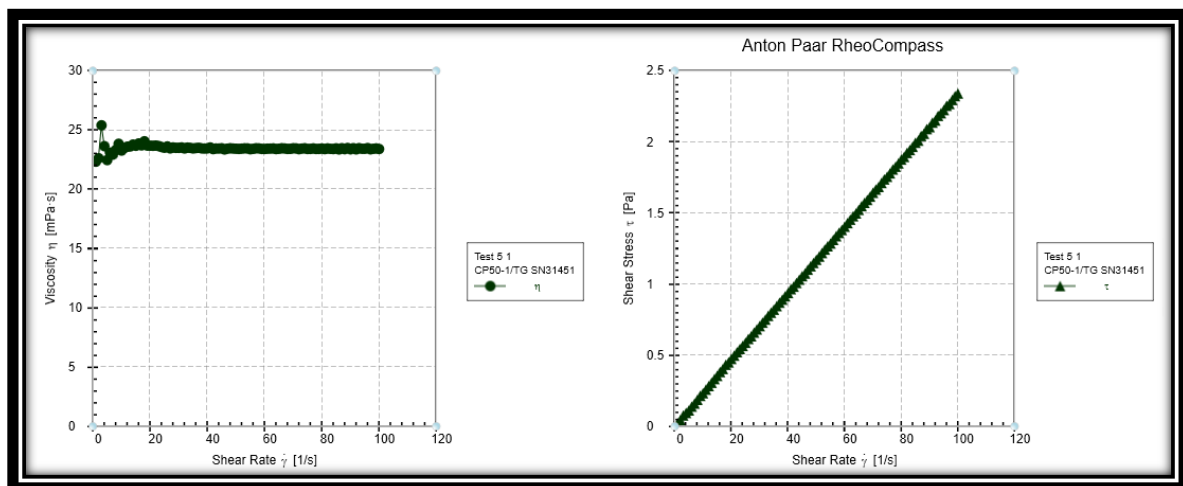


Figure 36. The rheological behavior of synthetic lubricating oil (C)



• Figure 37. The rheological behavior of synthetic lubricating oil (D)



• Figure 38. The rheological behavior of synthetic lubricating oil (E)

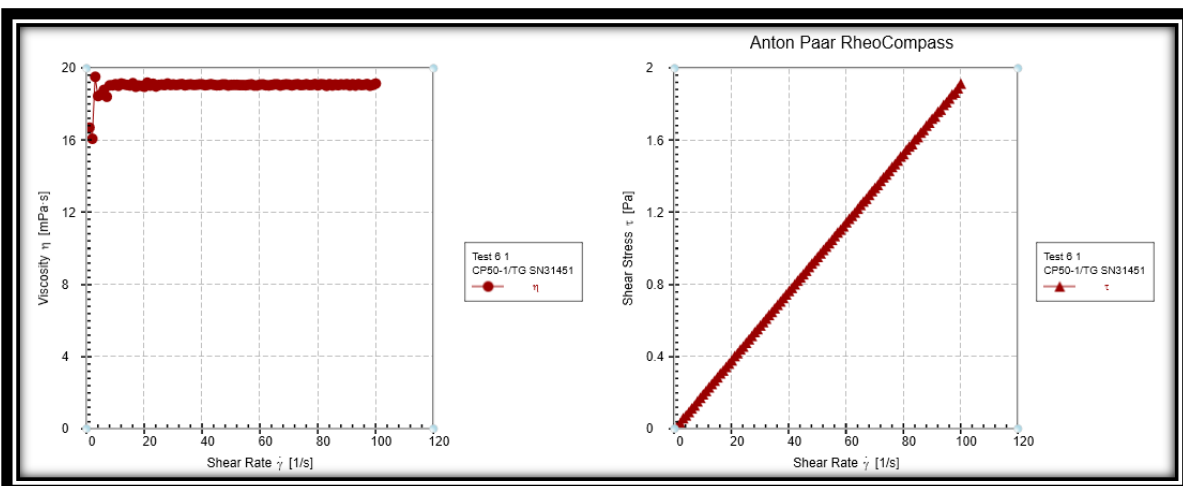


Figure 39. The rheological behavior of synthetic lubricating oil (F)

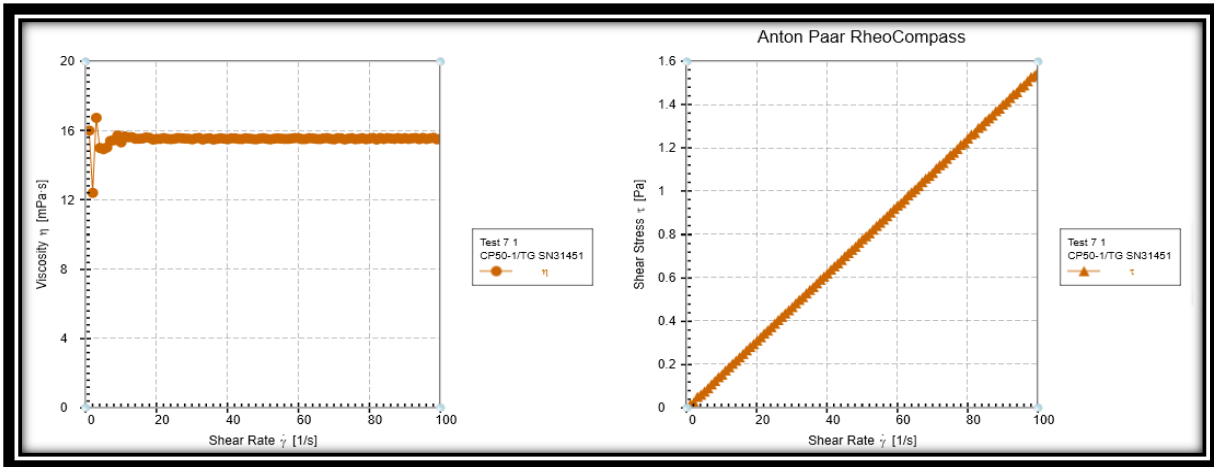
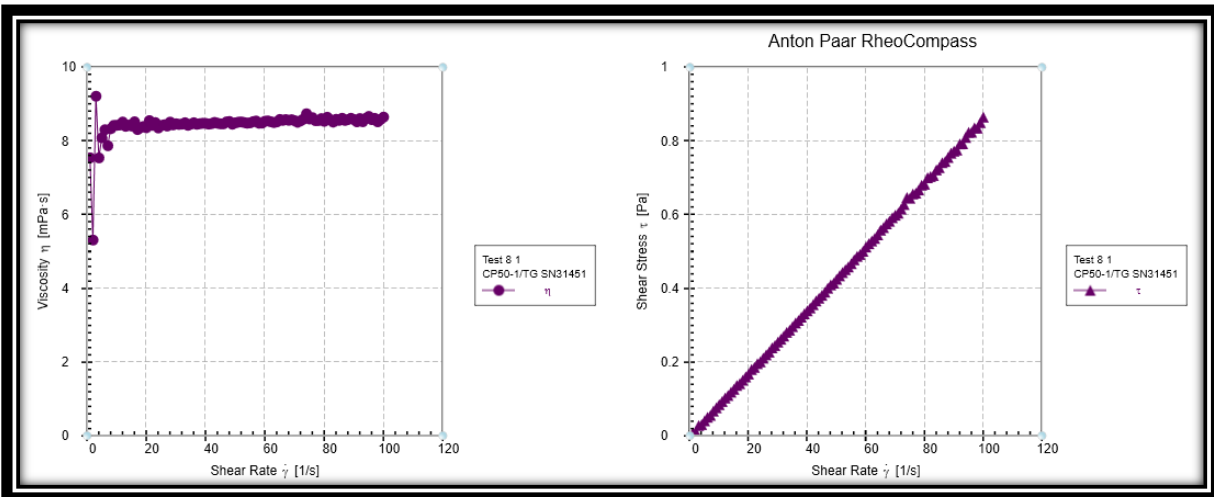


Figure 40. The rheological behavior of synthetic lubricating oil (G)



• Figure 41. The rheological behavior of synthetic lubricating oil (H)

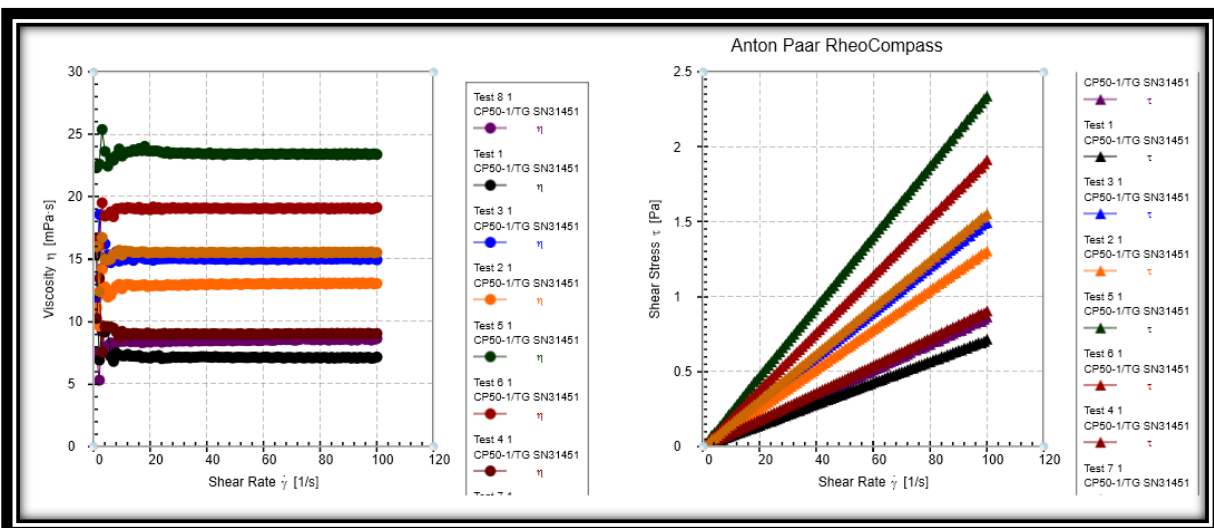


Figure 42. The comparative between rheological behavior of all synthetic lubricating oil (A. B. C. D. E. F. G and H)

References

- [1] Maione R and D'Elia L. Encyclopaedia of Hydrocarbons. Volume III. New Developments: Energy. Transport. Sustainability. Chapter 8 (transport). 8. 4 – Lubrication And Lubricants. (2007): 751-772
- [2] Ethan SZ. Sharma BK. Liu ZS. & Adhvaryu A. Lubricant base stock potential of chemically modified vegetable oils. *J. Agric. Food Chem.*, 2008; 56: 8919-8925.
- [3] Li W. Kong XH. Ruan M. Ma FM. Jiang YF. Liu MZ. Chen Y. and Zuo XH. Green waxes. adhesives and lubricants. *Phil. Trans. R. Soc. A.* 2010; 368: 4869-4890.
- [4] Cash W. Understanding the Differences between Synthetics. *Machinery Lubrication Magazine*. June 2015.
- [5] House T. Synthetic Esters: Engineered to Perform. *Machinery Lubrication Magazine*. April 2014.
- [6] Schaefer TG. Esters in Synthetic Lubricants. BOB is the oil guy. October 2011.
- [7] Sander J. When Do Synthetic Lubricants Make Sense? *Lubrication Engineers. Inc.* 2012.
- [8] Rudnick L. Synthetics. Mineral Oils. and Bio-based Lubricants Chemistry and Technology. CRC Taylor & Francis. 2006.
- [9] Greaves M. Oil Soluble Synthetic Polyalkylene Glycols a New Type of Group V Base Oil. *Lube Magazine*. United Kingdom Lubricants Association Ltd. August 2011
- [10] Ponnekanti N. Savita K. Development of ecofriendly/biodegradable lubricants: An overview. *Renew. Sust. Energ. Rev.*, 2012; 16: 764-774.
- [11] Anand S. War N. Chaudhari S. Chaudhar. P. A study of lubrication and its effect on steel in cold rolling mill: A review. *VSRD Int. J. Mech. Civ. Automob. Prod. Eng.*, 2013; 3: 87-92.
- [12] Chang T.-S. Yunus R. Rashid U. Choong TSY. Awang Biak DR. Syam AM. Palm oil derived trimethylolpropane triesters synthetic lubricants and usage in industrial metal working fluid. *J. Oleo Sci.*, 2015; 64: 143-151.
- [13] Li W. Wang X. Biolubricants derived from waste cooking oil with improved oxidation stability and low temperature properties. *J. Oleo Sci.*, 2015; 64: 367-374.
- [14] Salimon J. Salih N. Yousif E. Synthesis. characterization and physicochemical properties of oleic acid ether derivatives as biolubricants base stocks. *J. Oleo Sci.*, 2011; 60: 613-618
- [15] Kamal RS. Ahmed NS. and Nassar AM. Synthesis and Characterization of Mixed Esters as Synthetic Lubricants. *Pet Coal*. 2017; 59(6):736-746.
- [16] Erhan SZ. Sharma BK. Liu Z and Adhvaryu A. Lubricant Base Stock Potential of Chemically Modified Vegetable Oils. *Journal of Agricultural Food Chemistry*. 2008; 56: 8919-8925.
- [17] Nassar AM. Ahmed NS and Kamal RS. Preparation and Evaluation of Some Terpolymers as Lube Oil Additives. *Journal of Dispersion Science and Technology*. 2011; 32: 616-621.
- [18] Kamal RS. Ahmed NS. and Nassar AM. Synthesis and Evaluation of multifunctional lube oil additives. *Omniscriptum GmbH&Co.KG*. 2017: 56-63.
- [19] Al-Sabagh AM. Sabaa MW. Saad GR. Khidr TT and Khalil TM. Synthesis of polymeric additives based on itaconic acid and their evaluation as pour point depressants for lube oil in relation to rheological flow properties. *Egyptian Journal of Petroleum*; 2012; 21: 19-30.
- [20] Chhabra R P. Non-Newtonian Fluids: An Introduction. In *Rheology of Complex Fluids*. Deshpande AP. Kumer SPB. Krishnan. JM. Eds.; Springer Science business Media: New York. (2010)
- [21] Quoc-Hung N. and Ngoc-Diep N. Incompressible Non-Newtonian Fluid Flows. Mechanical Faculty. Ho Chi Minh University of Industry. Vietnam. *Progress in Fundamentals and Engineering Applications*. 2012.
- [22] El-Magly IA. Nagib HK. Mokhtar WM. Aspects of the behavior of some pentaerythritol ester base synlubes for turbo-engined. *Egyptian Journal of Petroleum*.2013; 22: 169-177.

To whom correspondence should be addressed: Dr. Rasha S. Kamal. Department of Petroleum Applications. Egyptian Petroleum Research Institute. Nasr City. P. O. Box 11727. Cairo. Egypt. dr.rasha.samir@yahoo.com

SUITABILITY OF JATROPHA OIL AS SURFACTANT IN STEAM ASSISTED RECOVERY OF NIGERIA BITUMEN

Fadairo Adesina, Ogunkunle Temitope, Oladepo Adebawale and Adeyemi Gbadegesin

Covenant University, Ota, Ogun State, Nigeria

Received March 1, 2018; Accepted April 27, 2018

Abstract

More ways to improve the normal high rates of steam assisted bitumen recovery techniques such as SAGD (Steam assisted gravity drainage) and CSS (Cyclic steam simulation) have been studied for some years now, and It has been discovered that the addition of surfactants on ore or injecting it with steam has recovered more bitumen than the injection of the typical steam, but due to the cost and reduction in availability of petro surfactants feed stock and the food competition created by using an edible feedstock for biodiesel surfactant there is need for the use of an alternative feedstock for biodiesel surfactants. In this project, the focus is on the use of jatropha oil (a non-edible feedstock) for biodiesel surfactant production was proposed.

The paper features series of experiments that were carried out to compare the strength of extraction of bitumen from tar sands using steam from water and steam or vapor from biodiesel (jatropha biodiesel) water mixture after spraying the core with biodiesel and finally toluene. The core was modified from the tar sand gotten from Imeri village in the southwestern part of Nigeria. The samples treated with biodiesel had better and improved recovery than the one with just steam from water, while toluene gives the over-all best recovery.

Keywords: *Jatropha oil; Surfactant; Oil recovery; Nigeria bitumen.*

1. Introduction

SAGD and CSS have proven to be the most effective thermal techniques in bitumen extraction from deep oil sands as they efficiently address factors that tend to reduce recovery of bitumen reservoir by a relative increase in reservoir temperature. In these methods, steam injected into a subsurface oil sands seam, condenses due to thermal energy losses and forms bitumen-water emulsions, which may be recovered by means of production wells [1-3]. Asphaltene fractions in the bitumen promote the formation of bitumen-water emulsions under thermal recovery conditions, and they act as surfactants reducing surface and interfacial tensions, thereby helping to break down the oil sands ore structure and promoting the release of bitumen from the ore [4-7].

Babadagli *et al.* [3] conducted steam assisted bitumen recovery experiments to determine the high recovery potential and efficiency increase of Tall and canola oil biodiesel and they compared it with recovery from injecting steam only. The first set of steam assisted bitumen recovery tests were performed on sands ore (8.5% bitumen, 86.2% sand, 4.9% moisture) using atmospheric pressure steam and injecting a canola oil derived BD at 1 g/kg-bitumen dosage into the low pressure steam line. The cumulative bitumen-water emulsion products were collected every 30 minutes intervals, and their bitumen contents were determined using the Dean-Stark extraction. The result shows that biodiesel dosages increase bitumen recovery efficiency in the early phase of the test. The disadvantage of the study is that canola oil is edible and the cost of canola seed is average \$630/ton as at June 2013 which is expensive compared to jatropha oil which is \$140/ton. Researches on the applications of jatropha oil in the bitumen extraction and processes have been advanced in the recent time because of its

market price, oil yield and not competition with human food. For instant Fadairo *et al.* [6] use the oil extract from jatropha for determining the softening point of Nigeria bitumen.

Use of surfactant additives to improve the efficiency of these thermal processes has been studied extensively over the decades [7] and the use of biodiesel or FAMEs as a surfactant additive have shown to improve the efficiency of thermal processes [3]. Biodiesel or FAMEs which is produced from the transesterification of edible and non edible feedstock (fatty acid glycerides) have shown to wet bitumen and water because of their hydrophilic (COOCH_3) and hydrophobic (C_nH_m) functional groups, thereby promoting the production of bitumen when introduced to oil sands. The use of edible feedstock for production of biodiesel poses problems to humans in terms of food completion, so we proposed the use of a non edible feedstock (jatropha oil) to produce jatropha biodiesel for the extraction of bitumen from oil sands via steam assisted recovery. Jatropha oil is produced from *Jatropha curcas*, *L.* seed which grows in tropical and subtropical climates across the developing world; it is very cheap feedstock compared to other feed stock.

This study used jatropha biodiesel in steam assisted bitumen recovery from oil sands gotten from Imeri village in the Southwestern region of Nigeria and compared it with the ordinary steam recovery of bitumen,

2. Methodology

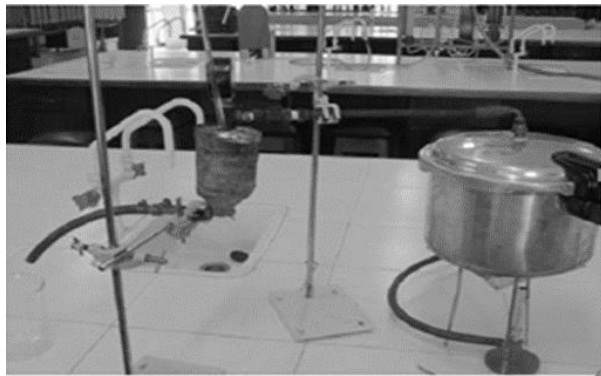


Figure 1. Pressure pot extractor set-up in Core Laboratory at Covenant University

The paper featured both the use of a pressure pot extractor to extract the bitumen from the core and Soxhlet extraction methods. The pot was modified to inject steam into an insulated chamber so has to extract heavy bitumen from the medium (core) inside the chamber (Figure 1), the extract along with condensed steam flows outside the chamber through an outlet connected to the end of the chamber. The extractor was designed and built to fulfill production situations where the pot and the connector act as the injector, the chamber with the medium in it serves as the reservoir, and the outlet is the producer.

2.1. Core preparation

The oil sands were gotten from Imeri village in Ondo state having a composition of 76% sand, 20% bitumen and 4% water. The oil sand was mixed with a larger proportion of sand in different percentages to form cores, the reason for mixing was because bitumen sand comes in molten form and would not readily form the core, so sand was added for the core to modify. The composition of the cores is given by the Table 1.

Table 1. Sample composition before experiment

Sample ID	Solvent	Solvent (mL)	Sample (g)	Bitumen (g)	Solid in Ore (g)
S1	Steam	300	223	89.2	133.8
S2	Steam	300	25.6	2.048	23.14
S3	Steam	300	26.8	1.876	24.55
S4	Steam	300	28.62	1.7172	26.56
S5	Steam	300	26.7	1.335	25.1
S6	Steam	300	27.7	1.108	26.37
BD1	Steam+Bio-diesel	300(25% BD)	226	90.4	135.6
BD2	Steam+Bio-diesel	300(25% BD)	23.3	1.864	21.06
BD3	Steam+Bio-diesel	300(25% BD)	27.4	1.918	25.1

Sample ID	Solvent	Solvent (mL)	Sample (g)	Bitumen (g)	Solid in Ore (g)
BD4	Steam+Bio-diesel	300(25% BD)	27.8	1.668	25.8
BD5	Steam+Bio-diesel	300(25% BD)	26.1	1.305	24.53
BD6	Steam+Bio-diesel	300(25% BD)	27.35	1.094	26.03
T1	Toluene	300	234.8	93.92	140.88

3. Experiments

The purpose of the work was to determine the effect of adding jatropha biodiesel in steam assisted bitumen recovery. The initial experiment, a pilot test involves using a Soxhlet extractor (Figure 2) for bitumen extraction from three (3) tar sand samples using different solvents (steam only, jatropha biodiesel assisted steam and toluene).



Figure 2. Setup of Soxhlet extraction for the pilot tests at Covenant University Petroleum Laboratory

The samples were labelled S1, BD1, and T1, which were denoted as steam only, jatropha biodiesel assisted steam and toluene respectively. The results obtained for jatropha biodiesel assisted steam showed high and improved recovery than the results obtained using steam from water alone as shown in Table 2. This prompted and advanced the study to carry out ten (10) more extractions using the fabricated heating mantle (pressure pot), five of the extraction were carried out using by steam injection denoted as case 1 (samples S1, S2, S3, S4, S5), and the other five extractions where carried out by injecting biodiesel assisted water vapor or steam denoted as case 2 (Samples B1, B2, B3, B4, B5). The experiment using

jatropha biodiesel assisted steam featured the spraying of jatropha biodiesel on the core as a surfactant and later the injection of steam or vapor from a mixture of 3000mL of water and biodiesel.

Table 2. Results obtained from three (3) tar sand samples using different solvents

Type of Solvent for Extraction	Vol. of solvent (mL)	Wt. of solvent (g)	Wet sample after extraction (g)	Bitumen extracts (g)	Unrecovered bitumen (g)	Bitumen recovered (%)	Bitumen unrecovered (g)
Steam	300	308.3	227.7	19.38	69.82	21.7	78.3
Toluene	300	249.6	221.9	38.1	55.82	40.6	59.4
Steam Assisted Jatropha Bio-diesel	300*	347.1	229.4	30.8	59.6	34.1	65.9

*(25% BD)

The cores labeled S1-S5 were extracted by steam and the cores labeled B1-B5 were extracted by biodiesel assisted steam. The mode of extraction was done to study the strength of extraction of oil from tar sand by injecting steam from water and the strength of extraction of oil from tar sand by steam injection of water biodiesel mixture after spraying biodiesel on the core. The extraction is based on pressurized steam from water and biodiesel, the injected steam or vapor temperature is lesser than the boiling point of the fluids or solvent involve. During the extraction, steam is produced by heating the fluid to about or above boiling point

in a particular medium, and the steam passes through a channel into a medium that holds or house the core, the steam forces oil out of the core leaving the residue.

Table 3 shows the results of the pilot test (S1, BD1, and T1) and the first five cores labeled S1 to S6 which were extracted via steam injection; it can be observed that as the Mass percentage fraction of bitumen decreases the extraction strength of steam reduces as percentage recovered becomes rapidly lower. The resulting condensates and extract from steam injection only were observed to stick to the gas beaker like bitumen to rock surface. The average temperature of extraction at 94°C and time of extraction was 4hrs.

Table 3. Effects of jatropha bio-diesel, water, and toluene on bitumen ore extraction

Sample ID	Extraction solvent	Wt. of recovered bitumen (g)	Wt. of unrecovered bitumen (g)	Bitumen recovery (%)	Percentage unrecovered (%)
S1	Steam	19.38	68.82	21.7	78.3
S2	Steam	1.5	0.548	73.6	26.4
S3	Steam	1.28	0.596	69	31
S4	Steam	1.16	0.5572	68	32
S5	Steam	0.8	0.535	60	40
S6	Steam	0.6	0.508	55	45
BD1	Steam+Bio-diesel	30.8	58.6	34.1	65.9
BD2	Steam+Bio-diesel	1.63	0.234	88	12
BD3	Steam+Bio-diesel	1.6	0.318	84	16
BD4	Steam+Bio-diesel	1.3	0.368	78	22
BD5	Steam+Bio-diesel	1.1	0.205	85	15
BD6	Steam+Bio-diesel	0.8	0.594	74	26
T1	Toluene	38.1	55.82	40.6	59.4

Samples labeled B1 to B6 that were sprayed by biodiesel first and were later extracted via injection of steam from water biodiesel mixture shows a higher percentage of bitumen recovered and as the percentage fraction of bitumen decreases extraction strength reduces but not rapidly. During the experiment it was witness that at a low temperature of 50°C the biodiesel in the mixture started vaporizing forming a foamy like substance which is channeled to the chamber and the resulting condensates and extract were observed all in a liquid suspension in the glass beaker i.e. the bitumen did not stick to beaker like in steam injection, it was soluble in the liquid suspension. The average temperature of extraction at 94°C and time of extraction was 3:30 hrs.

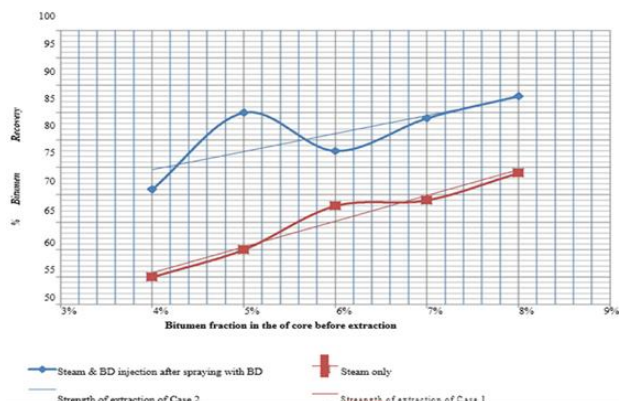


Figure 3 Percentage bitumen recovered vs. bitumen saturation of core samples

Analysis of figure 3: The graphs show the resultant recovery from the two methods; the biodiesel extraction curve is placed at a higher level than the steam extraction curve, therefore, showing that biodiesel had better recovery rates than ordinary steam. It also shows that the decline in the strength of extraction in steam is steeper than that of biodiesel i.e. steam injection will fail for more consolidated bituminous reservoirs where bitumen is drier than biodiesel. This can be attributed to the level at which the core was saturated with biodiesel when it was first sprayed on the core.

4. Discussion

The tables and graph above shows that Case 2 extraction method yielded more bitumen than Case 1 and this can be attributed to the effect of method and practices carried out in Case 2; which are

4.1. The effect of spraying biodiesel on the core

FAMEs (Fatty Acid Methyl Ester) have proved or been observed to wet both bitumen and water because of their hydrophobic (C_nH_m) and hydrophilic ($COOCH_3$) functional groups. Surfactant behavior of (JOFAME) Jatropha, oil Fatty Acid Methyl Esters, promotes wetting bitumen with water, so when jatropha biodiesel was sprayed into the core, it reduced the interfacial tension between bitumen and the sand particles at the surface making it easier for condensed vapor or steam to wet the core and mobilize bitumen for movement. But, since the core was already solidified sprayed biodiesel could not saturate the whole core as it could only penetrate cracks in the core, leaving a large volume (especially the inner part of the core) unsaturated.

4.2. The effect of injecting biodiesel -water vapor

The initial purpose of adding biodiesel to water was to generate steam or vapor with a fraction of biodiesel in it so as to ensure that the surfactant is continuously introduced in the core at any time during the extraction, so as to make up for the unsaturated volume of the core. But, during extraction when part of the biodiesel water mixture (80% biodiesel & 20% water) had to be injected first because its early vaporization, the effect was considered to be

- The early start time of thermal extraction as BD vaporizes earlier than steam
- Increase in saturation of surfactant in the core before actual steam from water is injected there by increases mobility of bitumen in the core
- Starts recovering bitumen before steam is generated in the water.
- Helps in the general mobilization of bitumen extract from the core into liquid suspension as seen in the extracts of Case 2

This was termed the "**first injecting phase**" in Case 2. After the BD water vapor goes, the larger fraction of water reaming is continuously heated till steam is generated

4.3. The effect of injecting steam from remaining water in Case 2

The initial purpose of Water was to create steam to assist in bitumen recovery and to also assist in creating a drive mechanism for Biodiesel to the core so as to create a continuous surfactant delivery to the core during extraction time. But, part of the biodiesel water mixture vaporized and had enough drive to reach the chamber, the effect of the remaining steam that was generated or injected when the temperature was about 88- 92°C or when water reached its boiling point where considered to be

- It increased the temperature of the chamber which favored viscosity reduction of the bitumen in the core.
- It continued the thermal extraction that started when part of the mixture vaporized earlier, and it cleans the residual bitumen left by the first vaporized mixture.

It has a longer injection and extraction time than the earlier vaporized BD and water. And was term as the "**second injecting phase**" in Case 2

4.4. The Effect of Varied Time on the Extraction Performance on both Case 1 and Case 2

The time taken for steam only to extract bitumen in a solidified core where sand particles are not produced is more than when bitumen are already lose from the sand particles by surfactant action in the same production condition. So the time of extraction For Case1 was longer so as to yield good recovery rates, but Case 2 took a lesser time of extraction not only because the bitumen is lose from sand particles but the solvent injection was in two phase (BD & water) and steam and had better recovery rates than Case 1.

5. Conclusion

The use of thermal methods in bitumen recovery in places where oil sands have large deposits like the Alberta oil sand deposits in Canada has increased due to increase in heavier oil demands because of the failing conventional oil market and its rapid depletion. These thermal methods (Steam injection) have shown high recovery rates even in the experiment carried out in this study (Case 1), but laboratory results of Case 2 (use of jatropha biodiesel as an additive in a steam injection) have shown to have higher recovery rates than steam injection only.

The paper also justifies the use of a non-edible, cheaper feedstock for biodiesel production, which was used as surfactant additive in steam assisted bitumen recovery from oil sands.

Acknowledgments

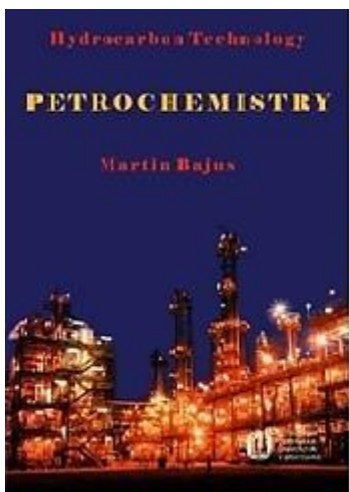
We wish to thank the Management of Covenant University Ota Nigeria for sponsoring this research and FatherHeroz Forte Technology Research Consortium for their technical support.

References

- [1] Babadagli T., Er V., Naderi K., Burkus Z., Ozum B. (2009) Use of BioDiesel as an Additive in Thermal Recovery of Heavy Oil an Bitumen Canadian International Petroleum Conference, Calgary, Alberta, Canada, June 16-18.
- [2] Yuan W, Hansen AC, Zhang Q. Vapor Pressure and Normal Boiling Point Predictions for Pure Methyl Esters and BioDiesel Fuels, Fuel,2005; 84: 943-950
- [3] Babadagli T, and Ozum B. BioDiesel as Additive in High Pressure and Temperature Steam Recovery of Heavy Oil and Bitumen, Oil & Gas Science and Technology – Rev. IFP Energies Nouvelles, 2012; 67(3): 413-421
- [4] Adegoke OS, Ibe EC. The tar sand and heavy crude resources of Nigeria. Proceeding of the 2nd International conference on heavy oils and Tarsands, Carcas 1982: 280-285.
- [5] Fagbote EO, Olanipekun EO. Characterization, Distribution, Sources and Origins of Aliphatic Hydrocarbons of the Soils of Agbabi Bitumen Deposit Area, Western Nigeria. African Journal of Scientific Research, 2012; 10(1): 1-24.
- [6] Fadairo A, Adeyemi G, Bello K, Olafuyi O. The Use of Jatropha Oil for Determining the Softening Point of Nigeria Bitumen Samples. Pet Coal, 2014; 56(4): 354-358.
- [7] Gonçalves LIB, Blaiterman G, Diniz JP, Moreno RBZL, Trevisan OV. Heavy Oil Recovery By Steam Injection – Numerical simulation On Production Strategy, CEP: 13083-970.

To whom correspondence should be addressed: Dr. Fadairo Adesina, Covenant University, Ota, Ogun State, Nigeria

BOOK REVIEW



Martin Bajus : **Hydrocarbon Technology - Petrochemistry**

Issued by Slovenská chemická knižnica FCHPT-STU
Bratislava, 2017, 1. Edition, 430 pages
Paperback, price 9,10 EUR
ISBN 978-80-89597-80-2

At the beginning of 2018 a fresh book on Hydrocarbon Technology – Petrochemistry, published by the Slovak Chemical Library at the Faculty of Chemical and Food Technology in Bratislava appeared on the book market. You can get the book from the bookseller Malé Centrum. The author of the book is Professor Martin Bajus, a Slovak leading expert in refinery, petrochemical, energy and recycling technologies. He started a school of pyrolysis at the Slovak University of Technology. The distinctive features of the successful Bratislava School of Pyrolysis are not only the results gained from research but also the industrial applications of these results into recommended petrochemical and recycling technologies, not only in Slovakia but also abroad (Czech Republic). Professor Bajus is one of the top Slovak scientists and inventors in the field of chemical technology. He is still active in science and as a teacher at the FCHPT.

This university textbook introduces the reader to current and interesting texts, written in a modern style of English. It represents the topical subject matter in a complex way. A wide and extensive coverage of the 430-page issue surely was a great challenge and required effort and patience on the side of the author. In particular, the most valuable is the information based on huge knowledge of the author on the hydrocarbon technology. The book is especially suited for university educators and students that study in bachelor, master or doctoral study programmes that train in chemical technology, possibly focussed on petrochemistry.

The second book in the series on hydrocarbon technology deals with petrochemical changes of hydrocarbons coming from oil and natural gas. These hydrocarbons are obtained in refinery processes and are the subject of the first book.

In the introduction, the author points out the importance of petrochemical processes in chemical technology in the direction: chemical science → chemical technology → hydrocarbon technologies → petrochemistry. The textbook explains basic principles and introduces causal relations between the decisive chemical and physical phenomena. The author does not have the intention to elaborate hydrocarbon technologies related to petrochemistry in an encyclopaedic form. In the first place, the author favours orientation in concepts before facts. The book Hydrocarbon Technology - Petrochemistry presents the basics of those chemical processes that are the building

stones of chemical technology. These processes include: thermodynamics, chemical kinetics, reactor calculations, as well as industrial catalysis.

Professor Martin Bajus has written so much needed pedagogically excellent text, which has been missing in the Slovak market for almost 30 years. He has developed an original concept of petrochemistry, supported by four pillars. The elementary source are hydrocarbons from crude oil and natural gas. Alternative raw materials and alternative technologies can be exploited because of excessive and cheap propane, ethane and methane from shale, strand and natural gases.

In particular, this applies to propylene, a growing production of which is gradually shifting from pyrolysis of liquid feedstocks to pyrolysis of lighter shale condensates. The utilisation of shale gas is exponentially growing, especially in the United States. The author also deals with the processing of biomass and waste. These two are understood as complementary to those resources that are to replace fossil raw-materials in the future.

The petrochemical industry is based on four pillars: pillar A is alkene, pillar B covers BTX aromatics, pillar C represents the C₁-technologies, and pillar D is heavily diversified by petrochemicals containing oxygen, halogens, nitrogen and sulfur.

The author has logically chosen from a wide range of processes. To know about individual processes means to understand the basics of the culture of chemical-engineering. As an example one can mention successful processes in oil refinery or production of chemicals from synthesis gas. Chemical engineers have had tremendous success in the development of high-capacity chemical technologies (production of methanol, Fischer-Tropsch synthesis, ammonia). However, in some other areas in the past, they were not so successful. Presently, these processes are gaining more and more importance. Such processes can be found in hydrogen technologies, bio-refineries, recycling technologies, microchannel technologies and nanotechnologies. These technologies are the subject matter of separate chapters of the book. Recently the focus has been lifted to the intensification of processes, such as energy technologies and sustainable technologies.

Most of the chapters introduce the individual processes in clear explanatory drawings and simplified flow-chart schemes presented in colour. For the sake of better clarity of the technology schemes, most of the depicted schemes exclude controlling systems, valves or pumps. After studying the book students will improve their conceptual thinking to design new processes.

The presented book serves as the basic study material for many subjects studied at the Faculty of Chemical and Food Technology, however, for some subjects it is just a supplementary study material:

- Petrochemistry
- Organic technology and petrochemistry
- Crude oil and hydrocarbon technologies
- Energy materials and technologies
- Recycling technologies
- Natural gas
- Alternative fuels
- Catalysis

I believe that the book Hydrocarbon Technology – Petrochemistry will be a welcome study material both for the students of the Faculty of Chemical and Food Technology, STU, but also for other students studying for higher education in the Slovak Republic. As a teacher with long-time practical experience I can recommend this book as a study material to all students that study chemical technology or similar field of science.

Viktor Milata